Microstructure-Based Process Modeling of Open Die Forging of a High Strength Martensitic Stainless Steel

by

Simin DOURANDISH

MANUSCRIPT-BASED THESIS PRESENTED TO ÉCOLE DE TECHNOLOGIE SUPÉRIEURE IN PARTIAL FULFILLMENT FOR THE DEGREE OF DOCTOR OF PHILOSOPHY Ph.D.

MONTREAL, DECEMBER 27TH, 2022

ÉCOLE DE TECHNOLOGIE SUPÉRIEURE
UNIVERSITÉ DU QUÉBEC

ACKNOWLEDGMENTS

Modélisation de procédé basée sur la microstructure de forgeage à matrice ouverte des arbres de turbine en aciers à haute résistance

Simin DOURANDISH

RÉSUMÉ

Dans les composants techniques, les aciers à haute résistance sont bien connus pour leur résistance à la corrosion et leur excellente combinaison de résistance et de ténacité. Le traitement thermique peut changer leurs propriétés et les rendre adaptées à une variété d'applications telles que les plates-formes offshores pour l'extraction du pétrole, les outils de coupe, les générateurs de vapeur, les récipients sous pression et les lames. La fabrication de ces gros composants commence par la séquence des opérations de coulée, de forgeage, de trempe et de revenu. Le but principal du forgeage du lingot coulé est d'éliminer les défauts de coulée qui se produisent pendant la solidification, y compris le retrait, la ségrégation, la porosité, l'inclusion non métallique et les fissures. Ces défauts sont initiés lors du grondement de l'acier liquide et/ou lors de la solidification dans le moule. Bien que l'optimisation du processus de coulée ait été utilisée pour réduire l'incidence de ces défauts, il est très difficile de les prévenir. Un défaut préjudiciable entraîne des propriétés hétérogènes dans le lingot coulé final, ce qui affecte considérablement les performances et l'aptitude des produits finis. Cependant, si les défauts sont trop grands, il est très difficile de guérir toute la porosité seulement le procédé de forgeage avant. Par conséquent, le calendrier de forgeage approprié et précis est important pour les industries de fabrication lourde. Le but principal de ce travail est d'examiner les mécanismes impliqués dans l'évolution microstructurale de l'acier inoxydable martensitique utilisée dans les industries pétrolières et gazières comme arbre de turbine pendant la rupture de la structure coulée. En outre, le comportement de déformation à chaud de l'acier étudié a été modélisé à l'aide du meilleur modèle de matériau prévisible. En utilisant un code d'éléments finis, les équations constitutives et les modèles d'évolution de microstructure sont mis en œuvre, puis l'évolution thermomécanique et de microstructure sont couplées.

La première partie de cette étude fournit la caractérisation des structures de coulée lors de la solidification. Des techniques avancées de caractérisation ont été utilisées pour déterminer la distribution, la composition chimique et l'identification des phases. Tous les facteurs déterminants ont été pris en compte pour étudier la précipitation et la ségrégation en phase pendant le processus de coulée.

La deuxième partie de cette étude consiste à effectuer les essais de compression isotherme à chaud à l'aide d'un simulateur thermomécanique, Gleeble^{TM} 3800, pour déterminer le comportement d'écoulement de l'acier inoxydable martensitique sous une large gamme de températures et de vitesses de déformation correspondant au procédé de forgeage industriel pour les lingots de grande taille. La contrainte d'écoulement mesurée a été corrigée en

considérant l'effet du frottement et du chauffage adiabatique. La contrainte d'écoulement double corrigée est utilisée pour développer un modèle précis afin de prédire le comportement d'écoulement du matériau. Le meilleur modèle de courbes de flux prédictives a été établi et sa précision a été vérifiée auprès de la mesure expérimentale. Plus précisément, la comparaison quantitative est effectuée entre les modèles Hansel-Spittel et les modèles à compensation de déformation pour déterminer la précision des modèles développés.

Le forgeage lourd est un procédé hautement non linéaire dans lequel la déformation plastique et la recristallisation modifient à la fois la microstructure et les conditions limites. Dans le forgeage à chaud, l'évolution de la microstructure influe sur les comportements de déformation en raison de ses effets sur la récupération dynamique, la recristallisation dynamique et la croissance du grain. En même temps, les paramètres de forgeage tel que la déformation, la température et l'évolution de la microstructure de commande de séquence de passage. Par conséquent, la troisième partie de ce projet est consacré à l'étude de l'effet des paramètres de travail sur l'évolution de la microstructure pendant le forgeage à chaud du MSS. Après une analyse expérimentale de l'évolution de la microstructure, les équations mathématiques qui décrivent les changements de microstructure ont été développées.
La prochaine étape consiste à intégrer quelques équations constitutives et des modèles de microstructure dans un simulateur d'éléments finis 3D pour prédire les variations de déformation, de fraction DRX, de taille de grain DRX et de critères de dommages. Une des industries de forgeage détermine les conditions de déformation dans lesquelles le lingot est susceptible de fissuration et de défaillance du composant. Il est donc très important de prévoir les conditions de déformation risquées ou la région du composant avec un facteur de dommage maximal.

Après validation de tous les modèles, le processus de forgeage du lingot de 13,5-tonne a été simulé par le système développé correspondant à la condition industrielle. L'influence des paramètres de travail, y compris la température, la déformation et le taux de déformation, sur l'évolution de la microstructure a été analysée. La simulation du processus de forgeage a été utilisée pour analyser la déformation, la température, la fraction dynamique du volume de recristallisation et les variations de la taille du grain. Sur la base du système de simulation développée, un autre procédé de forgeage à chaud optimal a été conçu.

Mots-clés: Acier inoxydable martensitique, Déformation à chaud, Simulation d'éléments finis, Évolution microstructure, Forgeage de lingots de grande taille, Recristallisation dynamique, Analyse des dommages, Équation constitutive, modélisation de matériaux

Microstructure-based process modeling of open die forging of turbine shafts made of high strength steels

Simin DOURANDISH

ABSTRACT

In engineering components, high-strength stainless steels are well known for their corrosion resistance and excellent combination of strength and toughness. Heat treatment can change their properties and make them suitable for a variety of applications such as offshore platforms for oil extraction, cutting tools, steam generators, pressure vessels, and blades. Manufacturing of these large components starts with the sequence of casting, forging, quenching, and tempering operations. The main aim of forging the as-cast ingot is to eliminate the casting defects that occur during solidification including shrinkage, segregation, porosity, non-metallic inclusion, and cracks. These defects are initiated during the teeming of the liquid steel and/or during solidification in the mold. Although casting process optimization has been used to reduce the incidence of these defects, preventing them is very difficult. A detrimental defect causes heterogeneous properties in the final cast ingot, which significantly affects the performance and suitability of the final products. However, if the defects are too big, it is very difficult to heal all the porosity just by the forward forging process. As a result, the appropriate and accurate forging schedule is significant for heavy manufacturing industries. It is the main purpose of this work to examine the mechanisms involved in the microstructural evolution of a martensitic stainless steel used in oil and gas industries as a turbine shaft during the breakdown of the as-cast structure. In addition, the hot deformation behavior of the investigated steel was modeled using the best predictable material model. Using a finite element code, the constitutive equations and microstructure evolution models are implemented, and then thermomechanical and microstructure evolution are coupled.

The first part of this study provides the microstructure characterization of casting structures during solidification. Advanced characterization techniques were used to determine the phase distribution, chemical composition, and phase identification. All determining factors were considered to investigate the occurrence of phase precipitation and segregation during the casting process.

The second part of this study is focused on isothermal hot compression tests using the thermomechanical simulator machine, Gleeble ^{TM} 3800, in order to determine the flow behavior of the investigated martensitic stainless steel under a wide range of temperatures and strain rates corresponding to the industrial forging process for large size ingots. The measured flow stresses were corrected by considering the effect of friction and adiabatic heating and then used to develop a model in order to predict the flow behavior of the material. The mathematical equations that best predict the flow curves model were established and the accuracy of the developed material model was verified with experimental measurements.

X

Heavy forging is a highly nonlinear process in which plastic deformation and recrystallization change both the microstructure and the boundary conditions. In hot forging, microstructure evolution impacts deformation behaviors due to its effects on dynamic recovery, dynamic recrystallization, and grain growth. At the same time, forging parameters such as strain, strain rate, temperature, and pass sequence control microstructure evolution. Therefore, the third part of this project was allocated to investigating the effect of working parameters on microstructure evolution during the hot forging of martensitic stainless steel. After experimental analysis of microstructure evolution, the mathematical equations which describe the microstructure changes were developed.

The next step was integrating the constitutive equations and microstructure models into a 3D finite element code to predict the variations of strain, dynamic recrystallization fraction, DRX grain size, and damage. The most important criterion in the forging industry is to determine the deformation conditions at which the ingot is susceptible to cracking and failure of the component. Therefore, the prediction of the risky deformation conditions or areas of the component is of great importance.

After the validation of all models, the forging process of a 13.5-ton ingot was simulated by the developed system based on industrial operational practice. The influence of working parameters including temperature, strain, and strain rate on microstructure evolution was analyzed. Simulation of the forging process has been used to analyze strain, temperature, dynamic recrystallization volume fraction, and grain size variations. Based on the developed simulation system, an optimum hot forging process was designed.

Keywords: Martensitic stainless steel, Hot deformation, Finite element simulation, Microstructure evolution, Large size ingot forging, Dynamic recrystallization, Damage analysis, Constitutive equation, Material modeling

TABLE OF CONTENTS

Page

XII

LIST OF TABLES

LIST OF FIGURES

Page

XXVI

LIST OF ABBREVIATIONS AND ACRONYMS

2D	Two Dimensions
3D	Three Dimensions
AISI	American Iron and Steel Institute
ARRE	Average Absolute Relative Error
BC	Boundary Condition
BCC	Body-Centered Cubic
BCT	Body-Centered Tetragonal
CAD	Computer-Aided Design
DMM	Dynamic Material Model
DRV	Dynamic Recovery
DRX	Dynamic Recrystallization
DRX	Dynamic Recrystallization
DSC	Differential Scanning Calorimetry
EBSD	Electron Back Scattered Diffraction
EDS	Energy Dispersion Spectroscopy
FCC	Face-Centered Cubic
FEM	Finite Element Modelling
FM	Free from Mannesmann Effect
GB	Grain Boundary
HAGB	High Angle Grain Boundary
HCL	Hydrochloric Acid
HS	Hansel-Spittle

HV	Hardness Vickers
JC	Johnson-Cook Model
JMAK	Johnson-Mehl-Avrami-Kolmogorov
KM	Kocks-Mecking Model
LAGB	Low Angle Grain Boundary
LMF	Ladle Metallurgy Furnace
MD	Modified Design
MSS	Martensitic Stainless Steel
MZA	Modified Zerilli-Armstrong Model
OD	Original Design
OLS	Optical Laser Scanning Microscope
PDM	Power Dissipation Map
R	Correlation Coefficient
SEM	Scanning Electron Microscope
SFE	Stacking Fault Energy
SIBM	Strain-Induced Grain Boundary Migration
TC	Thermocouple
WH	Work Hardening
XRD	X-Ray Diffraction

LIST OF SYMBOLS AND UNITS OF MEASURMENT
(INTERNATIONAL SYSTEM)

$A, A_1, A_2, n, \alpha, n_1, n_2,$	Arrhenius equation material constants
$A, m_1, m_2\ m_3\ m_4\ m_5\ m_6\ m_7\ m_8\ m_9$	Parameters of the Hansel-Spittel equation
b	Burgers vector (m)
$B_0\text{-}B_6/\ C_0\text{-}C_6/\ D_0\text{-}D_6/\ E_0\text{-}E_6$	Constants
C_0	Initial solute concentration (mol/L)
C_1, C_2	Carbides
C_L	Solute concentration (mol/L)
C_p	Specific heat (J/kg/°K)
D_L	Diffusion coefficient of solute (m^2/s)
D	Grain size (μm)
d_0	Initial grain size (μm)
D_{DRX}	Dynamic recrystallization grain size (μm)
d_g	Growth grain size (μm)
F_e	Eutectic ferrite
f_L	Fraction of residual melt
G	Shear strength (MPa)
h	Stock height (m)
K, m, K_1, K_2	Constants
k_0	Equilibrium partition coefficient
K_E	The consent of a substance
L	Liquid
M	Martensite
M_{gb}	Intrinsic boundary mobility (m^3/N.s)
M_{sb}	Mobility of the subgrain boundary (m^3/N.s)
P_{gb}	Driving force for the growth of recrystallized nuclei
Q	Deformation activation energy (KJ/mol)
R	Gas constant (J/K.mol)
r	Subgrain size (μm)
r_c	Critical subgrain size (μm)
t	Time (s)
T_m	Melting point (°C)
T_r	Reference temperature (°C)
T	Temperature (°C)
T_t	Transition temperature (°C)
w	Die width (m)
X_{DRX}	Dynamic recrystallization fraction (%)
Z	Zener-Hollomon parameter

XXX

α	Ferrite
γ	Austenite
δ	Delta ferrite
δ_N	Thickness of diffusion boundary layer (m)
Δ	Absolute average error
Δt	Time increment (s)
ΔE	Driving force
ΔT	Change in temperature (°C)
ε	Strain
ε_c	Critical strain
ε^*	Strain at maximum rate of dynamic softening
$\dot{\varepsilon}$	Strain rate (s^{-1})
$\bar{\varepsilon}$	Equivalent strain
η	Efficiency of power dissipation
θ	Work hardening rate (MPa)
θ_{II}	Slope of stress-strain curve (MPa)
μ	Friction coefficient
ξ	Instability criteria
ρ	Density (g/m^3)
σ_{max}	Maximum principal stress
$\bar{\sigma}$	Effective stress (MPa)
σ_{wc}	Uncorrected stress (MPa)
σ_c	Critical stress (MPa)
σ_E	Experimental flow stress (MPa)
σ	Flow stress (MPa)
σ_f	Corrected stress (MPa)
$\bar{\sigma}_p$	Average values of predicted flow stress (MPa)
$\upsilon_{\sigma\beta}$	Rate of subgrain coarsening
$\int \sigma d\varepsilon$	Area under the uncorrected stress-strain curve

INTRODUCTION

Martensitic stainless steel (MSS) is a type of stainless steel with a chromium content between 10.5 wt% and 18 wt%, which leads to chromium oxide layer formation on the steel surface and ensures high corrosion resistance (Krauss, 1999). The corrosion resistance of MSS also depends on the carbon content, the volume fraction of carbides dissolved in the matrix after austenitization, and the amount of carbide precipitation during tempering. Another important feature of this type of steel is the so-called "air hardening", which occurs due to the allotropic transformation into a martensite structure even when cooled in air, allowing a wide range of strengths and hardness to be achieved (Garrison & Amuda, 2017). Their high strength and corrosion resistance make them ideal candidates for critical components, such as turbine shafts, petrochemical equipment, surgical instruments, etc. The microstructure and mechanical properties of components made of MSS strongly depend on the manufacturing and the heat treatment processes (Y. Zhang et al., 2021).

The demand for large components of MSS for heavy industries such as aerospace, automotive, mining, oil, and gas extraction industry is increasing continuously. Manufacturing of large components begins with solidification and casting followed by high-temperature open-die forging in the austenite stable region (0.75 of the melting point) and then heat treatment (Di Schino, 2021). The forged products need to be cost effective in production and be characterized by excellent mechanical properties such as high strength, wear and corrosion resistance, toughness, and good notched impact strength (Banaszek, Bajor, Kawałek, & Garstka, 2021; Wolfgarten, Rudolph, & Hirt, 2020). However, the manufacturing of sound heavy forgings is extremely challenging due to the casting defects occurring during the ingot casting such as inhomogeneities in the microstructure, macrosegregation, porosities, and inclusions which deteriorate the quality of the products (Kane, Mishra, & Dutta, 2016). Therefore, the large size ingot in its as-cast state cannot be used in industry as a final production step. Although many investigations have been conducted to reduce the occurrence of casting defects and many numerical procedures have been used to optimize the process during solidification (Loucif et al., 2017; Loucif, Zhang, Jahazi, & Lapierre-Boire, 2020; C. Zhang, Loucif, Jahazi, & Morin,

2022; C. Zhang, Loucif, Jahazi, Tremblay, & Lapierre, 2018), the production of defect free castings is still a big challenge, particularly, for large-size castings and the occurrence of defects is inevitable. As the ingot size increases, the inhomogeneity of the microstructure and the segregation increase so that healing all defects becomes difficult even with subsequent thermomechanical treatments (Pickering, 2013). Therefore, selecting and designing the proper forging schedule are a necessity in order to reduce these defects and improve the mechanical and microstructural properties subsequently. Otherwise, inappropriate forging schedules result in failure or property degradation resulting in scrapping of the part.

Due to the importance of the casting process and its influence on the quality of the forged product, this project began with an analysis of the microstructural characterization and phase precipitation that occurred during the casting of large-sized MSS ingots and their effects on the quality of the forging. This study is the first to address the characterization of the microstructure of large ingots during solidification and solves a key industry issue.

Hot forging can change metals' shape as well as alter their service properties by changing their microstructure (Monajati, Jahazi, Yue, & Taheri, 2005). Controlling the mechanical and microstructural phenomena occurring during hot deformation is a key factor in improving forged product quality, especially for applications requiring high strength, hardness, and impact properties (Duan & Sheppard, 2003). During hot forming, complex softening and hardening processes occur which can have a significant influence on the choice of thermomechanical processing parameters and the change in microstructure (Humphreys & Hatherly, 2004). The dynamic microstructural mechanisms occurring during hot deformation are dynamic recovery (DRV) and dynamic recrystallization (DRX) as softening mechanisms and work hardening (WH) as a hardening mechanism. These mechanisms are the main determining factors in the microstructure evolution during hot forming including grain refinement, second phase precipitation, and segregation during deformation. Temperature, strain rate, and strain influence macroscopic plastic flow, deformation behavior, and microstructure evolution during hot deformation (Bontcheva & Petzov, 2003; Chamanfar, Jahazi, Gholipour, Wanjara, & Yue, 2014; Gao, Fu, Zhan, Lei, & Li, 2020). This study will

focus on generating comprehensive data on the flow stress and simulate microstructure evolution of the investigated MSS during the forging process that is scarcely available in other publications.

In recent years, several physical and empirical models have been developed to predict the material flow behavior and microstructure evolution of the different metallic alloys during hot deformation (Cojocaru et al., 2021; W. Li, Liang, & Zhang, 2022; Yong Cheng Lin & Chen, 2009; Xiao, Wang, Wu, & Yang, 2018). The most efficient method to improve the quality of the final forging is by modeling the microstructure evolution and prediction of the material flow behavior. Although constitutive modeling has been used to investigate the hot deformation behavior of MSS, most models ignored the impact of strain on high-temperature deformation behavior (Qi, Jin, Guo, Liu, & Chen, 2015). Additionally, the mechanisms of microstructure evolution for MSS have not been modelled, and the majority of the calculations were done on a lab scale (Y. Zhang et al., 2021). The present work intends to fill this gap by conducting a comprehensive microstructure and constitutive modelling for MSS, in which the developed mechanical and microstructure models account for strain and all process parameters are considered in the equations.

In heavy manufacturing industries, one of the biggest challenges is to establish a relationship between thermomechanical process parameters and the microstructure of materials. Additionally, traditional industrial forging methods that use trial and error to find the above relationships result in high setup and tooling costs which waste resources, time, and energy. Therefore, by taking the advantage of computational methods and implementing all microstructure and constitutive models into FEM software, the forging process could be simulated. Hot forging process simulation provides several advantages including reducing the number of the required experiment, determining the risky forging conditions, minimizing development time, reducing costs, predicting the flow stress and microstructure evolution, mapping working parameters at any time during forging, and finally optimizing the process parameters (Dindorf & Wos, 2020). The present PhD thesis has been defined in this context and the research work has been focused on some of the fundamental scientific gaps of this

subject and then apply the obtained results to the optimization process of the open die forging of large-sized ingots of a martensitic stainless steel used in energy and transportation industries. All these works are described in detail in 7 Chapters:

In Chapter 1, a comprehensive literature review is presented on the casting process and the defects that occur during the solidification of large-size ingots, as well as the parameters that affect the quality of the cast ingot and the ways to eliminate these defects. Then, the forging process and the parameters that result in defect generation and their effects on ingot quality are highlighted. The softening mechanisms that occur during hot deformation are then explained. This chapter also presents constitutive equations used to predict material behavior at high temperatures and the related microstructure evolution models. The numerical details for the implementation of the models are also discussed and an overview of researchers in the field of numerical simulations of the forging process at high temperatures is given.

The methodology of this project is presented in Chapter 2. The elaboration of the industrial and experimental measurements is provided step by step. All measurement equipment and software which are used for experimental tests and boundary conditions of simulations are explained.

The impact of forging temperature on the characteristic of eutectic phase precipitation in a large casting is discussed in Chapter 3. The analysis is focused on the correlation between the presence of the eutectic phase that forms during ingot solidification and the cracking propensity during forging. Advanced characterization techniques were used to determine the phase distribution, chemical composition, and phase identification. Thermodynamic simulations were carried out to determine the chemical composition of the eutectic phase. The experimental results are compared with simulation ones and an optimization is proposed to avoid the negative impact of these phases.

Chapter 4 is devoted to developing constitutive models for predicting material behavior during high-temperature forging and the selection of the model that best represents the experimental

results. This chapter also provides the implementation of the constitutive model into the FEM software and the simulation of hot compression tests. The microstructural evolution of the deformed sample is explained and correlated with the simulation results. Moreover, the analysis of the flow behavior of the material is carried out using the Dynamic Material Model. Chapter 5 focuses on the forging process simulation of the industrial-size ingot. The effect of forging parameters on microstructure evolution was evaluated by the implementation of microstructure-based FEM modeling. In this chapter, the parameters affecting the non-uniformity of microstructure evolution after forging are discussed. Also, results of the numerical simulation of the possible cracking during forging using a damage criterion proved the occurrence of surface cracking after deformation. Finally, the accuracy of implemented models was checked with the experimental results during the forging process.

Based on the results of chapters 4 & 5, the forging parameters were modified to see their effect on microstructure evolution in order to improve the quality of the final product and the results are presented in chapter 6. Specifically, this chapter discusses the effect of forging temperature, strain, and strain rate on the critical strain for the initiation of DRX, DRX fraction, DRX grain size, and damage initiation during the upsetting process of the studied steel. Finally, the optimized working parameters were identified and listed according to their effects on the microstructure.

Chapter 7 provides all simulation results of the entire forging process, including upsetting, FM, and Cogging as used in industry. Based on the optimized forging parameters explained in Chapter 6, a new forging schedule was designed and the results were compared with the original design.

CHAPTER 1

LITERATURE REVIEW

1.1 Introduction to Stainless Steels

A big concern with steels is that they are easily corroded when exposed to a salty or acidic atmosphere. For example, a piece of steel left in an acidic atmosphere will very quickly become rusted with the characteristic dirty brown color of steel rust. This concern was solved by the invention of stainless steel which is an alloy of iron that is resistant to rusting and corrosion due to its chemical composition (Lu et al., 2015). The main categories of stainless steels are austenitic, ferritic, duplex, and martensitic which were discovered in 1912 (Garrison & Amuda, 2017). The corrosion resistance of this alloy is due to the presence of chromium which forms a passive film that can protect the material in the presence of oxygen. Figure 1.1 shows that oxidation resistance also improves as chromium content is increased and this is prompted by adding a small amount of Mo or Ni to the chemical composition. Corrosion resistance can be increased further by increasing Cr to more than 11%, adding Ni to at least 8%, and adding Mo which also improves resistance to pitting corrosion (Davis, 1994).
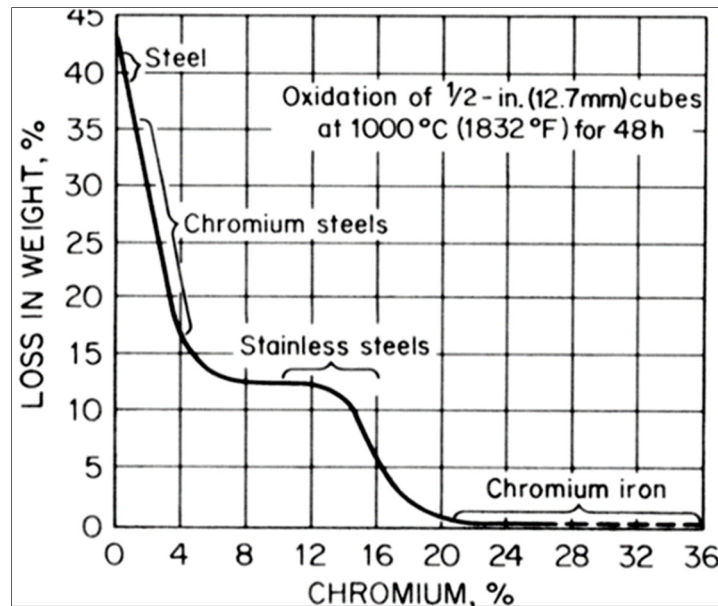
Figure 1.1 Oxidation of chromium steels at 1000 °C
Taken from Davis (1994)

The resistance to corrosion feature of stainless steels is in favor of many applications such as cookware, cutlery, surgical instrument, vehicles, industrial equipment, and the storage tanker for chemical and food products. All types of stainless steels except austenitic stainless steels are magnetic (Garrison & Amuda, 2017).

1.1.1   Martensitic Stainless Steel

Martensitic stainless steel (MSS) with tetragonal crystal structure (BCT) provides a wide range of properties and are used for an environment that required high toughness, high strength, high corrosion resistance, and good ductility. The heat treatment can adjust the mechanical properties of MSS. Heat treatment can change MSS' strength, which is influenced by the carbon content. Strength and hardness increase as C content increases, but ductility and toughness decrease. MSS typically contain 12 to 17% Cr and 0 to 5 % Ni which makes them the feature of good corrosion resistance, long and low maintenance life, and excellent recycling rate. All types of martensitic stainless steels are classified by the AISI and categorized in the

400 series (Garrison & Amuda, 2017). Figure 1.2 displays the compositions of five of the more popular AISI martensitic stainless steels.
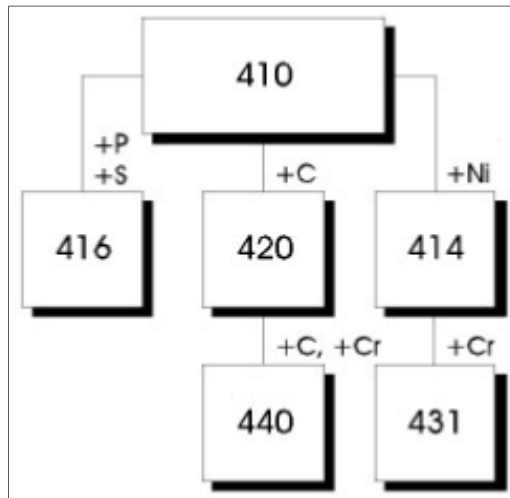
Figure 1.2 Martensitic grades
Taken from Garrison & Amuda (2017)

MSS is heat-treatable steel in which optimal mechanical and microstructure properties can be achieved through heatreatment. In order to achieve superior performance, heat treatment must be controlled precisely to achieve the desired combination of strength and ductility. The main heat treatment process is categorized into three steps (D. shen Ma, Chi, Zhou, & Yong, 2012): Austenitization:

The material is held at a high temperature for a specific time according to the complexity and size of the product and the required properties. The austenitization temperature should be high enough to allow sufficient carbide solution in austenite but should not exceed the temperature that grain growth takes place. The austenitization temperature is generally in the range of 925 °C -1070 °C. The chemical composition of MSS defines the impact of austenitization temperature and time on strength and hardness (Ma et al., 2012).
Quenching:

After austenitizing, the MSS quenches in oil, water, and air depending on steel grade. At M_s temperature, the austenite transforms to martensite and the temperature for finishing this transformation depends on the chemical composition. Almost all alloying elements reduce the

M_s which means that for the higher alloyed martensitic grades, the more retained austenite is in the microstructure due to the lower M_f. The quenched martensite is hard, brittle, and has high strength, high hardness, low ductility, and toughness. Lower austenitization temperature leads to finer austenite grain size and consequently finer martensite units of packets are obtained. This structure leads to higher strength and toughness (Ma et al., 2012).

Tempering:

The combination of austenitization-quenching leads to a hard martensite structure with a high level of internal stresses that can lead to cracking. Therefore, another process is needed after quenching to compensate for high strength and low ductility. Tempering is conducted to restore ductility at the expense of hardness and provides a balance of hardness and ductility. Figure 1.3 shows the influence of tempering on the hardness (HV) and impact toughness of MSS (Ma et al., 2012).
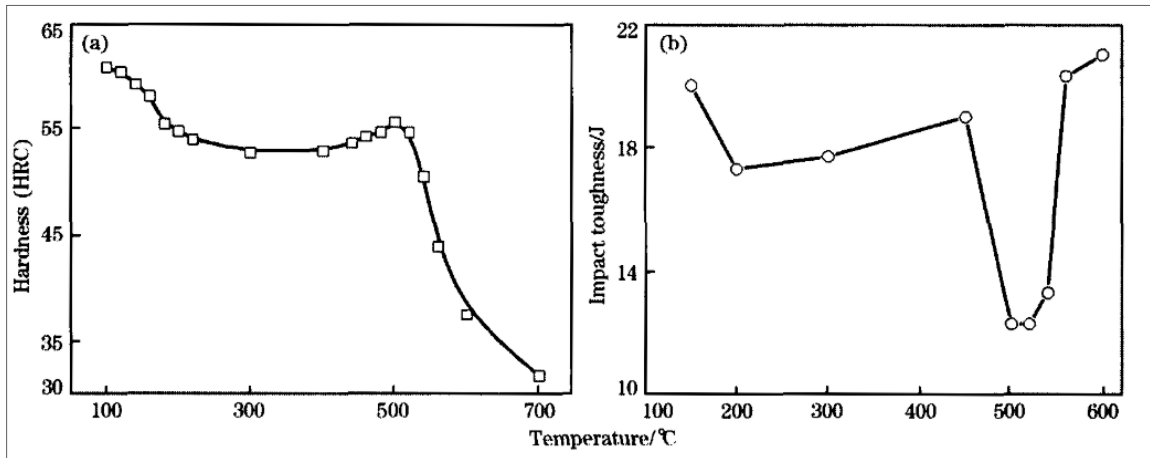
Figure 1.3 Effect of tempering temperature on
(a) hardness and (b) impact toughness of MSS steel
Taken from Ma et al. (2012)

1.1.2 Martensitic Stainless Steel Phase Diagram

The equilibrium microstructure of martensitic stainless steels at high temperature is mostly austenite based on the carbon content, Figure 1.4. The equilibrium microstructure of these steels is a mixture of ferrite and carbides at room temperature. During heating, austenite

reforms very quickly, but it takes a long time for it to transform back to ferrite during cooling. In consequence, these steels tend to convert to martensite on cooling from temperatures at which austenite is stable (Stone, Alexandrov, & Penso, 2017).
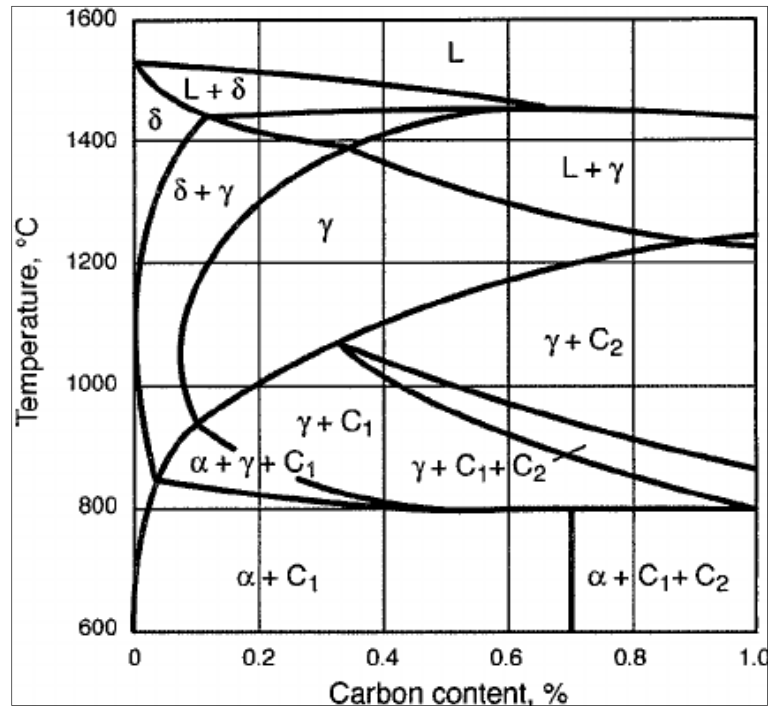
Figure 1.4 A ternary iron-chromium-carbon
constitution diagram at 13% Cr
Taken from Stone et al. (2017)

The heat treatment process parameters should be selected accurately. The optimized microstructure of MSS is free of δ-ferrite because its presence worsens the properties of these steel, reduces impact toughness, ductility, corrosion resistance, and resistance to fatigue fracture. Most researchers agree that a crack nucleates in the region of less strong δ-ferrite and then propagates into the martensite structure (Hull, 1973). The dual-phase microstructure of austenite and δ-ferrite is detrimental to the fracture toughness of MSS by facilitating the formation and propagation of the crack along the matrix/ δ-ferrite interface (Cardoso, Kwietniewski, Porto, Reguly, & Strohaecker, 2003). Therefore, based on the chemical composition of MSS, all parameters of each process including casting, forming, and heat treating should be preferred in single-phase austenite.

1.2   Casting

The casting process is an important stage before metal forming. According to the desired applications, various casting methods, such as investment casting, sand casting, die casting (high pressure and low pressure) etc., are used to produce various shapes and sizes of a workpiece (X. yu Qin, Su, Chen, & Liu, 2019). Most of the alloys contain dendritic structures, and different morphology of grains (equiaxed, columnar, and chill) after solidification in a mold, Figure 1.5. By releasing the latent crystallization heat from the crystallizing metal, the undercooling of the melt is reduced. As a result, some grains grow in a direction of the heat flow which results in columnar grains. Further cooling of the molten metal causes large grains of equiaxed metal to form in the central region (Li, Liu, Zhang, & Huang, 2021).
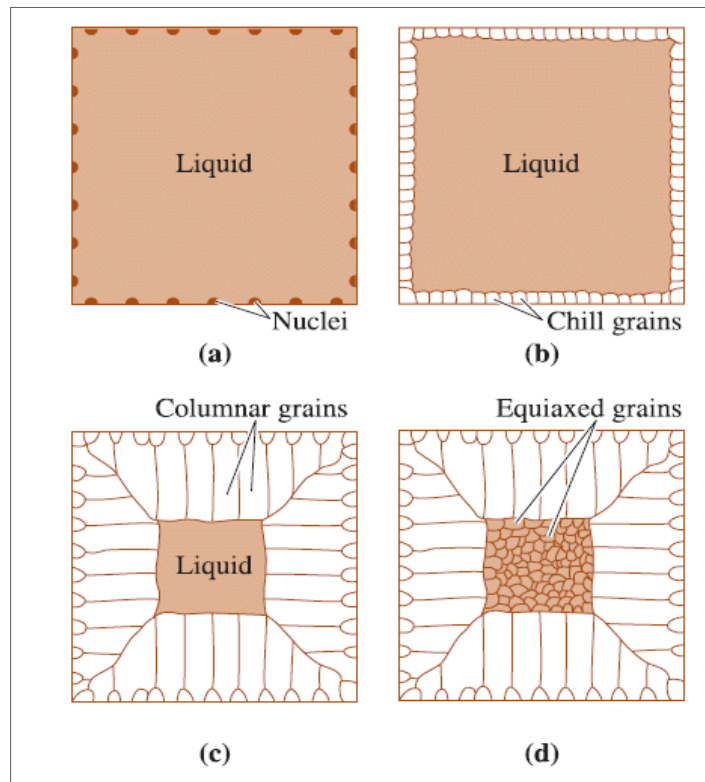
Figure 1.5 Various zone in an ingot casting
(a) nucleation (b) formation of outer equiaxed zone
(c) columnar zone (d) inner equiaxed zone
Taken from Askeland & Wright (2001)

1.3   As-Cast Microstructure

During the solidification of heavyweight steel ingots, various chemical and physical processes occur and the solidification process often takes 2 to 3 days. This slow cooling rate leads to casting defects such as V-segregation along the centerline, A-segregation in the columnar zone, hot top segregation, shrinkage cavity, and negative base segregation near the bottom in the equiaxed zone. The mass transfer during solidification is the basic mechanism for all macro-segregation types. It can severely limit the yield in the ingot casting process and, at the same time, cause problems in subsequent processing and steel properties (Pickering, 2013). Figure 1.6 shows a typical macrosegregation patterns that could be formed in cast ingots.

Two types of segregation take place during the solidification of an ingot. The origin of segregation in ingots is the liquid or solid movement within the mushy zone as a result of, solidification shrinkage, thermal contractions, and density difference in the interdendritic liquid (Zhang et al., 2018). Because of the non-equilibrium solidification, the temperature gradient has a large magnitude and the alloying elements migrate ahead of the solidification interface. Therefore, the chemical composition by the advancement of solidification is enriched with solutes, and most of the segregation is at the centerline. Many researchers investigated the effect of this segregation on the mechanical and physical properties (Loucif et al., 2018). They reported that the region with the enrichment of solutes can reach eutectic composition and eutectic solidification occur as a result. Zhou et al. reported that the volume fraction, distribution, and morphology of the eutectic phase could deteriorate the formability, impact properties, and also make the ingot susceptible to cracking during forging (Zhou, Shen, Chen, & Cui, 2011). As the quality of the final products is determined by the extent of the segregation, considerable efforts should be put into post solidification process to eliminate these segregations and homogenize the distributions of the alloying elements. Despite the importance of the as-cast state on the quality of the final forged products, very few studies have carried out investigations on the phenomena occurring during the solidification and how these phenomena affect the forging process. Specifically, this topic on the scale of heavy ingot

casting and the following heavy forging process has received much less attention. In addition, no report exists on this topic with the industrial scale for martensitic stainless steels.
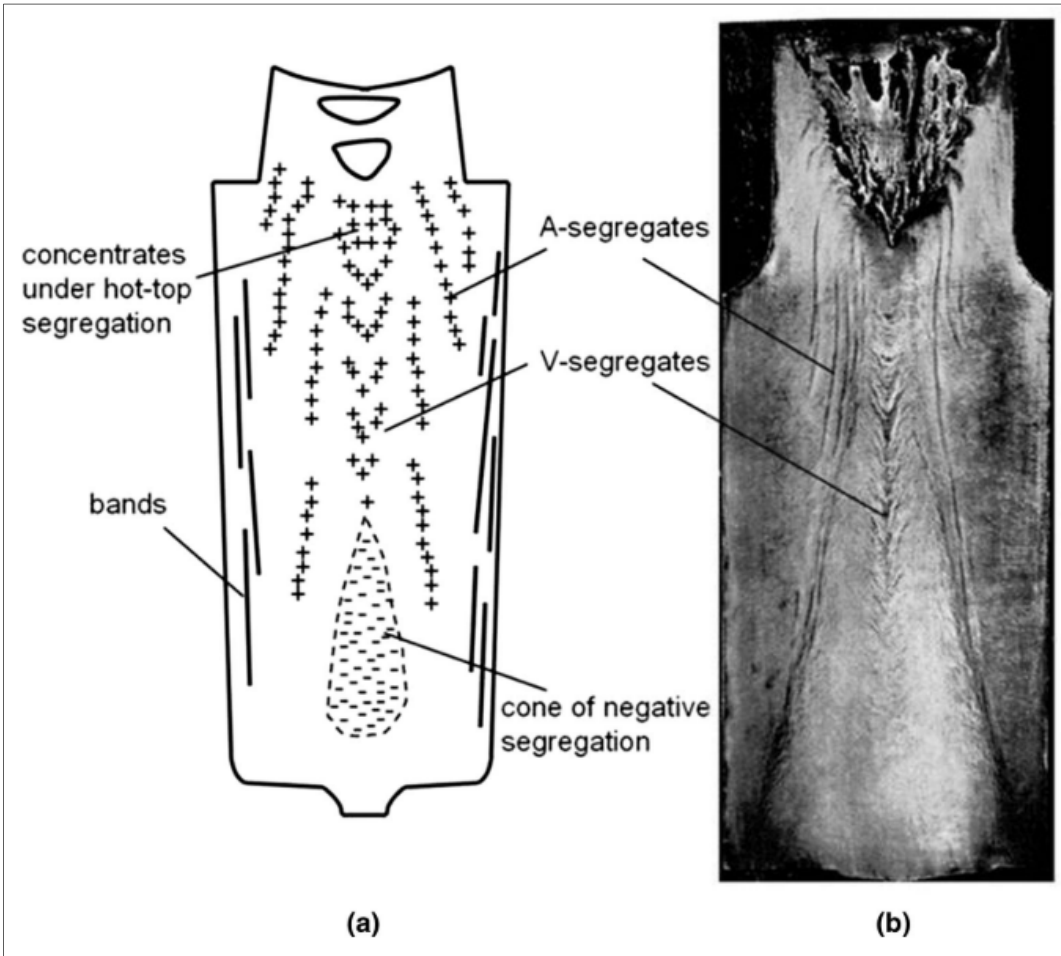
Figure 1.6 Typical macrosegregation patterns that could be formed in steel ingots (a) schematic representation and (b) sulfur print of a 10-ton ingot
Taken from Moore & Shah (1983)

1.4   Bulk Metal Forming

Most deformation processes can be categorized into one of two groups: bulk forming and sheet metal forming which can be hot, cold, and warm forming. In bulk-forming, large deformation or reduction-in-area is carried out to convert a billet, block, or ingot into a more complex shape or a 2D shape such as a sheet, rod, strip, or wire. The deformation processes include forging, swaging, extruding, rolling, and drawing (Dieter, Kuhn, & Semiatin, 2003).

1.4.1 Forging

Forging is a bulk metal forming process that uses a compressive force to form a workpiece at a high temperature. To forge metals, forging presses that are powered by hydraulics, electricity, or compressed air are most frequently used (Hauri, Graf, Awiszus, & Kawalla, 2018). According to the temperature, the forging process is classified into three types: cold forging, warm forging, and hot forging. In hot forging, the metal is heated to about 75% of its melting temperature which needs less energy and flow stress to form the metal (McQueen & Jonas, 1975). Excessive heat leads to decreasing yield strength and improving ductility. In addition, forging at high temperatures effectively increases the rate of production and aids in making the metal easier to shape as well as less likely to fracture. The most usage of hot forging belongs to iron along with its alloys for two main reasons: forming hard materials such as steel and iron will become more difficult if work hardening progresses and it is a more economical option than cold working. There are substantial advantages in hot forging including increasing ductility, less energy needed to work with the material, closing the porosities and pores, reduce chemical inhomogeneities due to increased diffusion. However, warping the metals during hot forging is possible if not carefully watched when heated, forged, and then cooled. In addition, hot forging can be more expensive than cold forging because of the heat treatment necessary to start the forging process. Another disadvantage of hot-forged components compared to cold-forged ones is their less accurate dimensional tolerance.

In cold forging, the process performs at or near room temperature (below the recrystallization temperature. When a metal, like aluminum, is already soft, cold forging is typically used. This technique typically costs less than hot forging, and the final product requires little or no finishing (Guo et al., 2013). The processes such as cold heading, cold drawing, extruding, bending, and coining are in the cold forging category. The disadvantages of cold forging are producing undesired residual stress, requiring higher force and more powerful equipment to form the material. Warm forging is carried out from above room temperature to below recrystallization temperature (www.totalmateria.com). Warm forging is used as an alternative process to cold forging. It has the potential benefits of lower tooling loads, lower press loads,

greater steel ductility, and no requirement for annealing before forging as compared to cold forging. Warm forging, up to 700 °C to 800 °C for steels, reduces the flow stress and forging pressures (Becker & Shipley, 2018; Dieter et al., 2003).

1.4.2   Closed Die Forging Process

Closed die forging is a forming process in which tools/dies move towards each other and cover the part completely or partially. Step 1 involves enclosing the hot metal in dies of a predefined shape. In Step 2, the dies are forced to give the impression of hot metal. Closed die forging is commonly used in the production of automobile components and hardware tools (http://www.alloysintl.com). Figure 1.7 illustrates the closed die forging process.
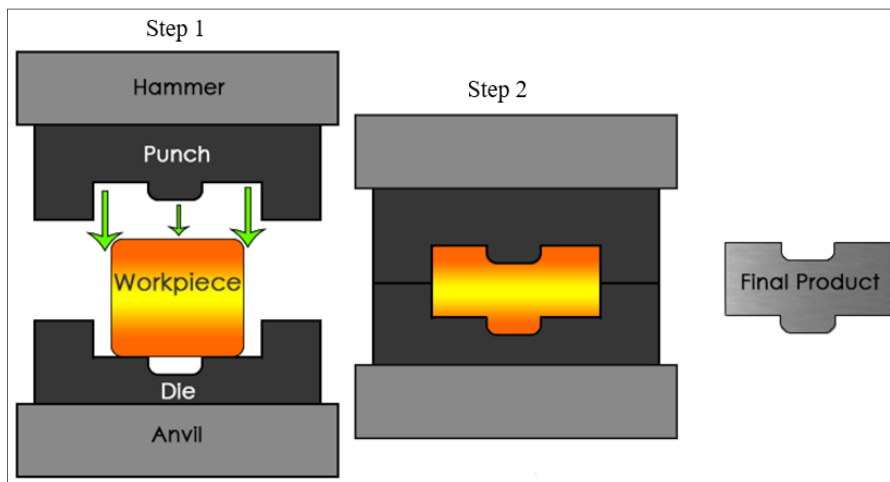
Figure 1.7 Closed die forging diagram
Taken from Alloys International, INC

1.4.3   Open Die Forging Process

In open die forging, the hot part is deformed between two dies (flat/ V-shape/ circular). Unlike the close die forging process, the workpiece is not restricted between dies. This kind of forging is generally used when a large product is required. The final product in this kind of forging does not have great accuracy and hence requires machining operation. Open die forging is used to produce simple parts such as heavy parts that weigh tons, discs, shafts, hubs, blocks,

cylinders, sleeves, flats, and some custom shapes (http://www.forgedproduct.com). Figure 1.8 shows the schematic of the open die forging process. The advantages of open die forging are less waste of the material, the capability of producing very large parts, breakdown of the as-cast microstructure, reduced chance of voids, finer grain size, and improved fatigue resistance and strength (http://www.canforge.com).
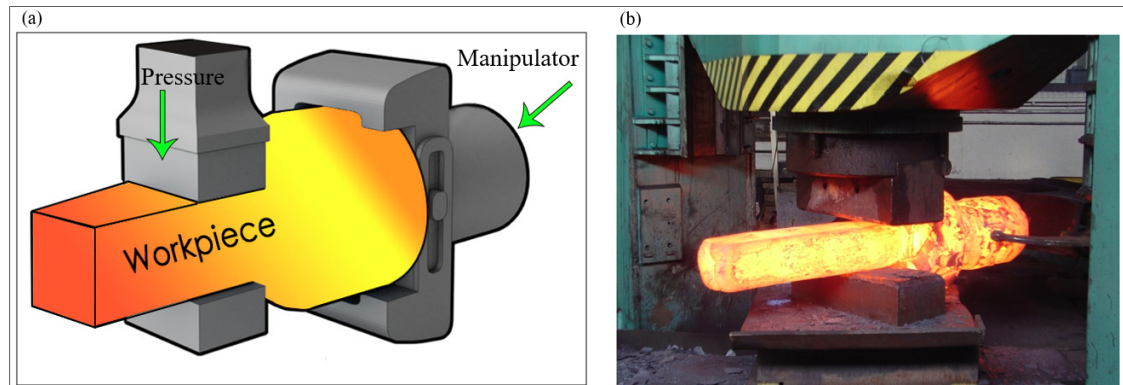
Figure 1.8 (a) Schematic of open die forging process (b) Real industrial open
die forging process
Taken from Chisen ® forged product

1.4.4   Forging Defects

Surface cracking:

This defect occurs due to the temperature difference between the surface and the center of the ingot. This may also be due to excessive strain concentration, steel grade, type of press, forging schedule, forging temperature, anvil shape, and the properties of the steel ingot (Kakimoto & Arikawa, 2014), Figure 1.9.
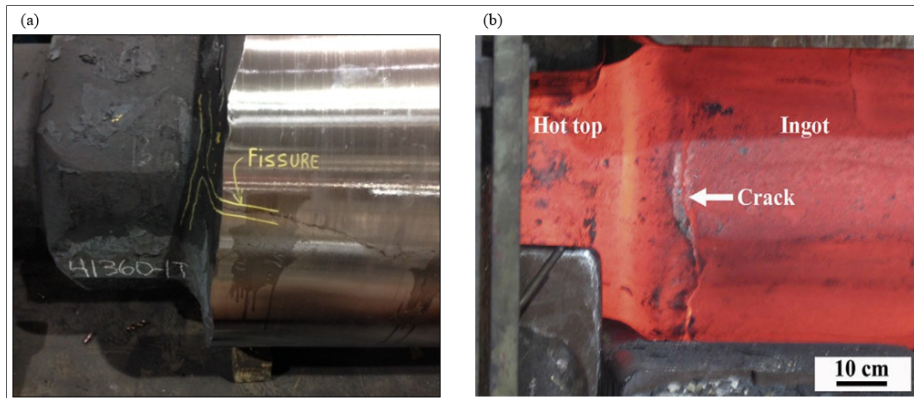
Figure 1.9 Surface cracking in industry Taken from (a) Finkl Steel Inc
(b) CFS Machinery Co., Ltd

Improper grain growth:

This defect occurs as a consequence of inadequate metal flow during casting, which alters the product's defined grain structure. It can be eliminated with the proper forge design (http://www.steelforging.org).

Residual stresses in forging:

Inhomogeneous deformation and improper cooling/quenching of the forged parts can be the main cause of this type of defect. The solution to avoid this defect is to cool down the forged parts slowly (http://www.steelforging.org).

Scale pits:

The poor cleaning of the forged surface leads to scale pits. This defect is typically connected to forging in an open environment with a large amount of dust and oxidation. Appropriate cleaning of the forged surface and the forging tools could be a solution for this defect (http://www.steelforging.org).

1.5   Ingot Breakdown Process

The process of ingot breakdown is effective to convert an as-cast structure to a wrought structure (Chadha, Shahriari, & Jahazi, 2016). During the large-sized casting process, defects in ingot casting can occur including shrinkage, porosity, macrosegregation, inclusion, and cracks. In addition, as explained in the as-cast microstructure section, there are three different types of grain structures composed of the chill zone, equiaxed zone, and columnar zone. Therefore, these mixed microstructures should be converted to a wrought microstructure which is uniform and equiaxed grains. Hot deformation causes grain refinement via static and/or dynamic recrystallization of the austenite. Moreover, the ingot casting defects should be eliminated through the ingot breakdown process (Uddagiri, Spee, Hubig, & Steinbach, 2020). Compression of the dendritic arms reduces the local diffusion distance and leads to a reduction of chemical heterogeneities present due to segregation. Non-uniform hot deformation, on the other hand, can result in undesirable duplex microstructures, which are a mix of fine and coarse grain sizes. Higher alloy concentrations in segregated regions can also cause non-uniform recrystallization (Tang, Cheng, Kou, & Li, 2015). Therefore, it is necessary to conduct hot-working process to eliminate all or some of these heterogeneities. Figure 1.10a shows the metallurgical features in large ingots resulting from the phenomena that occur during ingot solidification. During the ingot breakdown process, the ingot is hot forged at 75% of its melting point to reduce the forging load and increase the workability as shown in Figure 1.10b (Dieter et al., 2003).
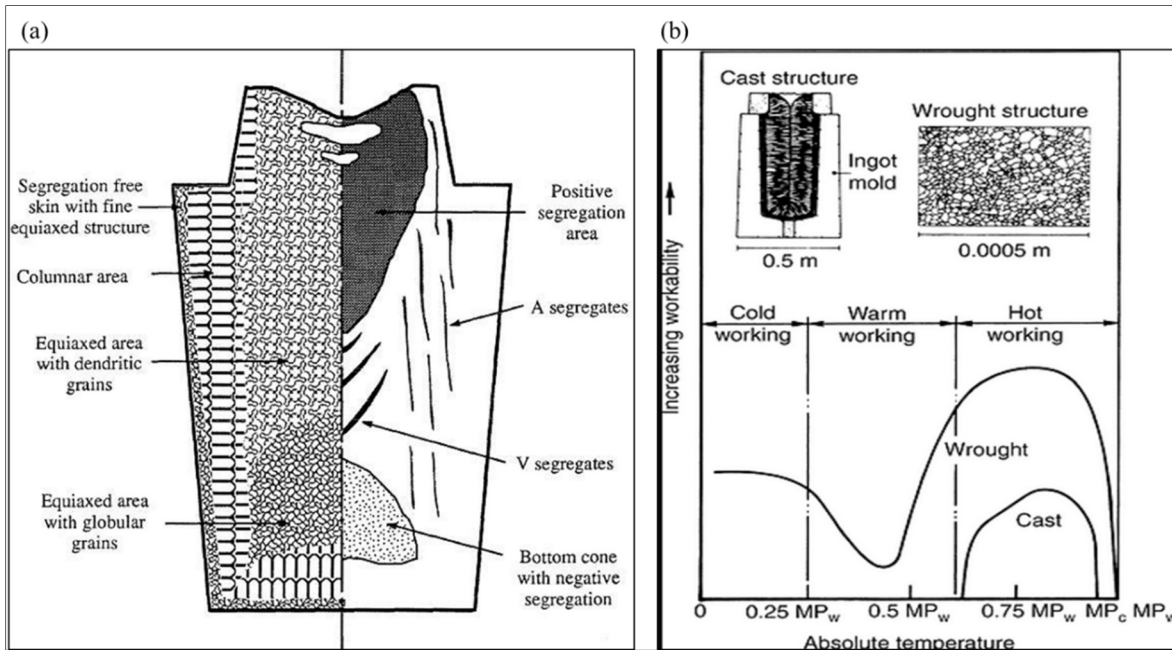
Figure 1.10 (a) Schematic representation of metallurgical features in large ingot (b) A schematic showing the relative workability of wrought and cast metals at hot, warm, and cold temperatures (MP$_c$ refers to the melting point of cast metals and MP$_w$ refers to the melting point of wrought metals)
Taken from Dieter et al. (2003)

1.6   Softening / Hardening Mechanisms during Hot Deformation

The alloy undergoes work hardening (WH), dynamic recovery (DRV), and dynamic recrystallization during hot deformation, which are three metallurgical phenomena that control the microstructure and mechanical properties. The types of flow curves that are a direct result of microstructural changes determine the hot working behavior of the material; Figure 1.11 shows three types of flow curves that occur during deformation.
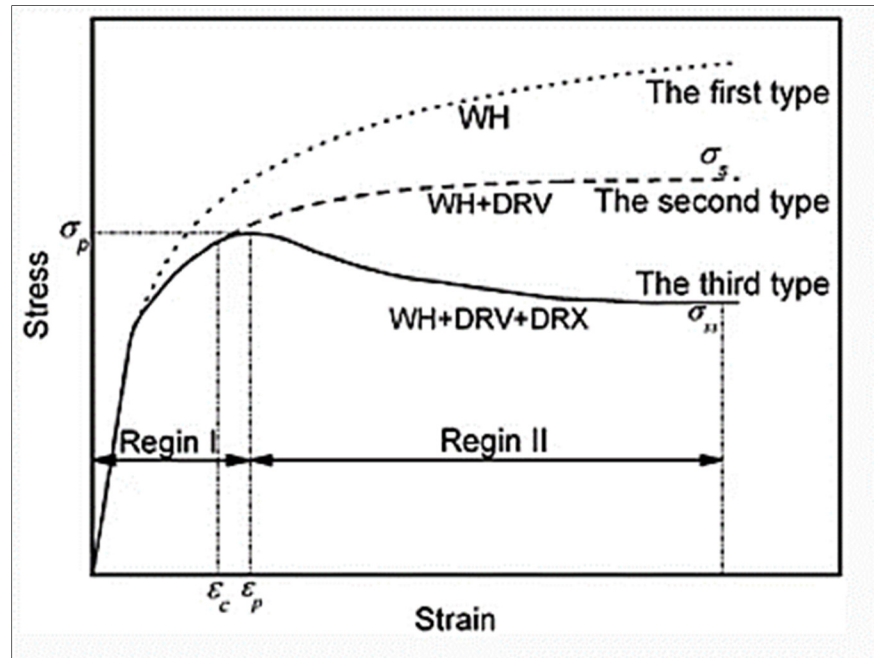
Figure 1.11 Schematic diagram of stress-strain curves of
three types of material response during deformation
Taken from Jonas et al. (2009)

Based on the deformation parameters, physical and mechanical properties of the material etc. the microstructure evolves differently. One of the important and effective material properties that affect the material response to the deformation is stacking fault energy (SFE). In materials with high SFE, the dislocation climb and cross-slip occur easily while in low or medium SFE (copper, nickel, and austenitic iron) it is difficult for dislocation to climb where there are few slip systems (Jonas et al., 2009). The mechanisms during hot deformation that leads to microstructure evolution are elaborated below:

1.6.1 Dynamic Recovery

During the deformation process, there is a continuous formation and annihilation of dislocations. The flow stress is sharply increased during the initial stage of deformation due to the formation and multiplication of dislocations. If the accumulation of dislocations is high enough, the dislocation annihilation and rearrangement develop and the microstructure of low

angle boundaries (LAGB) and subgrains develop and results in a plateau in the flow stress curve. The rearrangement of dislocation structures is primarily responsible for recovery (Humphreys & Hatherly, 2004). A series of events leads to recovery as shown in Figure 1.12.
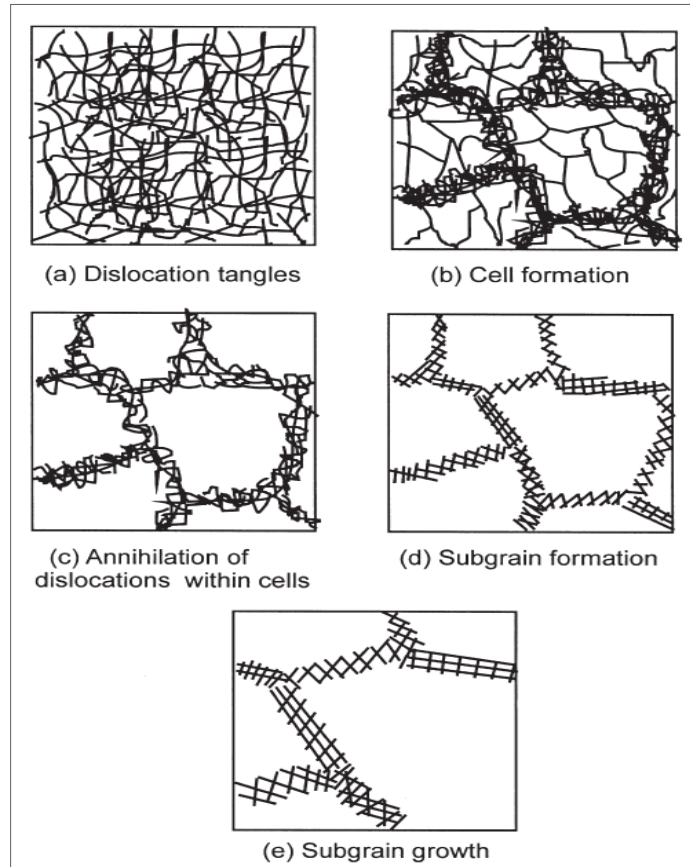
Figure 1.12 various stages in the recovery
of a plastically deformed material
Taken from Humphreys & Matherly (2004)

The deformation process in Figure 1.12a results in dislocation tangles in the structures. The random dislocation structure has been rearranged into cell structures in Figure 1.12b. For high-stacking fault energy (SFE) materials, this can occur simultaneously with deformation. In Figures 1.12c and 1.12d, cell boundary strengthening occurs in developed subgrain boundaries due to dislocation rearrangement and dislocation annihilation into the low-energy arrangement. In Figure 1.12e, the subgrain begins to grow during continued annealing, resulting in a decrease in internal energy overall (Humphreys & Matherly, 2004).

In recovery, the stress-strain curve exhibits a rise followed by a steady state of flow stress. During the early stages of deformation, dislocations interact and multiply, increasing the flow stress. As the density of dislocations increases, so does the rate of recovery, resulting in the formation of the microstructure of low-angle boundaries and subgrains. A steady state flow stress is acquired at this point, the dislocation density is constant, and work hardening and recovery rates have reached a dynamic equilibrium (Humphreys & Matherly, 2004). Figure 1.13 shows microstructural changes which occur during dynamic recovery.
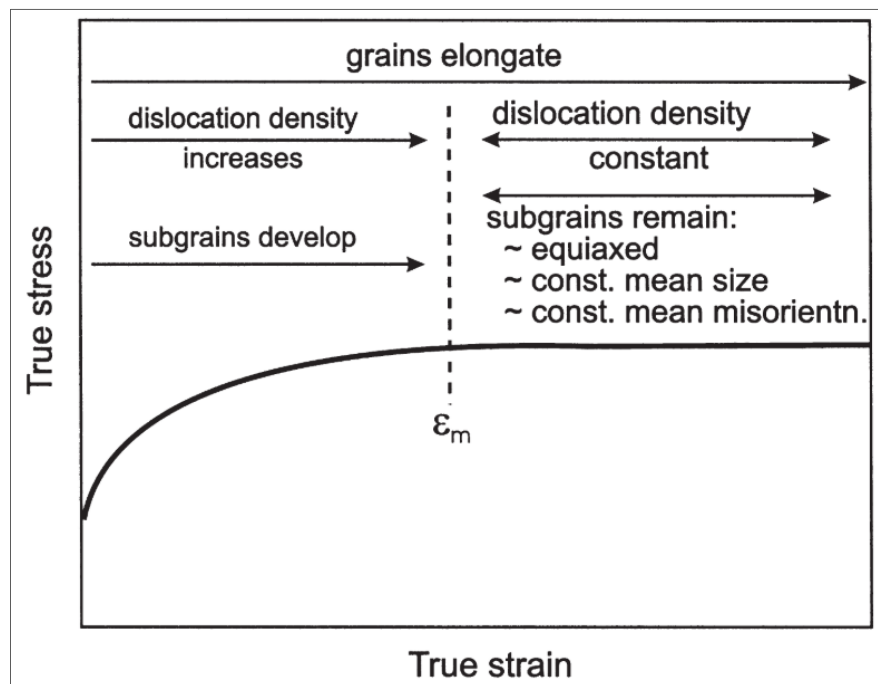
Figure 1.13 Summary of the microstructural changes
which occur during dynamic recovery
Taken from Humphreys & Matherly (2004)

1.6.2   Dynamic Recrystallization

Dynamic recrystallization (DRX) is a softening process that is dominant at high temperatures during forming of low-stacking fault energy (SFE) metals. It is known for producing a homogeneous grain structure by nucleating and growing new grains at old grain boundaries. DRX is most likely to begin at high-angle grain boundaries (HAGBs), which may exist in the

structure or form during straining. The grain boundary bulging is frequently referred to as the first step in the nucleation of DRX. This is commonly referred to as strain-induced grain boundary migration (SIBM) (Ebrahimi, Keshmiri, Maldad, & Momeni, 2012a). In many metals, including stainless steel, DRX is a common microstructural phenomenon during the actual hot working process (Ebrahimi et al., 2012a). An industrial process, such as hot forging or rolling, is more accurate when strains are determined to initiate and complete the DRX. When grain boundaries start to bulge through SIBM, it is known that the accumulation of dislocation density during hot working reaches a critical value. Near the peak strain of the DRX flow curve, SIBM occurs at a crucial strain. Locally bulged boundaries eliminate dislocations, which slows the rate of work hardening (Ebrahimi, Keshmiri, Momeni, & Mazinani, 2011). Poliak & Jonas (Poliak & Jonas, 1996) identified the critical strain as the intersection of work hardening vs. flow stress based on this method. Following the critical point, the expansion of local boundary bulges occurs and swallows up the previous boundaries, establishing the peak necklace structure. With further deformation, a greater number of nuclei generate and continue to replace the non-recrystallized grains entirely. At some point of deformation, the rate of DRX and dislocation accumulation is reached the equilibrium state resulting in a plateau in the flow curve. Figure 1.14 shows the development of the microstructure during dynamic recrystallization which demonstrates that the microstructure evolution depends on the ratio of the recrystallized and starting grain sizes (D_0/D_R). If (D_0/D_R)>2 then the microstructure develops as shown in Figure 1.14 a-d. However, if (D_0/D_R)<2 then the new grains all develop at about the same time because there are enough sites (i.e. old boundaries) for recrystallization to be complete in one cycle as shown in Figure 1.14e. Poliak & Jonas (Poliak & Jonas, 1996) have investigated the relationship between the initial grain size and the shape of the stress strain curves. For the microstructure evolution like Figure 1.14 a-d, the curves have a single peak followed by a plateau but for Figure 1.14 e, an oscillatory stress-strain curve results. The evolution of microstructure during DRV and DRX is schematically shown in Figure 1.15.
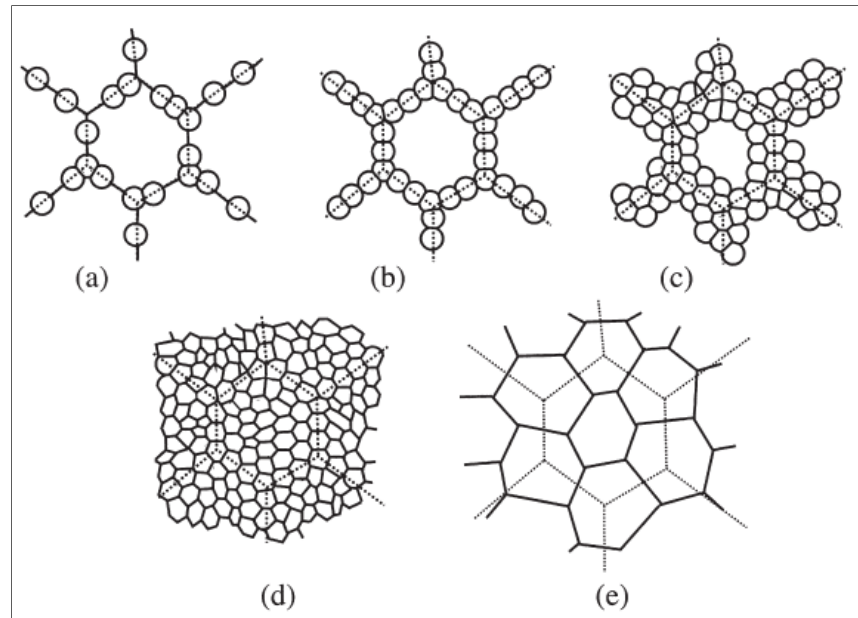
Figure 1.14 Schematic of microstructure evolution during dynamic
recrystallization (a)-(d) large initial grain size (e) small initial
grain size (The dotted lines represent the main grain boundaries)
Taken from Humphreys & Matherly (2004)
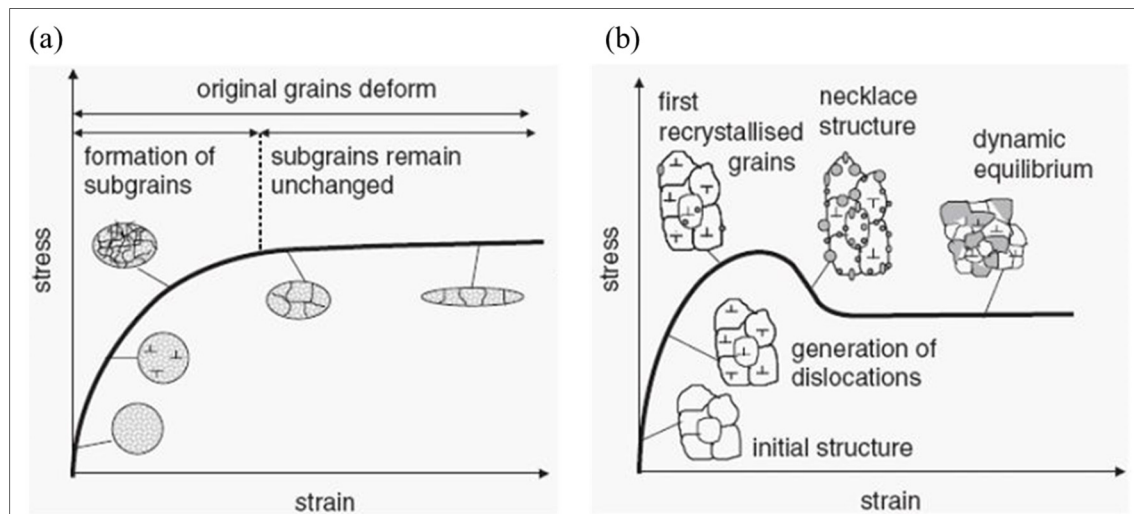
Figure 1.15 Microstructure evolution during hot deformation of a material showing (a)
recovery (DRV) and (b) dynamic recrystallization (DRX)
Taken from Alaneme & Okotete (2019)

The flow stress curve of the third type can be divided into four stages, Figure 1.16:

1) Linear hardening stage:

In this stage, a linear increase in flow stress take place which is due to an elastic deformation governed by work hardening (WH) resulting from dislocation multiplication. The dislocation generation and aggregation are continuously increasing and simultaneously DRV gradually strengthens and the stress increases to a critical value, ε_c, and DRX initiates.

2) Strain hardening stage:

The dislocation density is high enough for DRX nucleation. The stress gradually increases up to the peak due to counteracting the effect of WH and DRV/DRX.

3) Softening stage:

At this stage, there is a decrease in flow stress due to a dominant softening mechanism (DRX) and a secondary one (DRV) than WH. A large number of recrystallized nuclei are formed at this stage.

4) Steady-state stage:

The softening and hardening mechanism compete with each other and reach a dynamic balance and still, DRX is the main softening process (Kawulok et al., 2022).
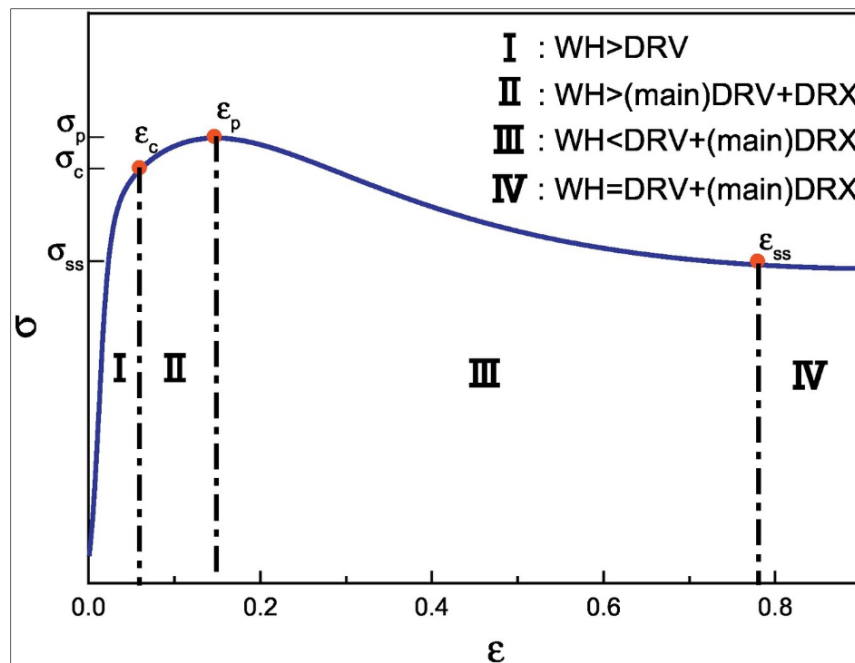
Figure 1.16 Schematic representation of different stages of
flow curve at elevated temperature deformation
Taken from Kawulok et al. (2022)

1.7   Determining Parameters on the Softening Mechanisms during Hot Forging

1.7.1   Stacking Fault Energy

The occurrence of softening mechanism during thermomechanical deformation depends on the relation between the rate of dynamic recovery and the velocity of the grain boundary migration. Stacking fault energy defines the ability of the material to rearrange/annihilate dislocations during thermal or thermomechanical processes. The relation between dynamic recrystallization (DRX) and dynamic recovery (DRV) during hot deformation for metallic materials is shown in Table 1.1. As it is shown, FCC metals such as Ag, Au, Cu, Ni, Pb, Pt, and the austenitic steels have low to medium stacking fault energy which means dynamic recovery occurs sluggishly and DRX is the dominant softening mechanism during hot deformation (Poliak & Jonas, 1996).

Table 1.1 The dynamic restoration process (DRX and DRV) operating during hot
deformation and the metallic materials
Taken from Poliak & Jonas (1996)

Restoration mechanism	Materials	Stacking fault energy (SFE)
Dynamic recrystallization (dDRX)	Au, Cu, Ni, Pb, austenitic Fe, and their alloys	Low (to medium)
Dynamic recovery (DRV)	Al, Mg, ferritic iron, and their alloys	High

Based on the MSS phase diagram in section 1.1.2, this steel is in the austenite phase during the hot forging process which has a low SFE value. Therefore, the main softening mechanism of MSS at high temperature is DRX (Humphreys & Hatherly, 2004).

1.7.2   Second Phase

Softening mechanisms could be varied in single-phase and multiple phases. In a single-phase austenitic structure, the equilibrium phase at the forging temperature of martensitic stainless steel, DRX can take place easily. However, when a second phase such as carbides and MnS are present or form during deformation, some interactions can either terminate or trigger DRX. The interaction generally depends on the precipitation size (Humphreys & Hatherly, 2004).

Fine particles can act as obstacles for high-angle grain boundaries movement and the pinning force overtakes the driving force for boundary bulging. As a result, DRX is hindered, and finer DRX grains form at higher strains. However, large particles (larger than 1 μm) stimulate DRX in which localized deformation zone forms around large particles and stimulates the nucleation of recrystallization (Apel, Böttger, Rudnizki, Schaffnit, & Steinbach, 2009).

1.7.3   Alloying Element

Alloying elements are divided into austenite and ferrite stabilizer elements. The former consists of Ni, Mn, and C, and the latter includes Cr, Si, and Mo. Each type of element has different stacking fault energy, which affects the rearrangement, and annihilation of dislocation, which is responsible for determining the softening mechanism. In addition, some alloying elements are strong carbide formers that form nanometric carbide particles. It has been proposed that adding some elements raises the peak stress due to the distribution of carbide particles or the effect of solute dragging on dislocation movement (Loucif et al., 2020). Another study reported that adding micro alloys to high-manganese steel leads to an increase in peak stress because of the locking effect of precipitated particles on the grain boundaries and also their effect on solid solution strengthening. Such solutes can alter the transformation behavior and delay recrystallization (Ezatpour, Torabi-Parizi, Ebrahimi, & Momeni, 2018).

Among alloying elements, chromium and carbon can strongly affect phase transformation during high-temperature forging. In martensitic stainless steels, chromium and other ferrite stabilizing elements expand the delta-ferrite phase field and lead to a dual phase (delta ferrite + martensite) at room temperature. On the other hand, austenite stabilizing elements expand the γ phase field and shrink the delta ferrite region. As a result, by increasing austenite to ferrite-stabilizing elements, a fully martensitic structure will be obtained after solidification (Stone et al., 2017). In their study, different chemical compositions were analyzed to show different solidification modes. Table 1.2 shows three different chemical compositions.

Table 1.2 Three chemical compositions for type 410 steel and weld metals
Taken from Stone et al. (2017)

Standard	C	Cr	Ni	Mo	Mn	Si	P	S	Cu
AWS A5.5	0.12	11.0-13.5	0.7*	0.75	1.0	0.9	0.04	0.03	0.75
AWS A5.9	0.12	11.0-13.5	0.70	0.75	0.6	0.5	0.03	0.03	0.75
ASTM A240	0.08-0.15	11.5-13.5	0.75	-	1.0	1.0	0.04	0.03	-

* Single values are maxima

Three solidification modes based on austenite to ferrite stabilizing elements ratio were proposed (L: liquid, δ: delta ferrite, γ: austenite, F_e: eutectic ferrite, M: martensite). The first one is related to higher austenite stabilizers that lead to fully martensitic microstructure after solidification:

$$L \rightarrow L + \delta \rightarrow \delta \rightarrow \delta + \gamma \rightarrow \gamma \rightarrow M$$
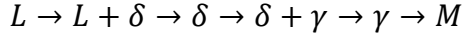
The second mode of solidification mode occurs when that ratio reduces resulting in an uncompleted austenite transformation and mixture of both delta ferrite and martensite:

$$L \rightarrow L + \delta \rightarrow \delta \rightarrow \delta + \gamma \rightarrow M + \delta$$
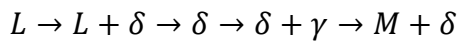
The third one happens when the material does not solidify as ferrite, leading to the formation of the eutectic ferrite where enriched in ferrite stabilizing elements. Eutectic ferrite, which is enriched then, becomes stable at room temperature leading to a primarily martensitic microstructure with eutectic ferrite along the grain boundaries:

$$L \rightarrow L + \delta + (\gamma + Fe) \rightarrow \delta + \gamma + Fe \rightarrow \gamma + Fe \rightarrow M + Fe$$
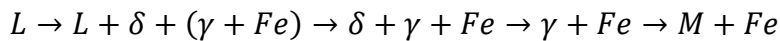
The general industrial approach in the high temperature forging of MSS is to minimize the volume fraction of the delta ferrite by controlling the ratio of austenite to ferrite stabilizer

elements and forging parameters because of its adverse effects on mechanical properties such as making material sensitive to crack propagation, reducing strength, and toughness, inhomogeneity of plastic deformation. The lack of toughness has been reported to be due to extreme amounts of delta ferrite in the weld metal. In general, optimizing the chemical composition toward an acceptable ferrite to austenite stabilizing ratio is not only important for as-cast microstructure but determines the microstructural evolution during high-temperature forging (Ezatpour et al., 2018; Stone et al., 2017).

1.7.4   Initial Grain Size

The initial grain size has a significant impact on the flow behavior of material subjected to DRX, with increasing grain size changing the flow curve shapes from multiple peaks to a single peak. In coarse-grained starting materials, single peak flow is associated with grain refinement, whereas multiple peak flow is associated with grain coarsening until the stable grain size required to initiate DRX nucleation is attained. The stable grain size is also affected by strain rate and deformation temperature. It is reported that the initial coarse microstructures retard DRX, while in fine microstructure this process accelerates because the nucleus density at a critical strain, required strain for DRX nucleation, in fine microstructure is much higher than the coarse one. In the fine grain material, each DRX nucleus growth is limited by boundary impingement, which leads to the development of intermediate grain size. The final grain size is strongly affected by the strain rate and temperature in a way that increases with temperature while decreasing with the strain rate (Momeni, Ebrahimi, Jahazi, & Bocher, 2014).

The relationship between grain size and working variables (T, ε, $\dot{\varepsilon}$) in the hot deformation process on martensitic stainless steel is reported in the following relation and confirms the above relationship (Momeni & Dehghani, 2010a):

$$D = 1958.6\, Z^{-0.06} \tag{1.1}$$

Where, Z is Zener–Hollomon parameter that incorporates the deformation temperature and strain rate.

$$Z = \dot{\varepsilon} \exp\left(\frac{Q}{RT}\right) \qquad (1.2)$$

Where, Q signifies the apparent activation energy, R is the gas constant and T is the absolute temperature. It is shown in Figure 1.17 that DRX grain size depends on the Z parameter so that it decreases with increasing in Z.
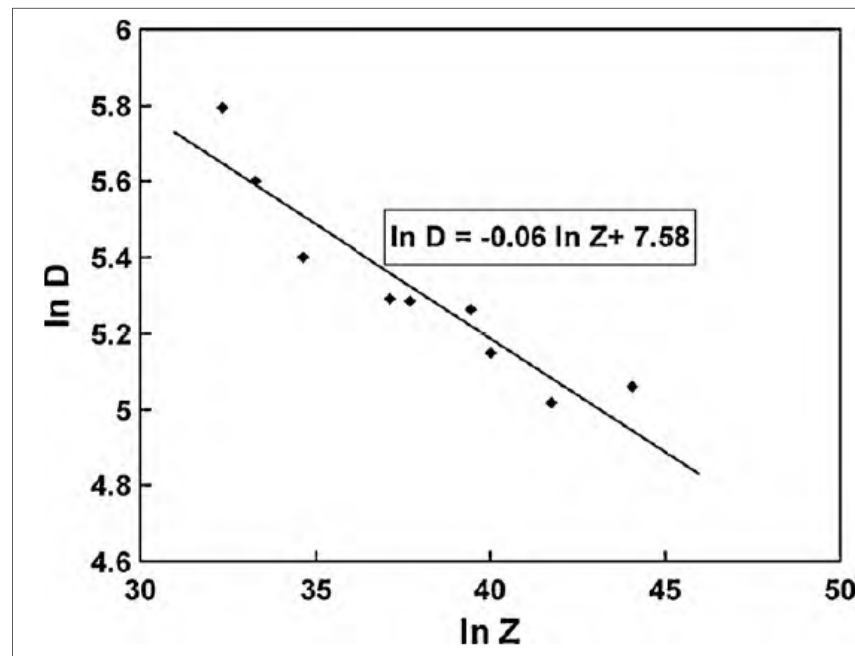
Figure 1.17 Dependence of DRX grain size on Z parameter
Taken from Momeni & Dehghani (2010)

Furthermore, the changes in grain size with changing T and ε were characterized by optical microscopy in Figure 1.18, which confirms that by increasing T and decreasing strain rate, the final grain size increases (Ebrahimi, Keshmiri, Mazinani, Maldar, & Haghshenas, 2013).
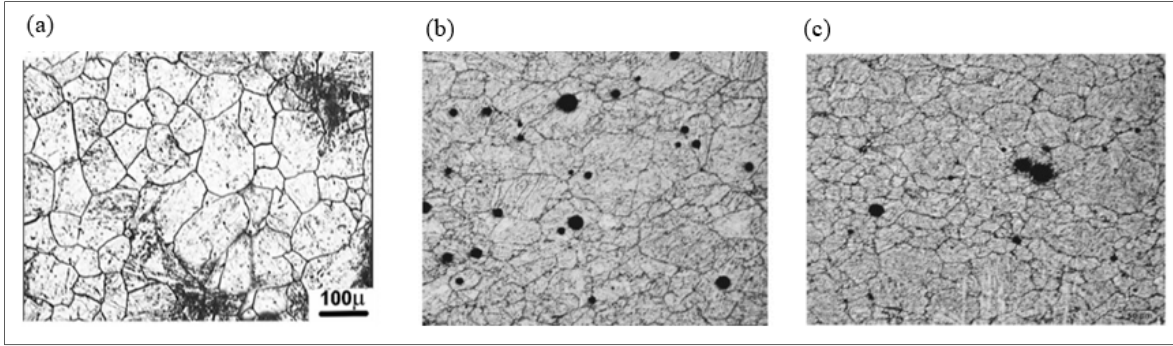
Figure 1.18 (a) Start microstructure (b) T=1000°C, ε=0.001 s^{-1} (c) T=900°C, ε=0.1 s^{-1}
Taken from Ebrahimi et al. (2013)

During high-temperature deformation, subgrains are subjected to two opposing effects. The first is that increasing strain causes them to grow larger while increasing stress causes them to shrink. Cram et al. proposed a relationship between the shrinking rate of subgrains caused by applied stress and their expansion caused by increasing strain (Momeni et al., 2014):

$$r = \frac{2\gamma_{sb}M_{sb}\varepsilon}{\dot{\varepsilon}} + \frac{1}{2}\frac{KGb\theta_{II}}{\sigma_s(\sigma_s-\sigma_0).K_2\left(1-\exp\left(-\frac{1}{2}K_2\varepsilon\right)\right)} \tag{1.3}$$

Using equation (1.6), it is possible to determine the subgrain size as a function of strain and this equation shows that subgrain size, r, increases with the strain. In contrast, classical nucleation theory predicts a drop in the critical subgrain size for nucleation (r$_c$) since increases the internal stored energy (ΔE) increases with an increase in strain (Momeni et al., 2014):

$$r_c = \frac{2\gamma_{gb}}{\Delta E} \tag{1.4}$$

In addition, subgrains grow during forging until those located near the boundaries act as the source of local bulging. The bulged boundaries are due to the high enough difference in dislocation density on the two sides of the grain boundaries, so the required driving force is met when the subgrains reach the critical size (Momeni et al., 2014).

It should be emphasized that strain energy may differ from grain to grain due to the inhomogeneity of deformation at the macroscopic level. As a result, during high-temperature forming, a wide range of subgrain sizes are created. It is generally accepted that the amount of stored energy just near the original grain boundary is higher relative to other regions and therefore the faster subgrain growth in these locations is more probable (Momeni et al., 2014). Rayleigh distribution has been used to explain the subgrain size distribution in deformed materials. Figure 1.19 shows the schematic of Rayleigh distribution and compared the subgrain size for two different strains. The image shows that the number of supercritical subgrains rises as strain does, which is compatible with the fact that dynamic recrystallization occurs as strain increases (Momeni et al., 2014). It can be concluded that the regions subjected to higher strain have higher potential for DRX nucleation because the condition for grain boundary bulging and the internally stored energy is accelerated.
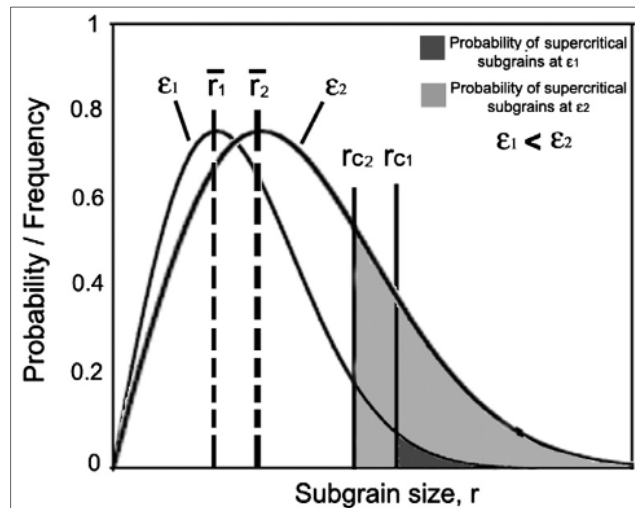
Figure 1.19 Schematic display of the subgrains
size statistical distribution according to the
probability theory at two strains of ε_1 and ε_2
Taken from Momeni et al. (2014)

1.7.5   Temperature-Strain Rate

At temperatures above 0.5 T_m, the restoration processes for material in low to medium SFE, martensitic stainless steels, are dynamic recovery (DRV) and dynamic recrystallization (DRX). These restoration processes are controlled by a thermally activated mechanism. When the

temperature is increased, DRX takes place more rapidly since it causes an acceleration in migration of HABs and more annihilation of dislocation substructures, increasing the number of different operating slip systems that leads to more homogenous deformation and also dissolving precipitates. According to the Zener-Holloman parameter, the flow curve exhibited for the DRX condition changes from multiple peaks to a single peak and shifts to a higher flow stress level as the temperature is decreased. In addition, at lower temperatures, a faster rate of work hardening delays the rate of work softening due to DRX, postponing the beginning of steady-state flow until higher strain levels.

The flow curve behavior changes from multiple peaks to single peaks as the strain rate increases and temperature decreases. That is because, at higher strain rates and lower temperatures, the higher work hardening rate slows down the rate of work softening due to DRX and both the peak and the onset of steady state flow are therefore shifted to higher strain levels. In case of multi-peak flow curve, the first cycle of DRX is completed before the next one is started and this behavior leads to the multi-peak flow curve. Otherwise, when successive cycles of DRX overlap, the material is partially recrystallized at a moment therefore a single-peak flow curve is expected. Figure 1.20 shows the flow curve of hot deformation of AISI 410, MSS, at a constant strain, strain rate. It can be concluded that at a higher temperature and lower strain rates, a cyclic behavior of the flow curve is observed for materials undergoing DRX (Momeni & Dehghani, 2010a).
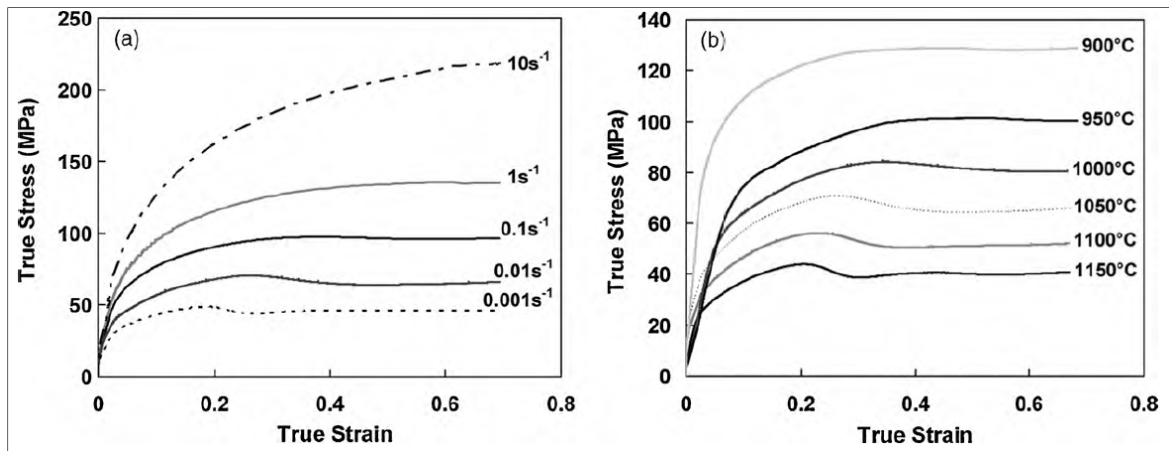
Figure 1.20 Typical DRX flow curves plotted at different
deformation conditions (a) 1050°C and (b) 0.01 s^{-1}
Taken from Momeni & Dehghani (2010)

Qi et al. (Qi et al., 2015) have done an investigation on microstructural evolution during hot compression tests of AISI 410 with variable temperature and strain rate. In their work, at the beginning of deformation, the stress increases quickly due to an increase in the work hardening rates. When deformation or strain continues, the growth of stress slows, and therefore the slope of stress decreases, which represents material softening due to dynamic recovery. To investigate the change in the microstructure, the deformation temperature and strain are changed as shown in the optical microscopic depicted in Figure 1.21.
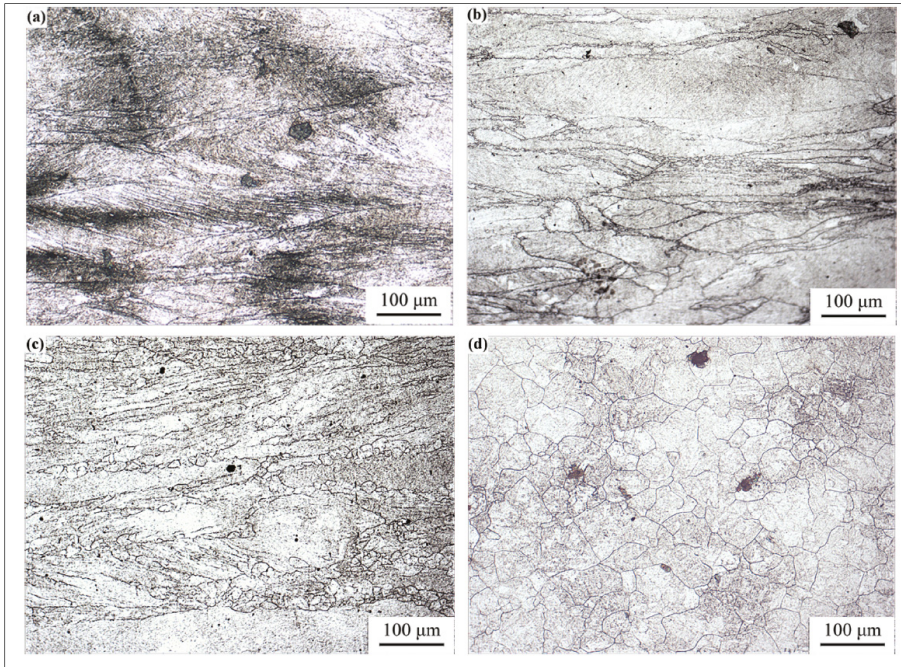
Figure 1.21 Metallographs showing the microstructure of AISI 410
stainless steel (a) T=1000°C - ε=10 s^{-1} (b) T=1200°C - ε=10 s^{-1} (c)
T=1050°C - ε=1 s^{-1} (d) T=1200°C - ε=0.1 s^{-1}
Taken from Qi et al. (2015)

Figure 1.21a shows that at T=1000°C and ε=10 s^{-1} only dynamic recovery occurs during deformation, whereas Figures 1.21b and 1.21c indicate that partial dynamic recrystallization took place under the T=1200 °C, ε=10 s^{-1} and T=1050 °C, ε=1s^{-1}, respectively. In Figure 1.21d, complete dynamic recrystallization at T=1200 °C, ε=0.1 s^{-1}. This means that decreasing temperature and increasing strain rate retard dynamic recrystallization (Qi et al., 2015).

1.7.6   Delta Ferrite

Delta ferrite in martensitic stainless steel forms during solidification and the amount of this phase depends on the chemical composition (mainly Cr and C), hot working temperature, and as-received microstructure condition. This phase adversely affects the mechanical properties, forming characteristics that possibly of inducing cracks and rejection of materials. Therefore,

decreasing the amount of this phase is a big challenge in the steel-forming industry (Niessen, Tiedje, & Hald, 2017).

The alloying elements either austenite or ferrite stabilizer, strongly affect the microstructure transformation during high-temperature deformation such as forging. By increasing the austenite to ferrite stabilizing ratio, the austenite zone expands and the delta ferrite zone shrinks, resulting in fully martensitic steel at room temperature. On the other hand, when that ratio is reduced, the austenite phase field shrinks due to an incomplete austenite transformation that leads to a mixture of either delta ferrite or martensite. Figure 1.22 shows the effect of ferrite stabilizers on the shrinkage or expansion of phase fields (Balmforth & Lippold, 2000).
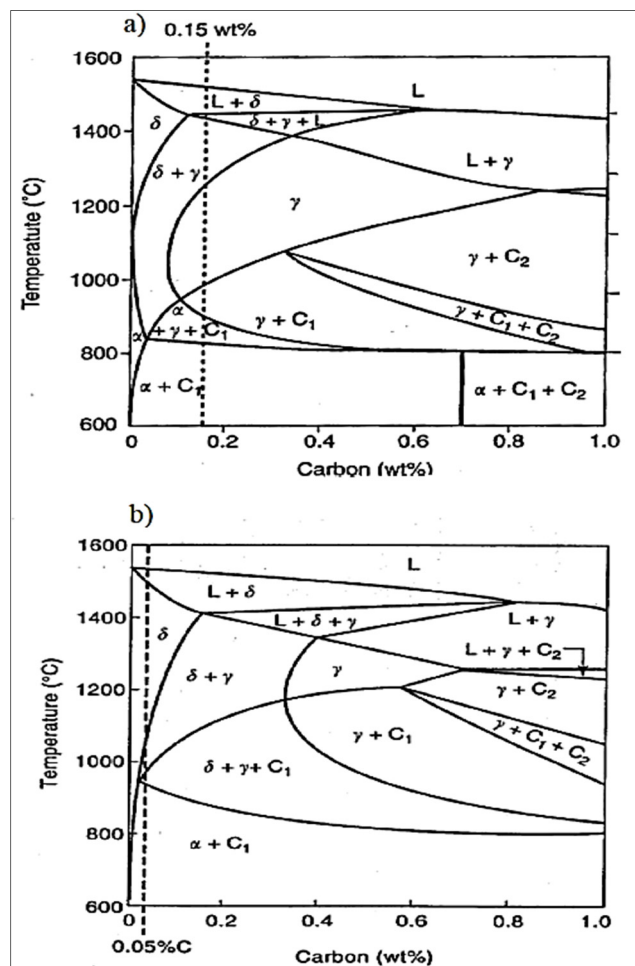
Figure 1.22 Comparison between two levels
of ferrite stabilizers (a) 13% Cr (b) 17% Cr
Taken from Balmforth & Lippold (2000)

With the saturation of ferrite-stabilizing elements, the stability of the delta ferrite at room temperature increases. Because ferrite-stabilizing elements are accumulated in the delta ferrite phase and the ferrite phase is softer than austenite at a given temperature, the condition will be favored for carbide precipitation growth around the delta ferrite phase. Furthermore, the rate of dislocation generation during deformation is significantly higher in the softer phase than in the harder one. In other words, the plasticity of multiphase materials in which the softer phase hardens faster than the harder phase. In martensitic stainless steels, the softer phase is delta ferrite during straining and the density of strain-hardened grains is higher than the other part. This inhomogeneity of internally stored energy leads to non-uniform plastic flow on a microscopic scale. Such non-uniformity can contribute to the nucleation of pores and cracks. As a result, increasing this phase contributes to a reduction in the strength and toughness of martensitic stainless steel (Stone et al., 2017).

In addition to the non-uniformity of plastic deformation because of the delta ferrite, working variables such as the strain rate and temperature play a crucial role in delta ferrite content. In an investigation (Qi et al., 2015) it is shown that by increasing deformation temperature and increasing strain rate, both the amount and size of delta-ferrite increases. The optical microscopic photo of AISI 410 stainless steel at different temperatures is depicted in Figure 1.23.
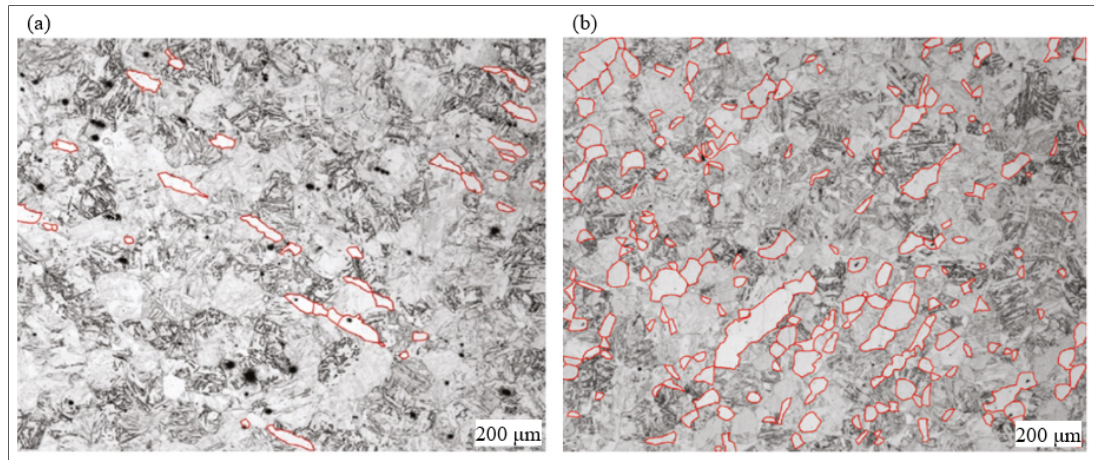
Figure 1.23 Optical images of microstructure of AISI 410 MSS
(a) T=1100 °C (b) T=1220 °C (red-outlined areas show delta-ferrite grains)
Taken from Qi et al. (2015)

1.8 Application of Stress-Strain Curves to Analyze Hot Deformation Characteristics

Softening mechanism characterization by experimental results:

After reaching the required amount of deformation for initiation of DRX, Critical strain, only a small amount of recrystallization appears at this strain and the flow stress continues to increase beyond these points until the strain hardening is balanced by total softening due to DRX. Ultimately, a strain-independent steady state is achieved, which illustrates the balance between the rates of hardening and restoration (Ebrahimi, Keshmiri, Maldad, & Momeni, 2012b). Poliak & Jonas (Jonas & Poliak, 2003) developed a double differentiation method to accurately identify the critical strain and stress for the initialization of DRX. This method can successfully detect the onset of DRX. The strain hardening rate ($\theta = d\sigma/d\varepsilon$) are calculated using the hot flow stress-strain curve data. The curves of strain hardening rate values in relation to the flow stress are shown in Figure 1.24.
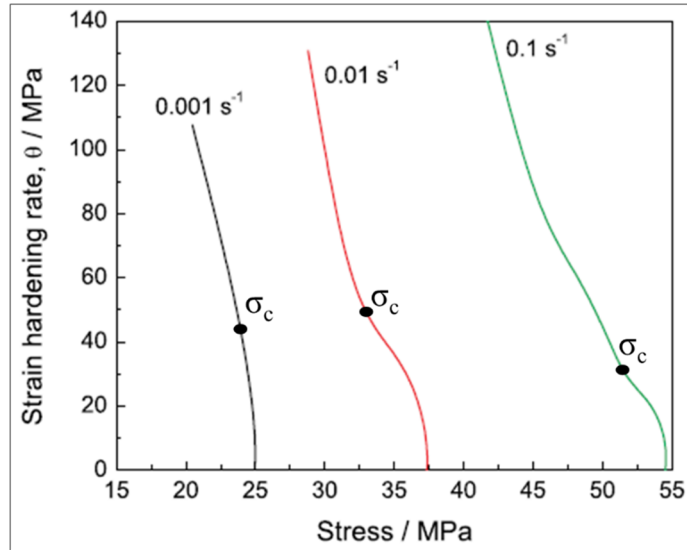
Figure 1.24 θ-σ curves of hot deformed steel at
1000 °C and different strain rates
Taken from Ebrahimi et al. (2012)

In the θ-σ curve, Figure 1.24, the peak stress in the stress-strain curve, σ_p, is obtained when θ equals zero (θ=0) and the inflection point of the θ-σ curve signifies the critical stress (σ_c) for the initiation of DRX. The strain hardening rate vs. strain is plotted to find the stain at which the rate of dynamic softening is maximized and in the θ-ε curve is the minimum point, ε^*, Figure 1.25.
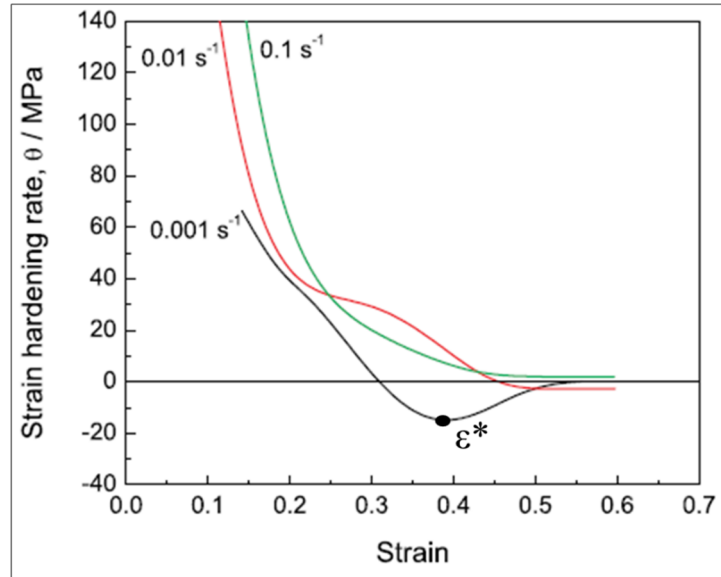
Figure 1.25 Strain hardening rates vs. strain for steel
deformed at 950 °C and different strain rates
Taken from Ebrahimi et al. (2012)

It is seen in Figure 1.26 that the value of ε^* increases with decreasing deformation temperatures and increasing strain rates. To calculate the volume fraction of DRX, the Avrami type model (Dieter et al., 2003) can be used:

$$X_{DRX} = 1 - \exp\left[-0.693\left(\frac{(\varepsilon-\varepsilon_c)}{\varepsilon^*}\right)^2\right]$$

(1.5)

Where X_{DRX} is the DRX fraction, ε_c is the critical strain for the onset of DRX, ε is the true strain, and ε^* is the strain for the maximum softening rate during dynamic recrystallization. The volume fraction of DRX would be determined as a function of strain at various deformation temperatures as the model was applied to the available data (Ebrahimi et al., 2012b). Similar to the experimental result, critical stress and strain for DRX initiation can be obtained by taking derivative of the stress-strain curve (Quan, Li, et al., 2011), Figure 1.26.
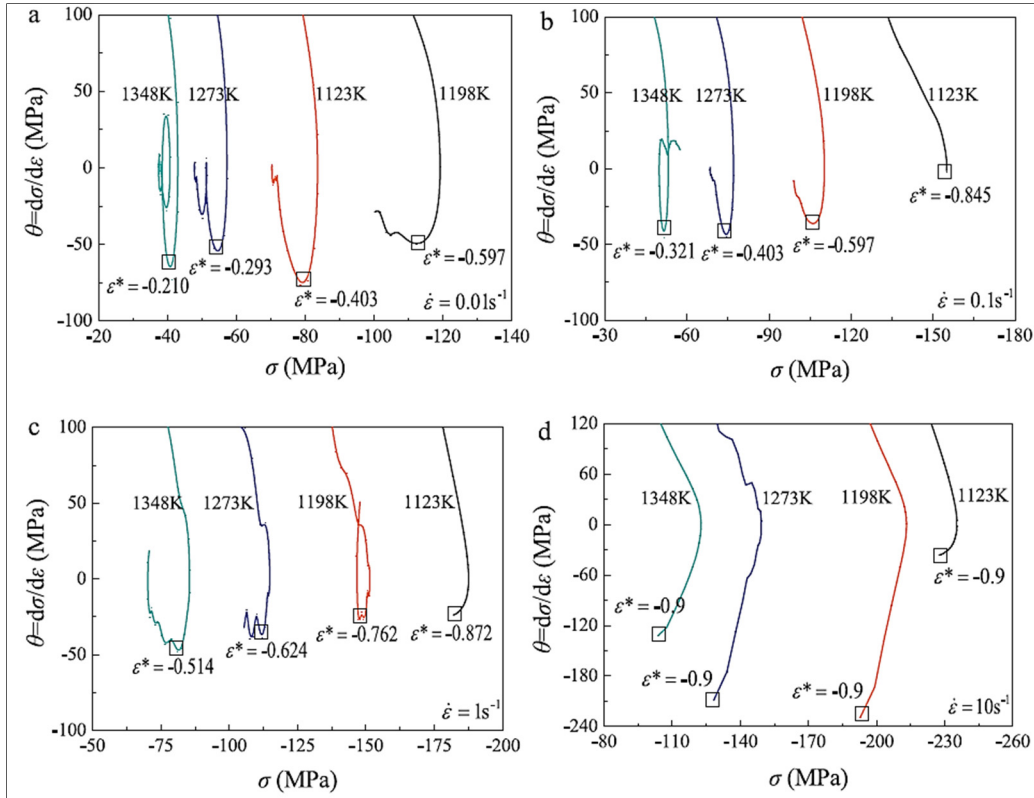
Figure 1.26 dσ/dε-σ curves after the peak of the stress-strain plots
at different deformation temperatures and strain rates of
(a) 0.01 s^{-1} (b) 0.1 s^{-1} (c) 0.5 s^{-1} and (d) 1 s^{-1}
Taken from Quan et al. (2011)

1.9 Constitutive and Microstructural Modeling of Open Die Forging Process

1.9.1 Constitutive Equation

The determination of dynamic response under certain deformation conditions is a highly important piece of information for optimizing the microstructure and mechanical characteristics. Working factors including strain, strain rate, and deformation temperature alter with flow stress, a crucial component during hot deformation. Mathematical relationships should be established to measure the response to a change in the strain, strain rate, and deformation temperature in order to assess this change in flow stress. Flow behavior is mainly due to work hardening (WH), Dynamic recovery (DRV), and Dynamic Recrystallization

(DRX). Constitutive models are used as input codes for finite element methods. As a result, the accuracy of the simulation's results is greatly influenced by the constitutive models' accuracy. Various models have been constructed to describe the hot deformation behavior of metallic materials under given loading conditions (Ren, Chen, & Chen, 2014). Different constitutive models are described in the following:

Strain-Compensated Arrhenius model:

The Arrhenius model is used to explain the relationships between strain rate, flow stress, and temperature, especially at high temperatures, through the hyperbolic law equation:

$$\dot{\varepsilon} = A_1 + \sigma^{n_1} \exp\left(\frac{Q}{RT}\right), \qquad \alpha\sigma < 0.8 \tag{1.6}$$

$$\dot{\varepsilon} = A_2 \exp(n_2\sigma) \exp\left(\frac{Q}{RT}\right), \qquad \alpha\sigma > 1.2 \tag{1.7}$$

$$\dot{\varepsilon} = A[\sinh(\alpha\sigma)]^n \exp\left(\frac{Q}{RT}\right), \quad \text{for all } \alpha\sigma \tag{1.8}$$

Where σ is the flow stress; $\dot{\varepsilon}$ the strain rate; Q activation energy; A_1, A_2, A, n_1, n_2, n, and α are the material constants; and R is the universal gas constant in the hot deformation process. To introduce the impact of temperature and strain rate on the deformation behavior of the material, the Zener-Hollomon parameter (Z) can be used as follows (Samantaray, Mandal, & Bhaduri, 2009):

$$Z = \dot{\varepsilon} \exp\left(\frac{Q}{RT}\right) = A[\sinh(\alpha\sigma)]^n \tag{1.9}$$

However, the Arrhenius model does not consider the strain, which significantly affects the flow stress. Therefore, based on the research by Anoop et al. (Anoop, Prakash, Giri, Narayana Murty, & Samajdar, 2018), the strain compensation approach is presented as Eqs. (1.13)-(1.16) in this project. Through these equations the values of α, n, Q, and A can be calculated at each strain following the above-explained approach.

$$n = B_0 + B_1\varepsilon + B_2\varepsilon^2 + B_3\varepsilon^3 + B_4\varepsilon^4 + B_5\varepsilon^5 + B_6\varepsilon^6 \tag{1.10}$$

$$\alpha = C_0 + C_1\varepsilon + C_2\varepsilon^2 + C_3\varepsilon^3 + C_4\varepsilon^4 + C_5\varepsilon^5 + C_6\varepsilon^6 \tag{1.11}$$

$$Q = D_0 + D_1\varepsilon + D_2\varepsilon^2 + D_3\varepsilon^3 + D_4\varepsilon^4 + D_5\varepsilon^5 + D_6\varepsilon^6 \tag{1.12}$$

$$\ln A = E_0 + E_1\varepsilon + E_2\varepsilon^2 + E_3\varepsilon^3 + E_4\varepsilon^4 + E_5\varepsilon^5 + E_6\varepsilon^6 \tag{1.13}$$

Finally, the flow stress can be represented as a function of the Zener–Hollomon parameter and implementation of the constants which are formulated as strain-dependent:

$$\sigma = \frac{1}{\alpha}\ln\left\{ \left(\frac{Z}{A}\right)^{\frac{1}{n}} + \sqrt{\left(\frac{Z}{A}\right)^{\frac{2}{n}} + 1} \right\} \tag{1.14}$$

Figure 1.27 depicts an example of flow stress obtained by Arrhenius equation for the hot compression process (Qi et al., 2015).
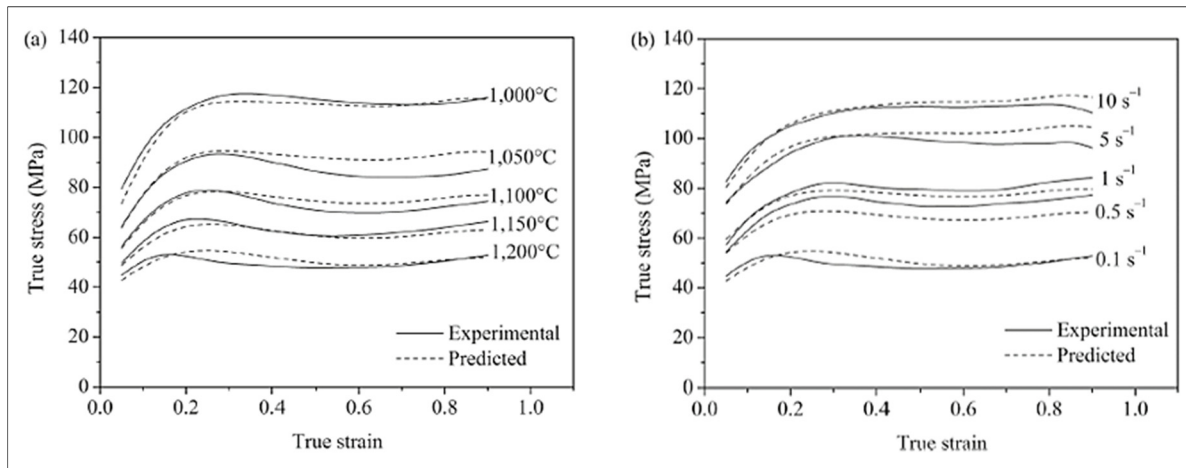
Figure 1.27 Comparisons between the findings predicted by the constitutive
equation and the corrected curve (a) $\dot{\varepsilon} = 0.1\ s^{-1}$ (b) T= 1200 °C
Taken from Qi et al. (2015)

Hansel-Spittel Model:

Hansel-Spittel is another constitutive model that predicts the relation between forming variables including strain, strain rate, and temperature. It is commonly known as HS equation and is used for various alloys like Al-0.7%Mg-0.4%Si, AZ31, 20MoCrS4, aluminum, and AA6082 alloy (Jandová et al., 2003).

$$\sigma = Ae^{m_1 T}\varepsilon^{m_2}\dot{\varepsilon}^{m_3}e^{\frac{m_4}{\varepsilon}}(1+\varepsilon)^{m_5 T}e^{m_7 \varepsilon}\dot{\varepsilon}^{T m_8}T^{m_9} \qquad (1.15)$$

Where, m_1 to m_9 determine the material's sensitivity to temperature, A is the material consistency at a given temperature (assumed isothermal conditions), and the calculated constants are applied in the equation for various variables in order to find the values of stress. The material response to the constitutive equation varies from alloy to alloy. To understand which model precisely tracks the experimental data, a comparison between simulated results and experimental data should be done. The model, which represents the best representation of the deformation behavior of the as-cast structure and particularly the occurrence of different softening processes results, will be employed in the simulation software. Figure 1.28 shows the comparison between Hansel-Spittel model results and experimental data for the hot deformation process (Liang, Liu, Li, Ding, & Zhang, 2020).
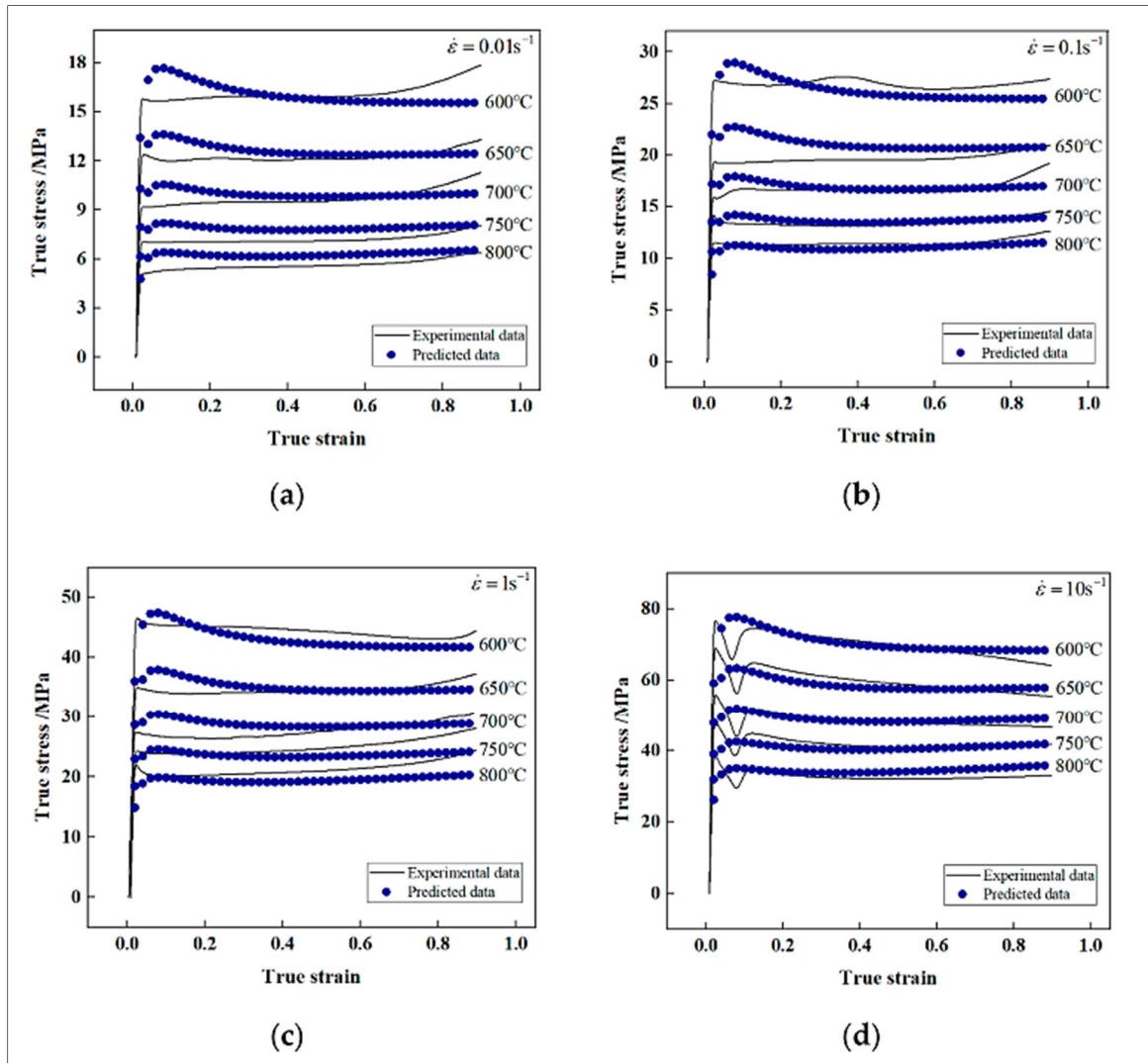
Figure 1.28 Comparisons of the experimental and predicted flow stress values at strain rates (a) 0.01 s⁻¹ (b) 0.1 s⁻¹ (c) 0.5 s⁻¹ and (d) 1 s⁻¹

Taken from Liang et al (2020)

Johnson-Cook (JC) Constitutive Model:

The J-C constitutive model is one of the most widely used models which was proposed by Johnson and Cook first (Johnson & Cook, 1983). As a semi-empirical model, it explains the behaviors of plastic materials at high strain rates, high strains, and high temperatures. This model can be expressed as follows:

$$\sigma = (A + B\varepsilon^n)\left(1 + Cln\left(\frac{\dot{\varepsilon}}{\dot{\varepsilon}_0}\right)\right)\left[1 - \left(\frac{T-T_r}{T_m-T_r}\right)^m\right] \tag{1.16}$$

Where $\dot{\varepsilon}$ & $\dot{\varepsilon}_0$ are the strain rate and the reference strain rate, σ is the equivalent flow stress, and ε is the plastic strain. T, T_m, and T_r are the temperature, the melting point, and the reference temperature respectively. The empirical parameters are as follows: B is the coefficient of strain hardening, A is the yield stress at reference temperature and reference strain rate, C is the coefficient of strain rate hardening, and n and m are the strain hardening exponent and the thermal softening exponent, respectively. Figure 1.29 shows the comparison between flow stress measure and predicted experimentally and mathematically, Johnson-Cook (JC) constitutive model.
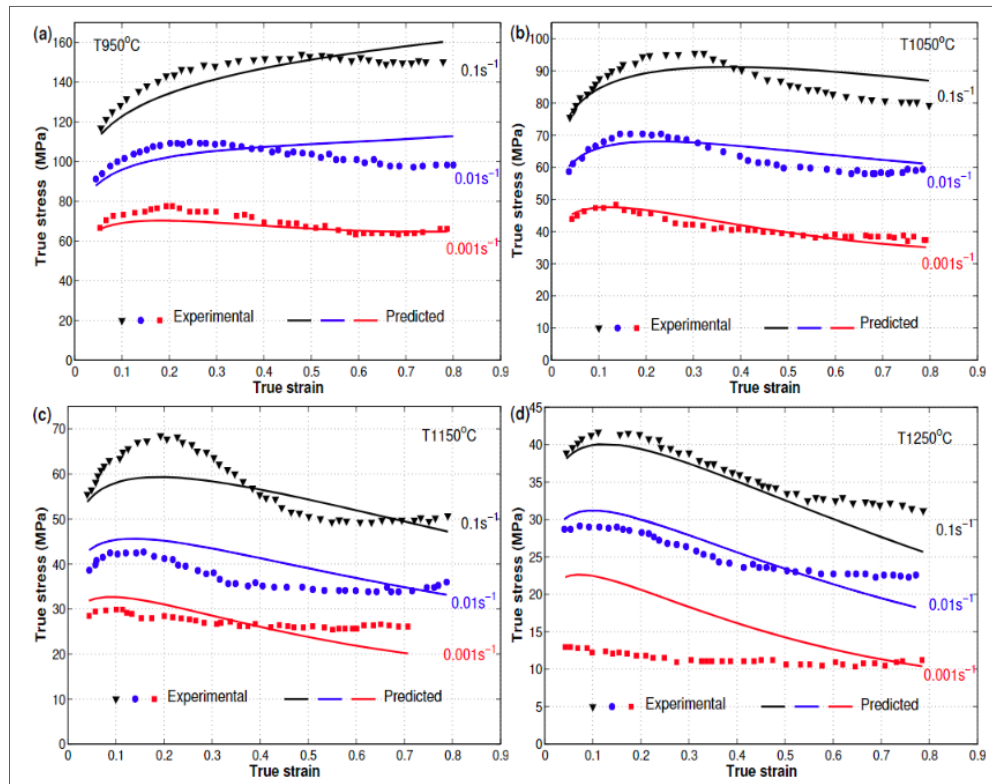
Figure 1.29 Comparisons of the JC model's predicted stresses (lines)
and experimental stresses (markers) at various temperatures and strain rates
(a) 950 °C (b) 1050 °C (c) 1150 °C and (d) 1250 °C
Taken from Shokry et al. (2019)

Zerilli-Armstrong Model:

Flow behavior could be predicted by Zerilli Armstrong model, according to this model, the flow stress is expressed as:

$$\sigma = (C_1 + C_2\varepsilon^n)\exp\{-(C_3 + C_4\varepsilon)T^* + (C_5 + C_6T^*)\,ln\dot{\varepsilon}^*\} \tag{1.17}$$

where C_1, C_2, C_3, C_4, C_5, C_6, n are material constants, ε is the true plastic strain, $\dot{\varepsilon}$ is the strain rate, $\dot{\varepsilon}^* = \frac{\dot{\varepsilon}}{\dot{\varepsilon}_0}$ is the dimensionless strain rate, $\dot{\varepsilon}_0$ is the reference strain rate, $T^* = (T - T_{ref})$ with T and T_{ref} being current and reference temperatures the reference temperature and reference strain rate (Samantaray et al., 2009). Figure 1.30 shows the comparison between the experimental and predicted flow curves at different temperatures.
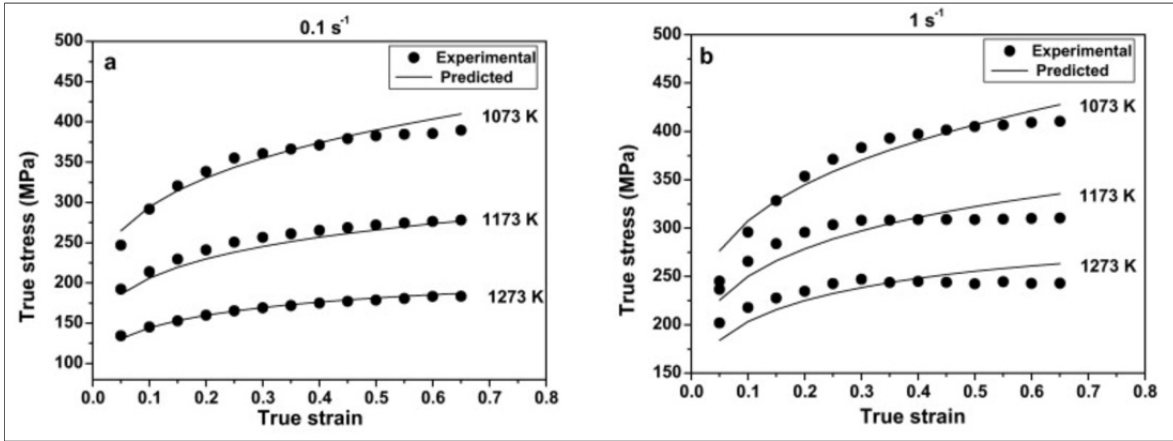
Figure 1.30 Comparison of experimentally obtained flow curves and those predicted by the modified Zerilli-Armstrong (MZA) equation at strain rates of (a) 0.1 s^{-1} and (b) 1 s^{-1} for the temperature range 1073–1273 K (at intervals of 50 K)
Taken from Samantaray et al. (2019)

The predictability of constitutive models for each material defines which model could predict the material behavior of the material at high temperatures. At least, the model with the least error value would be selected for prediction. The accuracy of each model is verified by employing average absolute relative error (AARE), correlation coefficient (R), and relative error (Δ). The relative error measures how accurately a model can predict future values, and

AARE is created by calculating the relative error term by term. The R shows the linear relationship between experimental and calculated values. Their expressions are shown as follows (Rudra, Das, & Dasgupta, 2019):

$$AARE = \frac{1}{N} \sum_{i=1}^{N} \left| \frac{\sigma_E - \sigma_p}{\sigma_E} \right| \tag{1.18}$$

$$\Delta = \frac{1}{N} \sum_{i=1}^{N} \left| \frac{\sigma_E^i - \sigma_P^i}{\sigma_E^i} \right| \times 100 \tag{1.19}$$

$$R = \frac{\sum_{i=1}^{N}(\sigma_E^i - \overline{\sigma}_E)(\sigma_P^i - \overline{\sigma}_P)}{\sqrt{\sum_{i=1}^{N}(\sigma_E^i - \overline{\sigma}_E)^2 \sum_{i=1}^{N}(\sigma_P^i - \overline{\sigma}_P)^2}} \tag{1.20}$$

Where σ_E is the experimental data and σ_P is the calculated value based on the proposed constitutive equations. $\overline{\sigma}_P$ and $\overline{\sigma}_E$ are the mean values of σ_P and σ_E, respectively and N is the number of data points.

Although extensive works conducted on material modeling and employing different constitutive equations for flow stress prediction of different grades of steels, less attention has been paid to the development of the microstructure-base model. Specifically, with regard to martensitic stainless steels, most studies worked on the characterization of hot deformation using constitutive equations and very few works focused on hot deformation behavior with considering the relationship between working parameters and microstructure. The combination of microstructure-base models and microstructure evolution during the hot deformation process is very rare, specifically for martensitic stainless steel. In addition, there is a significant lack of research on the microstructure-base modeling in large-scale practice which is necessary for heavy forged products during process design.

1.9.2   Microstructural Evolution Model

Heating and single-hit deformation are the two processes that dominate microstructural change during open die forging. The target temperature, heating rate, and holding time all have a significant impact on how the grain size evolves during the heating process. Dynamic recrystallization (DRX) dominates the microstructural evolution during single-hit deformation at high temperatures and affects the final forging's grain size distribution for metals with

moderate to low stacking fault energy (F. Chen, Cui, & Chen, 2014). Prediction of microstructure evolution is critical in hot metal forming due to the significant impact of microstructure changes on the mechanical properties of the forged products. Therefore, understanding the microstructural changes and softening mechanism is a necessity in obtaining the desired properties. Sellar et al. were a pioneer in modeling complex recrystallization mathematically and developed a set of formulas that relates the important metallurgical variables to the working parameters (Sellars & Whiteman, 1979). Several phenomenological models have been proposed during the past 50 years to forecast grain evolution during heating and DRX (F. Chen et al., 2014; Jeong, Cho, & Park, 2005; Park, Kim, Na, & Yeom, 2001). To date, the researchers such as Hodgson et al. (Hodgson & Gibbs, 1992), Laasroui and Jonas (Laasraoui & Jonas, 1991), Nanba et al. (Nanba et al., 1992), and Kim et al. (S. Il Kim & Yoo, 2001) were employed the phenomenological models to predict the microstructure evolution during hot deformation for metals and alloys. It is well-known that dynamic recrystallization depends on the initial grain size, strain, strain rate, and deformation temperature, which change over time. Recrystallization and grain growth processes can be predicted using the traditional JMAK model (Johnson-Mehl-Avrami-Kolmogorov), which is mathematically stable (Hallberg, 2011). The global recrystallization kinetics can be described by the semi-empirical analytical model JMAK, as has been demonstrated for more than a decade as X (t) illustrate the recrystallized grain fraction as a function of time (t):

$$X(t) = 1 - e^{-b.t^n} \qquad (1.21)$$

The Avrami coefficient, represented by the exponent (b), is highly sensitive to changes in temperature. The Avrami exponent (n) is connected to the mechanism of phase change, for instance, if the nucleation rate is stable or even rises as the transformation proceeds, or if it falls to zero shortly after the start of growth.

Despite the importance of microstructure evolution analysis in the forming industries, there are very few publications and investigations on this topic, specifically for large-scale forging

processes. In addition, the phenomenological models that can accurately predict the microstructure evolution are relatively rare for martensitic stainless steel.

1.9.3   Dynamic Material Model (DMM)

For analyzing the hot deformation behavior, the dynamic material model (DMM) was developed by Prasad et al. (Prasad, 2013). In this model, the first step is drawing the processing map to draw the power dissipation map (PDM) of the specified material. The use of a "processing map" can optimize hot working processes and control microstructure without employing costly and time-consuming trial-and-error methods. The safe and unsafe hot working conditions can be identified in the processing map. The risky hot working conditions such as adiabatic shear band, flow localization, intergranular cracking, and dynamic strain aging are indicated based on the response of the material to the applied working parameters (Prasad, Rao, & Sasidhara, 2015). The identified domains in a processing map are favored by the dynamic recrystallization mechanism due to the softening process increasing the intrinsic workability. In addition, in this method, the efficiency of power dissipation under different working parameters is determined through DMM (Quan, Kang, Ku, & Song, 2011). All equations related to DMM are explained in Chapter 4. Momeni et al. (Momeni & Dehghani, 2010a) investigated the hot deformation behavior of 410 MSS using a constitutive equation and processing map. The processing map was developed for 410 MSS through the superimposition of the power dissipation and the instability maps. The regions with low and high workability were identified and the optimized and safe working conditions were achieved in a temperature range of 1000-1125 ºC and the strain rate of 0.001-10 s^{-1}. Figure 1.31 shows the processing map of 410 MSS that the dark regions mean the unsafe working condition for this alloy and counter numbers represent percent efficiency of power dissipation. The equations of developing processing map were explained in detailed in chapter 4.
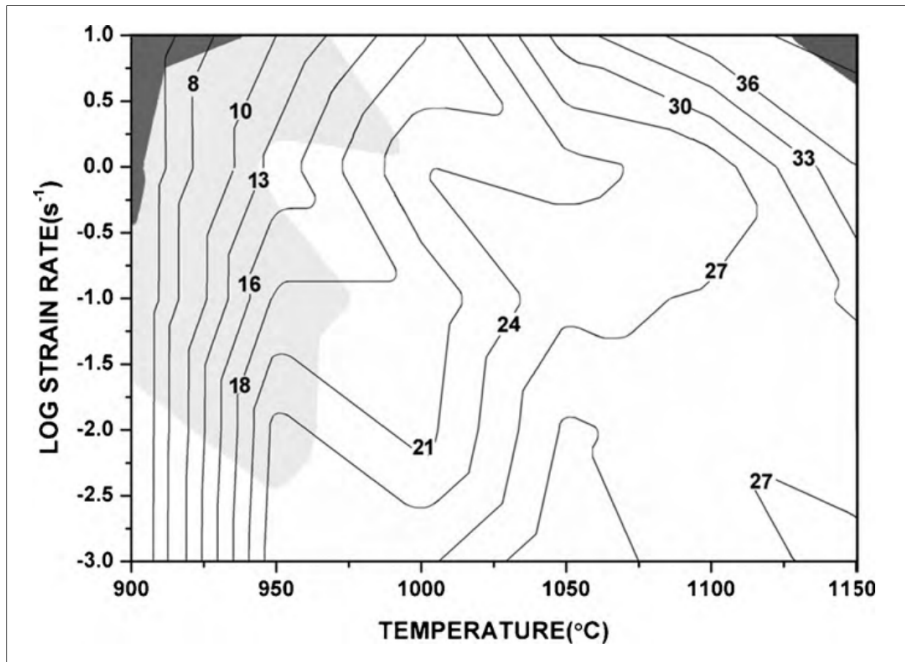
Figure 1.31 AISI 410 MSS processing mapcreated by superimposing
the power dissipationmap with the instability map
Taken from Momeni & Dehghani (2010)

Qi et al. (Qi et al., 2015) worked on the effect of working parameters on the hot working of
410 MSS. Figure 1.32 shows how strain affects the evolution of unsafe domains.
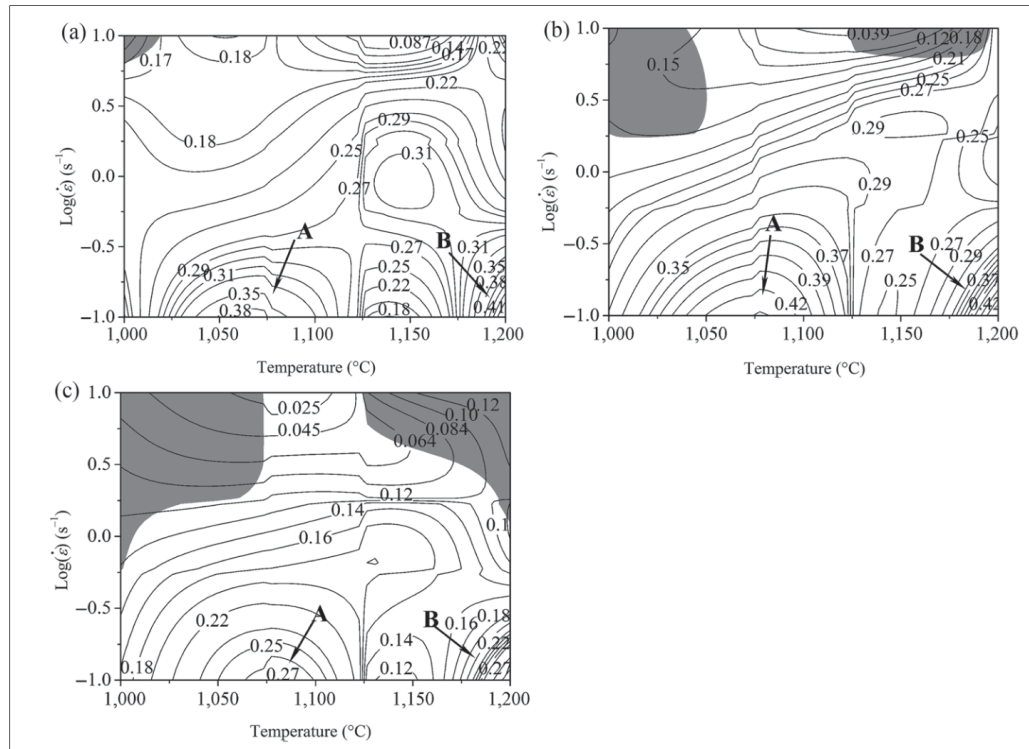
Figure 1.32 AISI 410 steel processing maps with various
genuine strains (a) ε = 0.3 (b) ε = 0.6 and (c) ε = 0.9
Taken from Qi et al. (2015)

The shaded regions are the instability regions where the area is changing by increasing the amount of deformation degree. Figure 1.32 corresponds to the hot working conditions of temperature range 1000 °C -1200 °C and strain rate of 0.1 s^{-1}-10 s^{-1}. This condition has almost no instability regions which means that this alloy can be hot worked at low strain without risk of flow instability. However, by increasing the strain, the area of instability regions increases and this region occurs in a similar position for both strains 0.6 and 0.9. The area of instability region is higher for the strain of 0.9 than 0.6. The maps mean that the strain on hot working significantly affects the instability regions and unsafe regions for hot working. Therefore, this study suggested the optimum process parameters with a deformation temperature of 1050 °C –1200 °C and a strain rate of 0.1 s^{-1}-1 s^{-1}.

Regarding the effect of strain, some studies indicated the possibility of the internal cracks and wedge-type cracks increasing with increasing the deformation degree which greatly reduces

the mechanical properties of steels (Prasad et al., 2015). Thus, the processing window of the studied steel becomes smaller with increasing strain.

Regardless of the research employed the processing map for the prediction of safe hot working regions, there is a shortcoming in considering the effect of strain on flow instability and workability. In addition, small number of studies have validated the processing map with the microstructural observations and this validation has been uncommon for martensitic stainless steels.

1.9.4   Fracture Criterion

Restrictions within die forming, internal microstructure evolution, and alterations within the forming die could produce complex deformation and stress state during hot deformation. These factors could affect negatively the final quality of the forged products (Bitterlin et al., 2016). For example, cracking phenomena could take place in case of complex stress or strain concentrations. Therefore, some fracture models were developed to predict the damage and cracking behavior and underlying mechanism of material during hot deformation. By taking the advantage of these models, metal forming designers look for a hot optimum forging schedule that produces defect-free products. During the hot deformation process, the material undergoes different levels of work hardening (WH), dynamic recovery (DRV), and dynamic recrystallization. As explained in the previous section, these metallurgical phenomena manipulate the microstructure evolution such as grain refinement, phase transformation, and second-phase precipitation. These changes affect the strength of the grain interior and grain boundaries and make the material susceptible to cracking and damage if the applied stress or stress exceeds the critical value (Y. Zhang et al., 2021). For example, by weakening the grain boundaries, the voids will nucleate, aggregate, and further convert to microcracks. This sequence results in damage and fracture. In addition, working parameters including temperature, strain, and strain rate can significantly change the macroscopic plastic flow and further promote the damage cracking (F. Chen, Ren, Chen, Cui, & Ou, 2016a).

Different fracture criteria were proposed by researchers including Freudenthal (Freudenthal, 1950), Cockcroft & Latham (Cockcroft & Latham, 1968), Brozzo et al (Brozzo et al. 1972) , and Oyane (Oyane, Sato, Okimoto, & Shima, 1980). In the developed models, the critical damage value was identified and above this value, the material is in a risky condition for cracking propagation and damage. The Oyane criterion was originally proposed for cold forming application rather than hot forming While Brozzo and Latham & Cockroft model are widely used for the hot forming process (Y. Zhang et al., 2021). All damage models were listed in Table 1.3.

Table 1.3 Damage models
Taken from Brozzo (1972), Freudenthal (1950),
Cockcroft & Latham (1968) Oyane et al., (1980)

	Cockcroft & Latham	Oyane	Brozzo
Damage model	$C = \int_0^{\bar{\varepsilon}} \dfrac{\sigma_{max}}{\bar{\sigma}}\, d\bar{\varepsilon}$	$\int_0^{\bar{\varepsilon}_f} \left[1 + \dfrac{1}{a}\dfrac{\sigma_m}{\bar{\sigma}}\right] d\bar{\varepsilon}$	$\int_0^{\bar{\varepsilon}_f} \dfrac{2\sigma_1}{3(\sigma_1 - \sigma_m)}\, d\bar{\varepsilon}$

Ghazani et al. (Ghazani & Eghbali, 2018) used a ductile damage criterion, Latham-Cockoft model, to predict the locations with maximum damage value during the hot compression test, Gleeble size, of AISI 321 austenitic stainless steel. In this model, the ductile fracture starts when tensile strain energy exceeds a critical value. Figure 1.33 shows the distribution of Latham-Cockroft damage value after hot deformation of the sample at 800 ºC and strain rate of 0.01 s^{-1}. It is seen that the damage factor is distributed non-uniformly and points A and B have a maximum value. This means that at these two points the ductile fracture may initiate from these regions.
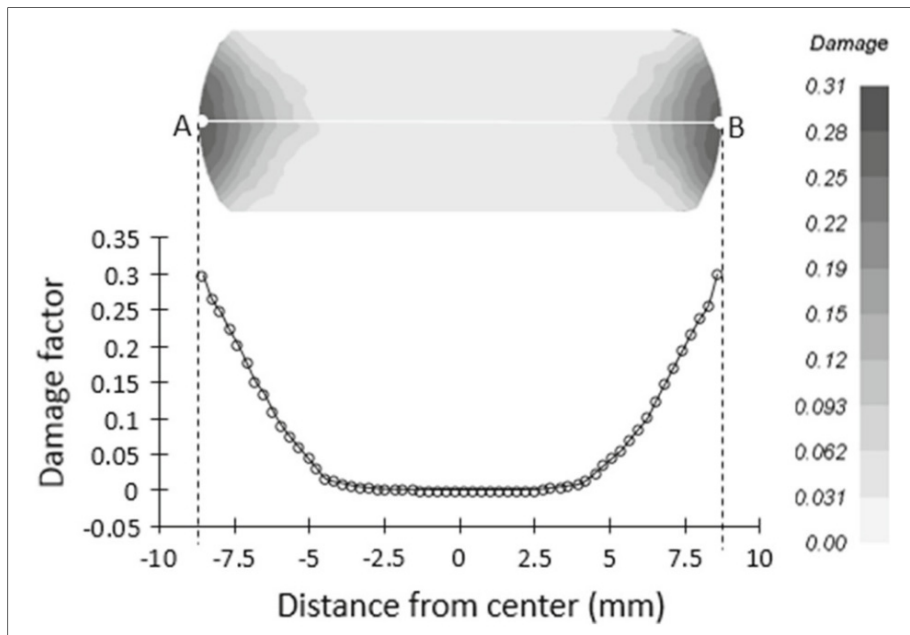
Figure 1.33 Distribution of Craft-Latham damage
inside deformed sample
Taken from Ghazani & Eghbali (2018)

Most studies focus on the damage and fracture of the material subjected to the elevated thermomechanical process in a laboratory-scale process, either a hot compression test or a hot tensile test. Therefore, there is a lack of scientific investigation in the damage analysis of large-sized hot forging and its relation to microstructural observations. In addition, damage and fracture analysis for martensitic stainless steel during hot forging is very scarce.

1.10   Numerical Simulation of Open Die Forging Process (FEM)

The flow stress during the hot forging process is affected by softening and hardening mechanisms such as WH, DRV, DRX, etc. (Yong Cheng Lin, Chen, & Zhang, 2009). Owing to the significant effect of microstructure evolution on mechanical properties, it is essential to establish a link between the thermomechanical and process variables and the evolution of the material's microstructure (Wei et al., 2013). However, due to the continuous variation of microstructure and boundary conditions by plastic deformation during forming, analyzing the forging process is very difficult and challenging especially in heavy forging where all

variations and complexities are greater. Moreover, the trial and error method in heavy forging is neither economical nor productive to find the properties of the material and optimize the forging schedule (Choi, Chun, Van Tyne, & Moon, 2006). Therefore, significant progress has been made in creating numerical methods to forecast and explain the evolution of the microstructure and the behavior of deformation during hot forging. By taking advantage of this procedure, the properties of the product are predicted without trial and error by combining the constitutive equation and microstructure evolution models and implementing them into the different kinds of commercial finite element methods (FEM) software. There is several commercial FEM software such as Forge NxT, DEFORM, SuperForm, and Marc to predict the microstructural evolution during hot metal forming (F. Chen et al., 2016a). Jang et al. (Jang, Ko, & Kim, 2000) used the finite element method to predict the microstructure evolution during a hot-forging process of 85*42 mm cylinder of C-Mn steel by integrating the microstructure models and the rigid-thermoviscoplastic model and implementing them into a 3D FE simulator. They found the non-uniformity of deformation and working parameters distribution and the DRX is concentrated at the center of the material during deformation. Krishna et al. (Krishna & Jena, 2019) investigated the analytical and numerical modeling of the open die forging process on mild steel. Figure 1.34 shows the forging simulation setup of the laboratory scale at the end of the open-die-forging. The simulation results including total deformation, Maximum principal stress, and equivalent strain are shown in Figure 1.35.
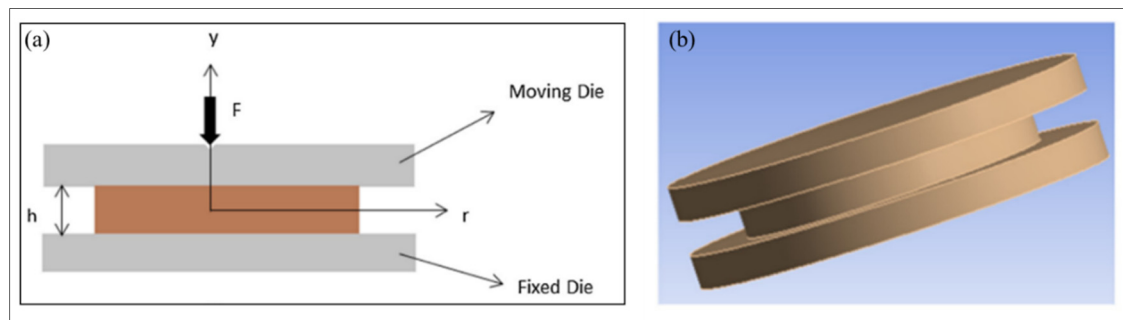
Figure 1.34 (a) forging of elliptical disk (b) 3D-model view
Taken from Krishna & Jena (2019)
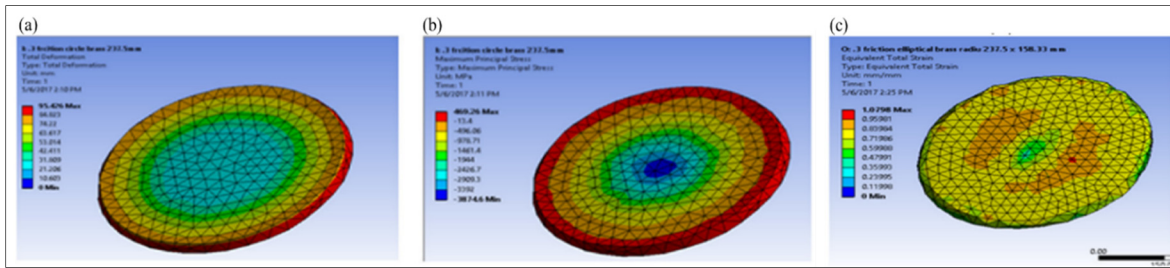
Figure 1.35 Simulation results of (a) directional deformation (b) maximum principle stress
(c) equivalent total strain
Taken from Krishna & Jena (2019)

Jin et al. (Jin, Li, Wu, & Dong, 2015) coupled the microstructure evolution models with the finite element method to analyze the DRX and deformation behavior of low carbon steel under hot working. In this study, the different zones regarding the amount of deformation degree were shown and similar to the previous studies, the central area has the highest deformation extent. The amount of deformation is ordered from the highest to lowest for the region I, III, and II respectively. Figure 1.36a shows the three deformation regions and four characteristic points in the cylinder specimen and Figure 1.36b indicates the time dependence of equivalent strain of points A, B, C, and D.
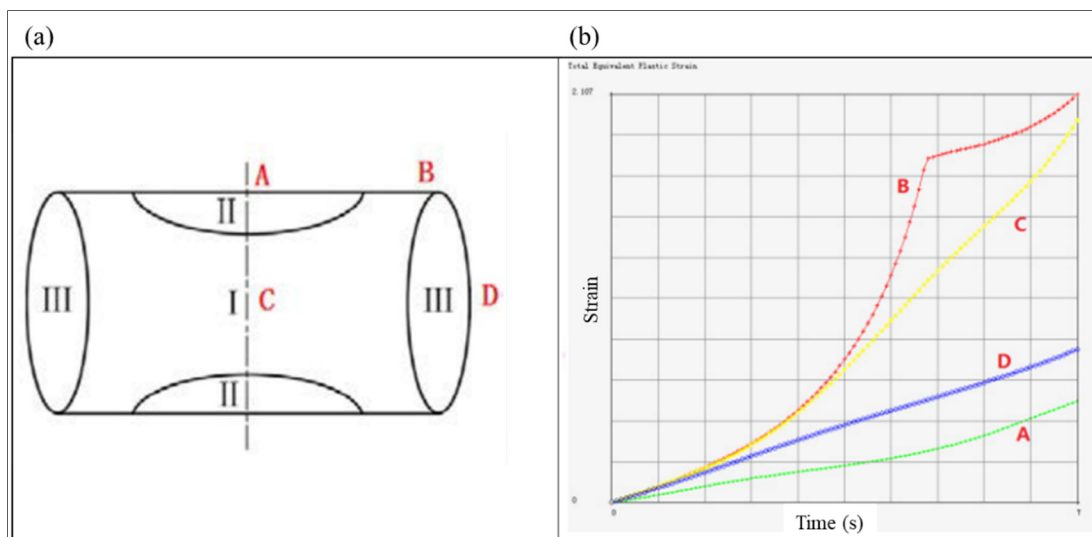
Figure 1.36 (a) Three deformation regions and four characteristics
points in the cylinder specimen (b) time dependence of
equivalent strain at points A, B, C, and D
Taken from Jin et al. (2015)

The simulation results display that height reduction has a significant effect on the strain distribution and the largest strain belongs to the central region and the lowest related to the two ends of the specimen, Figure 1.37.
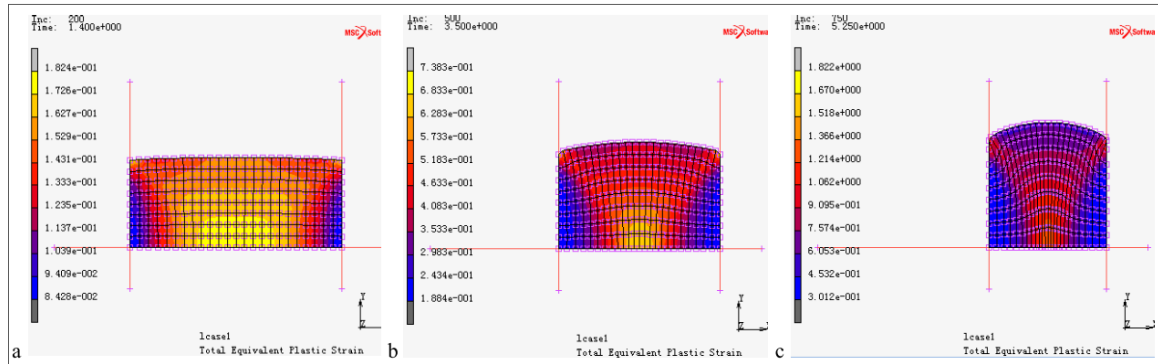
Figure 1.37 Distribution of equivalent strain at various height decrement of
a) 2.1 mm (b) 4.2 mm (c) 6.3 mm
Taken from Jin et al. (2015)

The DRX fraction is shown in Figure 1.38a and the variance of that with time in Figure 1.38b. It is seen that the central region is almost fully recrystallized where point C is located. However, at points A and D the strain is not enough for fully DRX, Figure 1.38b. The DRX grain evolution is also predicted and compared with the experimental results, Figure 1.39. The finest grain size is related to point C with a higher amount of DRX fraction, 55 μm and 57.8 μm simulated and experimental measurement. The largest grain size is related to region II which is 109.6 μm while the initial grain size was 123.8 μm. These measurements demonstrated that the developed model can be used to predict the microstructure evolution of this alloy.
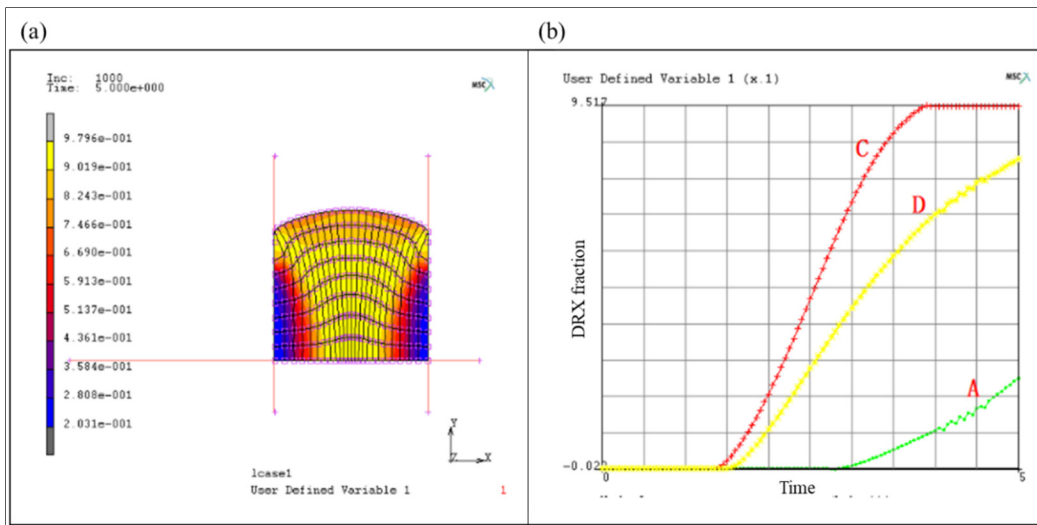
Figure 1.38 Distribution of DRX volume fraction at the decline of 6.3 mm
(b) different DRX fractions with time
Taken from Jin et al. (2015)
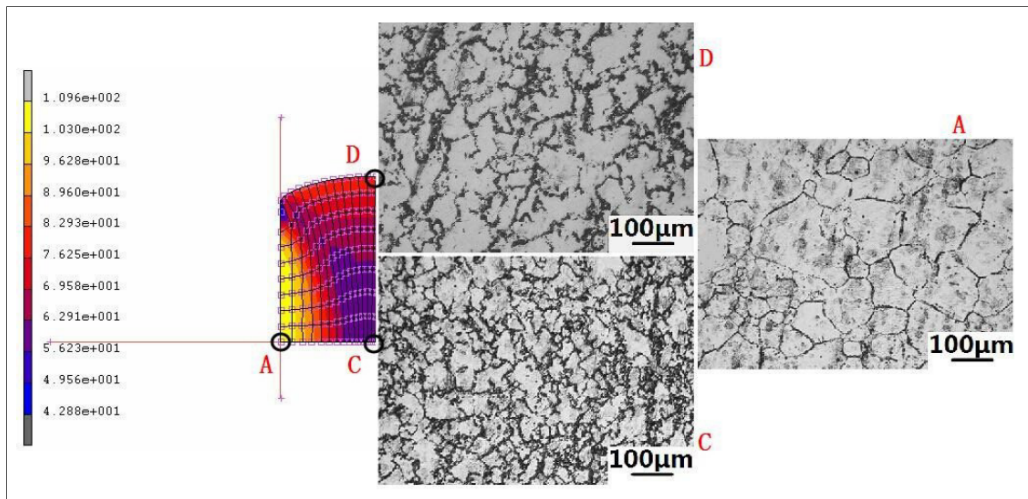
Figure 1.39 Comparison between the experimental and simulated results
of average grain size when the reduction is 6.3 mm
Taken from Jin et al. (2015)

Despite the relatively good research that has been done on the simulation of the hot forging process of steels, very few works have been done about the simulation of heavy forging or complicated processes, and almost most of the research was on the laboratory scale. Chen et al. (F. Chen et al., 2016a) simulated the forging process of the turbine blade of high-strength

steel by integrating the thermomechanical coupled finite element method, based on FE software. They investigated the effect of thermomechanical parameters and deformation history on microstructural evolution. In the microstructure observation, Figure 1.40, the non-uniformity of microstructural evolution at two different zones was characterized.
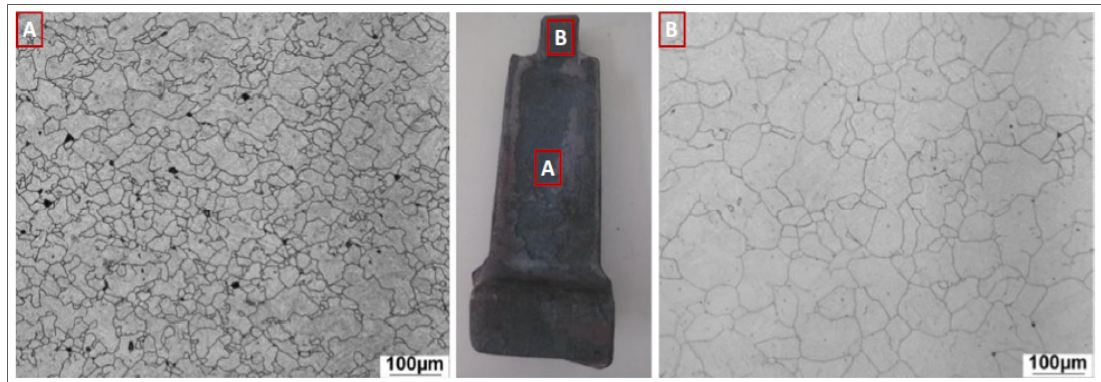
Figure 1.40 Optical microscopic in different zones of the forging
Taken from Chen et al. (2016)

Figure 1.41 shows the working parameters distribution of the forging after hot deformation. It can be found that working parameters distribute unevenly.
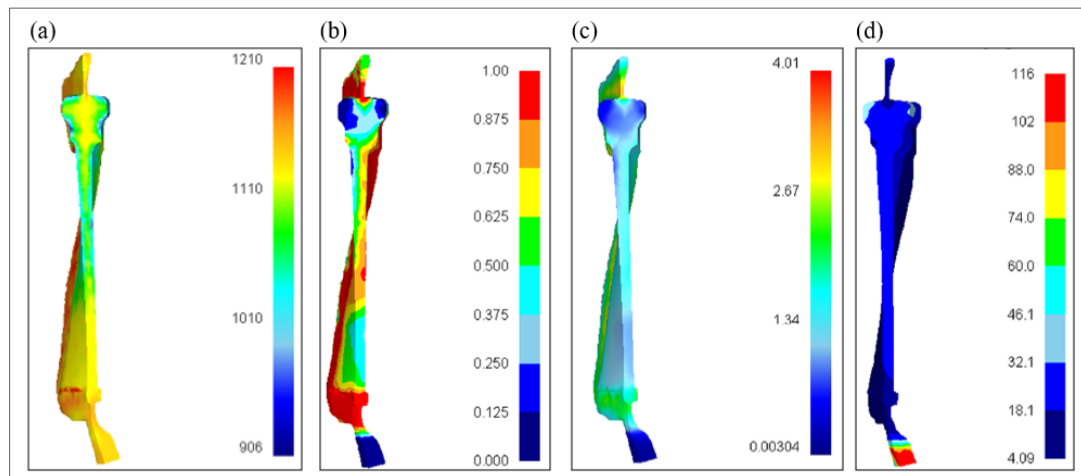
Figure 1.41 The distribution of (a) Temperature (b)
DRX volume fraction (c) effective strain (d) Average grain size
Taken from Chen et al. (2016)

Wang et al. (S. Wang et al., 2016) investigated the numerical simulation and experimental verification of microstructure evolution in large size pipe made of ASTM-TP316LN. The forging process was simulated using DEFORM-3D software and the microstructure evolution

was analyzed. Figure 1.42 shows the finite element mesh system of the initial steel ingot and the new mesh system of the forged workpiece. The effective strain distribution is shown for both surface and interior of the ingot at the end of the process, Figure 1.43.
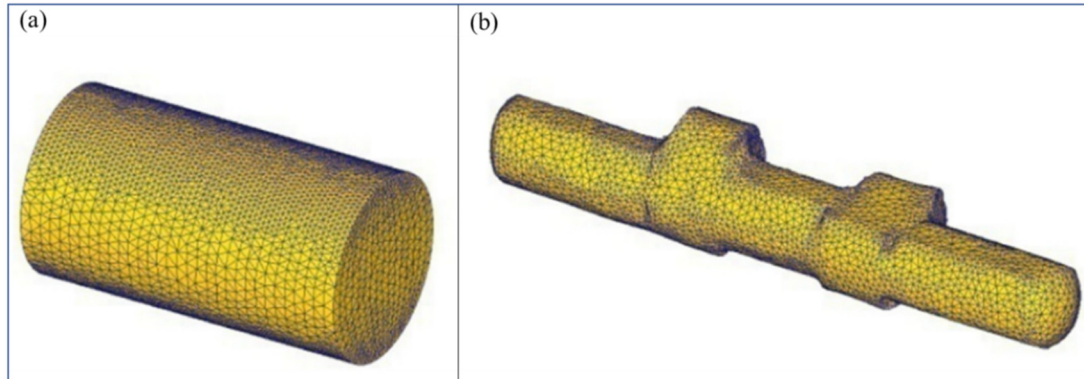
Figure 1.42 The finite element mesh system of the (a) initial steel ingot
(b) forged workpiece
Taken from Wang et al. (2016)
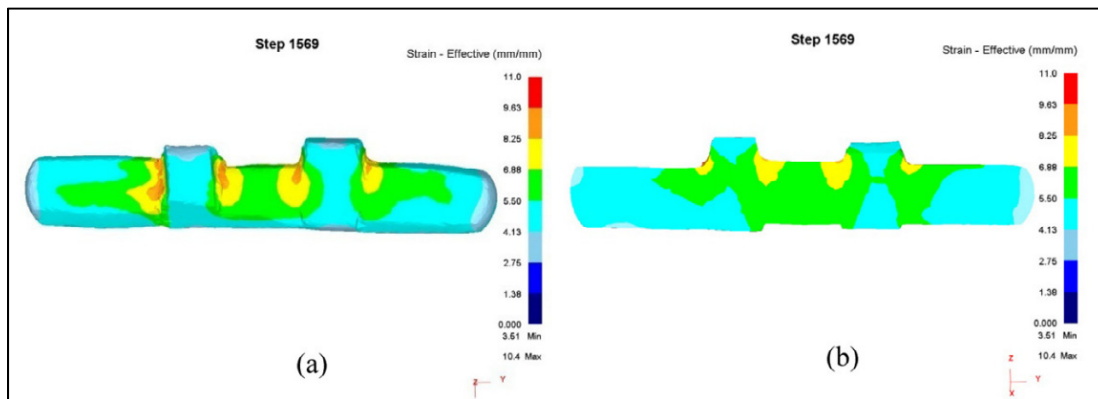
Figure 1.43 Distribution of effective strain (a) surface (b) interior
Taken from Wang et al. (2016)

The simulation and experimental microstructure evolution compare together. Figure 1.44 shows the grain size evolution from both and inside of the ingot. The locations where the grain size measures experimentally are shown in Figure 1.45 and the metallography images are shown in Figure 1.46 for all points.
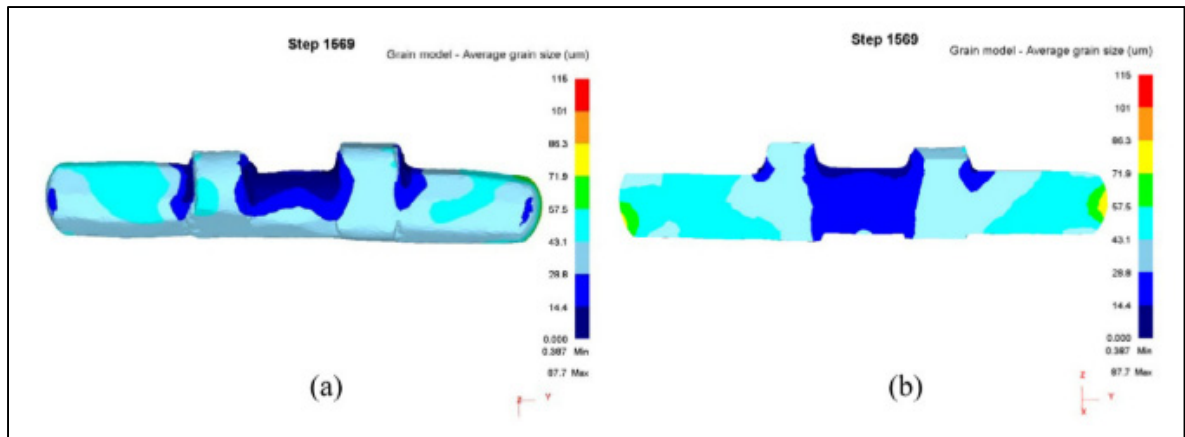
Figure 1.44 Distribution of average grain size (a) surface (b) interior
Taken from Wang et al. (2016)
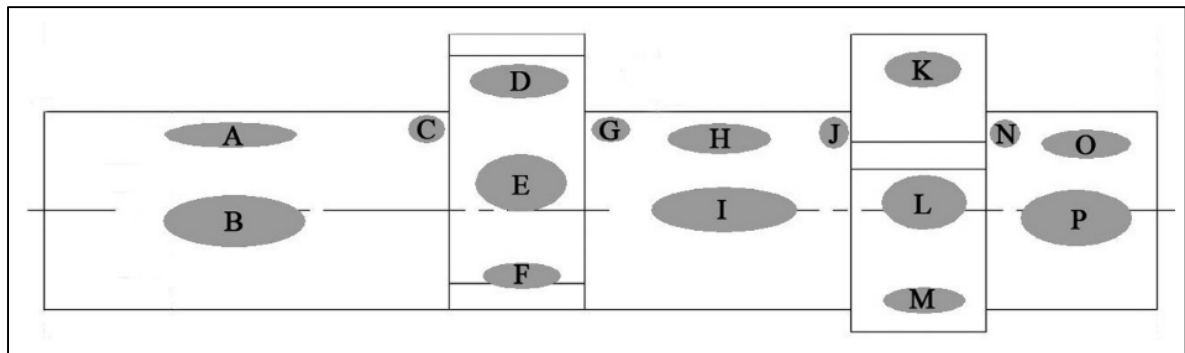
Figure 1.45 Schematic diagram of the representative sections in forged workpiece
Taken from Wang et al. (2016)
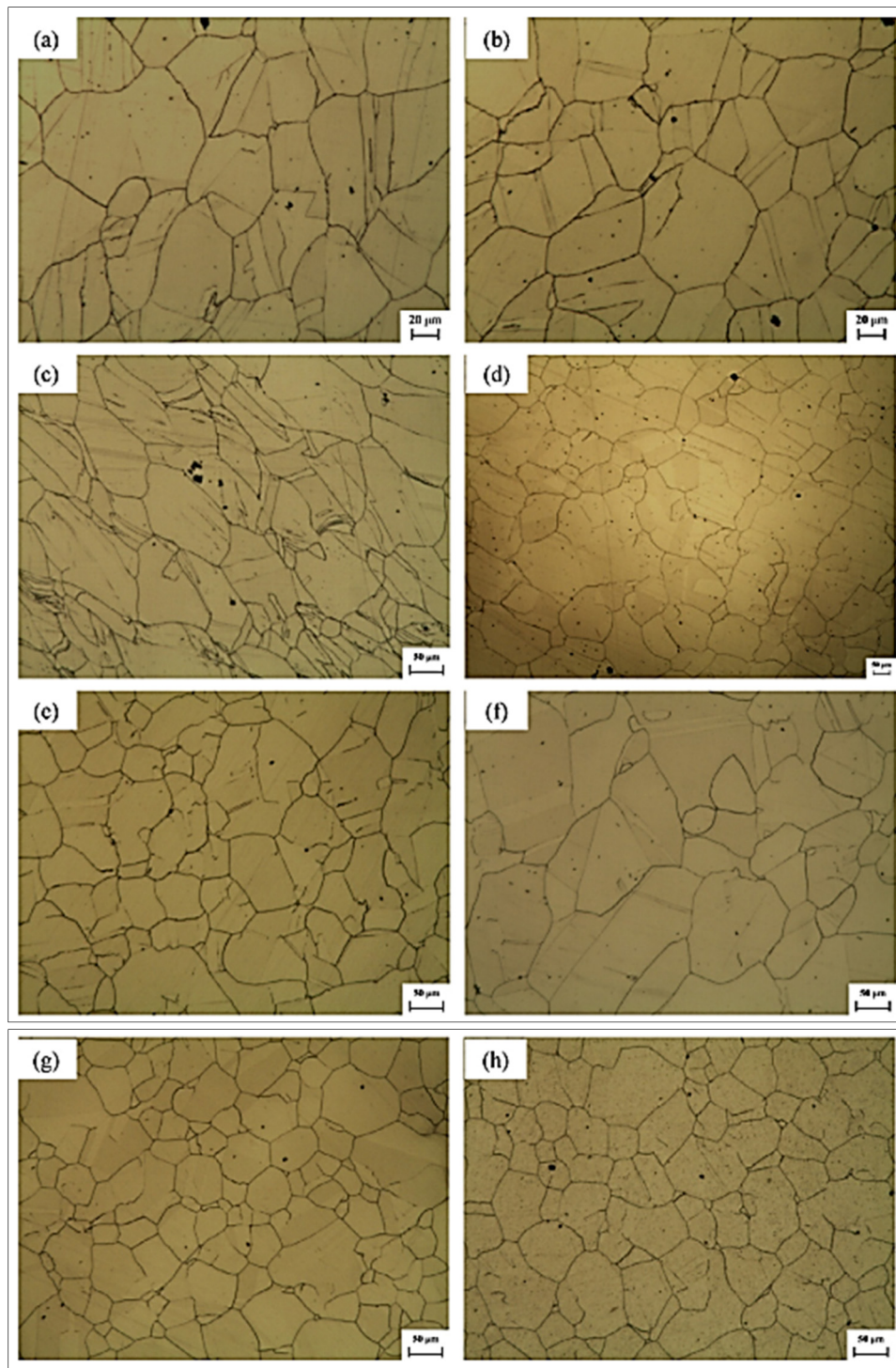
Figure 1.46 Microstructure of different locations
as shown in Figure 1.44
Taken from Wang et al. (2016)

For validation of the model, the grain size obtained from the simulation and experiment process were measured, Table 1.4.

Table 1.4 Average grain sizes comparison between experiment and simulation results (μm)
Taken from Wang et al., (2016)

Section requirement	A	B	C	D	E	F	G	H	I	J	K	L	M	N	O	P
	180															
Actual product	52.51	40.96	62.13	109.39	67.24	76.82	52.88	54.00	41.96	55.36	102.18	80.38	92.22	43.66	90.67	59.57
Simulation results	50.3	50.3	21.6	36.0	36.0	36.0	18.0	21.6	21.6	18.0	36.0	36.0	36.0	21.6	43.15	50.3

FEM simulation was used to determine the maximum possible level of plasticity with no risk of damage or cracking phenomena at elevated temperatures. The fracture models were explained in section 1.9.4. Kukuryk et al. (Kukuryk, 2021) investigated the deformation, stress state, and fracture prediction during the cogging process after several hits. Three damage criteria were compared in this study. Figure 1.47 illustrates the distribution of the damage factor for the three damage criteria of cracking following the fourth pass of the forging. Among the three selected criteria, the smallest values of crack formation factor were achieved for M. Oyane et al. ($\theta_O = 0.25 - 0.37$), whereas the largest values belong to Brozzo ($\theta_B = 0.632 - 0.685$). The intermediate values were achieved by Cockcroft and Latham model ($\theta_{C-L} = 0.456 - 0.513$). Based on the damage analysis, it is concluded that the corners of the forging subjected to deformation have the largest crack formation factors. The damage value is maximum where the largest values of the effective stress are concentrated, and also the corners have the lowest temperature. The relationship between working parameters and damage factor was made, Figure 1.48.
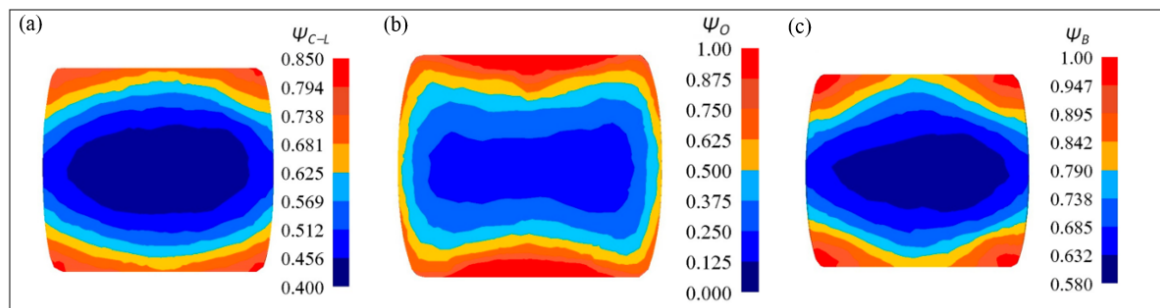
Figure 1. 47 Distribution of the damage factors (a) Cockcroft and Latham
(b) Oyane and (c) Brozzo after the eighth pass of the forging
Taken from Kukuryk (2021)
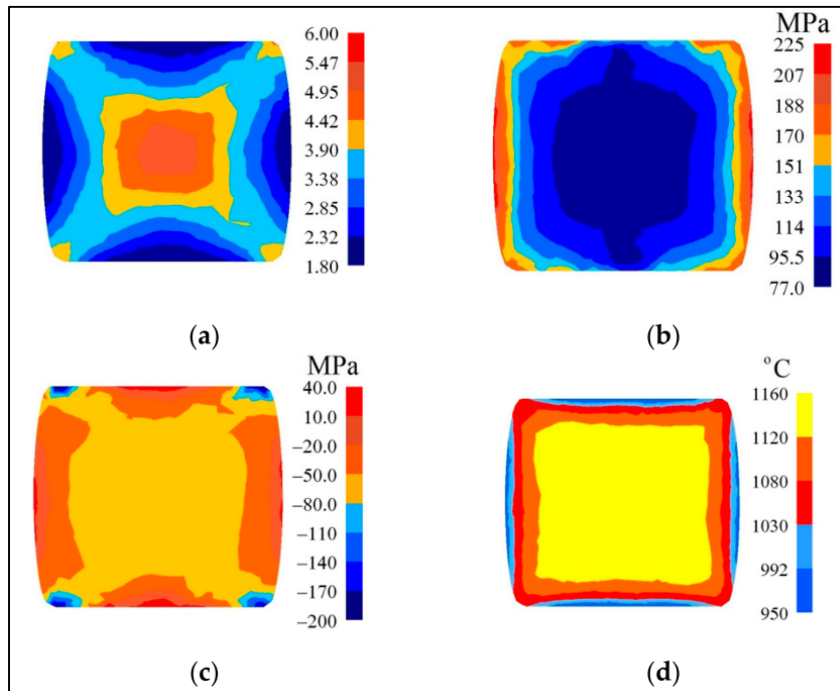
Figure 1.48 After the eighth pass of the forging with flat anvils
distribution of the (a) effective strain (b) effective stress
(c) mean stresses (d) and temperature
Taken from Kukuryk (2021)

Kakimoto et al. (Kakimoto & Arikawa, 2014) developed the predictive method of surface cracking in hot forging using numerical simulation and high-temperature tensile test. Latham-Cockroft criterion was implemented into Forge2D software. Numerical simulation was performed by implementing the Latham & Cockroft formula to predict the location with a higher value of damage factor. Simulation of the 2-pass forging process using a flat die was conducted at 1000 °C at the end of the process, the surface temperature reaches 800 °C. Figure 1.49 shows the contour of the damage factor after 2-pass forging. As shown, the highest damage value belongs to the surface of the ingot.
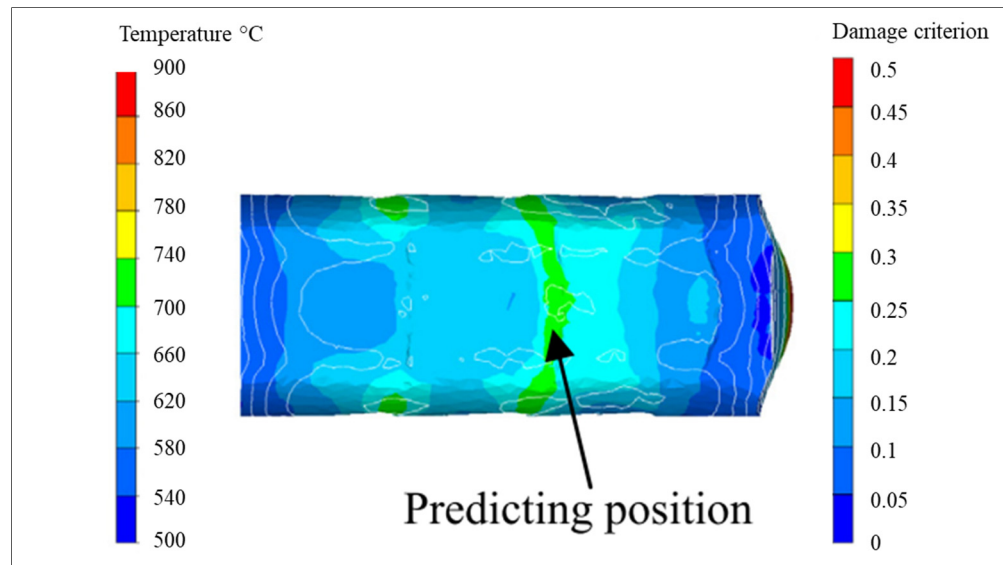
Figure 1.49 Map of C-value in 2-Pass forging
(Die edge R=100 mm, Feed=600 mm)
Taken from Kakimoto & Arikawa (2014)

In general, few studies have examined the prediction of deformation and microstructure evolution in heavy forging by the numerical approach. The heavy manufacturing industries are incredibly costly and optimizing the forging process without trial and error experimentally is highly valuable. Also, there is a big lack of investigation on this topic for martensitic stainless steel while this alloy is widely used in many industries that required large components such as aerospace, oil & gas, water, etc.

1.11 Challenges and Objectives

The literature review provided a large number of studies on the material flow behavior and the softening mechanisms occurring during the hot deformation process for martensitic stainless steels. However, among works concerning the material behavior during forging, only experimental investigation in the lab scale has been mainly considered and very few investigations worked with the numerical approach on the industrial scale. Moreover, most of the investigations focused on the characterization of hot deformation behavior using constitutive equations on a small scale while very few investigations worked on the microstructure evolution during forging and no report exists with this approach on the

industrial scale for martensitic stainless steels. Data on simultaneous analysis of material flow behavior and microstructure evolution of martensitic stainless steel along with large size products are very rare. Also, the damage analysis of the large ingot during the forging of martensitic stainless steels is not reported in the studies.

The primary goal of the current work is to fill the above gaps in the scientific and industrial communities. As mentioned in Chapter 1, the large size ingot in the as-cast form has several defects and heterogeneities such as cast microstructure, porosity, voids, and segregation which deteriorate the mechanical properties. These heterogeneities are reduced/eliminated with the design of a proper forging schedule. Such design would require an in-depth understanding of the fundamental microstructure evolution mechanisms that take place during hot forging. Thus, the first objective of this project is the macro and microstructural characterization of phase transformation occurring during the solidification of the large ingot of martensitic stainless steel. In this part, experimental characterization and measurement results were used to analyze the phase identification and effect of working parameters on its distribution. This part of the present thesis is aimed to address the question of effective factors in the phase transformation during the solidification of large-size ingots which leads to crack susceptibility during forging. The second purpose of this project is to establish a precise material model that can predict the flow stress of MSS at high temperatures and can be employed to simulate the forging process. Among extensive works on material modeling, very few investigations have developed microstructure-base models to analyze the microstructure evolution during forging. Therefore, hot compression experiments were designed and conducted to analyze the effect of working parameters on the flow stress and microstructure evolution.

The third objective is to develop microstructure evolution models based on the experimental results and validate them with microstructure characterization. In addition, the constitutive equation and microstructure models were integrated and coupled together, then implemented into the FEM simulation code. Such work has not been previously reported on this subject for MSS. In this part, the large size ingot was simulated according to the industrial forging

conditions for the first time and microstructure evolution and damage analysis during forging were investigated.

The last objective of this project is to optimize the forging schedule according to the results of the third objective. To do this, the effect of working parameters including strain, strain rate, and temperature on microstructure evolution and damage criterion were investigated. Finally, the new working parameters were proposed to the industrial partner and applied at the industrial scale.

CHAPTER 2

EXPERIMENTAL MATERIALS AND METHODS

2.1   Introduction

In this chapter, specifics of the thesis's measurements at industrial and laboratory scales are given. To design the laboratory tests for an industrial-scale setup, the specifics of the experimental measurements will be the first step. Then, a microstructure analysis will be presented. The material modelling and microstructural evolution models and their implementation into the FEM software will be provided. After the validation of the models with the experimental results, the industrial scale of the forging process was simulated.

2.2   Forging Process Description

The present investigation was conducted in collaboration with Finkl steel, St-Joseph-de-Sorel, Quebec (Finkl Steel). After melting the solid steel scrap and different refining operations are conducted to capture impurities and improve micro cleanliness, toughness, and isotropic properties. Vacuum degassing is the next step to ensure the lowest amount of hydrogen, oxygen, and nitrogen level resulting in super-quality steel. The molten steel is ready for the casting process which is done by pouring it into the mold. After solidification and demolding, the ingot is transferred to the forging furnace to heat up to the forging temperature. The ingot is formed using two forging hydraulic presses, 5000 tons and 2000 tons. Figure 2.1 shows the hydraulic forging press in the industry.

Figure 2.1 Hydraulic forging press

2.3 Hot Compression Test Design

2.3.1 Temperature Measurement

Ingot temperature was measured by a high-performance thermal camera. The reading temperature started from when the ingot was taken out of the forging furnace until the end of the forging operation. Figure 2.2 shows the setup of the thermal camera and the camera (http://www.flukeprocessinstruments.com).

Figure 2.2 Forging temperature measurement by Thermal camera

2.3.2 Sample Preparation

The material was provided and prepared by Finkl Steel-Sorel Forge, Sorel, Quebec, Canada. Figure 2.3 shows the location and the size of compression samples. Figure 2.3c shows the cylindrical specimen that was cut from the center of the ingot with a diameter of 10 mm and a height of 15 mm.
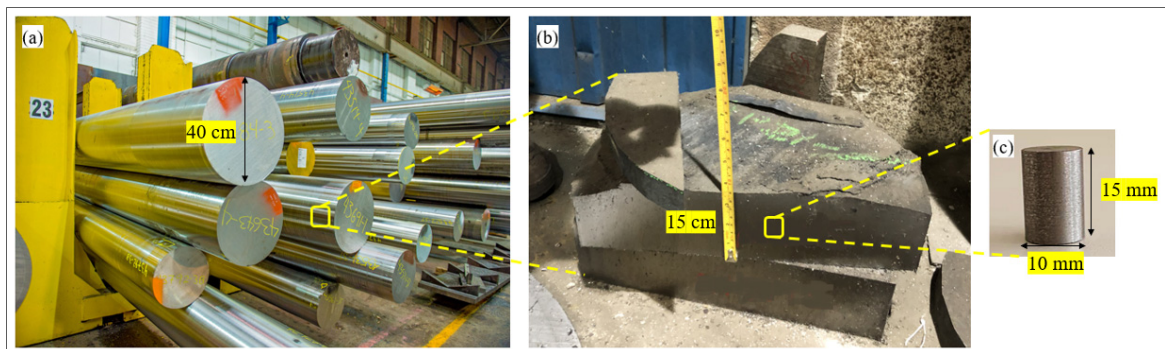
Figure 2.3 (a) Round forged ingot (b) Regions of the cut block of the compression samples (c) Compression sample

2.3.3 Determination of the Holding Time

A preliminary heat treatment testing was done to determine the suitable holding time to achieve uniform temperature distribution as well as a microstructure. The industrial size ingot for hot compression tests. Three holding temperatures were selected. The temperature reading was recorded by three thermocouples (k type) which were welded by a spot welder machine. The samples were heated from room temperature up to 1230 °C for three different time holdings. After reaching the minimum difference between the thermocouple readings, it was considered that the temperature was uniform throughout the samples. This time was selected as the holding time for the hot compression tests. Figure 2.4a shows the sample with thermocouples and the schematic diagram of the thermal schedule for the heat treatment cycle is depicted in Figure 2.4b.
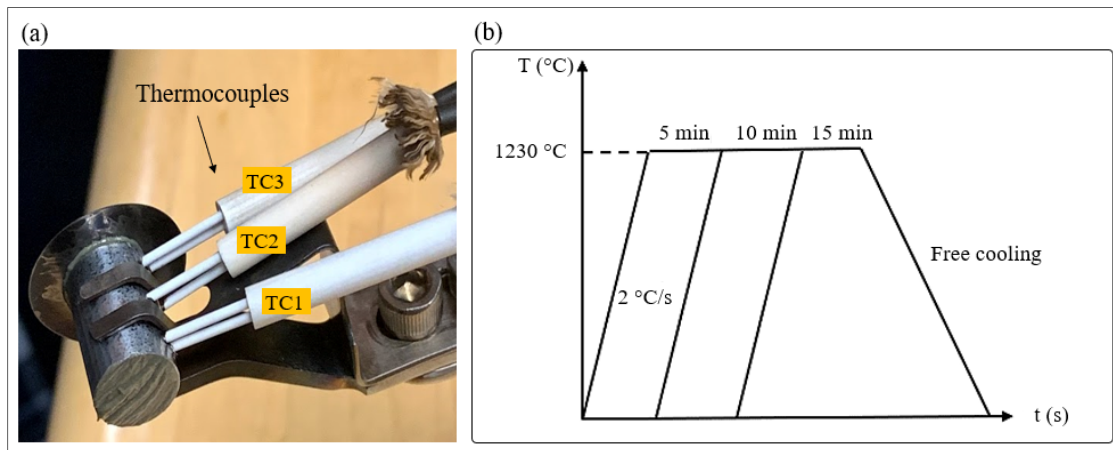
Figure 2.4(a) Deformation sample with welded thermocouples to measure the temperature (b) schematic of thermal schedule for the heat treatment cycle

Based on the readings, 15 minutes of holding time is sufficient for uniform heat distribution in the specimen. The grain size was measured before and after holding the sample for 15 minutes at a high temperature to make sure not to have significant grain growth during holding. Figure 2.5a shows the as-received microstructure and Figure 2.5b shows the microstructure after 15-minute holding at 1230 °C. By comparison of the microstructure before and after heating, it is

observed that a 15-minute holding time at 1230 °C is acceptable because of the negligible difference in grain size.
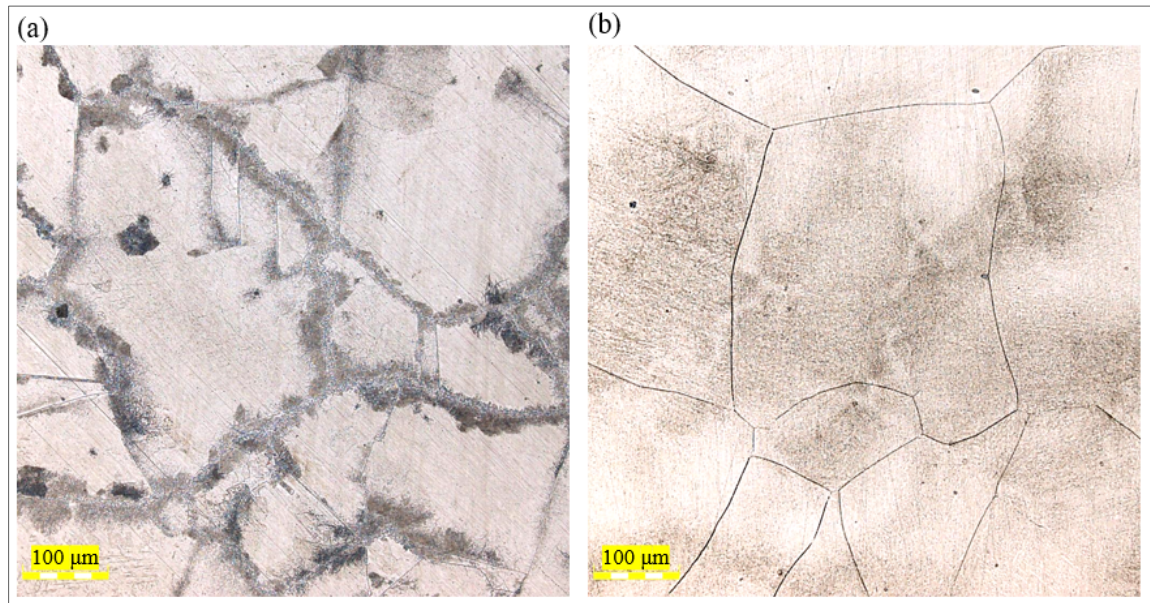
Figure 2.5(a) As-received microstructure, (b) the microstructure after holding 15 minutes at 1230 °C

2.3.4 Determination of Strain Rate and Strain

The hydraulic press data was recorded in industrial location and by plotting press pressure and press position, the range of the strain rate and strain can be calculated.

2.3.5 Hot Compression Tests

Gleeble ^{TM} 3800 thermomechanical simulator machine was used for hot compression tests. This machine is the most powerful standard system provided by Dynamic Systems Inc. The system's adaptability opens a wide range of testing and simulation options, but thanks to its exceptional capabilities, hot rolling and multi-hit forging simulations are particularly well-suited to it. Figure 2.6 depicts the machine setup for the tests, as well as the sample ready for compression.
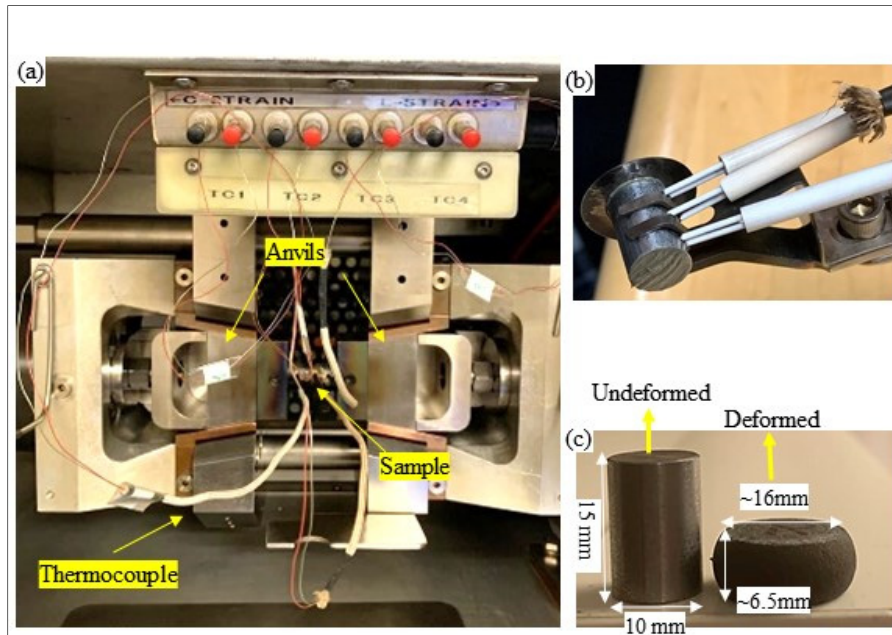
Figure 2.6 (a) Test chamber with specimen installed (b) Compression
sample (c) Sample before and after compression

2.3.6   Microstructure Analysis

The deformed samples were cut parallel to the forming axis, then they were hot mounted by the LaboPress-1. The samples were polished mechanically using conventional techniques until 1μ polishing paper. The residual fine scratches were eliminated using an IM4000Plus ion milling system. To reveal the microstructure, the samples were etched with Villela solution. For microstructure characterization, an Olympus LEXT OLS4100 laser confocal microscope was used. For scanning electron microscopy characterization, a HITACHI TM3000 was employed. The phase identification of the microstructure was examined by a SU8230 HITACHI. The EBSD data were post-processed using QUANTEX ESPRIT software. The XRD measurement was carried out using X'Pert[3] MRD PANalytical with Cu Kα. The JmatPro and ThermoCalc thermodynamic software were used to simulate the phase diagram and phase proportions over a wide range of temperatures and chemical compositions. Figure 2.7 shows all equipment used for the microstructure analysis.
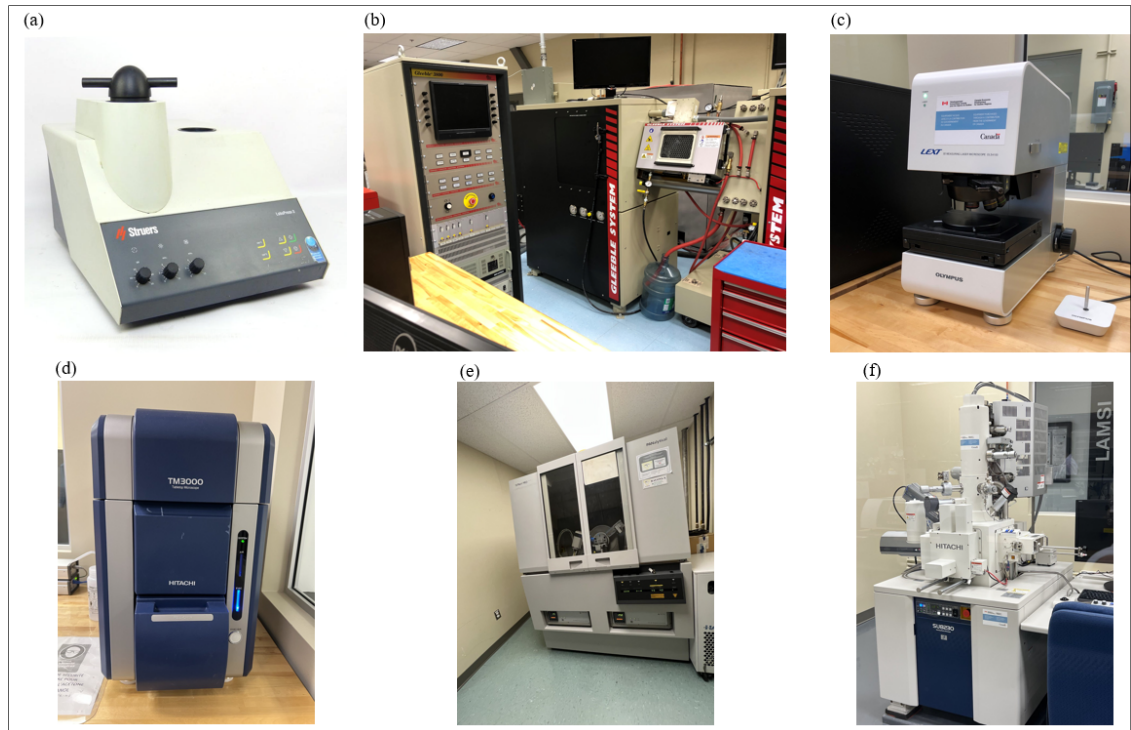
Figure 2.7 Experimental test and analysis equipment (a) Hot mounting machine (b) Gleeble thermal-mechanical simulators (c) Olympus LEXT OLS4100 laser confocal microscope (d) Scanning electron microscopy TM3000 (e) X'Pert^3 MRD PANalytical (f) Scanning electron microscopy SU8230

2.3.7 Flow Stress Analysis

The hot compression data was obtained after deformation from the Gleeble machine and plotted for all deformation conditions. The raw stress data were corrected because of friction and adiabatic heating. After correction, the flow stress-strain curves were used to determine the characteristic points including peak stress and strain, critical stress and strain, maximum softening rate, steady state stress, etc.

2.3.8 Material Modelling

To predict the material flow behavior, the material constitutive equations were used. These models make a relationship between flow stress, deformation temperature, and strain rate

during high-temperature deformation. Each model that can predict the flow behavior more accurately is selected for implementation into the simulation software. To analyze the microstructural evolution during hot deformation, the DRX model was developed based on the compression test data for the studied material. Both the constitutive equation and the DRX model were coupled and implemented into the simulation software.

2.3.9   FEM Simulation

Simulation parameters for open die forging were set under the industrial forging schedule. The boundary conditions including forging temperature, pass reduction, strain rate, material properties, etc. were imported as an input to the FEM software. The constitutive equation and DRX model, which is codded with FORTRAN user subroutines, were implemented into the Forge NxT software (http://www.transvalor.com). Figure 2.8 shows the Forge NxT software environment.

Figure 2.8 Forge NxT 3.0 workplace

The geometry of the ingot and the dies in the industrial size were designed by the CATIA software and imported to the simulation software with the STP extension. After conducting the forging simulation, the results were interpreted and analyzed. Finally, the working parameters were optimized in order to improve the quality of the final forging product.

The following chapters present the project's outcomes and conclusions. Chapter 3 fulfilled the first objective of this project which is the microstructural characterization of a large size MSS ingot and phase transformations that take place during ingot casting.

CHAPTER 3

INFLUENCE OF EUTECTIC PHASE PRECIPITATION ON CRACKING SUSCEPTIBILITY DURING FORGING OF A LARGE SIZE MARTENSITIC STAINLESS STEEL FOR TURBINE SHAFT APPLICATIONS

S. Dourandish [a], M. Jahazi [a], G. Ebrahimi [b], L. Ebacher [c]

[a] Department of Mechanical Engineering, École de Technologie Supériere,
1100 Notre-Dame West, Montreal, Quebec, Canada H3C 1K3
[b] Materials and Metallurgical Engineering Department, Faculty of Engineering,
Ferdowsi University of Mashhad, Iran
[c] Finkl Steel-Sorel Inc., 100 McCarthy, Saint-Joseph-de-Sorel, Québec, Canada J3R 3M8

Summary

Ingot casting on a large scale produces several defects and heterogeneities which deteriorate the mechanical properties. These heterogeneities are reduced/eliminated with the design of a proper forging schedule. Such design would require an in-depth understanding of the fundamental microstructure evolution mechanisms that take place during solidification and hot forging. Thus, in this chapter, macro and microstructural of phase transformations occurring during the solidification of a large size ingot of a martensitic stainless steel were carried out to identify the different phases and investigate the effect of working parameters on their distribution. Three different zones of a large size ingot were selected for studying the microstructure evolution. Based on the obtained results, it was determined that forging temperature and solidification rate were the two most effective parameters influencing the volume fraction and morphology of the phases transforming during the solidification of the large size ingot. The formation sequence of these phases leads to crack susceptibility during cooling.

3.1 Literature Review

MSS belong to the family of high-strength alloys and are widely used for rotors, turbine shafts, and pump bodies due to their good balance of high strength, ductility, and corrosion resistance (Momeni, Dehghani, Heidari, & Vaseghi, 2012). The casting process of the large size ingots of a metallic alloy is an industrial challenge due to the occurrence of macrosegregation during solidification, especially at the center of the ingot (Loucif et al., 2018). Besides, variable macrostructures including very fine grains in the chill zone, columnar grains, and equiaxed grains can be seen along the radial direction of the cast ingot (Suwas & Ray, 2014). These inhomogeneity of alloying elements distribution and macrostructure can modify thermophysical properties (Miettinen, 1997) and microstructure (Chadha et al. 2016; Loucif et al. 2017).

MSS are rarely used in the as-cast state and the cast ingots generally go through an open die forging process carried out at temperatures about 0.75 of the melting point of the alloy. Finally, normalization, quenching, and tempering treatments followed by machining operations are applied to obtain the final component (e.g., Turbine shafts). Prior to the open die forging operation, cast ingots are reheated for tens of hours, in the case of large size ingots, to reach the forging temperature. Therefore, the selection of the reheating/forging temperature is of critical importance to achieve the full breakdown of the as-cast dendritic structure, eliminate solidification porosities, and reduce the chemical (macrosegregation) inhomogeneity (Chadha, Shahriari, Tremblay, Bhattacharjee, & Jahazi, 2017; Dieter et al., 2003)

The post forge microstructure is generally composed of martensite, delta ferrite, and carbides (Ghadar, Momeni, Tolaminejad, & Soltanalinezhad, 2019). Among these phases, delta ferrite is formed at high temperatures, and its volume fraction, morphology, and distribution could have a significant impact on the quality of the final product. For example, it has been reported that increasing the content of the delta ferrite deteriorates the impact properties and decreases tensile strength, ductility, and toughness (Chae & Koss, 2004; Cowie & Tuler, 1991; Kwon & Asaro, 1990). In addition to the delta ferrite, carbides formed during the solidification of MSS

and coarse carbides in the microstructure act as a preferential site for crack initiation and deteriorate the corrosion resistance of the alloy. Finally, the combined presence of delta ferrite and coarse carbides could significantly reduce the formability of the alloy during high-temperature forming operations (Miotti Bettanini et al., 2018). Specifically, R. S. Qi et al. reported that the size, morphology, volume fraction, and distribution of the eutectic phase are always a big challenge in the heavy forging of MSS and are often associated with crack propagation during deformation, which may result in the scrapping of large size components (Qi et al., 2015). The present research work was initiated following observation of cracks after forging a 21 metric tons X38CrMo 16 martensitic stainless steel ingot with the view to understand the fundamental relations between process parameters and microstructure evolution and prevent future cracking.

The eutectic phase precipitation is the result of the decomposition of liquid into two solid phases at the final solidifying phase (Matsubara, Sasaguri, Shimizu, & Kon Yu, 2001). Boccalini et al. (Boccalini & Goldenstein, 2001) investigated the effects of the chemical composition and cooling rate on the development of the solidified microstructure of high-speed steel. They reported that the solidification sequence started with the precipitation of primary delta ferrite from liquid followed by the formation of austenite through a peritectic reaction and then proceeded to the formation of eutectic carbides, M_2C, M_6C, and MC, through a eutectic reaction. It has also been reported that the total eutectic volume fraction increases with increasing the carbon content, W/Mo ratio, V content, and decreasing cooling rate. Guo et al. (Guo et al., 2013) investigated the precipitation sequence of different phases during the solidification of a high chromium steel ingot. The DSC curve and isopleth diagram revealed that the primary austenite formed in the liquid at 1380 °C, then the eutectic reaction occurred in the residual liquid with the eutectic phase composed of austenite + carbide and distributed along the grain boundary. Zhou et al. (Xuefeng Zhou, Fang, Gang, & Jiang, 2010) studied the effect of cooling rate during solidification on the characteristics of the eutectic phase. They reported that at a low cooling rate, 0.9 K/s, eutectic carbides presented a needle-like or lamellar shape while with increasing cooling rates, the carbides developed into a rod-like shape. It must be mentioned that the solidification sequence in MSS is off eutectic, which means that the first

delta ferrite phase forms from liquid followed by the formation of austenite and then carbide (Janovec, Svoboda, & Blach, 1998). Off-eutectic solidification starting with the initial formation of γ dendrites, followed by a eutectic reaction of $L \rightarrow \gamma +MC$ has also been reported for other alloys, such as IN718 (Formenti, Eliasson, Mitchell, & Fredriksson, 2005). Some investigations have shown that the precipitation of eutectic carbides could only occur under slow cooling rates or during aging treatments and that fast cooling, suppresses its formation (Ebrahimi, Keshmiri, & Momeni, 2011; Kipelova, Belyakov, & Kaibyshev, 2013).

Despite the significant impact of the formation and characteristics of the eutectic phases during the solidification of martensitic stainless steels, there is very little data available in the literature on the macro and microstructural characterization of the above phases in the cast state of these steels. The present work addresses this aspect and investigates the influence of forging temperature on the characteristics of eutectic phases in a large casting made of X38CrMo16 martensitic stainless steel. More specifically, the investigation focuses on establishing possible correlations between the characteristics of the eutectic phases and the cracks observed during the forging of the ingot. For this purpose, advanced characterization techniques were used to determine the phase distribution, chemical composition, phase identification, and morphology in three different zones of the ingot. Moreover, a thermodynamic simulation was utilized to determine the formation region of each phase at the forging temperature and the corresponding eutectic composition. The experimental investigation results were then correlated with the thermodynamic simulation to optimize the selection of the forging temperatures and minimize defect generation.

3.2   Experimental Procedures

The chemical composition of the samples, X38CrMo16 MSS, was determined using a SPECTROMAX, Optical Emission Mass Spectrometer. Three measurements were made for each sample and the average value was used in Table 3.1. The microstructural characterization was carried out for two different forging temperatures, 1204 °C and 1260 °C. These

temperatures were selected based on a preliminary study that allowed narrowing the 'optimum' temperature for the reheating stage of the castings before the open die forging operation.

Table 3.1 Chemical composition of X38CrMo16 used in this investigation (wt. %)

Element	C	Mn	P	S	Si	Ni	Cr	Mo	Cu	Fe
Content	0.37	0.88	0.03	0.024	0.32	0.48	15.21	1.1	0.042	Bal.

The samples were provided by Finkl Steel-Sorel, Quebec, Canada. The production cycle starts with melting using a 45-ton electric arc furnace followed by ladle metallurgy degassing and refining processes along with tight control of the chemical composition. The casting process is bottom pouring the molten steel at about 1570 °C into the mold. The solidified ingot is then taken to the forge furnace and heated up to the forging temperature (1200 °C-1260 °C). The next step after forging is heat treating the sample through the quench and tempering cycle.

The samples used for the present investigation were cut from the center I, quarter (Q), and surface (S) of the final round product forging in 1204 °C and from the center of the final round product forging in 1260 °C in the as-annealed condition, as shown in Figure 3.1. Two different forging temperatures were used on two different ingots but with the same chemical composition, forge plan, and heat treatment. The heat treatment for both ingots started with holding the ingots at 537.77 °C for 65 hours then followed by austenitizing at 954.44 °C for 17 hours and cooling at approximately 14.17 °C/hr until 343.33 °C. Finally, tempering was done at 648.88 °C with 1.5 hr/in.
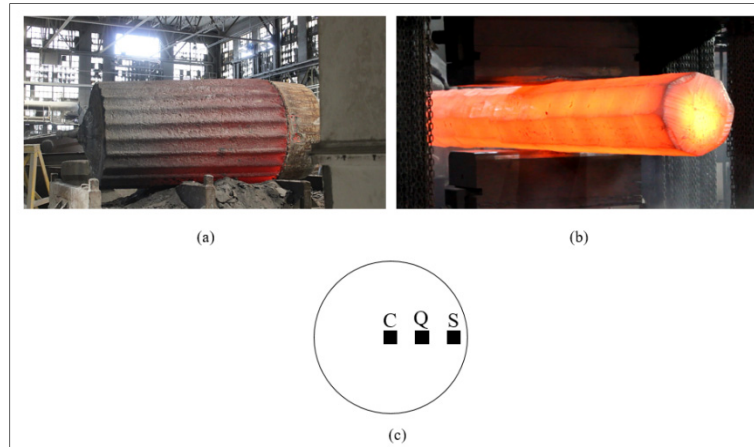
Figure 3.1 (a) As-cast ingot (b) As-forged ingot
(c) Schematic illustration depicting the sample
location used in material characterization

The specimens were individually mounted and polished from 600 to 1200 grade SiC paper, then finished with 1 μm diamond grain paste. To reveal the microstructure, as-annealed samples were etched with Villela solution composed of 1 gr of picric acid, $(O_2N)_3C_6H_2OH$, 5 ml of hydrochloric acid, HCL and 100 ml of ethyl alcohol, C_2H_5OH for approximately 25 s. For microstructural characterizations, an Olympus LEXT OLS4100 laser confocal microscope was used. For scanning electron microscopy characterizations, a Hitachi SU8230, at 10 Kv and 5 Kv equipped with Brukers energy-dispersive spectroscopy EDS Quad detector (QUANTAX FlatQUAD) was employed. The phase identification of the microstructure was examined by a SU-8230 HITACHI equipped with a Bruker e⁻Flash HR⁺ electron backscatter diffraction (EBSD) detector using 10 Kv and a pixel size of 64.9 nm. The total map size and working distance were 3158 $μm^2$ surface area and 15 mm respectively. The EBSD data were post-processed using QUANTAX ESPRIT software. For the EBSD analysis, the specimens were mechanically polished down to 0.5 μm. Then, the residual fine scratches and deformed surfaces were eliminated using an IM4000Plus ion milling system under 6 Kv accelerating voltage and 25 rpm rotation speed for 40 min.

The XRD measurement was carried out using X'Pert3 MRD PANalytical with Cu Kα radiation (λ=1.541 A°) with an angle between 20 to 90 degrees (2-theta), the step size of 0.02 degrees

and use of monochromator. Also, Thermo-Calc thermodynamic software with steel and Fe-Alloy database and 2020a version was employed to simulate the phase diagrams and phase proportions over a wide range of temperatures and chemical compositions.

3.3 Results

3.3.1 Microstructure Analysis

Optical microscopy observation of the ingot forged in 1204 °C, Figure 3.2, revealed the presence of a white phase, primarily precipitated along the grain boundaries. The volume fraction of the white phase was different from the surface to the center regions. The highest amount was found in the central region and a notable decrease towards the surface. As shown in Figure 3.2 (a-c), in the center region, the blocky and coarse white phase can be seen clearly, while in the quarter region, Figure 3.2 (d-f), a few blocky precipitates as well as film-like phase along the grain boundary are present. As the distance from the center increases, the quantity of the white phase decreased in favor of a thin film-like along the grain boundary, Figure 3.2 (g-i). The thickness of the film-like phase varied along the grain boundaries and was between 0.5 μm and 1 μm.
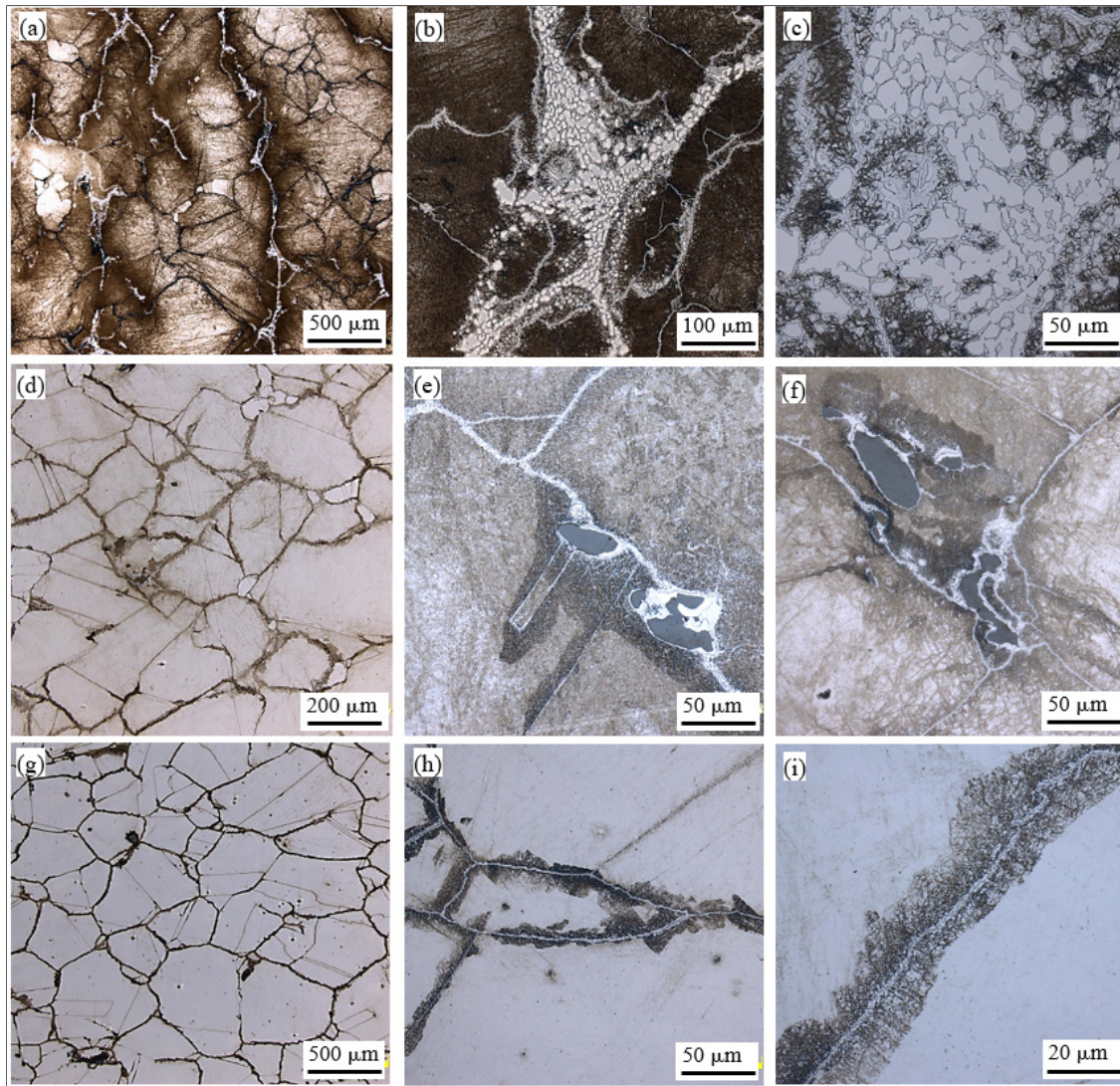
Figure 3.2 Microstructure of deformed X38CrMo16 in 1204 °C etched by Villela (a-c) Centre: (d-f) Quarter (g-i) Surface

Figure 3.3 shows illustrative examples of the microstructure of the three regions for the ingot which was forged in 1260 °C. Microscopic observation revealed the presence of coarse white phases, which were discontinuous and distributed locally, as opposed to what was observed when the forging was carried out at 1204 °C (Figure 3.2).
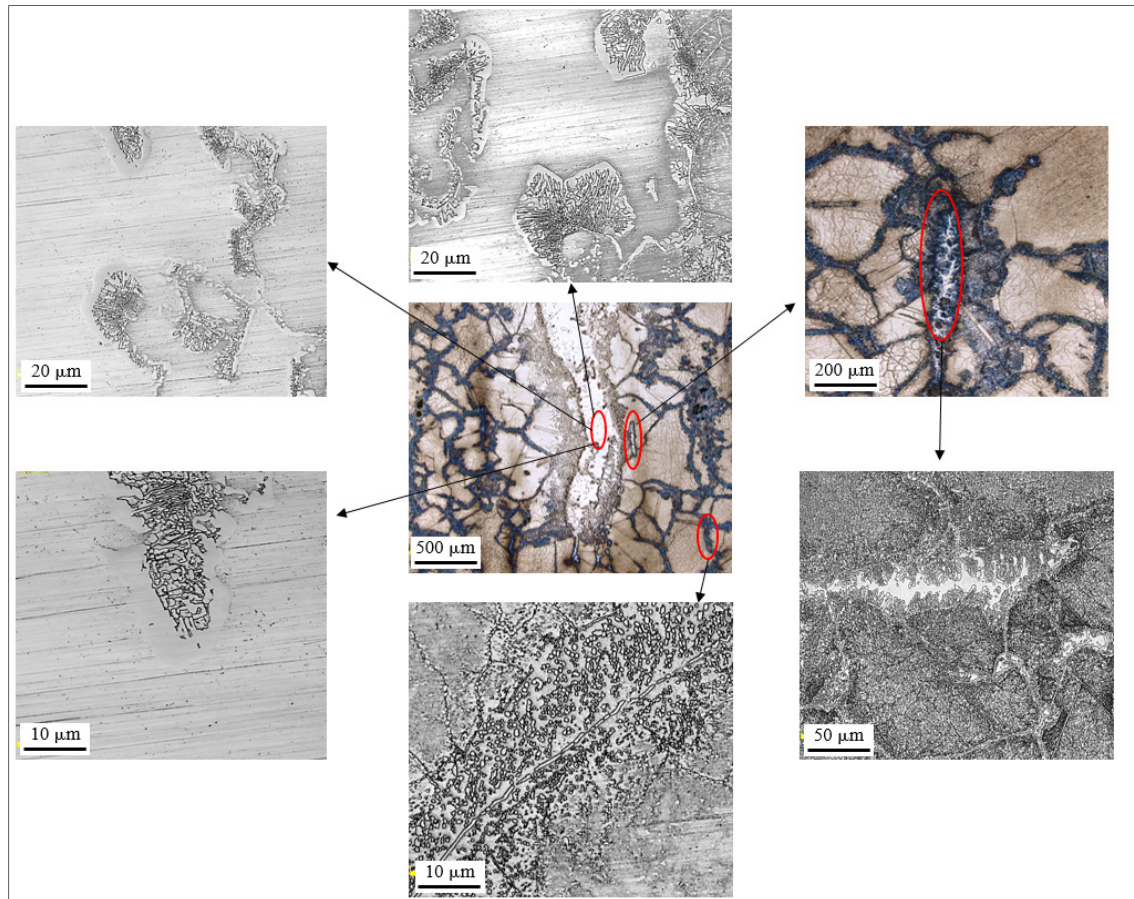
Figure 3.3 Microstructure of deformed X38CrMo16 in 1260 ℃ etched by Vilella

Elemental analysis by EDS was conducted for ingots forged in 1204 ℃ and 1260 ℃ and the results are reported in Figure 3.4 and Figure 3.5, respectively. The analyses revealed that in both cases, a significant enrichment of alloying elements such as Cr, Mo, and C in the white phase as compared to the original composition of the steel (0.37 % C, 15.21 % Cr, and 1.1 % Mo (wt.%)). The carbon contents reported in Figures 3.5 could be compared with the nominal composition (0.37 % C). However, it must be noted that although the EDS analyses were done using a high-resolution EDS detector (QUANTAX FlatQUAD) the obtained values are not absolute and should be regarded as relatively only for comparison purposes.

Spectrum point (wt.%)	Fe	C	P	Cr	Ni	Mo	Mn
1	78.71	2.41	0.07	16.46	0.23	1.54	0.58
2	32.05	4.05	0.32	58.48	0	2.09	0.41
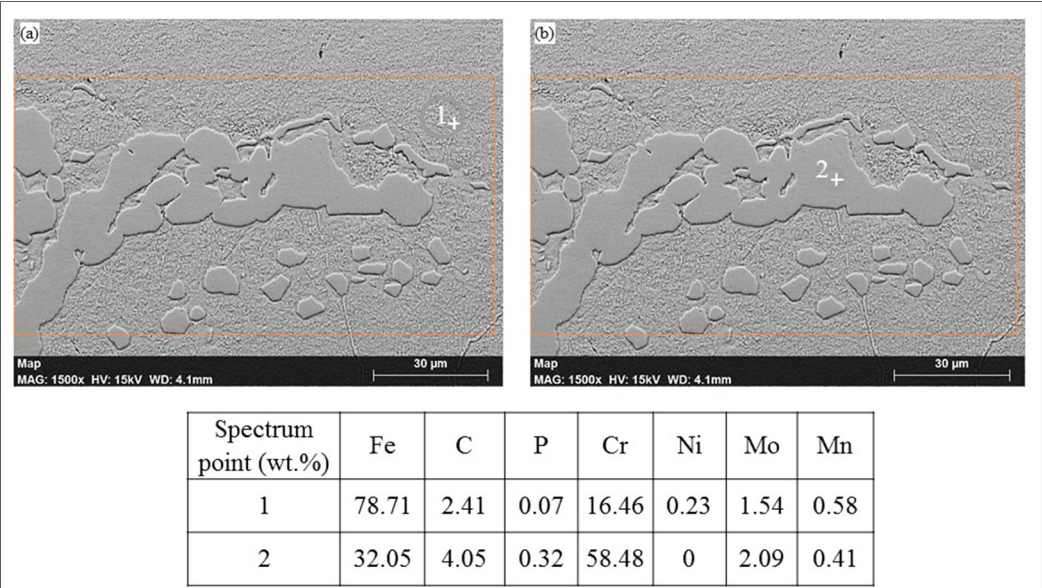
Figure 3.4 Chemical composition analysis measured by EDS for the ingot with 1204 °C forging temperature (a) Matrix (b) White phase

Spectrum	C	Al	Si	P	S	V	Cr	Fe	Cu	Nb	Mo	Mn
1	2.41	0.11	0.21	0.06	0	0.37	61.97	28.2	0	0.15	6.20	0.51
2	1.84	0.04	0.59	0.07	0	0.07	14.48	80.59	0	0.01	1.24	1.07
3	1.82	0.03	0.51	0.03	0	0.02	13.04	82.72	0	0.01	0.73	0.89
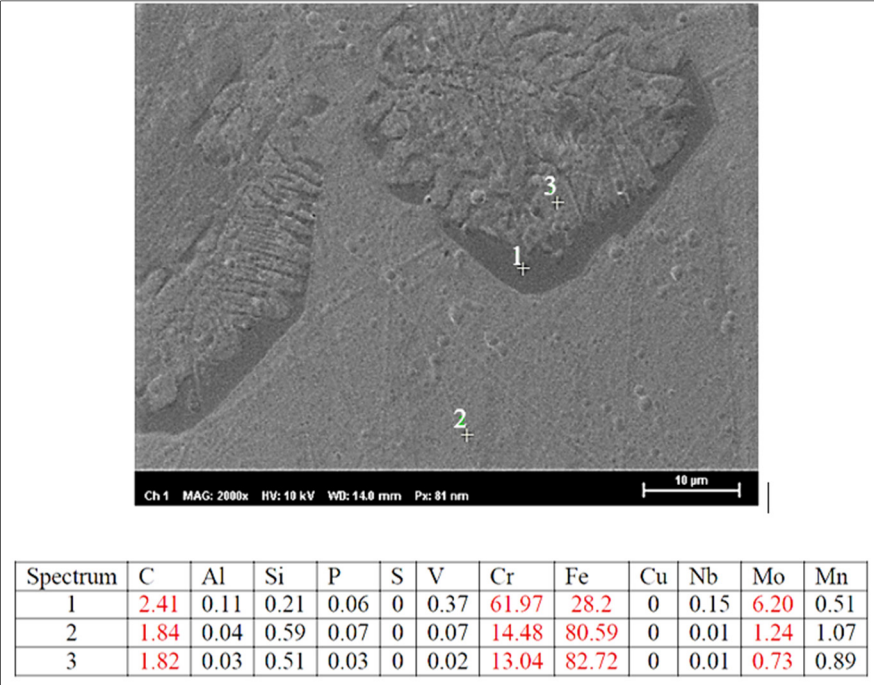
Figure 3.5 Chemical composition analysis measured by EDS for the ingot with 1260 °C forging temperature

In order to better identify the formation and composition of the white zones, a simulation of phases formed between 500 ℃ to 1500 ℃ was carried out using Thermo-Calc software, and the results are reported in Figure 3.6. During equilibrium solidification, the start temperature for $M_{23}C_6$ carbides precipitation is around 1100 ℃ and the stable phases at room temperature are ferrite, $M_{23}C_6$, M_2P, and MnS. As well, the eutectic temperature is 1243.42 ℃ with 20.5 %Cr and the primary ferrite structure starts to be formed when the temperature decreases to 1468.39 ℃. The diagram would be more discussed in the next section.
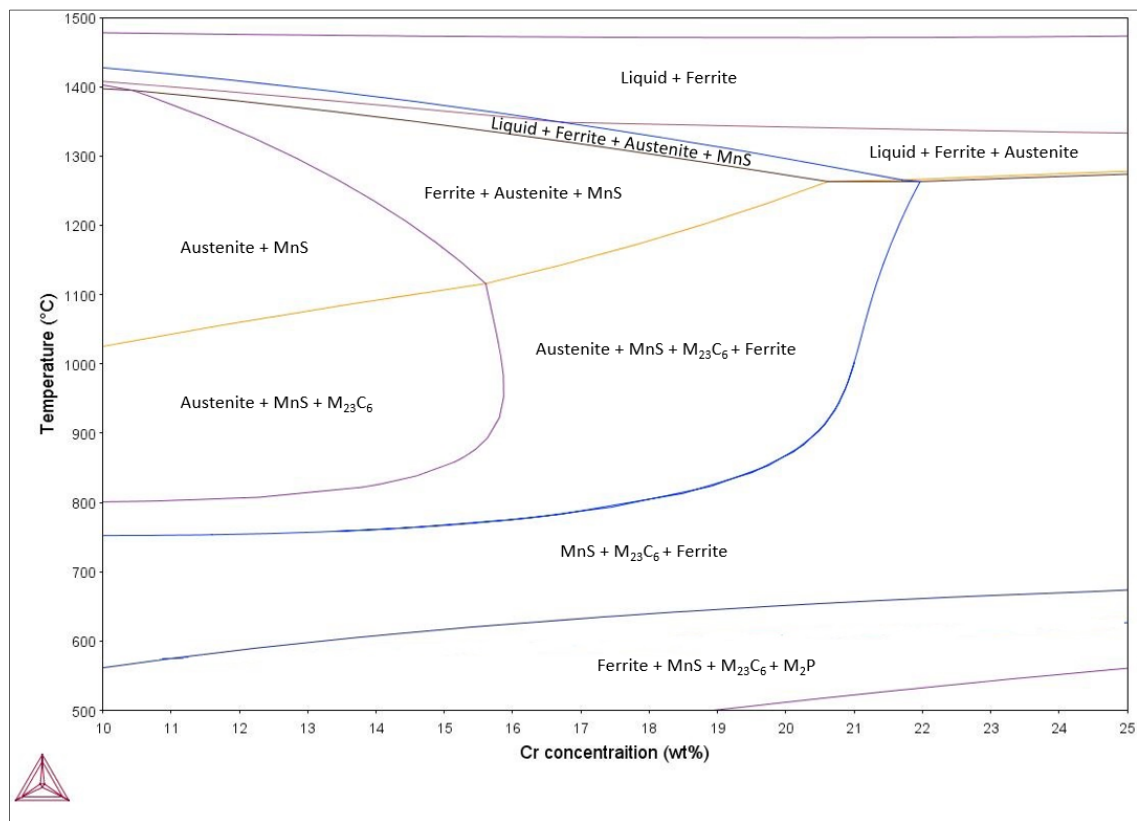
Figure 3.6 Thermo-Calc phase diagram simulation between 500 ℃ and 1500 ℃
using the composition of Table 3.1

X-ray diffraction data of the center of both ingots forged in 1260 ℃ and 1204 ℃, extracted from a computer-controlled system, are presented in Figure 3.7. The data were plotted in the form of the square root of X-ray intensity [Sqrt (counts/sec)] versus 2θ (degrees) to better reveal the weaker peaks. The 2θ range for the specimens of this study was between 20 to 90

degrees with a step size of 0.02 degrees. In Figure 3.7, the peaks were indexed using high score Plus software with a standard database (PLU2020).
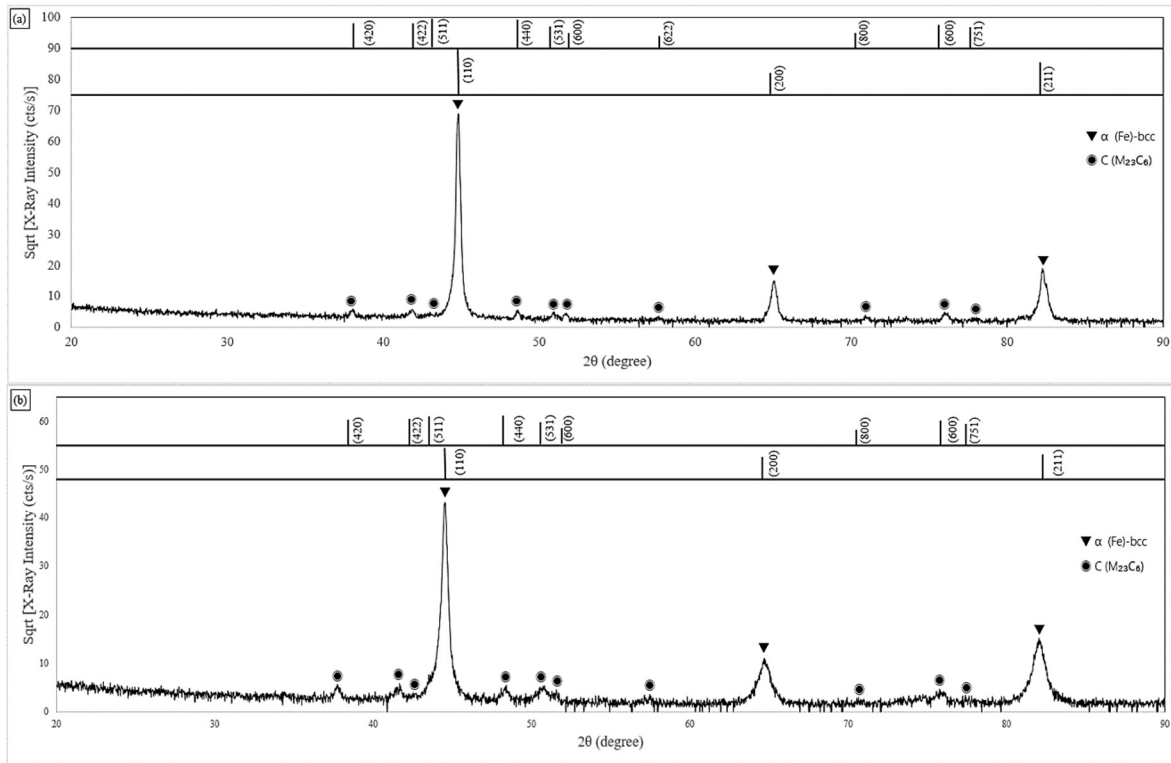
Figure 3.7 XRD pattern of as polished X38CrMo16 specimen forged at (a) 1260 °C
(b) 1204 °C

SEM micrograph and elemental map of the white phase by EDS are reported in Figure 3.8 for both testing conditions. The Figure depicts the significant reduction of Fe and a sharp increase in Cr and Mo. This observation confirms that the alloying element enrichment detected in the white phase is present along the interface between the matrix and the white phase.
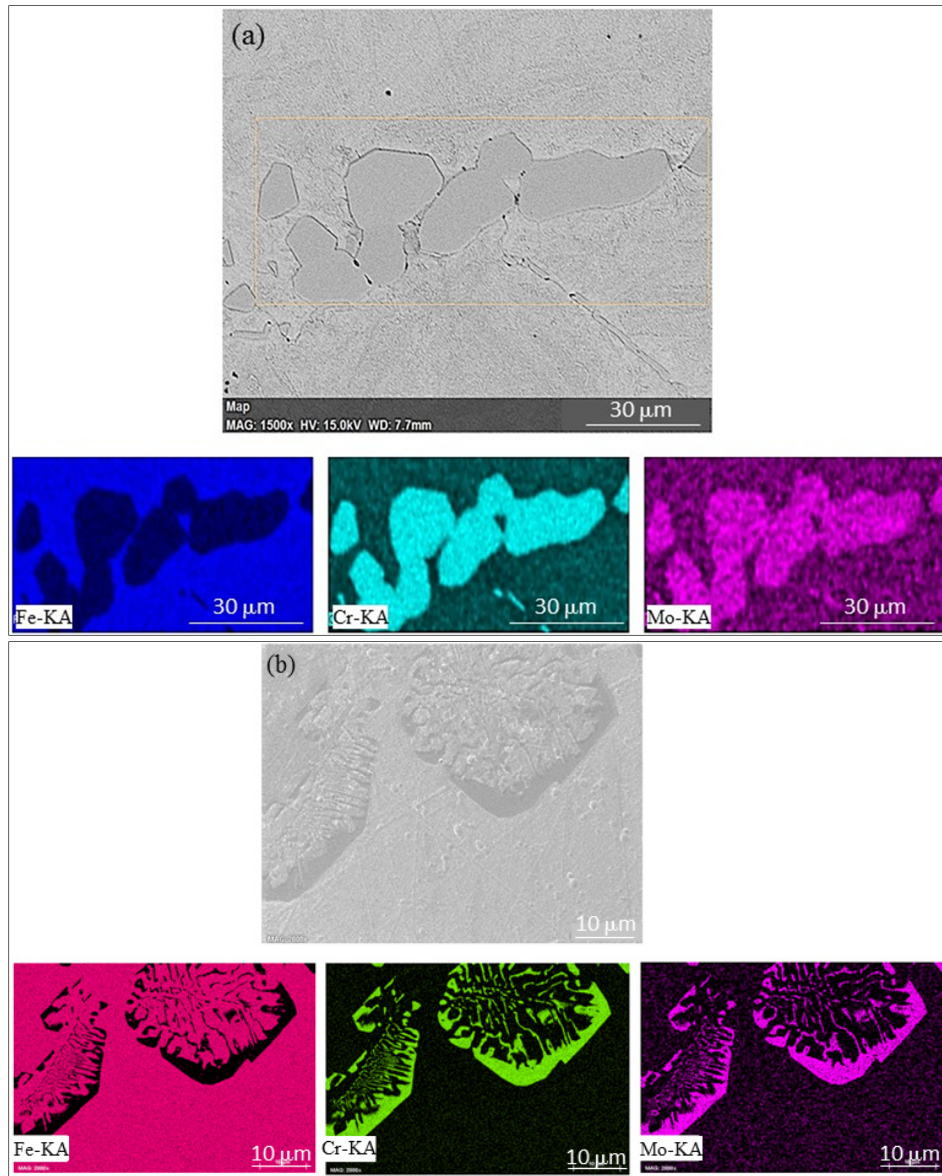
Figure 3.8 SEM micrograph and elemental map by EDS of the
white phase of forging temperature (a) 1204 ℃ (b) 1260 ℃

3.4 Discussion

In ingot casting, the macrostructure of the as-cast material along the radial direction is composed of three distinct zones from the mold wall to the center of the ingot (Pineda & Martorano, 2013). The significant magnitude of the temperature difference between the mold

wall and the melt leads to the rapid cooling of the zones in contact with the wall resulting in the nucleation of equiaxed and fine grains forming what is commonly called the "chilled zone". With the advancement of the solidification interface, the temperature gradient decreases, and the crystals gradually grow dendritically in certain crystallographic directions. In this zone, the grains grow along a preferred orientation parallel to the heat flow direction, resulting in the formation of columnar grains. The third zone at the center of the ingot is called the "equiaxed zone" which consists of equiaxed grains oriented randomly (Uddagiri et al., 2020). The above distinction of the three zones in the cast ingot will be used in the following to analyze the obtained results.

3.4.1   Off-Eutectic Non-Equilibrium Solidification

The non-equilibrium solidification process of large castings with off-eutectic composition may lead to two types of segregation (Porter, Easterling, & Sherif, 2021). There is macrosegregation which causes compositional variations over large distances (tens of centimeters), and there is microsegregation that takes place on the scale of grain boundaries and secondary dendrites arm spacing (Loucif et al., 2018). The extent of microsegregation depends on solidification conditions such as local cooling rates, thermal gradients, and changes in chemical composition. These factors control the migration of solutes at the solid/liquid interface so that by increasing the distance from the mold wall, the thermal gradient ahead of the solidification interface is gradually decreased and more solutes are released into the liquid. With the advancement of solidification, the residual melt, rich in solutes, primarily congregates in the root zones of the dendrites due to lower thermal dissipation in these zones. Consequently, the eutectic transformation takes place at the final solidification zones, dendrites, and grain boundaries and produces two composite solid phases (Ferrite + $M_{23}C_6$). As shown in Figure3.6, the equilibrium phase diagram predicted by Thermo-Calc, the phase sequence during the solidification process of X38CrMo16 includes:

$L \rightarrow L + \text{Ferrite} \rightarrow L + \gamma + \text{Ferrite} \rightarrow L + \gamma + \text{Ferrite} + \text{MnS} \rightarrow \gamma + \text{Ferrite} + \text{MnS} \rightarrow \gamma + \text{MnS} \rightarrow \gamma + M_{23}C_6 + \text{MnS} \rightarrow \gamma + \text{Ferrite} + M_{23}C_6 + \text{MnS} \rightarrow \text{Ferrite} + M_{23}C_6 + \text{MnS} \rightarrow \text{Ferrite} + M_{23}C_6 + \text{MnS} + M_2P$
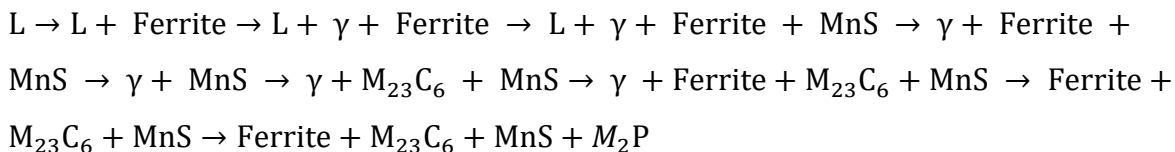
And the eutectic transformation that occurs along the grain boundaries is:

$$L \rightarrow Ferrite + M_{23}C_6$$
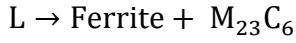
It is shown in Figure 3.6 that X38CrMo16 is an off-Eutectic alloy with 15.20 %Cr in nominal composition and 21.5 %Cr in eutectic composition. By solidification proceeding, the solute distribution depends on the advancing rate of the solidification interface and the diffusion coefficient of the solute in the liquid phase. According to the Scheil equation (Wu et al., 2000), the solute distribution in a definite volume can be described by the following equation:

$$\underline{C_L} = C_0 f_L^{(K_E-1)} \tag{3.1}$$

Where $\underline{C_L}$ ($\frac{mol}{L}$) is the solute concentration in the residual melt, C_0 ($\frac{mol}{L}$) represents the initial solute concentration, f_L is the fraction of residual melt, and K_E (the ratio of the concentration of a substance in one medium or phase to the concentration in a second phase) describes the effective partition coefficient. On the other hand, K_E and solidification rate could be related to each other using the following relation reported by Burton et al. (Burton, Kolb, Slichter, & Struthers, 1953):

$$K_E = \frac{K_0}{K_0 + (1 - K_0) ex p\left(-\frac{R\delta_N}{D_L}\right)} \tag{3.2}$$

Where k_0 is the equilibrium partition coefficient of solute, R ($\frac{m}{s}$) is the solidification rate; δ_N (m) the thickness of diffusion boundary layer in advance of the solidification interface; D_L ($\frac{m^2}{s}$) the diffusion coefficient of solute in a liquid phase. It is clear that the higher the K_E, the lower the $\underline{C_L}$ or the smaller the solute concentration in the residual melt.

In the chill zone, the cooling rate I is the highest, and a large number of grains nucleate simultaneously. The higher R leads to smaller $\underline{C_L}$ because of increasing K_E. Therefore, the solute partition during solidification is nearly suppressed. Under these conditions, most of the solutes are trapped in the pre-solidified grains and lower number of solute atoms are ejected into the melt in front of the solidification front. It can be seen in Figure 3.2 (g-i) that the thin film-like eutectic carbides are precipitated along the grain boundaries. By taking distance from the mold wall (in the columnar zone), the thermal and constitutional supercooling as well as R becomes smaller and $\underline{C_L}$ increase correspondingly. So, more solutes are rejected into the bulk melt from the solidification front. As shown in Figure 3.2 (d-f), the liquid metal in the dendrite and grain boundary zones reaches the eutectic composition. At the center of the ingot (i.e., in the equiaxed zone), the thermal transfer is much smaller as compared with the two other zones, and therefore after complete solidification, the eutectic carbide precipitate in the center of the ingot along the dendrite and grain boundaries, as revealed in Figure 3.2 (a-c).

3.4.2   Identification of the Eutectic Phase

To detect and identify the eutectic phase, EBSD measurements were conducted by considered phases including austenite-Fcc, ferrite-Bcc, and chromium carbide. To identify the type of carbide and other phases, we selected different types of chromium carbides and $M_{23}C_6$ was the best well-matched carbide with a minimum zero solution percentage (zero solutions are points in the scan for which no indexing solution could be found for the corresponding pattern). The results show that the chromium-rich regions could be related to $M_{23}C_6$ carbide (in blue) precipitated in a matrix of delta ferrite (in red), Figure 3.9.
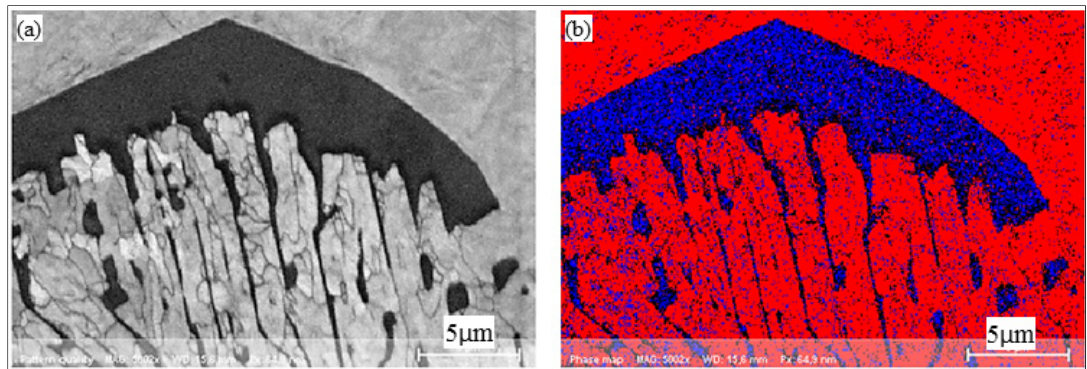
Figure 3.9 EBSD orientation mapping of the specimen (a) band-contrast image
(b) phase map (blue-$M_{23}C_6$ phase, red-ferrite phase

The distribution and volume fraction of the eutectic phase plays a crucial role in changing the mechanical properties, which may lead to cracking and part rejection during the forging operation. Therefore, the forging temperature must be adjusted in a way to do not reach the eutectic phase composition. Specifically, in the present study, the formation temperature of the eutectic phase is 1243.42 °C and thus the forging temperature of 1260 °C is higher than the eutectic temperature transformation. This means that the eutectic phase precipitated along the grain boundaries would be liquid when forging was carried out at 1260 °C. In contrast, when forging at 1204 °C, no liquid phase is expected to be present.

Very little or no data is available in the literature on the forging of high-strength steels in the presence of a liquid phase and its impact on crack initiation. K. Higashi et al. studied the effect of the liquid phase on tensile elongation of superplastic aluminum alloys and reported that macroscopic melting begins to occur when the forging temperature is higher than the eutectic temperature. They also found that, as the presence of the eutectic phase was increasing at the grain boundaries, the shear stress could not be transferred across them resulting in crack initiation (Higashi, Nieh, Mabuchi, & Wadsworth, 1995). In another study, Vaandrager and Pharr (Vaandrager & Pharr, 1989) reported that by applying the stress, the liquid phase quickly redistributed and squeezes out of highly stressed boundaries and flows into less highly stressed boundaries. If the volume fraction of the liquid is increased, deformation proceeds by grain boundary sliding accommodated by the formation of cavities in the liquid which adversely

affects the formability of the material. Finally, in a recent publication, Chen et al. (Y. Chen, Luo, Zhang, Wei, & Zhao, 2015) investigated the effect of temperature on the segregation and deformation mechanism of α+Ti$_2$Cu alloy during semi-solid forging. They found that by increasing the forging temperature, a continuous liquid layer is formed at the grain boundaries that move along the grain boundary during deformation and a significant amount, similar to a macrosegregated zone, of the Ti$_2$Cu phase is formed.

In the present study, as reported in Figure 3.3, at the higher forging temperature, the higher amount of the eutectic phase present in the material, results in the formation of continuous bands of large macrosegregated zones which could be the source of cracking; while at the lower forging temperature, a more discontinuous phase distribution is observed thereby reducing any cracking risk.

3.5   Conclusions

This chapter investigated the characteristics of eutectic phase precipitation as a function of the forging temperature in a large diameter ingot made of X38CrMo16 martensitic stainless steel and the following conclusion were obtained:

1.   The eutectic carbides in the off-eutectic X38CrMo16 martensitic stainless steels primarily precipitated at the grain boundaries.

2.   The morphology and distribution of the eutectic phase varied from the outer wall to the inner wall along the radial direction of the mold. Different morphologies consisting of thin film-like carbides, skeleton-like and blocky carbides were revealed.

3.   The volume fraction of the precipitated eutectic phase was affected by the cooling rate during solidification. Increasing the cooling rate suppressed the solute migration to the liquid phase which led to decreasing the amount of eutectic carbide. In contrast, a significant amount of eutectic phase precipitated along the grain boundaries at the center of the ingot which experiences the lowest cooling rate.

The 'ideal' forging temperature which was determined based on the findings of Chapter 3 was proposed and put into industrial practice. The next chapter will examine the hot workability of MSS by conducting a hot compression test and developing a microstructure-based constitutive as the second objective of this project.

CHAPTER 4
HOT WORKABILITY EVALUATION OF A MARTENSITIC STAINLESS STEEL THROUGH MATERIAL MODELLING AND FINITE ELEMENT SIMULATION

S. Dourandish [a], H. Champliaud [a], J-B Morin [b], M. Jahazi [a],

[a] Department of Mechanical Engineering, École de Technologie Supériere,
1100 Notre-Dame West, Montreal, Quebec, Canada H3C 1K3
[b] Finkl Steel-Sorel Inc., 100 McCarthy, Saint-Joseph-de-Sorel, Québec, Canada J3R 3M8

Summary

In this chapter, the hot deformation behavior of martensitic stainless steel was investigated by conducting hot compression tests using a Gleeble-3800 thermo-mechanical simulator. Developing a precise model to predict the hot deformation behavior of MSS was one of the objectives of this chapter. A material model that accounts for the influence of strain was established and then employed in simulating the forging process of MSS by implementation into the commercial finite element simulation code, FORGE-NXT. Moreover, microstructure maps for the entire volume of the specimen were determined and the occurrences of different softening phenomena were predicted as a function of hot deformation parameters. The flow behavior of the material was also analyzed using the Dynamic Material Model and the unstable regions were identified. The approach proposed in this chapter, which integrates microstructure-based finite element simulation combined with a three-dimensional processing map, can be used for rapid and accurate optimization of the hot deformation process of martensitic stainless steels.

4.1   Literature Review

Hot forging of large size ingots made of MSS is a challenging processing step during the manufacturing of structural components that require high strength, good corrosion resistance and toughness such as valves, shafts, rotors, and bolting of gas turbine blades (Bitterlin et al., 2016; Mahmoudi, Torkamany, Sabour Aghdam, & Sabbaghzadeh, 2011; Ren et al., 2014). The main concern during the forging of these steels is the occurrence of large variations in the microstructure (e.g., austenite grain size) between the center and the surface of the forged part (Sanrutsadakorn, Uthaisangsuk, Suranuntchai, & Thossatheppitak, 2012). Such variations are at the source of cracking during the hot forging operation or can lead to unacceptable variations in properties in different regions of the final product.

The manufacturing process consists of alloy production in electric arc furnaces, followed by ingot casting and open die forging. During the latter step, the heterogeneous cast structure is broken down into a more refined microstructure and improved chemical homogeneity through the thickness of the large size forged block (Dimiduk et al. 1998; F. Qin et al. 2017). The flow characteristic of a hot forging process consists of competing mechanisms of strain hardening, also called work hardening and softening phenomena such as DRV and DRX. These mechanisms are affected by hot working parameters like temperature, strain, and strain rate (McQueen and Jonas 1975, Ebrahimi et al. 2012a, Jonas and Poliak 2003, Marchattiwar et al. 2013), optimizing these working parameters, related to metal forming, is of critical importance for the heavy forging industries and therefore the hot forging process should be designed carefully to obtain both the right shape and microstructure.

To accurately predict microstructure evolution and flow stress behavior during the ingot breakdown process at high temperatures, the development of reliable constitutive models is essential (Gao, Zhan, Fan, Lei, & Cai, 2017). In this regard, isothermal hot compression tests are typically used to simulate the material response to thermomechanical processes, and then constitutive material models are developed to describe the stress-strain curves at different temperatures and strain rates (Goetz & Semiatin, 2001; YE, GONG, YANG, LI, & NIE, 2019).

Different models have been developed to assess the individual and mutual influences of hot working process parameters on the flow stress evolution of stainless steel. Han et al. (Han, Qiao, Sun, & Zou, 2013) studied the hot deformation behavior of 904L superaustenitic stainless steels using the Arrhenius-type constitutive model. They reported that processing variables including strain, strain rate, and deformation temperature had a significant effect on the occurrence of DRX which was accelerated by increasing temperature and decreasing strain rate. Samantaray et al. (Samantaray et al., 2009) used the modified Zerilli-Armstrong (MZA) model to analyses the high-temperature flow behavior of austenitic stainless steels in a variety of grades, including 304L, 304, 316L, 304 (as-cast), and alloy D9. They discovered that the developed model accurately predicted the elevated temperature flow behavior over the entire ranges of strain rate, temperature, and strain. However, while a large number of efforts have been invested into the hot deformation behavior of austenitic stainless steels, little data is available on the martensitic grades.

In order to develop microstructure-based predictive tools for optimum thermomechanical processing, finite element simulation is used to predict the strain, strain rate, and temperature all over the volume of the material as a function of processing conditions (Ivaniski, Epp, Zoch, & Da Silva Rocha, 2019). The implementation of a constitutive model would therefore allow correlating microstructure evolution to the local variations in the strain, strain rate, and temperature. The constitutive models, which can predict the material flow behavior, are integrated into the FEM software. However, a very limited number of microstructure-based models have been integrated with the FEM software, and no report is available on the implementation of such models to study the hot workability of martensitic stainless steels. Another predictive tool to determine the hot workability of a material based on changing the working parameters including temperature, strain, and strain rate is the processing maps proposed by Prasad et al. (Yeom, Kim, Park, Choi, & Lee, 2007). The maps are developed based on the Dynamic Material Model (DMM), which provides processing conditions for a defect-free final product through optimizing the hot working parameters. The DMM technique provides guidelines for avoiding the flow instability domains where inhomogeneous deformation and localized flow could take place. It also allows determining and locating the

domains where a fine and homogenous microstructure develops during hot deformation. The different domains are obtained by the superimposition of a power dissipation map and an instability map for different temperatures, strain rates, and strains (Srinivasan, Prasad, & Rama Rao, 2008). A large number of data have been reported on the application of the DMM method to various alloys, including stainless steels (Babu, Mandal, Athreya, Shakthipriya, & Sarma, 2017; Pu, Zheng, Xiang, Song, & Li, 2014; Venugopal, Mannan, & Prasad, 1992) but very few are on martensitic stainless steels (Chegini, Aboutalebi, Seyedein, Ebrahimi, & Jahazi, 2020; Xiaoqin Zhou, Ma, Feng, & Zhang, 2020). Furthermore, very little or no data is available on microstructure-based FEM modelling of hot deformation of stainless steels and its combination with processing maps in general and martensitic ones, in particular (F. Chen, Ren, Chen, Cui, & Ou, 2016b).

In the present chapter, the actual stress derived from the Gleeble machine was corrected due to effect of deformation heating and friction effect. An accurate constitutive model for a modified AISI 410 MSS which describes the flow stress in terms of hot working variables including strain, strain rate, and deformation temperature is developed. A comparison is made between the experimental flow stress data and the one calculated by the established constitutive equations. The constitutive model that best predicts the flow curves was then implemented into the FEM code Forge NxT 3.0® software through the development of an original user subroutine (UMAT). The simulation results were first compared to the experimental ones for validation purposes and then were further utilized to analyze the effect of hot working parameters on microstructure evolution during the hot deformation process under different conditions. The DMM method was used to generate 3D processing maps which were correlated with the FEM and experimental results to discuss the hot deformation mechanisms and to determine the optimum hot working conditions.

4.2 Material and Experimental Procedures

The material used for the current investigation was supplied by Finkl Steel-Sorel Forge, Quebec, Canada. The production cycle starts with melting using a 45-ton electric arc furnace

followed by ladle metallurgy degassing and refining processes along with tight control of the chemical composition. After the ingot-casting step, the solidified ingot is taken to the forge furnace and heated up to the forging temperature (1200 ºC - 1260 ºC). The hot-forged ingot undergoes heat-treatment steps including the quench and tempering cycle. The samples for the isothermal compression test were cut from the ingot after hot forging. Figure 4.1 shows the position where the compression samples were cut from the large size block and Table 4.1 displays the nominal chemical composition of the X12Cr13 used in this investigation.

Figure 4.1 An image depicting the position of the Gleeble tests
samples in the industrial-sized ingot

Table 4.1 The nominal chemical composition of the X12Cr13 (%wt.)

Element	C	Mn	Cr	Si	P	Mo	Cu	Ni
Content	0.14	1.03	11.71	0.25	0.02	0.19	0.15	0.48

The hot-compression tests were performed on cylindrical specimens with a diameter of 10 mm and a height of 15 mm based on the ASTM E209 standards with Gleeble 3800® thermomechanical simulator, Figure 4.2a, at four different temperatures, 1050 ºC, 1100 ºC, 1150 ºC, and 1200 ºC and four strain rates, 0.001 s^{-1}, 0.01 s^{-1}, 0.1 s^{-1}, and 1 s^{-1}. The selected thermomechanical processing parameters are representative of the actual industrial forging process. The specimens were heated up to the test temperature at a heating rate of 2 ºC/s, held for 15 min, and then subjected to compressive deformation at the selected strain rates. To

ensure maximum uniformity and stability of temperature distribution over the entire sample and obtain a similar grain size, as the initial microstructure, three sets of thermocouples, one at the center and another two at the edges, as shown in Figure 4.2b, were used to determine the optimum holding time of the target temperature. Figure 4.2c shows a sample before and after the hot compression test, respectively.
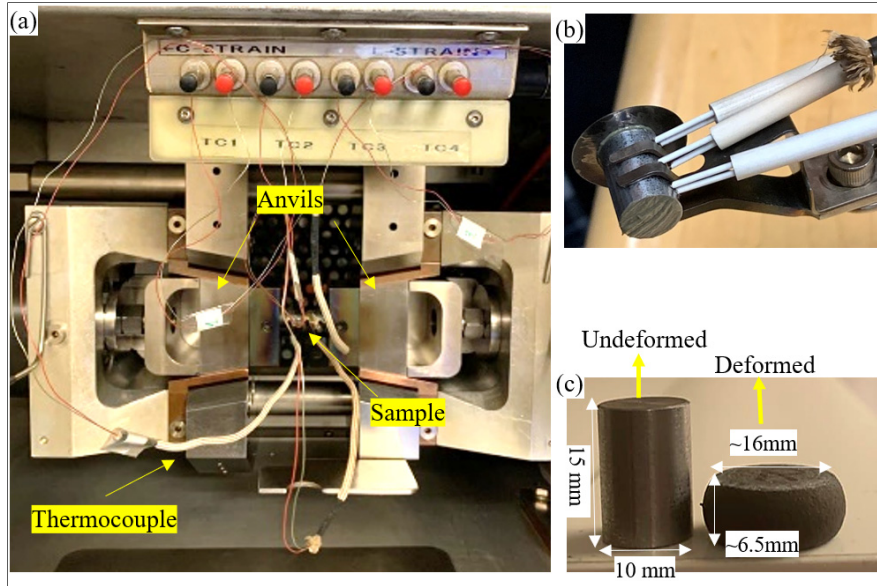
Figure 4.2 (a) Hot compression setup in the Gleeble machine (b) three thermocouples placed at different locations of the sample for precise measurement of holding time (c) Sample before and after hot compression test

The temperature readings of all three thermocouples (TC) were recorded (Figure 4.3a) and once the target temperature of 1230 ºC was reached, time was calculated until all three thermocouples gave the same reading. This confirmed the best time for uniform heat distribution in the specimen. On this basis, a 15-minutes holding time was determined for the temperature homogenization and used in all experiments. Figure 4.3b, displays the schematic of the hot compression experiments, where it can be seen that after the 15 min holding time the deformation is applied. Tantalum sheets of 0.1 mm thickness were used as a lubricant between the sample and the deformation anvils which are made of pure tungsten.
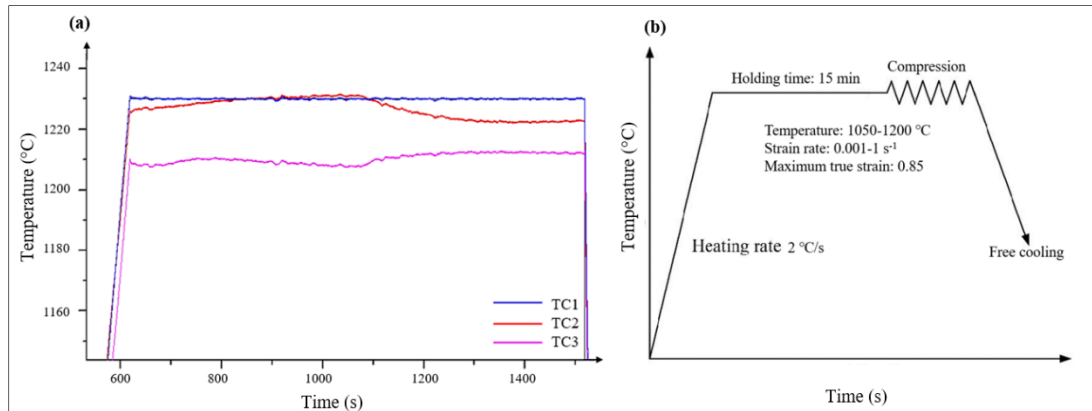
Figure 4.3 (a) Influence of holding time at high temperature on temperature homogenization (b) Schematic illustration of a hot compression test

After cooling to room temperature, the deformed samples were cut parallel to the compression axis by a precision cutter machine for microscopic examinations. The specimens were mechanically polished down to 0.5 μm and to reveal the microstructure, they were etched with Vilella solution composed of 1 gr of picric acid, $(O_2N)_3C_6H_2OH$, 5 ml of hydrochloric acid, HCL and 100 ml of ethyl alcohol, C_2H_5OH for approximately 25 s. For microstructural characterizations, an Olympus LEXT OLS4100 laser confocal microscope was used.

4.3 Results and Discussion

4.3.1 True Stress-Strain Curves

Figure 4.4 displays the true stress-strain curves obtained from hot compression tests conducted at various deformation temperatures and strain rates. It is seen that stress-strain curves are significantly affected by changing the temperature and strain rate. When the temperature is constant, the flow stress increases as the strain rate rises, but the flow curves sharply decline as the temperature rises.
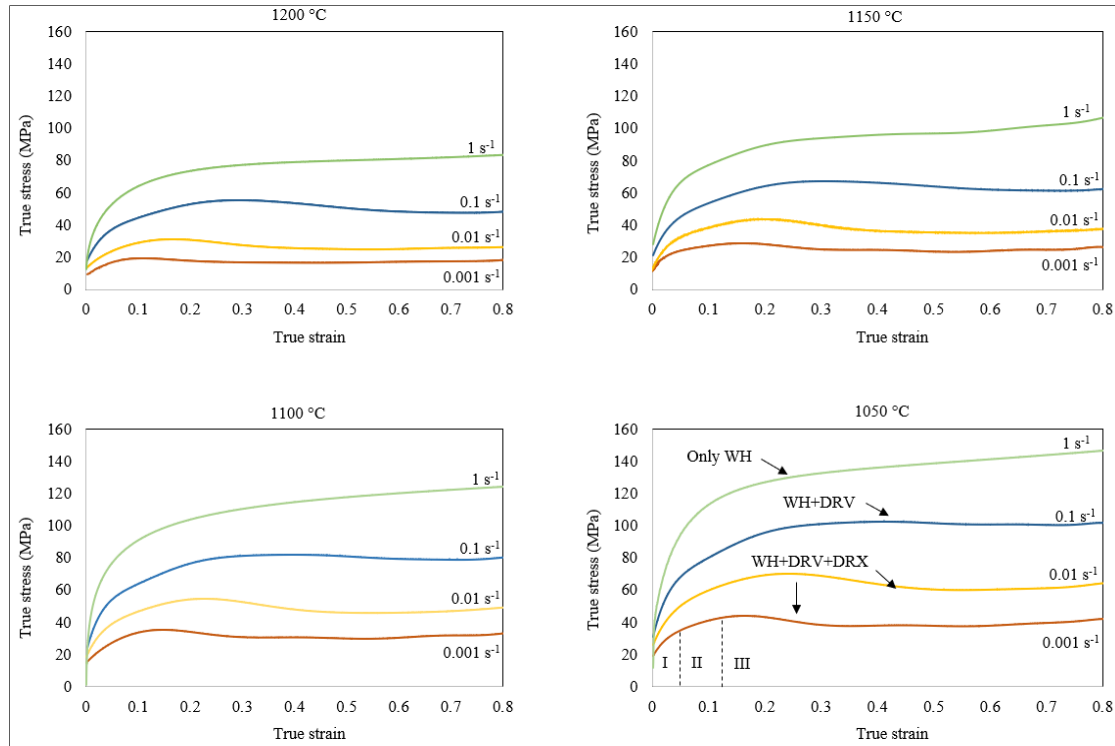
Figure 4.4 True stress-true strain curves of the investigated steel at different deformation conditions

From the stress-strain curves of Figure 4.4, three different stress changes can be observed with increasing stress. At the beginning of deformation (I), the stress increases significantly due to work hardening (WH). In the second stage (II), flow stress shows a continuous reduction with increasing stress until a peak point. This illustrates that thermal softening, due to DRV and DRX, becomes more and more overcoming until it exceeds WH. In the third stage (III), the stress curve shows three different patterns with the increasing strain: i) gradual decrease to a steady state with DRV/DRX softening. This is the case for all deformation temperatures and strain rates between 0.001 and 0.1 s^{-1} except those in 1050 ºC and 1100 ºC; ii) higher stress levels without significant softening and work-hardening in 1050 ºC and 1100 ºC and strain rate of 0.1 s^{-1}; and iii) continuous increase with significant work hardening (all deformation temperatures and strain rate of 1 s^{-1}) (Babu et al., 2017). Therefore, it can be concluded that the softening due to DRX, characterized by a flow curve with a single peak followed by a steady-state flow, takes place at high temperatures and low strain rates. With higher strain rates

and lower temperatures, the peak stress and the start of steady-state flow are therefore shifted to higher strain levels because the higher work hardening rate slows down the rate of softening brought on by DRX. The drop observed in stress is because of dynamic recrystallization occurrence at all temperatures and strain rates of 0.001 s^{-1}-0.1 s^{-1} in Figure 4.4 (Venugopal et al., 1992). Figure 4.5 shows the microstructure evolution at the end of deformation which is characterized by a significant grain refinement due to DRX, Figure 4.5b, in comparison with the initial microstructure, Figure 4.5a. However, at the strain rate of 1 s^{-1}, the flow curves are characterized by a continuous increase (without any peak), which is generally considered an indication of material undergoing DRV, Figure 4.5c.
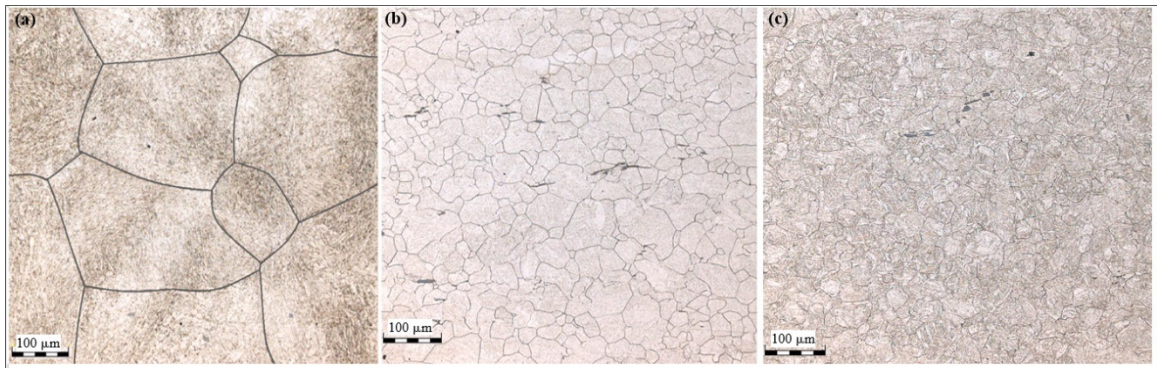
Figure 4.5 (a) Initial microstructure of the as-received steel (b) Microstructure of deformed samples in 1150 ºC and 0.1 s^{-1} (c) 1050 ºC and 1 s^{-1}

4.3.2 Corrections for Deformation Heating and Friction Effects

Deformation heating correction:

During the hot compression test, part of the accumulated deformation energy can be transformed into heat resulting in a higher temperature than the nominal one (Saksala, 2019). This difference, directly, related to the applied strain rate (Nasraoui, Forquin, Siad, & Rusinek, 2012) can cause some errors in measuring stress values by the equipment and needs to be corrected. The flow behavior is considered as occurring under isothermal circumstances when the deformation lasts for a long enough period to allow the generated heat to dissipate into the surrounding environment at a low strain rate. Higher strain rates make it impossible to

completely remove the deformation heating from the sample, which causes the sample temperature to increase. In this case, the process will be adiabatic. The following expression proposed by Goetz, R. Le is often used to correct the adiabatic heating effect (S. Li, Li, He, & Wang, 2019):

$$\Delta T = \frac{0.95\,\eta}{\rho C_p} \int_0^\varepsilon \sigma d\varepsilon \qquad (4.1)$$

Thermal efficiency, η, is calculated as follows:

$$\eta = \begin{cases} 0 & \dot{\varepsilon} \leq 10^{-3}\text{s}^{-1} \\ 0.95 + (0.316)\log\dot{\varepsilon} & 10^{-3}\text{s}^{-1} \leq \dot{\varepsilon} \leq 1.0\text{ s}^{-1} \\ 0.95 & \dot{\varepsilon} \geq 1.0\text{ s}^{-1} \end{cases} \qquad (4.2)$$

The values of ρ and C_p in the case of the investigated steel were calculated using JmatPro simulation software (www.sentesoftware.co.uk/jmatpro) for different temperatures and are listed in Table 4.2.

Table 4.2 Density and specific heat for different temperatures

Temperature (°C)	1050	1100	1150	1200
Specific heat (J/gr °C)	0.64	0.65	0.66	0.67
Density (g/cm^3)	7.5	7.48	7.45	7.43

The temperature increases were calculated using Eqs. (4.1) and (4.2) for strain values in the range of 0-0.8. Table 4.3 shows the variation of ΔT with $\dot{\varepsilon}$ for samples deformed at different strain rates and temperatures.

Table 4.3 Values of temperature increase during hot compression tests

0.001 s^{-1}		0.01 s^{-1}		0.1 s^{-1}		1 s^{-1}	
T (°C)	ΔT	T (°C)	ΔT	T (°C)	ΔT	T (°C)	ΔT
1050	2.91	1050	4.74	1050	7.64	1050	15.90
1100	2.38	1100	3.675	1100	6.12	1100	13.48
1150	1.81	1150	2.85	1150	4.97	1150	11.05
1200	1.23	1200	1.95	1200	3.84	1200	8.87

The results show a maximum temperature correction of about 16 ºC at the temperature of 1050 ºC and a strain rate of 1 s^{-1} that needs to be taken into consideration. The isothermal flow stresses (corrected for deformation heating), σ_c, were then determined using the following relationship (Castellanos, Rieiro, Cars, Muoz, & Ruano, 2007):

$$\sigma_c(\varepsilon, \dot{\varepsilon}, T_0) = \sigma_{wc}(\varepsilon, \dot{\varepsilon}, T_0) - \frac{\partial \sigma_{wc}(T_0)}{\partial T_0}\bigg|_{\varepsilon\dot{\varepsilon}} \Delta T \qquad (4.3)$$

Where σ_{wc} is the flow stress uncorrected for deformation heating and T_0 is the initial temperature. Figure 4.6 shows the correction of the adiabatic heating effect on true-strain curves of X12Cr13. The difference between corrected and uncorrected curves is increasing with increasing strain rate and decreasing temperature.
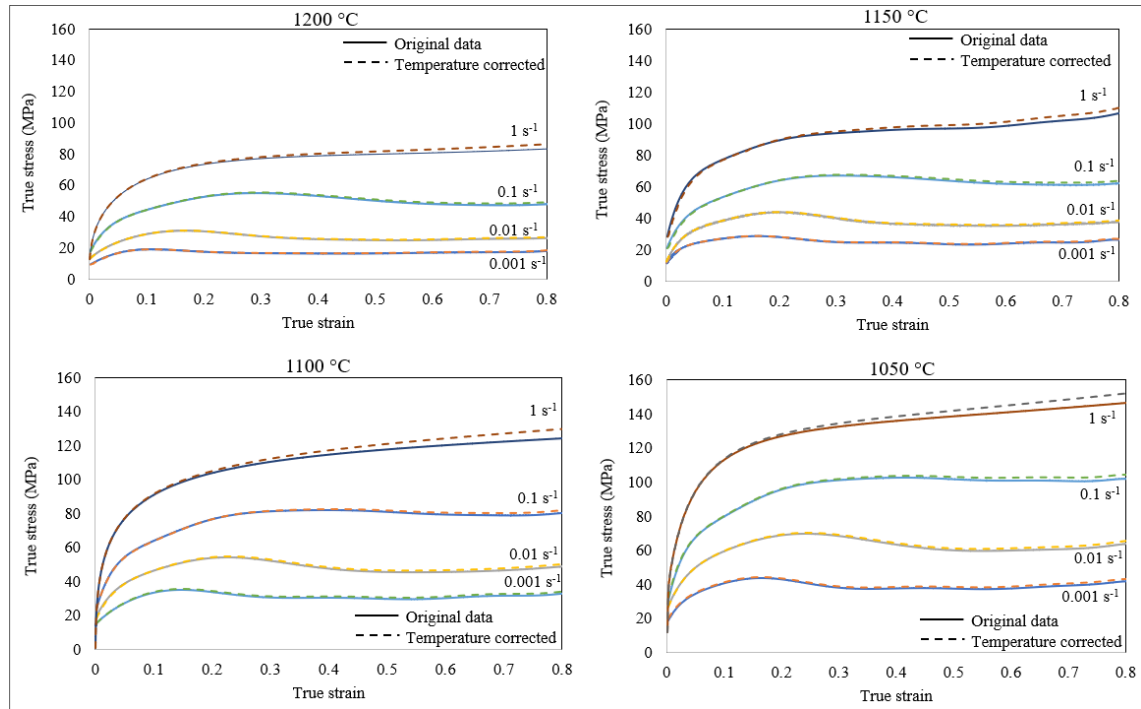
Figure 4.6 Flow stress curves corrected for the effect of adiabatic heating

Friction Correction:

The presence of friction at the anvil-specimen interface leads to the formation of the dead zone and inhomogeneous deformation and therefore introduces errors in measuring the flow stress

during hot compression tests. Despite the use of tantalum sheets to reduce friction, the impact of friction between the anvil and the specimen grows as the strain increases (Y. P. Li, Onodera, Matsumoto, & Chiba, 2009).
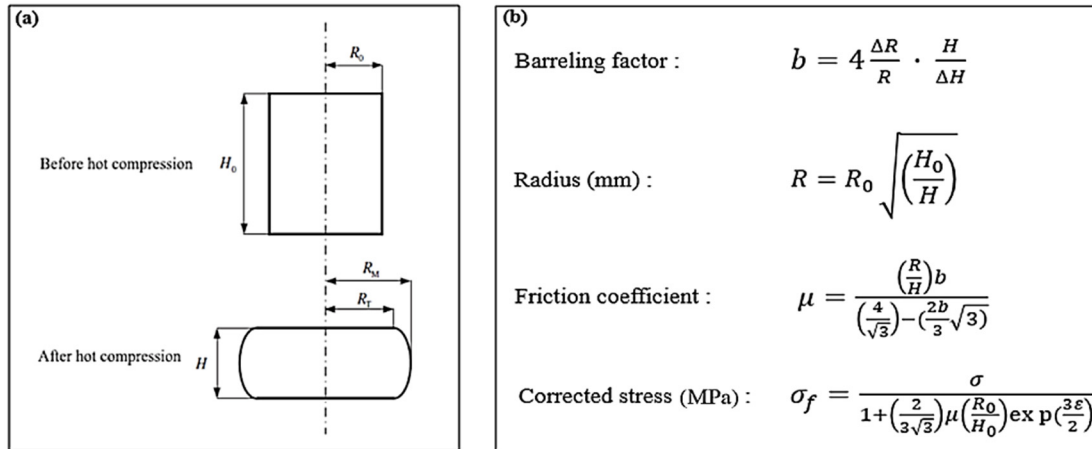
Figure 4.7 (a) A simple representation of the sample's geometry before and after the compression test (b) Friction corrected formulas
Taken from Li et al. (2009)
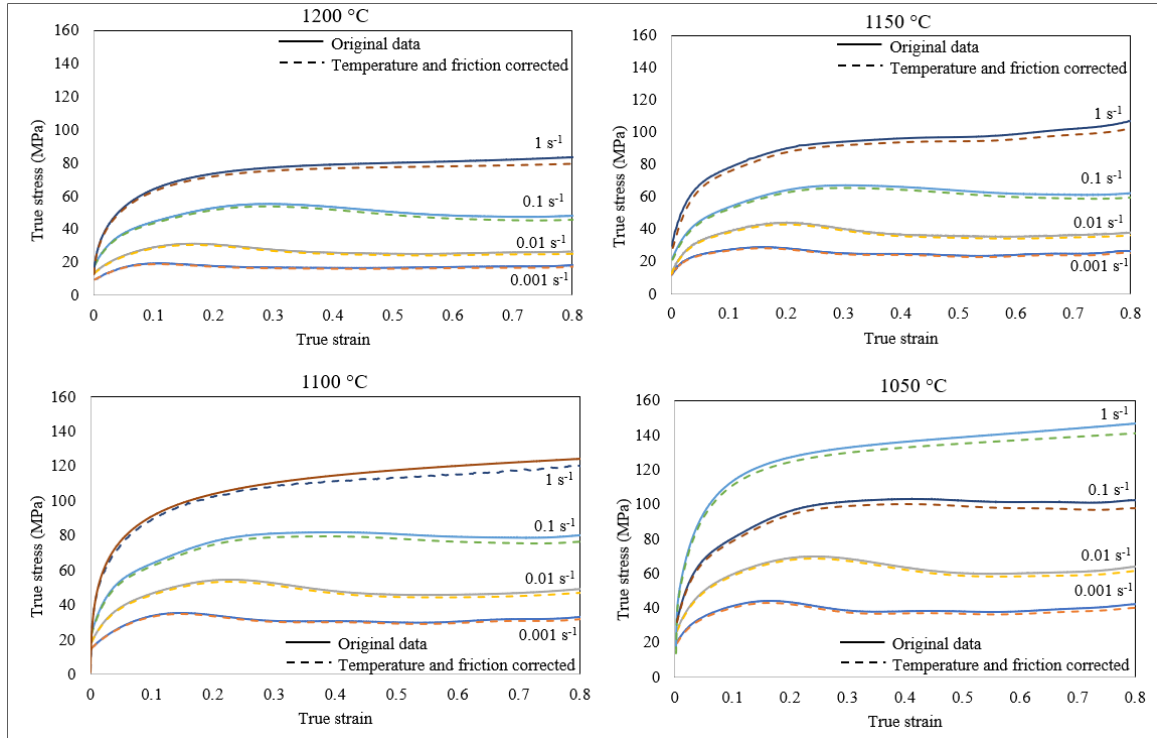
Figure 4.8 Corrected flow stress curves due to the friction and adiabatic heating effects for tested temperatures and strain rates

Figure 4.7a shows a schematic representation of the solid compression test where H_0 and R_0 are the initial height and radius of the cylinder, respectively. R_M and R_T are the maximum and top radius of the cylinder after deformation, respectively. H is the height of the cylinder after deformation. To correct the flow stress, the friction coefficient μ was initially calculated using the equation "Friction coefficient" reported in Figure 4.7b (F. Chen et al., 2016a). In this Figure, b is the barreling factor, ΔR is the difference between the maximum and top radius ($\Delta R = R_M - R_T$), ΔH is the difference between the initial and final height. After calculation of constants, the flow stress can be corrected by the equation "corrected stress" shown in Figure 4.7b, where σ is the measured flow stress, isσ_f is the corrected flow stress, and ε is the measured deformation degree. The corrected flow stresses for both adiabatic heating and friction effects are shown in Figure 4.8. The experimental stress curves are higher than the corrected ones which means that the effect of friction was greater than adiabatic heating on flow stress. The corrected flow stress curves were then used in the establishment of the constitutive equation.

4.3.3   Constitutive Modelling

Hansel-Spittel Model:

The Hansel-Spittel constitutive model (Hansel and Spittel, 1978), is currently implemented in Forge NxT 3.0® simulation software. This model relates flow stress to strain, strain rate, and temperature through the following equation:

$$\sigma = Ae^{m_1 T}\varepsilon^{m_2}\dot{\varepsilon}^{m_3}e^{\frac{m_4}{\varepsilon}}(1+\varepsilon)^{m_5 T}e^{m_7 \varepsilon}\dot{\varepsilon}^{m_8 T}T^{m_9} \tag{4.4}$$

Material constants, A and m_1 to m_9, can be derived from the stress-strain data obtained from hot compression tests (Liang et al., 2020). In an initial stage, the above model was applied to the investigated steel and the different material constants were calculated and are provided in Table 4. 4:

Table 4. 4 Parameters of Hansel-Spittel equation.

A	m_1	m_2	m_3	m_4	m_5	m_7	m_8	m_9
-135.39	-0.024	0.297	-0.103	-0.0002	-0.0013	0.139	0.00026	24.02

Figure 4.9 shows the comparison between the experiment and calculated flow stress based on the Hansel-Spittel model. It can be seen that the difference between experimental and predicted stress is significant, especially at higher strain rates. The results also show that this model is not able to predict the softening behavior of the studied alloy for any of the investigated deformation conditions. Therefore, another constitutive model is needed to more accurately predict the flow stress behavior of the investigated steel.
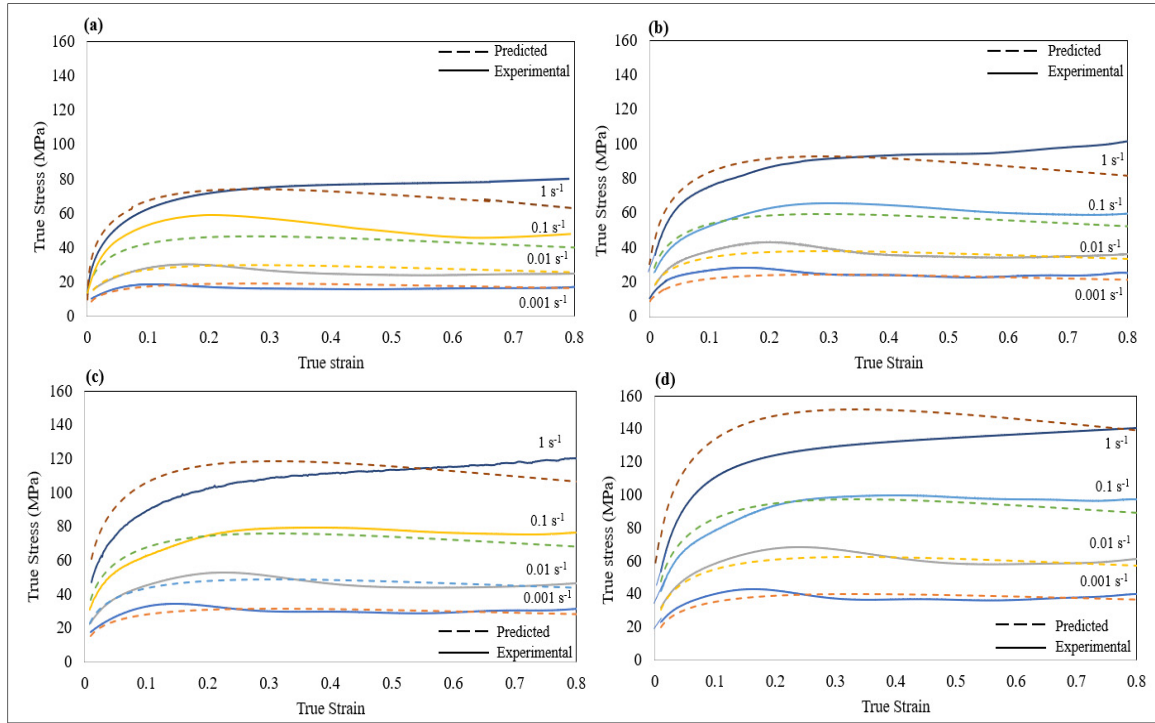
Figure 4.9 Comparisons between the experimental and calculated flow stress developed by Hansel-Spittel model at four strain rates and temperatures of (a) 1200 ºC (b) 1150 ºC(c) 1100 ºC (d) 1050 ºC

Arrhenius Model:

The Arrhenius-type equation initially proposed by Sellars and McTegart relates the strain rate, temperature, and activation energy at a constant strain value, through the following equation (Sellars & McTegart, 1966):

$$Z = \dot{\varepsilon} \exp\left(\frac{Q}{RT}\right) = A[\sinh(\alpha\sigma)]^n \tag{4.5}$$

Where Z is the Zener-Hollomon parameter, Q is the activation energy required to overcome deformation barriers, A, α (MPa^{-1}), and n are material constants, R is the universal gas constant, T is the temperature in Kelvin, $\dot{\varepsilon}$ is the strain rate, and σ is the applied stress. Based on Eq. (4.5), the flow stress of the material can be expressed at a given strain as follows:

$$\sigma = \frac{1}{\alpha} sinh^{-1} \left[\left(\frac{Z}{A} \right)^{\frac{1}{n}} \right] \tag{4.6}$$

The predicted stress is calculated using the following expression after some algebraic calculations:

$$\sigma = \frac{1}{\alpha} \ln \left\{ \left(\frac{Z}{A} \right)^{\frac{1}{n}} + \sqrt{\left(\frac{Z}{A} \right)^{\frac{2}{n}} + 1} \right\} \tag{4.7}$$

The Arrhenius equation has the advantage to be physics-based by including the activation energy term and therefore is more sensitive to changes in the microstructure. The strain rate during high-temperature deformation is given by (Jabbari Taleghani, Ruiz Navas, Salehi, & Torralba, 2012; McQueen & Ryan, 2002):

$$\dot{\varepsilon} = AF(\sigma)\exp(-\frac{Q}{RT}) \tag{4.8}$$

Where $F(\sigma)$ is in the form of power function:

$$F(\sigma) = \begin{cases} \sigma^{n1} & \alpha\sigma < 0.8 & (4.9) \\ \exp(\beta\sigma) & \alpha\sigma > 1.2 & (4.10) \\ [\sinh(\alpha\sigma)]^n & \text{(for all } \sigma) & (4.11) \end{cases}$$

The constants n_1 and β are the slopes of the curves $\ln\dot{\varepsilon}$ vs. $\ln\sigma$ and $\ln\dot{\varepsilon}$ vs σ, respectively, as indicated in Eqs. (4.12) and (4.13) and illustrated in Figure 4.10.

$$n_1 = \frac{\partial \ln\dot{\varepsilon}}{\partial \ln\sigma} \tag{4.12}$$

$$\beta = \frac{\partial \ln\dot{\varepsilon}}{\partial \sigma} \tag{4.13}$$

α constant is calculated by dividing the Eq. (4.13) in Eq. (4.12):

$$\alpha = \frac{\beta}{n_1} \qquad (4.14)$$

Similarly, the constant n is the slope of the curve $\ln \dot{\varepsilon}$ vs. $\ln[\sinh(\alpha\sigma)]$ as indicated in Eq. (15) and reported in Figure 4.10d:

$$n = \frac{\partial \ln \dot{\varepsilon}}{\partial \ln[\sinh(\alpha\sigma)]} \qquad (4.15)$$

For determining constant A, the activation energy, Q, should be calculated first. For a specific strain rate, the slope of $\ln[\sinh(\alpha\sigma)]$ vs. T^{-1} gives the values of $\frac{Q}{nR}$ by linear regression of each curve. Thus, Q is obtained by substituting R = 8.314 J.mol^{-1}. K^{-1} and calculating n:

$$Q = Rn\frac{\partial \ln[\sinh(\alpha\sigma)]}{\partial\left(\frac{1}{T}\right)} \qquad (4.16)$$
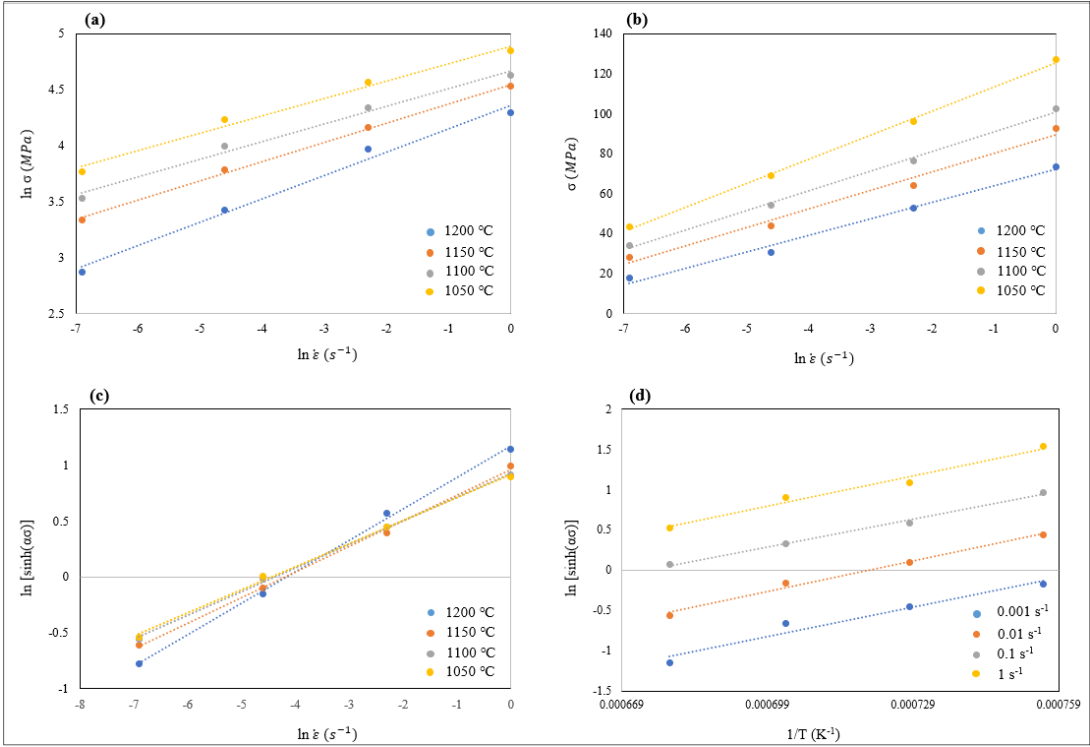
Figure 4.10 Plots for determination of the constants (a) n₁ (b) β (c) n (d) Q at a deformation temperature of 1200 ºC, 11500 ºC, 1100 ºC, and 1050 ºC. The constants represent the slope of the respective curves determined using linear regression

Finally, "A" is the intercept of the curve $\ln Z$ vs. $\ln[\sinh(\alpha\sigma)]$. The constant values are listed in Table 4.5, and the plots used to obtain all constants are shown in Figure 4.10.

Table 4.5 Material constants in the Arrhenius model

β (MPa⁻¹)	n_1	α (MPa⁻¹)	n	Q (KJ.mol⁻¹)	ln A
0.097021	5.3010	0.0181	3.95	412.948	31.463
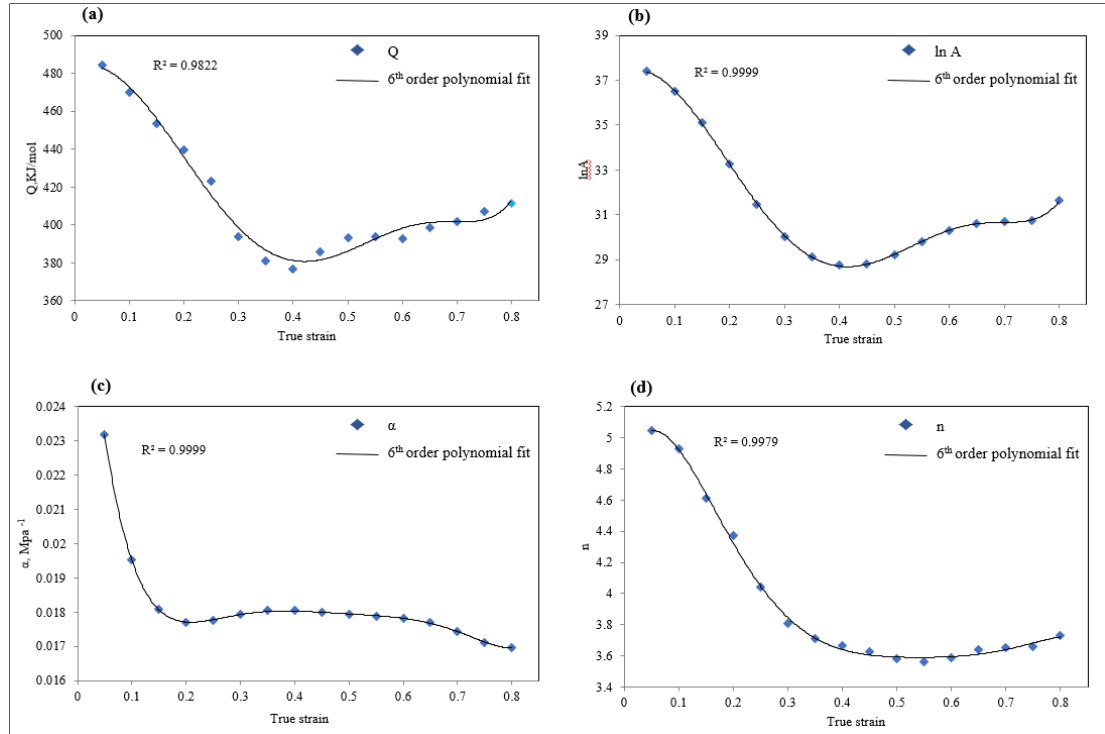
Figure 4.11 The polynomial fit of order 6 of variation of (a) Q (b) ln A (c) α
and (d) n (The blue square denotes experimental data and the black line
denotes polynomial models)

As indicated above, the Arrhenius equation is based on constant strain condition. Moreover, as shown in Figure 4.8, the impact of a strain on the flow stress is significant; thus, it is necessary to take the strain term into account for a more accurate constitutive equation. The evolution of the above material constants with strain could be described through polynomial functions of the strain, as also reported in the literature (Ashtiani & Shahsavari, 2016; Z. Zhou et al., 2017). As illustrated in Figure 4.11, in the present study, it is possible to obtain an accurate fitting of the different constants with the applied strain using a sixth-order polynomial. The sixth-order polynomial fit results are obtained as given in Eq. (4.17):

$$n = 4.776 + 11.181\varepsilon - 140.46\varepsilon^2 + 517.92\varepsilon^3 - 901.73\varepsilon^4 + 766.97\varepsilon^5 - 256.54\varepsilon^6$$

$$\alpha = 0.0307 - 0.2058\varepsilon + 1.2646\varepsilon^2 - 3.8842\varepsilon^3 + 6.3855\varepsilon^4 - 5.3762\varepsilon^5 + 1.8174\varepsilon^6$$

$$Q = 485.31 + 29.685\varepsilon - 1353.9\varepsilon^2 - 4448.6\varepsilon^3 + 29723\varepsilon^4 - 45492\varepsilon^5 + 22050\varepsilon^6$$

$$ln\,A = 37.311 + 11.868\varepsilon - 213.31\varepsilon^2 + 30.281\varepsilon^3 + 1724.8\varepsilon^4 - 3112\varepsilon^5 + 1598.6\varepsilon^6$$

$$(4.17)$$

After developing the models of n, α, Q, and ln A by considering the effect of the strain, the flow stress can be predicted using Eq. (4.7) which relates the stress to the Zener-Hollomon parameter, strain rate, deformation temperature, and the material constants as a function of the strain (Samantaray et al., 2009).

4.3.4   Verification of the Developed Constitutive Equations

The predicted value should be compared with the actual value in order to determine how well-developed constitutive models predict the hot deformation behavior of martensitic stainless steel. As shown in Figure 4.12, a good agreement can be observed between the experimental data and the predicted values for all the experimental conditions used in this work.
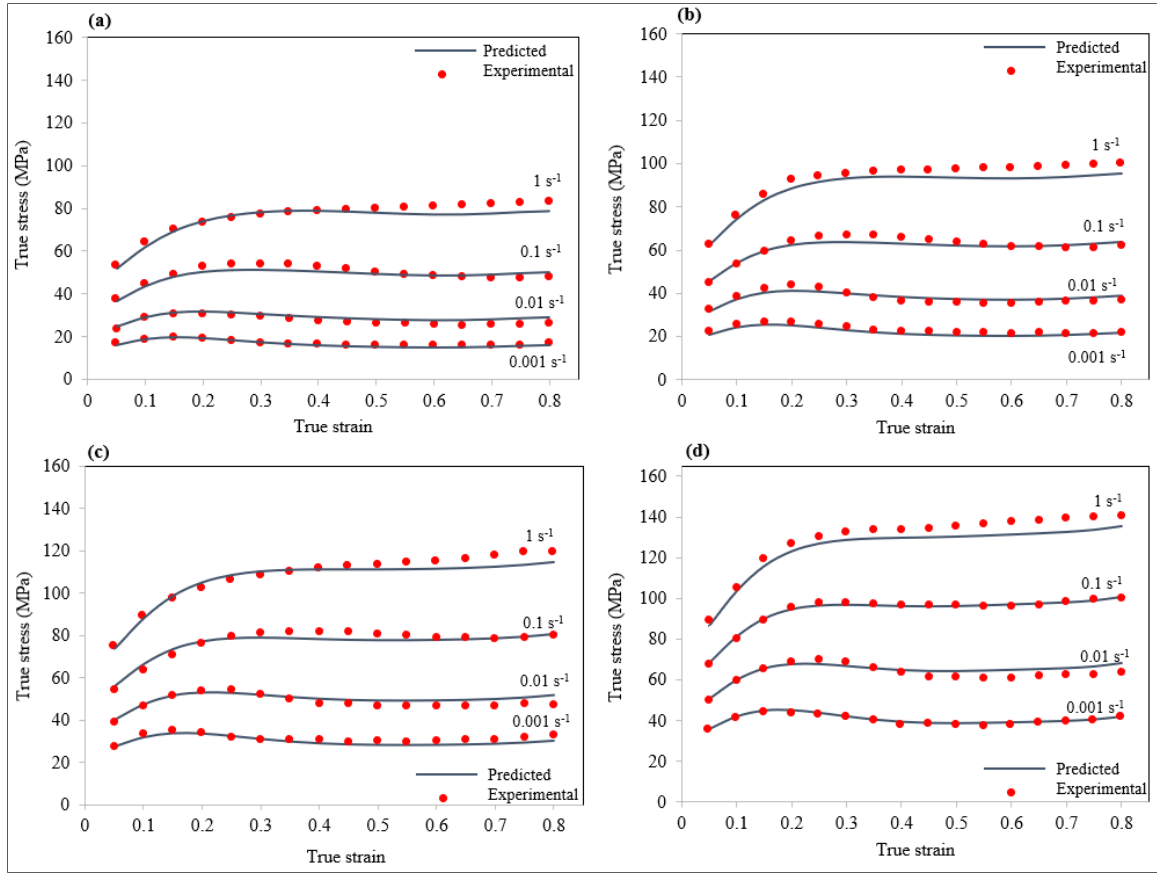
Figure 4.12 Comparisons of the flow stress between the experimental and calculated developed by Arrhenius model at 4 strain rates and 4 temperatures of (a) 1200 °C (b) 1150 °C (c) 1100 °C (d) 1050 °C

The reliability and accuracy of the Arrhenius model were compared in terms of correlation coefficient (R) and the average absolute relative error (ARRE- Δ):

$$R = \frac{\sum_{i=1}^{N}(\sigma_E^i - \bar{\sigma}_E)(\sigma_P^i - \bar{\sigma}_P)}{\sqrt{\sum_{i=1}^{N}(\sigma_E^i - \bar{\sigma}_E)^2 \sum_{i=1}^{N}(\sigma_P^i - \bar{\sigma}_P)^2}} \qquad (4.18)$$

The absolute average error (Δ) is expressed as:

$$\Delta = \frac{1}{N}\sum_{i=1}^{N}\left|\frac{\sigma_E^i - \sigma_P^i}{\sigma_E^i}\right| \times 100 \qquad (4.19)$$

Where σ_E is the experimental data and σ_P is the calculated value based on the proposed constitutive equations. $\overline{\sigma}_P$ and $\overline{\sigma}_E$ are the mean values of σ_P and σ_E, respectively and N is the number of data points. The calculated R coefficient is shown in Figure 4.13, where a good correlation can be observed between the measured and calculated data.

(a) Correlation plot: R=0.9963, AARE=3.29 %. X-axis: Experimental stress values (MPa); Y-axis: Predicted stress values (MPa). Legend: Data point, Linear fit.

(b)

$\dot{\varepsilon}\ (s^{-1})$	Δ (%)			
	1200 °C	1150 °C	1100 °C	1050 °C
0.001	3.06	4.6	4.54	2.03
0.01	5.04	4.2	4.13	3.73
0.1	3.15	1.36	2.32	0.81
1	2.68	3.36	1.37	3.25
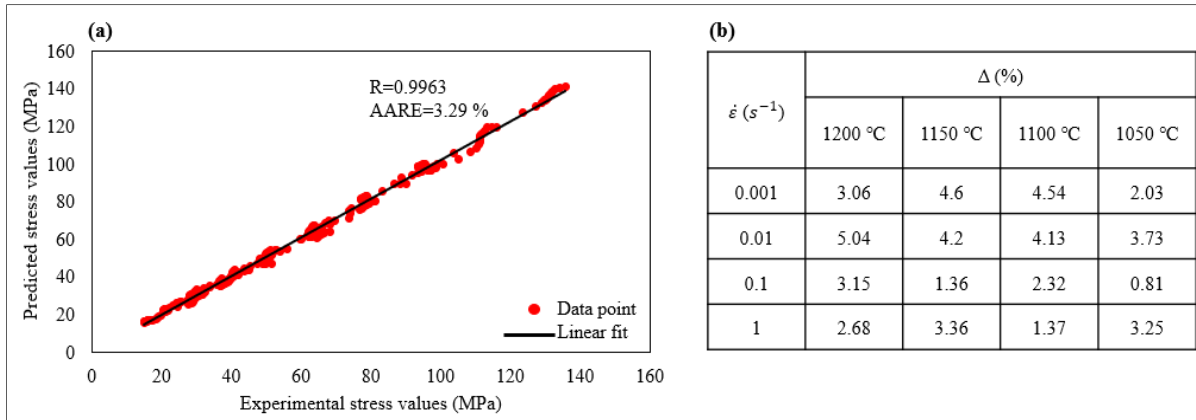
Figure 4.13 (a) Correlation between the experimental and calculated flow stresses by the developed constitutive equation (b) Value of Δ at different temperatures and strain rates

It should be noted that the R coefficient value represents how strongly the predicted and experimental values are related linearly. However, because the model is frequently biased towards higher or lower values, a higher R-value is not always a sign of the model's greater accuracy. Therefore, an unbiased statistical parameter, Δ, is used to evaluate the accuracy of the Arrhenius model in prediction (Sanrutsadakorn et al., 2012). The lower is the absolute average error, the higher is the predictability of the model. The values of Δ at different temperatures and strain rates are listed in Figure 4.13b. It can be seen that the maximum value is 5.04 % at the strain rate of 0.01 s^{-1} and the deformation temperature of 1200 °C. The minimum value is 0.81% at the strain rate of 0.1 s^{-1} and the deformation temperature of 1050 °C and the mean value of Δ for all the deformation conditions is 3.29% which is a very small error. As a result, the established constitutive equations are capable of well-describing flow stress, strain rate, temperature, and strain. However, the developed constitutive equation should be implemented in Forge NxT 3.0® software in order to predict temperature, strain, and strain rate maps in different locations of the specimen and then validate the predictions through microstructure examination.

4.3.5 Microstructure-Based FEM Simulation

A specific user subroutine was developed to implement the constitutive equation in the FE code. For the analysis, the three-dimensional finite element method was performed to simulate the hot compression process. The boundary conditions for the FE simulations were similar to the experimental tests (i.e., temperature, strain rate, strain, and thermal exchange between piece and anvils). The friction factor was selected as 0.35 and the convergence tests were performed by changing the element size to ensure accuracy. The numerical simulations were performed on a FEM model discretized with four-node tetrahedral elements. Figure 4.14a and 4.14b show the meshed finite element models before and after deformation respectively and Figure 4.14c shows a comparison between the predicted and experimental data of force versus time where good and acceptable predictability of the model is demonstrated.

According to simulation results, the strain distribution can be illustrated as a contour plot aided by color series at the temperature of 1050 ºC-1200 ºC, shown in Figure 4.15 (a-d). In this Figure, the non-uniformity of deformation distribution is seen. The specimen is roughly divided into several deformation zones (non-uniformity) according to the severity of deformation, which leads to different flows of material during hot deformation and different microstructure evolution. Figure 4.16 shows the microstructure evolution during an upset operation at 1200 ºC and a strain rate of 0.1 s^{-1}. The specimen was cut parallel to the compression axis by a precision cutter machine for carrying out a metallographic examination. The numbers in Figure 4.16a, represent strain levels that the material experienced during hot deformation, based on the map of strain distribution, and the yellow dotted lines show the dead zones. In Figure 4.16 (b-e), the microstructure of the corresponding four zones is shown.
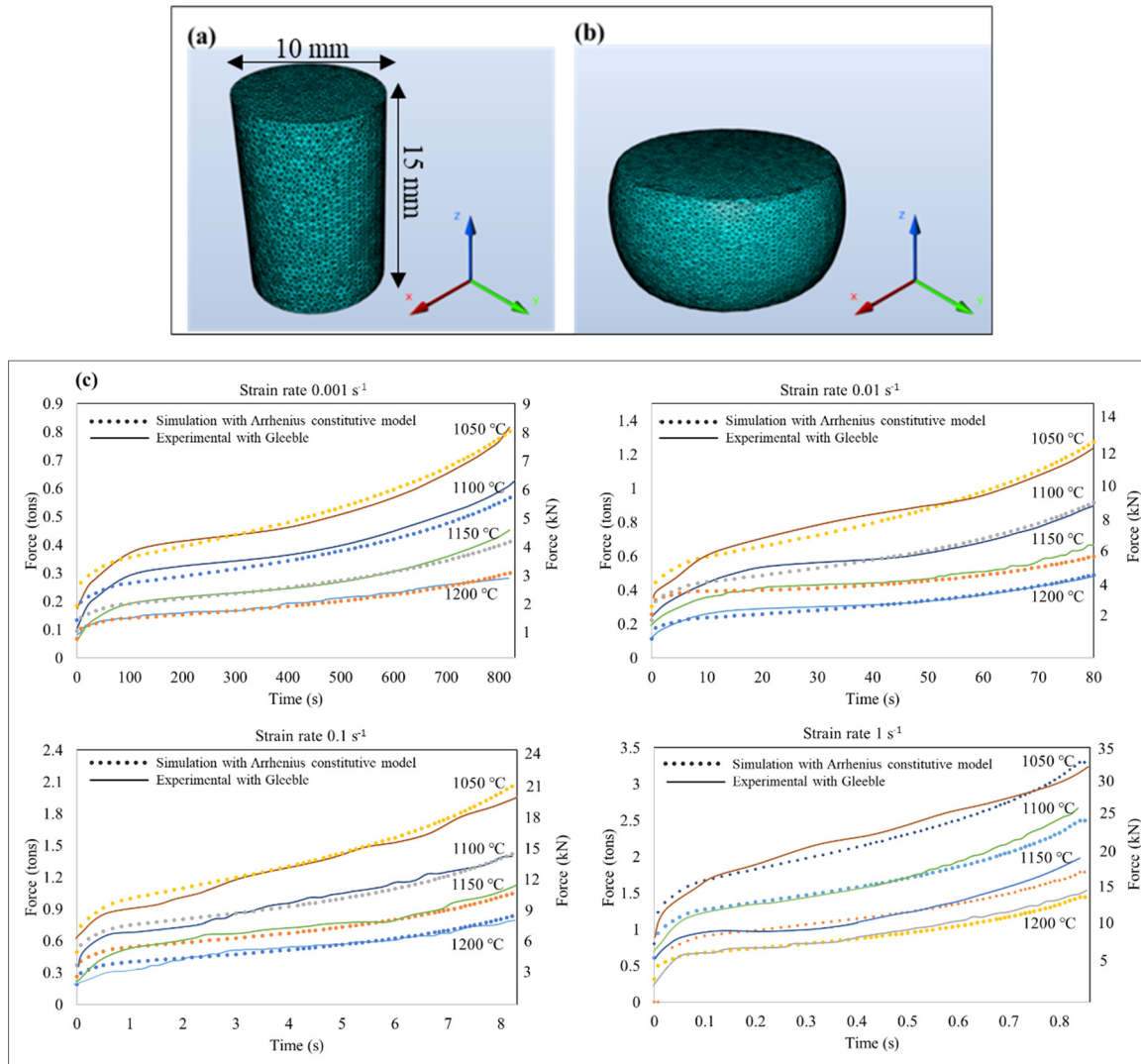
Figure 4.14 FE model (a) before deformation (b) FE model after deformation (c) Force versus time plot of experimental and predicted for all deformation conditions
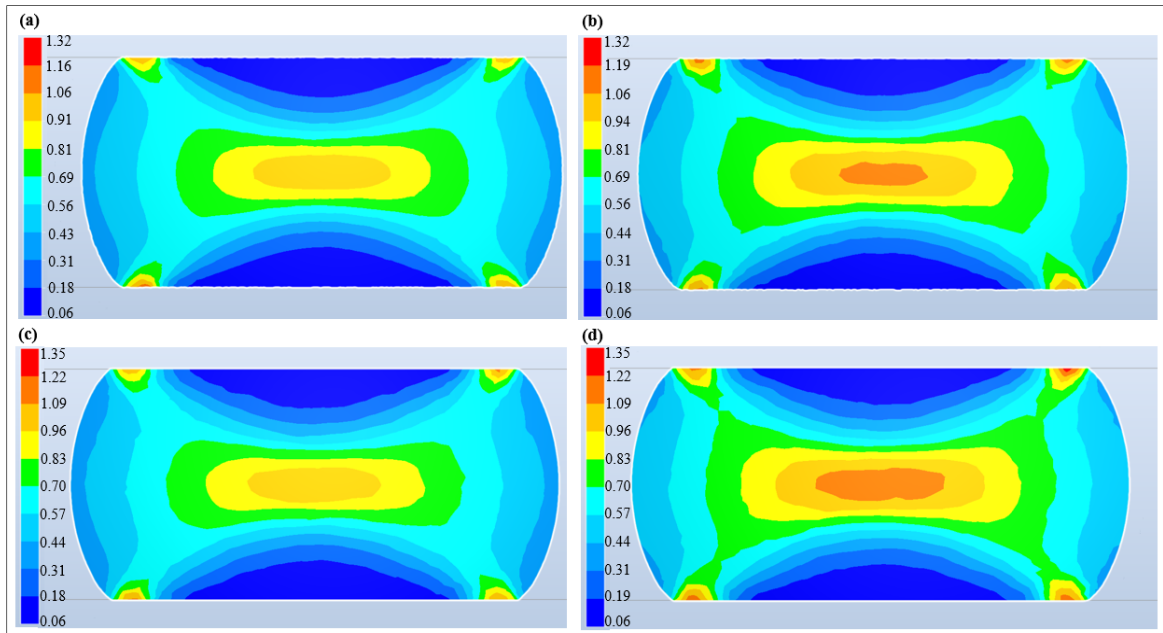
Figure 4.15 FE results of effective strain distribution in the sample deformed to a strain of 0.8 and a strain rate of 0.1 s⁻¹ (a) 1200 ºC (b) 1150 ºC (c) 1100 ºC and (d) 1050 ºC
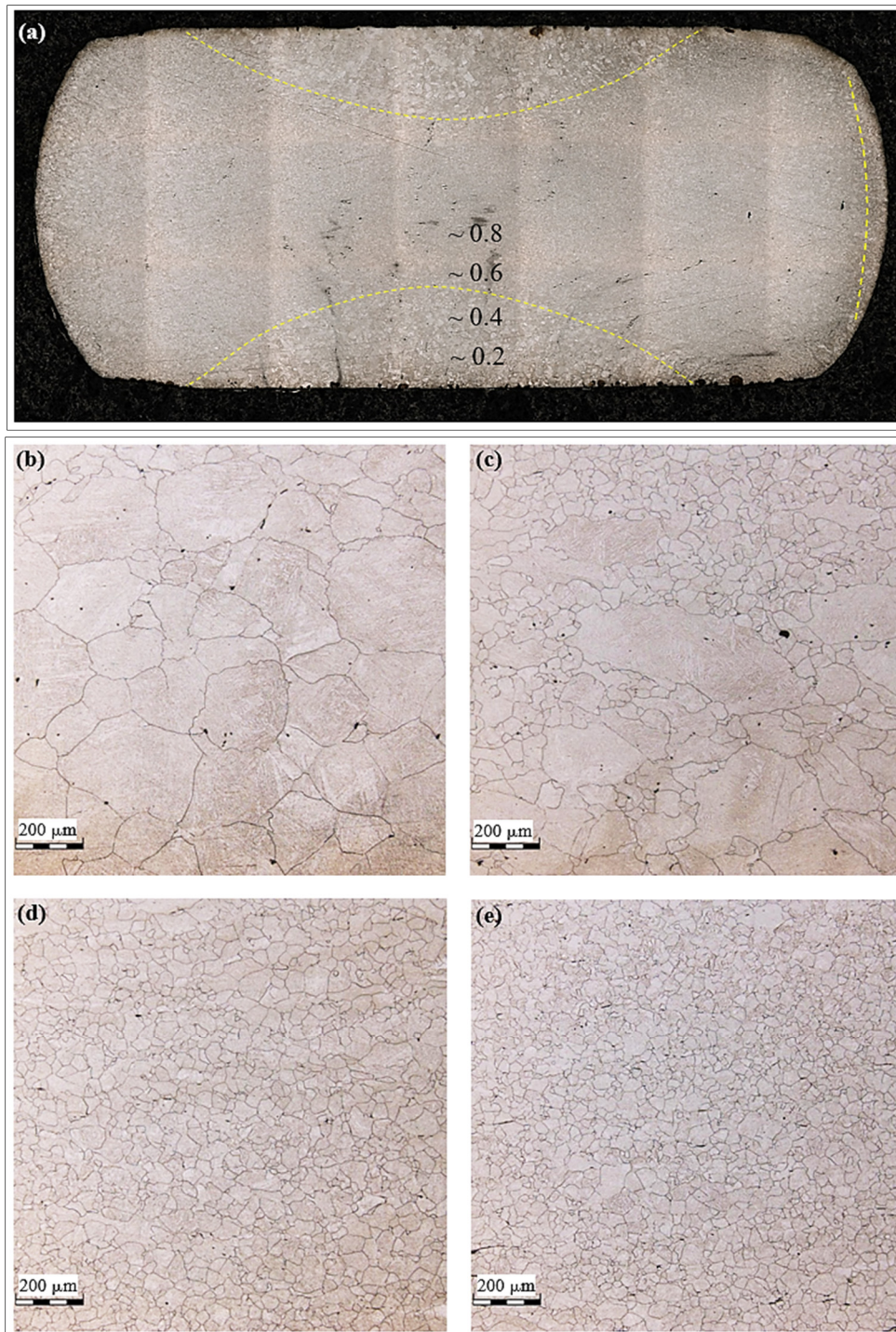
Figure 4.16 (a) Optical microscope views of deformed samples in 1200 ºC
and a strain rate of 0.1 s^{-1} to strains of (b) 0.2 (c) 0.4 (d) 0.6 (e) 0.8

As shown in Figure 4.16b, for material regions that experienced a strain of 0.2, the microstructure remained unchanged due to a low degree of deformation. By increasing strain, Figure 4.16c, the nucleation of new grains around the initial grain boundaries can be seen indicating that the workability of the material increased through recrystallization. The microstructure at a strain of 0.4 is heterogeneous with a mix of deformed and undeformed grains which makes the material susceptible to the occurrence of defects and wedge cracking; thereby, deteriorating the mechanical properties. However, the material is fully recrystallized at the strain of 0.6 and 0.8, as shown in Figure 4.16d and 4.16e, respectively.

4.3.6   Processing Map

The part with fewer defects in the final production process signifies the ideal processing conditions and higher workability of metal, which means the higher plastic deformation ability that a metal can be deformed easily without fracture during the forming process. In 1997, Prasad and colleagues proposed the Deformation Mechanism Model (DMM) which produces the flow instability domains (Yeom et al., 2007). This model is an analytical method used to determine optimum deformation temperature and strain rate ranges in hot forming operations. Based on the DMM, the workpiece undergoing hot deformation goes through a process of power dissipation (P), defined by Eq. (4.19). The total input power is dissipated through plastic work that is converted into heat (G), and changes in the microstructure (J), such as flow localization, DRV, DRX, phase transition, and shear band formation (Rao, Prasad, & Suresh, 2011).

$$P = G + J = \int_0^{\dot{\varepsilon}} \sigma d\dot{\varepsilon} + \int_0^{\sigma} \dot{\varepsilon} d\sigma = \sigma \dot{\varepsilon} \qquad (4.20)$$

The flow stress, at constant strain and deformation temperature, is given by (Prasad et al., 2015):

$$\sigma = K\dot{\varepsilon}^m \qquad (4.21)$$

Where K is a material constant, m is the strain rate sensitivity and can be represented as follows:

$$m = \frac{\partial(\ln\sigma)}{\partial(\ln\dot{\varepsilon})} \qquad (4.22)$$

Power dissipation efficiency, η, is defined as the ratio of J co-content to the maximum possible power dissipation (J_{max}). This parameter is important for determining the extent of power dissipation due to microstructural changes during hot deformation and it is written as follows:

$$\eta = \frac{J}{J_{max}} = \frac{2m}{m+1} \qquad (4.23)$$

η represents the ability of the workpiece to change its microstructure upon deformation. A power dissipation map is created by plotting the contours of η as a function of temperature and strain rate. By plotting contours of η as a function of temperature and strain rate, a power dissipation map is obtained. Softening mechanisms such as DRX and DRV are associated with η. The power dissipation map, however, is insufficient to completely define the hot working behavior of an alloy in the cases of void formation or wedge cracking. Identifying the unwanted sections marked by the unstable flow is crucial for doing this, and in particular for optimizing the processing settings. In order to locate these areas and create an instability map that can be placed over the iso efficiency contours to produce the final processing map, the instability criteria are specified. Instability maps are developed based on Ziegler's plasticity theory to the dissipation functions of the dynamic materials model. A dimensionless parameter for microstructural instability based on Kumar-Prasad and Murty-Rao criteria, (W. J. Kim & Jeong, 2020), respectively is given by:

$$\xi(\dot{\varepsilon}) = \frac{\partial \ln\left(\frac{m}{m+1}\right)}{\partial \ln\dot{\varepsilon}} + m < 0 \qquad (4.24)$$

According to Sneddon et al. (Sneddon, Hill, & Jahsman, 1965) regions with negative ξ values are more likely to experience mixed microstructure, flow localization, or adiabatic shear bands.

The 2-D Processing Maps at Various Strains:

By superimposing the power dissipation and flow instability 2D contour maps at a specific strain, 2D processing maps could be created. Figure 4.17 shows the 2D processing maps of the X12Cr13 investigated steel at various strains with an interval of 0.2. The Figure shows that as strain is increased, maximum power efficiency rises while the flow instability area first rises up to 0.4 strain before decreasing. In addition, the flow instability happened at the maximum strain rate ($\dot{\varepsilon} = 0.182$ s^{-1} – 1 s^{-1}). The occurrence of such flow instability could be related to the limited time for dislocation movement due to the high strain rate and the subsequent inhibition of softening processes such as DRV and DRX. According to Momeni et al. (Momeni & Dehghani, 2010b), these circumstances could limit strain accumulation to particular areas and favor the development of wedge cracks, voids, and shear bands. Therefore, hot working parameters should be selected carefully to avoid regions with a negative value for the flow instability parameter which corresponds to the gray-shaded region in Figure 4.17.
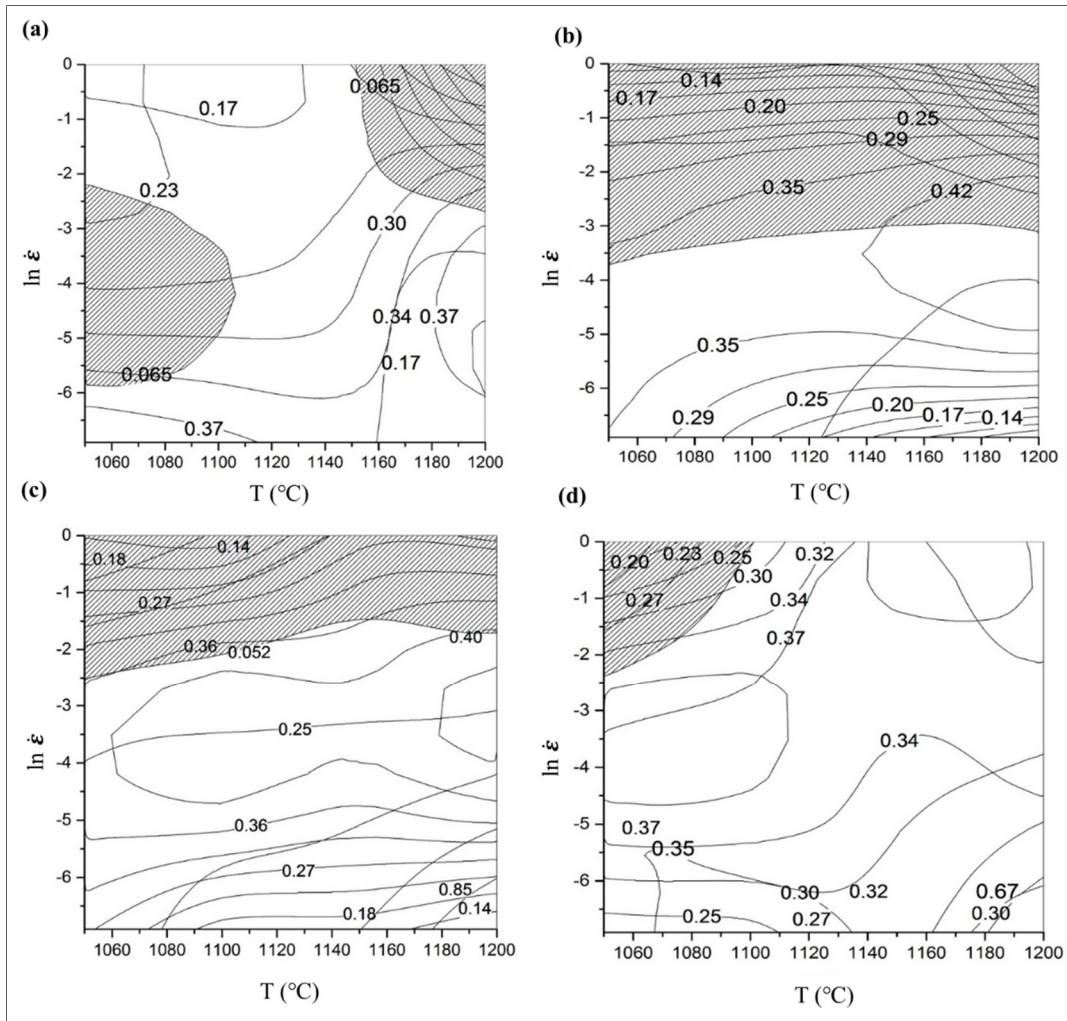
Figure 4.17 The 2D processing map at various strains: (a) 0.2 (b) 0.4 (c) 0.6 (d) 0.8

Continuous 3D Processing Maps:

In the power dissipation maps of Figure 4.17, the color of the grid is related to the value of the power dissipation efficiency parameter η. As shown in Figure 4.18, η value increases by increasing strain and temperature. This means that higher η leads to higher workability and increased potential for microstructural changes. As mentioned above, the deformation should be carried out in the region with the highest η-value because significant microstructural evolution via DRX occurs in this region.
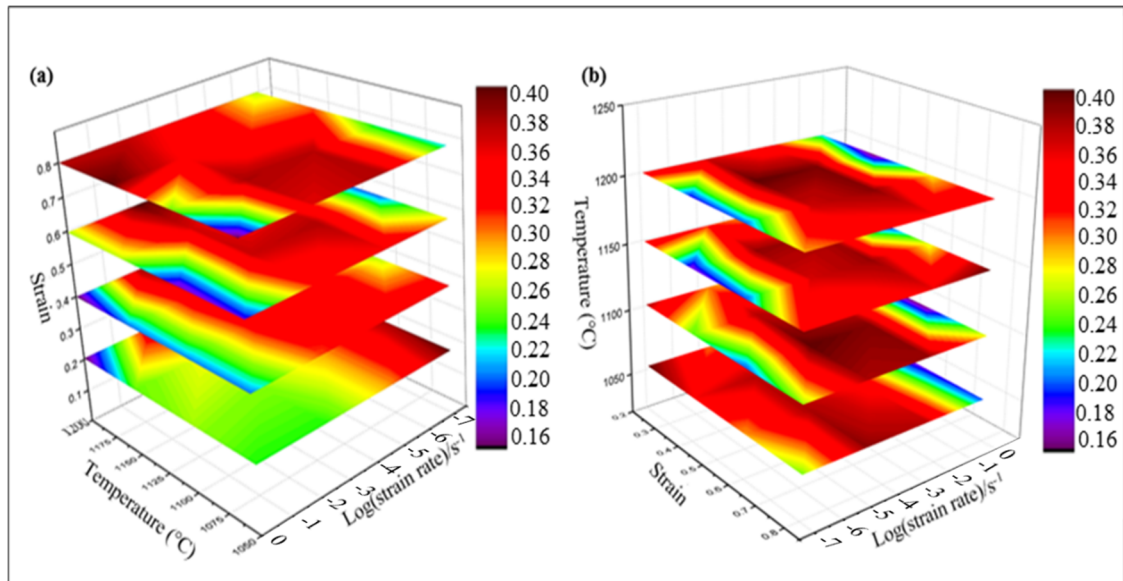
Figure 4.18 The 3D power efficiency map as a function of (a) Strain (b) Temperature

The processing map has been used to identify unstable and risky situations through the determination of two factors: power dissipation and flow instability domains. The results obtained in the present investigation show a good agreement between the DMM results and those obtained with FEM simulation and microstructure observations. These results are interesting as it is the first time such a comparison is made between the predictions of the two methods and supported by experimental evidence. Specifically, the non-uniformity of strain distribution during the deformation, predicted by the FEM analysis, was confirmed by microstructure examination, as reported in Figure 4.16. The processing map analysis shows that regions that experienced a lower strain have negative instability values and low power efficiency which means that they have low workability. In Figure 4.16c, the microstructure at a strain of 0.4 is heterogeneous and is expected to have inconsistent mechanical properties. This finding agrees with the negative instability criteria reported in Figure 4.17b. On the other hand, as reported in Figure 4.16d and Figure 4.16e, the material is fully recrystallized at the strains of 0.6 and 0.8, respectively. The DMM analysis also showed that under these conditions, the instability criteria have a positive value (not gray-shaded regions) which means higher workability as shown in Figures 4.17d.

4.4   Conclusions

The hot workability of MSS was studied using microstructure-based numerical simulation. The following conclusions can be drawn from this chapter:

1. The flow stress curves of the compressed X12Cr13 steels in the range of 1050 ºC -1200 ºC and the strain rate range of 0.001-1 s^{-1} display a significant sensitivity of flow stress to strain rate, temperature, and strain.

2. A constitutive equation based on the Arrhenius model was developed in the present work and its validity was confirmed showing a more accurate prediction than the Hansel-Spittel model.

3. The developed constitutive model was integrated into the Forge NxT 3.0® software and showed good correlations with the predictions of flow instability domains obtained using the Dynamic Material Model.

Using the results of chapter 4, the following chapter has accomplished the next objective of this project. In CHAPTER 5, the developed models (microstructure and constitutive) were employed to simulate the large-scale forging process and the effect of forging parameters on the microstructure evolution are discussed.

CHAPTER 5

NUMERICAL SIMULATION AND EXPERIMENTAL VALIDATION OF MICROSTRUCTURE EVOLUTION DURING THE UPSETTING PROCESS OF A LARGE SIZE MARTENSITIC STAINLESS STEEL

S. Dourandish [a], M. Jahazi [a], J-B. Morin [b], A. Loucif [b]

[a] Department of Mechanical Engineering, École de Technologie Supériere,
1100 Notre-Dame West, Montreal, Quebec, Canada H3C 1K3
[b] Finkl Steel-Sorel Inc., 100 McCarthy, Saint-Joseph-de-Sorel, Québec, Canada J3R 3M8

Summary

This chapter addresses the microstructure evolution, plastic deformation, and damage sensitivity (cracking possibility) during the hot forging of martensitic stainless steel using experimental and simulation analysis. For simulating the forging process of the large size ingot, the elasto-viscoplastic model was coupled with the semi-empirical model, JMAK, in the FORGE NxT® 3.1 finite element code. The effect of forging parameters on microstructure evolution was investigated by analyzing the simulation results. It was then possible to determine the volume fraction and size distribution of the dynamically recrystallized grains at the end of the upsetting process and therefore select the optimum post upsetting process parameters in order to obtain the optimum microstructure at the end of forging. Sensitivity to damage during hot forging is investigated based on the Cockcroft & Latham model with the aid of FE calculation. The good agreement obtained between the predicted and experimental results indicates that the implemented dynamic recrystallization model provides a realistic representation of microstructural evolution during the hot upsetting process of the investigated martensitic stainless steel.

5.1 Literature Review

Heavy parts and components made of highly alloyed steels used in, aerospace, automotive, defense, and oil and gas industries are produced by ingot casting (C. Zhang et al., 2018). However, during the solidification of large size ingots, defects such as macrosegregation, porosity, and mixed morphology of the grains lead to anisotropic performance (Chadha et al., 2017; Y. Kim, Cho, & Bae, 2011; C. Zhang et al., 2022). Therefore, the ingots are subjected to a hot forging process to ensure a healthy internal structure, reduce porosities, and break down their as-cast microstructure. The forging equipment used and the selection of the process parameters have a major impact on the quality of the forged products (Z. Wang, Xue, & Zhao, 2018). Changes in thermomechanical parameters (strain, strain rate, and temperature) could lead to different metallurgical phenomena resulting in various types of microstructures that directly affect the mechanical properties (Jang et al., 2000). Dynamic recrystallization (DRX), dynamic recovery (DRV), and static recrystallization (SRX) are the main microstructure development processes affecting the grain size distribution of the final forging in metals with medium to low stacking fault energy (Ebrahimi, Momeni, & Ezatpour, 2018). The above processes as well as other microstructural changes (e.g., precipitation, phase transformation, etc.) are highly dependent on the selection of the thermomechanical parameters (Ding, Hirai, Homma, & Kamado, 2010). Therefore, in order to achieve the desired mechanical properties, all over the volume of the forgings, the impact of the process parameters needs to be quantified in each location of the ingot. The latter becomes a major challenge when it comes to the forging of very large size components made of newly developed alloys (Bontcheva & Petzov, 2003). Performing large-scale experimental trials is both difficult and highly cost intensive. For this, extensive laboratory-scale investigations have been carried out to develop numerical models for predicting microstructure evolution during hot forging (Bontcheva & Petzov, 2003). As a pioneer, Sellars et al. (Sellars & Whiteman, 1979) modeled the complex recrystallization process mathematically with a set of phenomenological models which related important metallurgical variables to the Zener-Hollomon parameter, time, temperature, and grain size. Poliak and Jonas developed a model to predict the critical strain for the initiation of

recrystallization, with the assumption that DRX is accompanied by flow localization (Poliak & Jonas, 1996).

In recent years, numerical simulation has proved to be an effective way to analyze the deformation behavior and microstructure development process during the hot deformation process (Cho, Jeong, Cha, Bae, & Lee, 2005; Jiang, Wang, Lu, & Li, 2007; Na, Yeom, Park, & Lee, 2003). Chen et al. (F. Chen et al., 2016a) simulated the upsetting process of X20Cr13 steel on laboratory scale samples with a diameter of 10 mm and a height of 15 mm and used the finite element method (FEM) to predict the microstructure evolution during the hot forging process. The authors reported that the DRX volume fraction and grain size are non-uniformly distributed after forming process and this heterogeneity increases as the complexity of the product shape increases. They also reported that strain (degree of deformation) plays a key role in the distribution of DRX volume fraction and average grain size during the upsetting process (F. Chen et al., 2016a). Jang et al. (Jang et al., 2000) simulated the deformation behavior and microstructure evolution during the hot forging of a C-Mn steel on laboratory scale samples by coupling a rigid-thermoviscoplastic and a recrystallization model and validated their simulation results by experiments. Lin et al. (Y. C. Lin, Chen, & Zhong, 2008) simulated the hot upsetting process of a 42CrMo steel concluded that the microstructure evolved unevenly at the end of the upsetting and that the strain rate and the deformation temperature are the critical factors for the evolution of the microstructure. They also found that the maximum deformation degree occurred at the center of the cylindrical sample and the material was fully recrystallized at this location. Katajarinne et al. (Katajarinne, Somani, Karjalainen, & Porter, 2004) investigated non-uniform microstructural evolution during hot deformation of a Nb-Ti microallyed steel. They concluded that a heterogeneous final microstructure has a negative effect on mechanical properties, especially impact toughness. Santana de Oliveira et al. (De Oliveira et al., 2017) discussed the softening mechanisms of AISI 410 under hot torsion simulation and calculated the DRX fraction using the Avrami equation. They concluded that the onset of DRX was delayed by decreasing the temperature and increasing the strain rate and therefore in locations where such conditions prevailed heterogeneous microstructural development took place.

On the other hand, one major challenge facing forming industries is the phenomenon of ductile fracture, which occurs during metal forming operations such as forging, rolling, and extrusion (Kukuryk, 2021). In heavy parts production, the presence of temperature, strain, and strain rate gradients from the surface to the center of the part could result in the formation of heterogeneous grain size distribution. If the size difference between adjacent grains becomes very large then the formability decreases and there is even a risk of crack formation at the interface (Ruijie et al., 2022). Using the FEM, Pasoodeh et al. (Pasoodeh, Alimirzaloo, & Tagimalek, 2021) investigated the parameters that promote deformation non-uniformity and crack initiation during the upsetting process of AISI-1045 steel with 25 mm diameter and 40 mm length samples. They reported that friction between the surface of the billet and press tool, the tri-lateral compressive stress and strain, and the various heat radiation are all factors influencing strain non-uniformity distribution, leading to the appearance of inner and surface crack initiation in the forged part. Kakimoto et al. (Kakimoto & Arikawa, 2014) also reported that strain concentration, steel grade, type of press, draft schedule, forging temperature, anvil shape, and the properties of the steel ingot surface are also other factors that could induce surface cracking. Some researchers have also reported that a partially recrystallized microstructure influences the strength of the grain and can cause the nucleation of voids, their coalescence, and further evolution into microcracks, which get coarser, and eventually result in fractures (Pasoodeh et al., 2021; Wen et al., 2019; Y. Zhang et al., 2021).

To quantitatively predict the ductile fracture condition and the region facing the greatest risk of cracking, different fracture models have been developed by researchers, including Cockcroft-Latham (Cockcroft & Latham, 1968), Oyane (Oyane et al., 1980), Brozzo (Brozzo, 1972), Clift (Clift, Hartley, Sturgess, & Rowe, 1990), and Freudenthal (Freudenthal, 1950). According to the damage criteria, cracks should be anticipated when the cumulative damage reaches and exceeds the associated critical damage value. Among the fracture models, Cockcroft-Latham and Brozzo are the most used in hot forging applications. These models have the advantage of being applicable in the multi-axial conditions of stress in forging (Q. Ma, Lin, & Yu, 2009). Kakimoto et al. used the Cockcroft-Latham criterion to predict surface cracking in hot forging using numerical simulation. They found that the maximum cracking

risk belongs to the surface of the forged part where the tensile stresses generated during the axial deformation of the part are at their maximum and could result in surface cracks (Kakimoto & Arikawa, 2014).

The above literature review demonstrates that strong correlations exist between the hot forging parameters, microstructure evolution, and susceptibility to cracking; however, no comprehensive research has been conducted to analyze these changes for large-size parts, either experimentally or numerically. In particular, no such work has been reported for large-size forged ingots of martensitic stainless steels (MSS) that are used for critical components in the energy and transportation industries.

The present chapter aims to fill this gap and focuses on the application of constitutive models of a martensitic stainless steel developed in chapter 4 and employed for the simulation of hot forging of a large size industrial scale ingot. Specifically, the effects of thermomechanical parameters on microstructure evolution and grain size during the upsetting step, where the most significant microstructural changes take place, are considered by coupling the physics-based microstructural model to a visco-elastoplastic mechanical model. The models were then implemented into the FEM code Forge NxT 3.1® through the development of an original user subroutine (UMAT) forming simulation software. Variations in temperature, stress, effective strain, damage, DRX fraction, and DRX grain size were thus predicted. Furthermore, the simulation results were validated by comparisons with experimental results.

5.2   Materials and Methods

Finkl Steel, Sorel, Quebec, Canada provided the materials used in this investigation. The chemical composition of the alloy X12Cr13 is shown Table 5.1.

Table 5.1 Chemical composition of the X12Cr13 (wt.%)

C	Mn	Cr	Si	P	Mo	Cu	Ni
0.14	1.03	11.71	0.25	0.02	0.19	0.15	0.48

Hot compression tests were conducted on cylindrical samples measuring 10 mm and 15 mm in diameter and height, respectively, and by using a Gleeble-3800 thermomechanical simulator machine. The samples were prepared from industrial-size ingots. All thermomechanical processing parameters were selected according to the industrial forging process. Specifically, a temperature range of 1050-1200 °C at an interval of 50 °C and a strain rate of 0.001-1 s^{-1} were used. After the tests, the experimental data were used to develop the constitutive material model to predict flow stress and were used at the simulation stage. The predicted material model was compared with the data corresponding to experimental results to ensure the accuracy and validity of the model, Chapter 4. The samples were cut in parallel to the compression axis by a precision cutter machine for metallographic examination. The specimens were etched with a Vilella solution composed of 1g of picric acid, $(O_2N)_3C_6H_2OH$, 5 ml of hydrochloric acid, HCL and 100 ml of ethyl alcohol, C_2H_5OH for approximately 25 s. The microscopic images were obtained using an Olympus LEXT OLS4100 laser confocal microscope. The Microstructural Image Processing (MIP4) software (http://en.metsoft.ir) was used to determine the grain size before and after deformation.

5.2.1   Material Flow Analysis

The Hansel-Spittel constitutive model was implemented into the simulation software, but after the predicted flow stress and the stress measured from the experimental tests were compared, it was concluded that the model could not accurately predict the softening behavior of the studied alloy for all deformation conditions, Chapter 4. Therefore, another constitutive model was employed to accurately predict the material flow behavior of the investigated steel. The Arrhenius-type equation proposed by Sellars and McTegart is a strain-dependent relationship that relates the strain rate, temperature, and activation energy through the following equation (Sellars & McTegart, 1966):

$$\sigma = \frac{1}{\alpha}\ln\left\{\left(\frac{Z}{A}\right)^{\frac{1}{n}} + \sqrt{\left(\frac{Z}{A}\right)^{\frac{2}{n}} + 1}\right\} \qquad (5.1)$$

And Z is:

$$Z = \dot{\varepsilon}\exp\left(\frac{Q}{RT}\right) = A[\sinh(\alpha\sigma)]^n \tag{5.2}$$

where Z is the Zener-Hollomon parameter, Q is the activation energy required to overcome deformation barriers, A, α, and n are material constants, R is the universal gas constant, T is the temperature, $\dot{\varepsilon}$ is the strain rate, and σ is the applied stress. Softening processes such as DRX and DRV occur during hot metalworking operations like hot rolling, extrusion, and forging. For materials with low or medium SFE such as stainless steel, DRX is the dominant softening process that takes place when a critical deformation, ε_c, is reached (Jin et al., 2015). The DRX fraction during deformation can be calculated by relating the strain, strain rate, deformation temperature, and initial grain size. The equations in this context are based on the JMAK model (Hallberg, 2011):

$$X = 1 - e^{-b.t^n} \tag{5.3}$$

where b and n are the Avrami coefficients. This equation was coded with a FORTRAN 90 user subroutine into the Forge NxT software. The constants of the equation in Table 5.2 were calculated based on the Gleeble-3800 test results and metallographic analysis. Figure 5.1 shows the procedure of the numerical analysis for microstructural evolution prediction.

Table 5.2 Equations describing the microstructure evolution
Taken from Sellars & Whiteman (1979)

Parameters	Equation
Critical strain	$\varepsilon_c = 0.626 \times d_0^{0.576} \dot{\varepsilon}^{-0.058} \exp(\dfrac{50344}{R.T})$
Zener-Hollomon	$z = \dot{\varepsilon} \exp(\dfrac{430258}{RT})$
Dynamic recrystallization fraction	$X_{drx} = 1 - \exp(-0.693\left(\dfrac{\varepsilon - \varepsilon_c}{\varepsilon_{0.5}}\right)^2)$
50% recrystallization	$\varepsilon_{0.5} = 5.05 \times 10^{-3} d_0^{0.47} \dot{\varepsilon}^{0.12} \exp(\dfrac{26128}{R.T})$
Recrystallized grain size	$D_{drx} = 30500 \dot{\varepsilon}^{0.242} \exp(\dfrac{-78572}{RT}).X_{drx}^{0.191}$
Flow stress (Arrhenius model)	$\sigma = \dfrac{1}{\alpha} sinh^{-1}\left[\left(\dfrac{z}{A}\right)^{\frac{1}{n}}\right]$
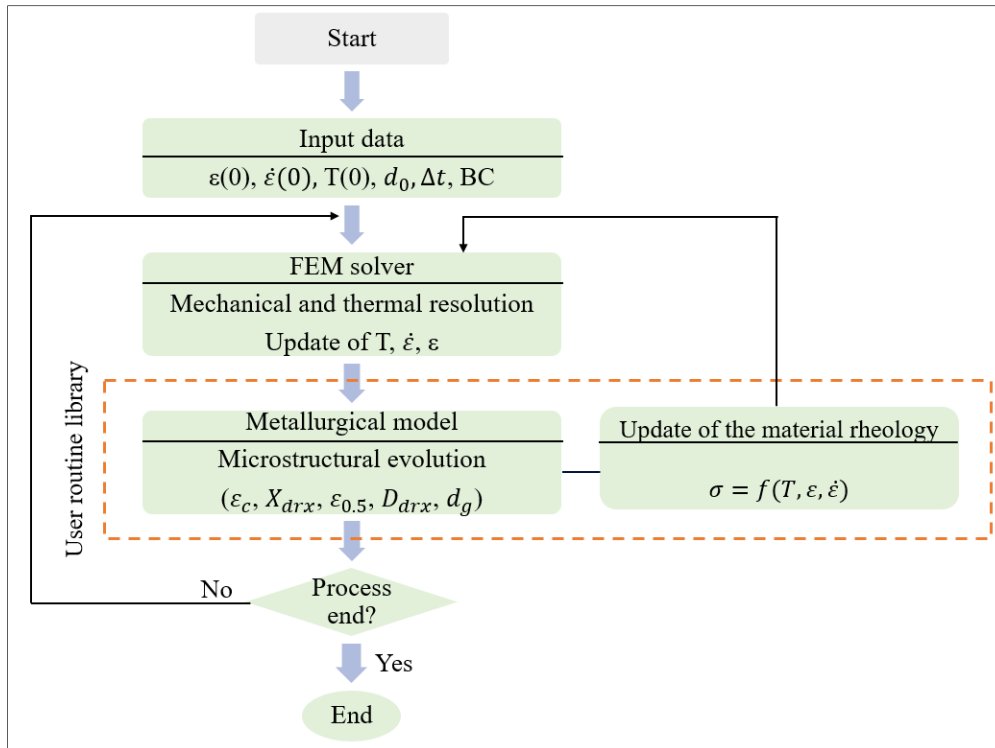
Figure 5.1 Numerical analysis procedure to predict the
microstructural evolution using FORGE NxT software

5.2.2 Boundary Conditions for Simulation

Simulation parameters such as the forging temperature, die velocity, and deformation degree were calculated and measured according to the real industrial forge schedule. The amount of deformation and die velocity were recorded by Finkl Steel's equipment during the open-die forging, as shown in Figure 5.2a. The open die forging process, upsetting, was done using a 5000-ton press capacity (Figure 5.2b). The temperature was measured by a high-performance thermal imager, ThermoView® pi20, and the setup of the camera and the image captured are shown in Figure 5.2c.

Figure 5.3a shows the as-cast ingot after solidification, which is ready to be transferred to the forging furnace and heat up to forging temperature and hold for several hours for homogenization of the chemical composition and to reduce the segregation that occurs during the casting process. During the upsetting, the height of the billet is reduced by the hydraulic press.

The complete meshed CAD model is shown in Figure 5.3b. Due to symmetric conditions, as shown in Figure 5.3b, a quarter of the 42" ingot was modeled and used for the simulation step (Figure 5.3c). In Forge NxT software, an efficient tool to trace down the evolution of deformation is 'sensor' which can only be inserted on deformable objects. The sensors can be installed on the surface of the objects or inside objects. Six sensors were installed as shown in Figure 5.3c to track the results. The 3D linear tetrahedral mesh was selected with volumetric elements, with a fine mesh size to provide high convergence. Table 5.3 shows the boundary conditions used for the upsetting simulation.
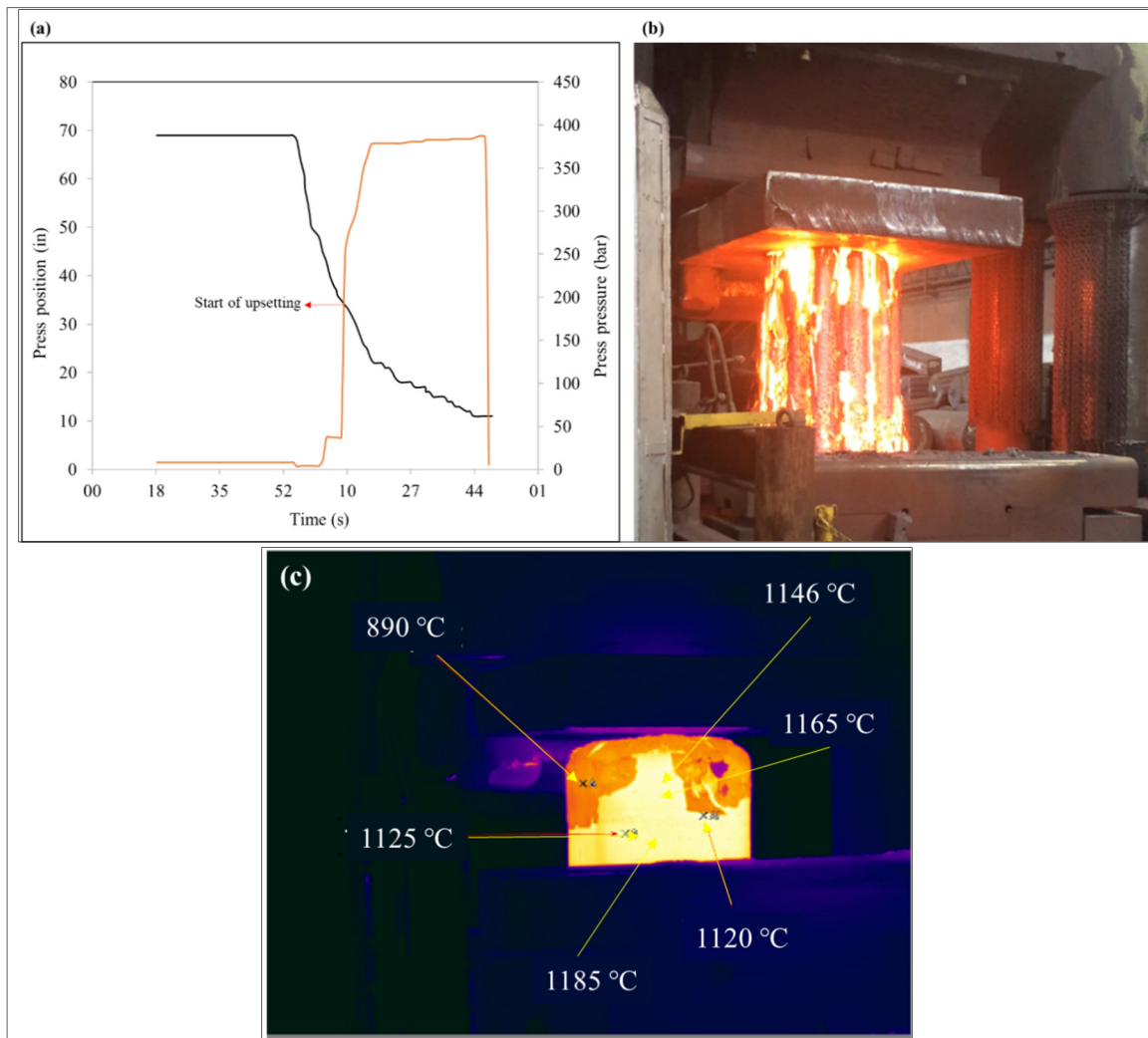
Figure 5.2 (a) 5000-ton press data for measuring the simulation parameters (b) 5000-ton hydraulic press and thermal camera (c) images taken by the thermal camera
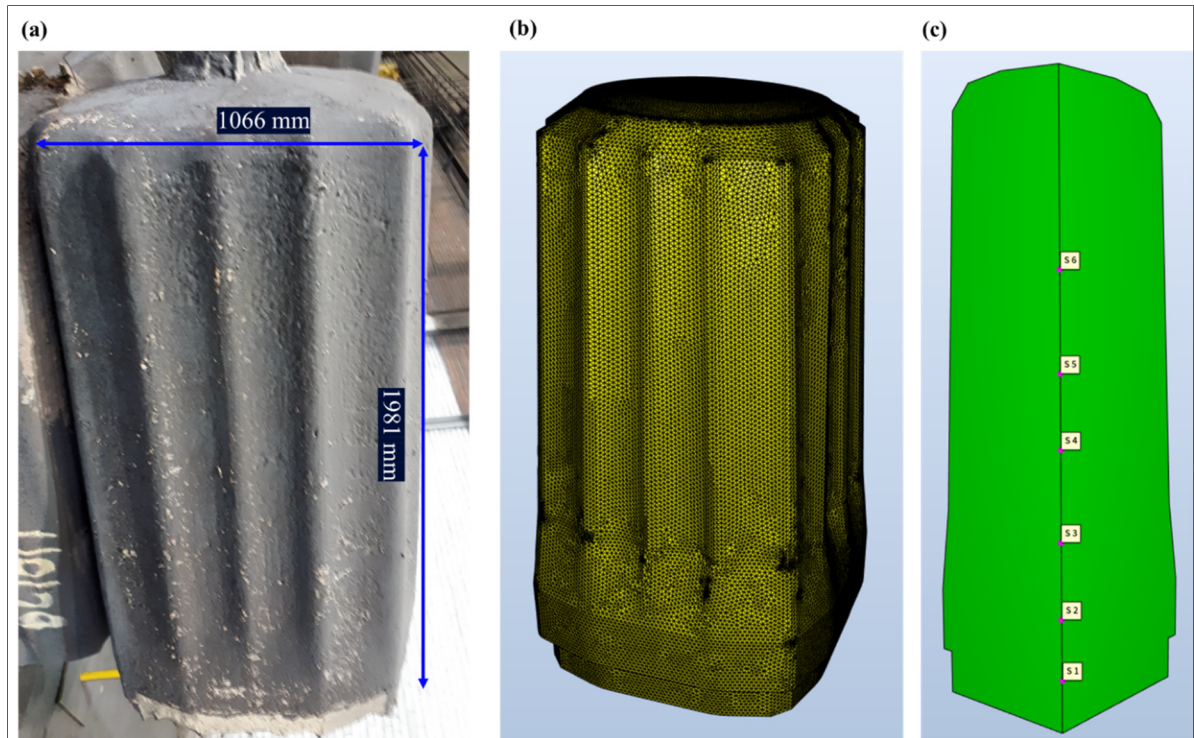
Figure 5.3 (a) 42-inch as-cast ingot (b) meshed finite element model (c) ¼ of the model

Table 5.3 Input data for FEM analysis

Parameters	Value
Unit	SI
Temperature (°C)	1200
Friction factor	0.35
Die temperature (°C)	400
Environment temperature (°C)	35
Press velocity (mm/s)	23.35
Initial billet height (mm)	1960
Final billet height (mm)	1143

5.2.3   Damage Analysis

To identify areas susceptible to deterioration during the forging process, the stress and strain states for deformed ingots were determined with the application of a finite element simulation. Among the fracture criteria, the Latham-Cockroft damage criterion (Cockcroft & Latham,

1968) was selected in this study. It involves the standardization of stress by dividing the maximum stress by the equivalent stress as follows:

$$C = \int_0^{\bar{\varepsilon}} \frac{\sigma_{max}}{\bar{\sigma}} \, d\bar{\varepsilon} \tag{5.3}$$

Where $\bar{\varepsilon}$ is the equivalent strain, σ_{max} is the maximum principal stress, $\bar{\sigma}$ is the effective stress, and $\bar{\varepsilon}$ is the effective strain. The damage parameter C is a function of temperature and strain rate, and the metallographic structure. The damage formula was implemented into the FORGE NxT 3.1® software through a user subroutine and utilizes the remeshing function. A larger damage value means the material is more likely to crack. The damage value for martensitic stainless steel during hot forging which leads to surface cracking was reported as 0.5 and 0.6 (De Oliveira et al., 2017; Kukuryk, 2021).

5.3   Results and Discussion

5.3.1   Simulation Results of Strain/Strain Rate Distribution During Upsetting

Strain distribution during upsetting plays a crucial role in the analysis of microstructure evolution. From the contour of Figure 5.4a, it can be seen that the strain distribution is not uniform throughout the ingot. A lower strain value is related to the contact zones with anvils (upper and lower dies) and a maximum corresponds to the center and upper half of the ingot due to different upper and lower diameter of the ingot. The strain decreases gradually by approaching the surface of the ingot. The sensors are assigned to track parameter changes during the deformation from the beginning to the end of the process. Figure 4b shows the strain versus time of 6 sensors, with the maximum strain level seen for point S 6. Figure 5.5a and 5.5b show the strain rate contour and the strain rate value of 6 sensors during the upsetting. The average strain rate with the industrial condition is 0.015 s⁻¹ for the upsetting process.
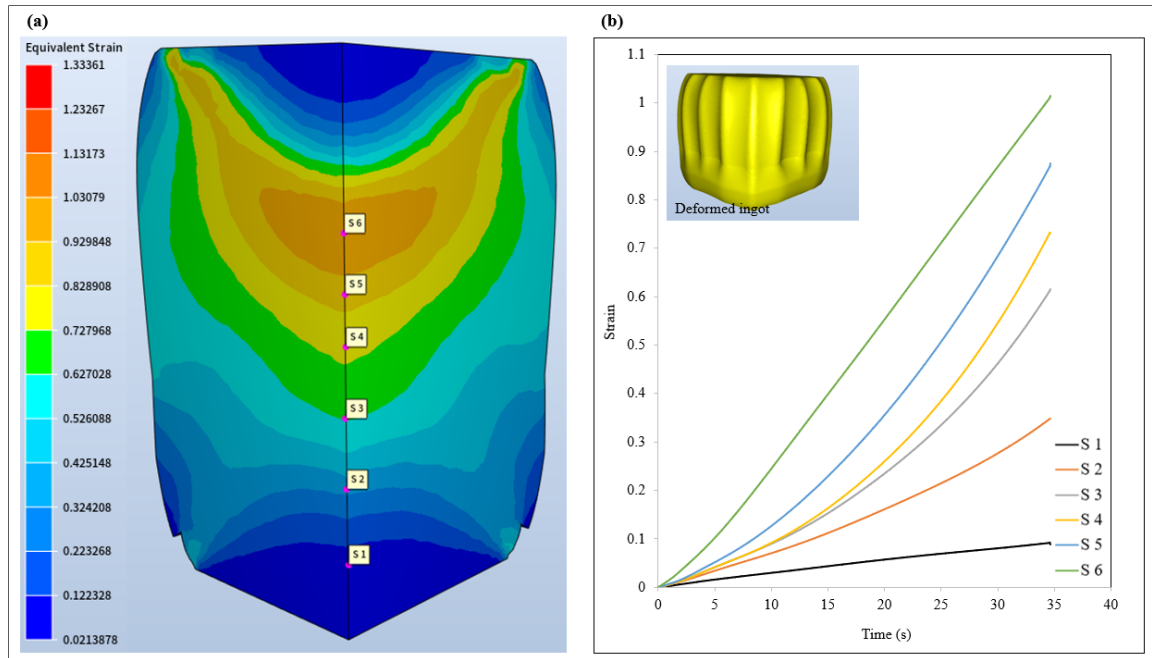
Figure 5.4 Simulation result (a) distribution of strain (b) diagram of strain evolution of 6 sensors during the upsetting
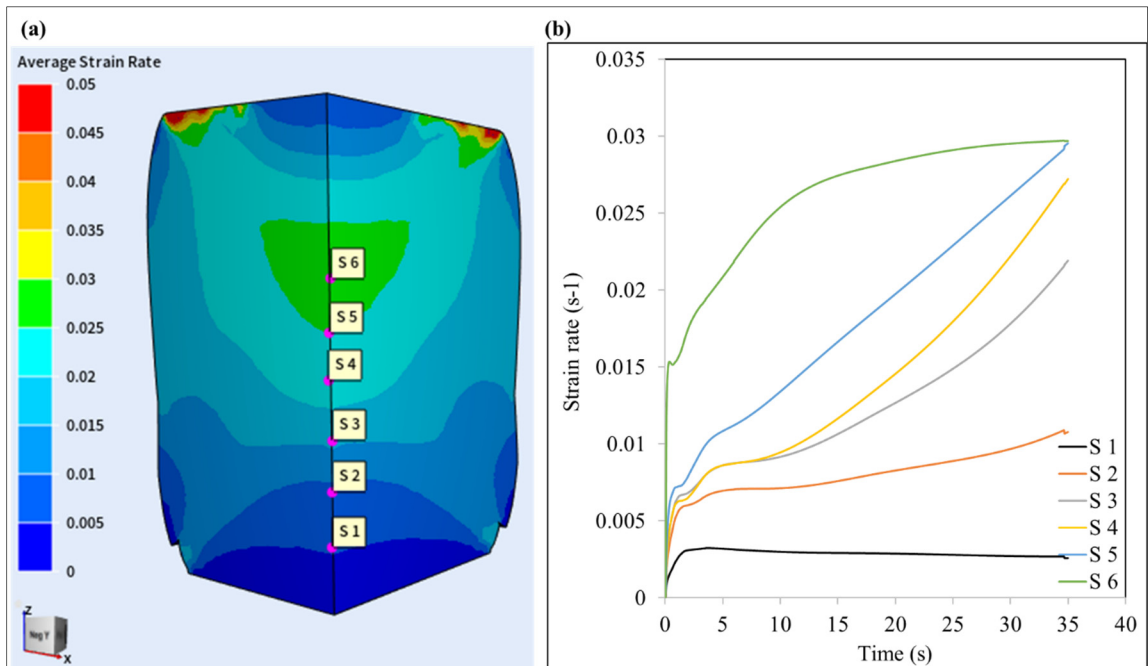
Figure 5.5 Simulation result (a) distribution of strain rate (b) diagram of strain rate evolution of 6 sensors during the upsetting

5.3.2   Critical Strain for Initiation of Dynamic Recrystallization

Dynamic recrystallization phenomena require a critical amount of deformation to occur at a given temperature. The critical strain equation, ε_c, is shown in Table 5.2 as a power law. After constant calculations, the equation was implemented into the Forge NxT 3.1® software through a user subroutine. Figure 5.6a and 5.6b represent the map of ε_c and the values of ε_c for the six points. All points except for S 1 reach the critical value at different periods of process time due to the uneven distribution of the strain. The point with the maximum strain, S 6, reaches the critical value sooner than the other points. However, no value appears in the diagram for point S 1 because it is situated in the dead zone, which has not experienced enough deformation for DRX initiation. This means that in this area, DRV is the dominant softening mechanism.
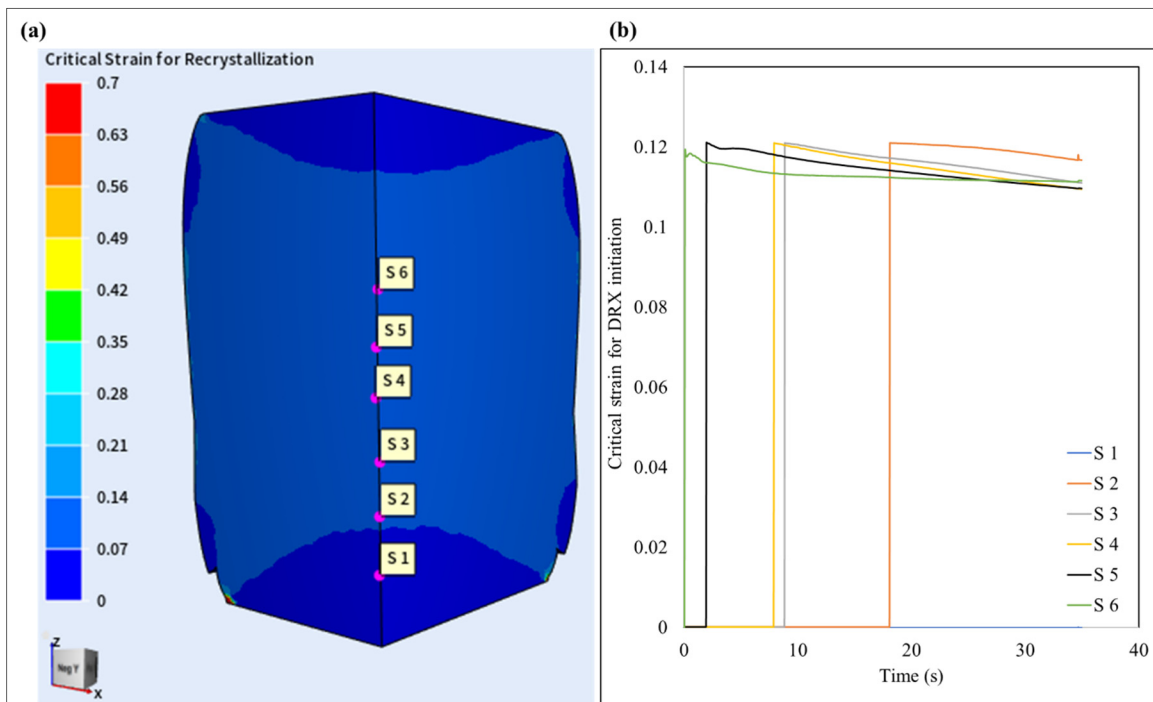
Figure 5.6 Simulation result (a) distribution of critical strain for DRX initiation
(b) diagram of critical strain evolution of 6 sensors during the upsetting

5.3.3　　　Dynamic Recrystallization Distribution

Figure 5.7a shows the map of DRX volume fraction distribution under industrial deformation conditions. It is revealed that the fraction of dynamic recrystallization has a direct relationship with the strain: it rises with increasing strain and falls with decreasing strain. Moreover, the DRX volume fraction distribution is inhomogeneous, itself due to the inhomogeneous strain distribution, as reported in Figure 5.5a. This means that the strain distribution directly affects the microstructural evolution during upsetting. The maximum DRX fraction is located at the center, toward the top of the ingot, where the workpiece experiences its maximum deformation degree, while the minimum is related to the top and bottom of the ingot in contact with the upper and lower dies. Figure 5.7b depicts the DRX fraction of six sensors versus time, and it is seen that the DRX fraction of point S1 is close to zero while that of S6 reaches 100% DRX. The DRX starts at a different time for each point because of uneven strain distribution, and the points with higher strain values start DRX sooner than the other points.
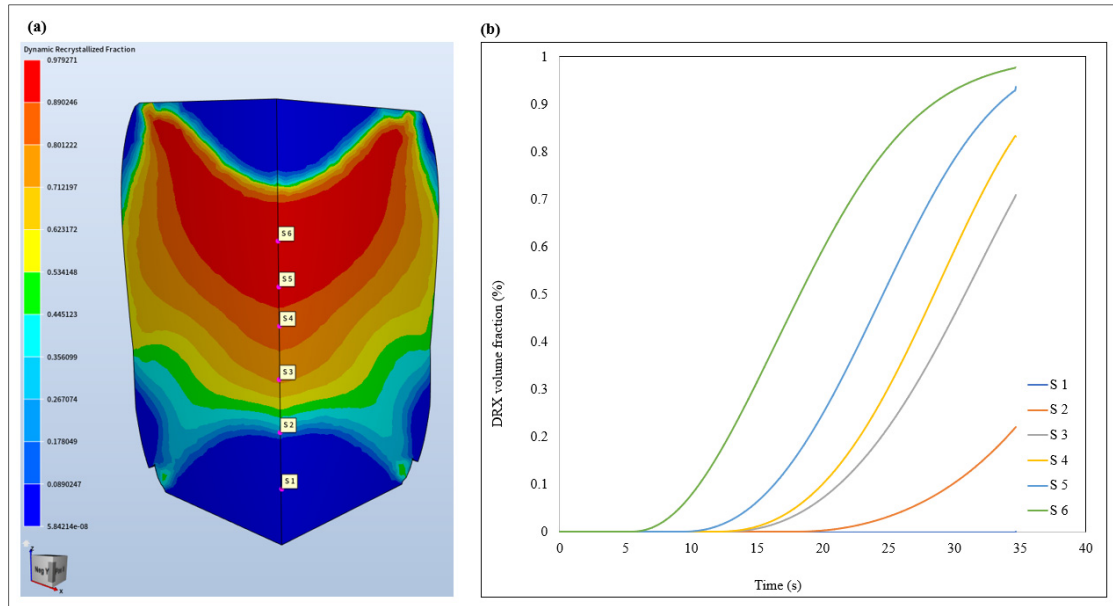
Figure 5.7 Simulation result (a) distribution of DRX at the end of upsetting
(b) diagram of DRX fraction evolution of 6 sensors during the upsetting

Figure 5.8 presents a whole model in order to illustrate the different percentages of DRX volume fraction at the end of upsetting where the material volume that does not undergo the DRX phenomenon and how much of the material is fully recrystallized.
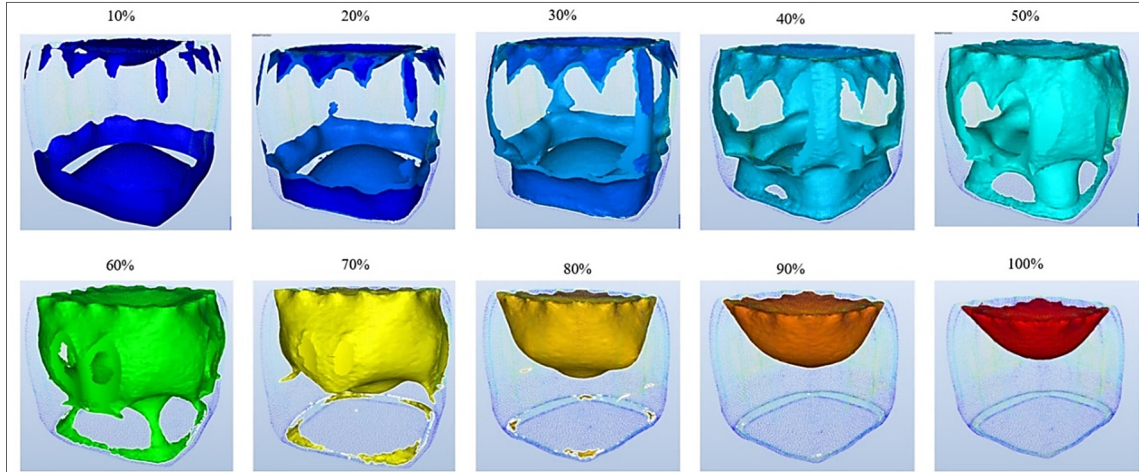
Figure 5.8 Iso volume of DRX fraction in different percentages at the end of upsetting

5.3.4   DRX Grain Size Distribution

Figure 5.9a presents the DRX grain size map. Similar to previous parameter contours, the grain size distribution is also uneven, and the higher the strain, the bigger the grain size. As the point reaches the critical strain, ε_c, the DRX initiates. The moment for DRX grain nucleation is shown in Figure 5.9b, and as the deformation proceeds, the nuclei get coarser. In the regions where the nucleation starts sooner, the nuclei have more time to grow, but the points with lower DRX volume fractions have finer grain sizes as the grains are at the start of the recrystallization stage. In general, the nuclei start out very fine and continue growing until the next recrystallization cycle. The DRX grain size, therefore, increases as the DRX percentage increases. For the zones with complete DRX, the grain size is around 73 μm, which is 70.8% smaller than the initial grain size.
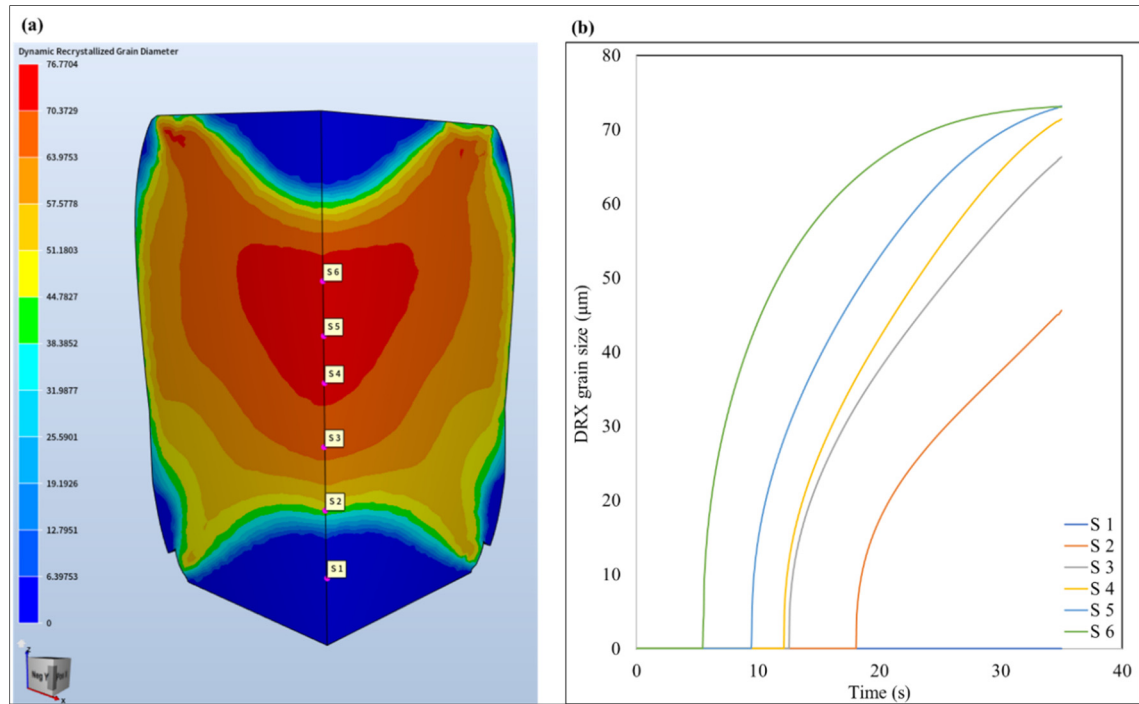
Figure 5.9 Simulation result (a) distribution of DRX grain diameter at the end
of upsetting (b) diagram of DRX grain diameter evolution of 6 sensors
during the upsetting

5.3.5 Distribution of Average Grain Diameter

This section shows the grain size distribution of recrystallized and non-recrystallized (dead zone) materials. Figure 5.10a shows the grain size map, with the red zones experiencing the minimum deformation. As shown in Figure 5.10b, the grain size of S 1, which is located in the red zone, remained unchanged from its initial value.
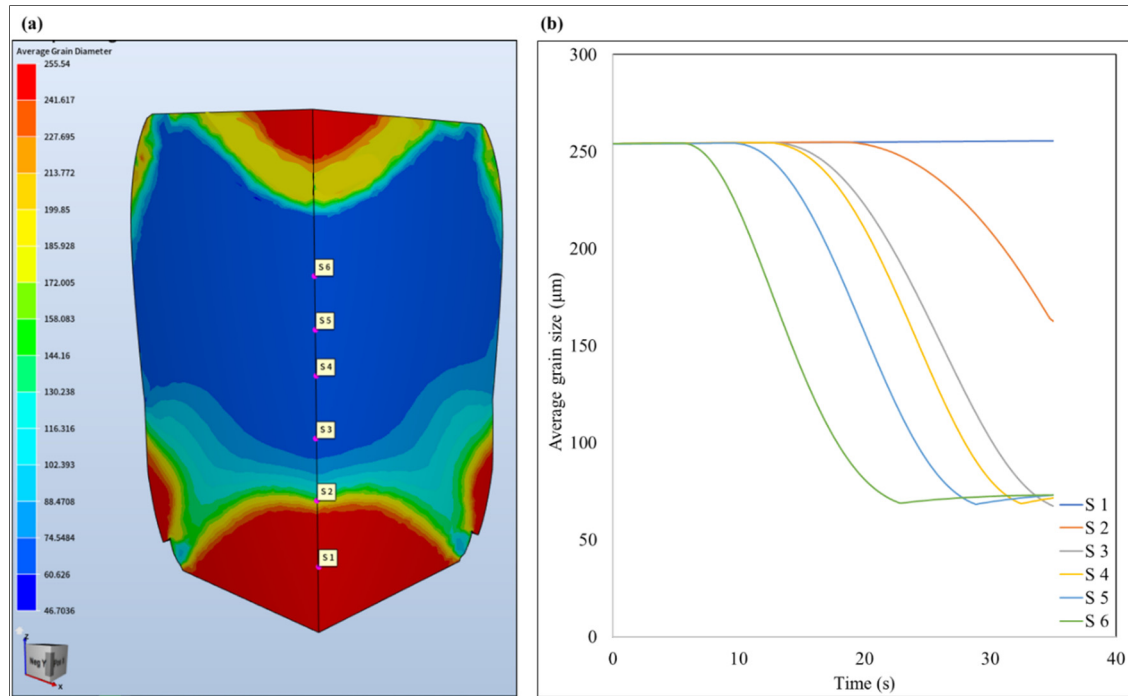
Figure 5.10 Simulation result (a) distribution of average grain diameter at the end of upsetting (b) diagram of DRX fraction evolution of 6 sensors during the upsetting

The damage analysis was carried out to find the most sensitive areas to crack formation. In the damage criteria, it was assumed that a crack will be initiated in a deformed material only when a threshold value, defined based on the used criteria, is exceeded (Kukuryk, 2021). Figure 5.11a shows the contour of the damage factor for Latham Cockcroft damage criteria at the end of upsetting. As expected, the surface of the ingot has the highest likelihood of crack formation, which means that the surface of the ingot is in danger of cracking. Figure 5.11b depicts two sensors selected on the surface and inside of the ingot, with two different cracking risk levels. In Figure 5.11c, the area with the highest cracking risk, the surface, experiences a higher maximum principal stress value. This means that the maximum level of tensile stress was achieved on the surface of the ingot. The combination of non-uniform microstructure evolution and high tensile stresses could lead to the formation of surface cracks. Therefore, based on the above analysis, it is possible to develop new forging schedules that would result in more uniform microstructures and higher mechanical properties while avoiding surface cracks during the deformation process.
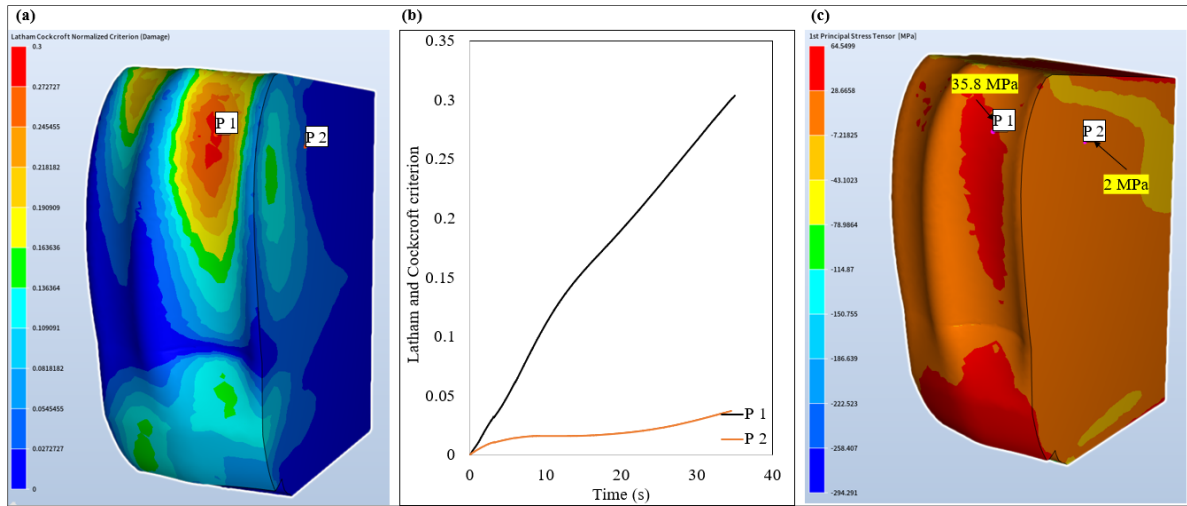
Figure 5.11 Simulation results (a) distribution of Cockcroft and Latham damage criteria (b) diagram of damage factors evolution of two sensors on the surface and inside of the ingot (c) distribution of maximum principal stress

5.3.6 Verification of the Simulation Results with Experimental Measurement

Compression tests were conducted using the Gleeble-3800 thermomechanical simulator machine. In a previous chapter, the Arrhenius model was validated as a predictive constitutive equation by comparison with experimental results, and the model was implemented into the FORGE NxT® software with good agreement. The DRX fraction and critical strain for the initiation of DRX were calculated for all deformation conditions. The characteristic points, including the peak stress and peak strain, critical stress and strain, and the maximum softening rate, were calculated using the methodology proposed by Poliak and Jonas named the double-differentiation technique (Jonas & Poliak, 2003). The microstructure evolution of the deformed sample was characterized for comparison with the microstructure-based FEM model prediction results. Figure 5.12a and 5.12b show the microstructure before deformation and the cross-section of the deformed samples in the 1200 °C-0.1 s^{-1} condition, respectively. Three zones were selected to show non-recrystallized, partially recrystallized, and fully recrystallized materials under hot compression tests. The microstructure of the dead zones, top and bottom in contact with the anvils, remained unchanged. However, the serrated grain boundaries (black arrows) in Figure 5.12c, zone 1, indicate that the dislocation accumulation and migration have

started at these locations, but the deformation degree is not sufficient to accumulate and nucleate a nucleus. Figure 5.12d, zone 2, shows the partial recrystallization which means that the DRX starts locally. At this zone, the material reaches the critical strain for DRX initiation but does not exceed the complete recrystallization strain. Figure 5.12e, zone 3, shows the center of the deformed sample, which has uniform and fine recrystallized grains, and the material is fully recrystallized at this zone. As can be seen, the recrystallized grains are much finer than the initial grains.
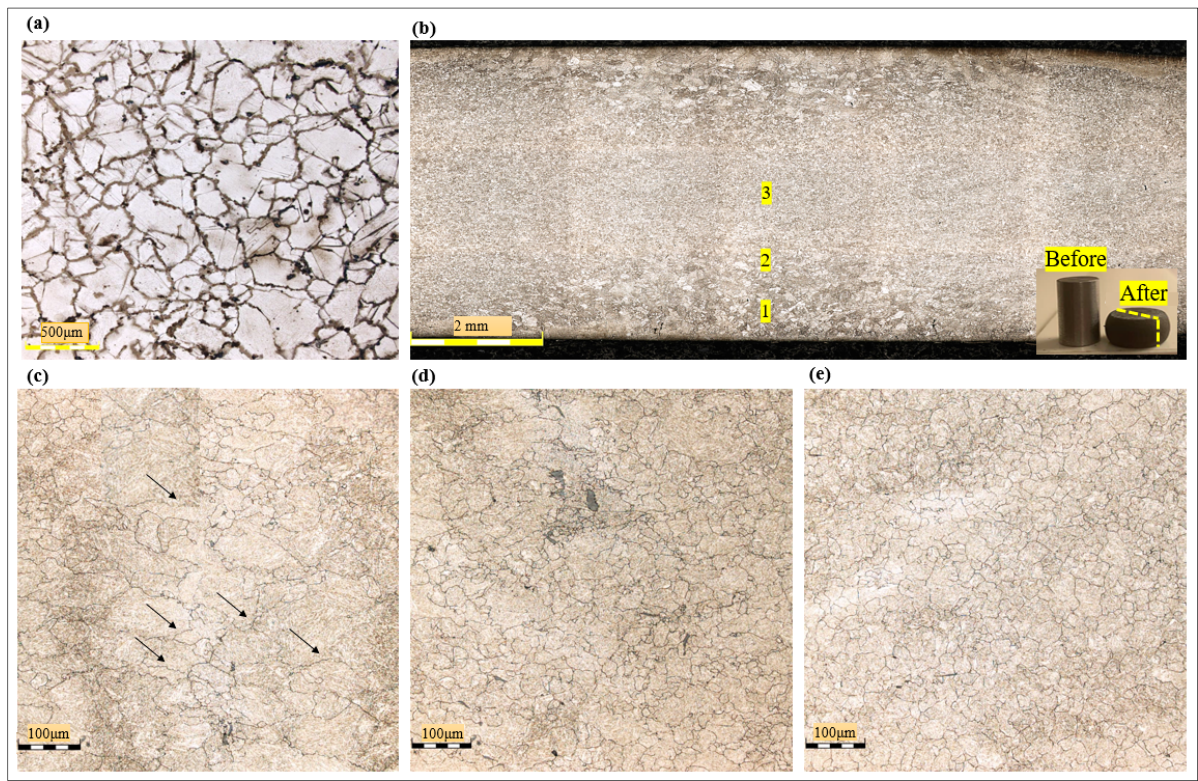
Figure 5.12 (a) Initial microstructure before hot compression test (b) stitching image of a cross-section of the deformed sample (c) unchanged microstructure of zone 1 with serrated grain boundary (d) mixed microstructure of zone 2 (e) fine and uniform microstructure of zone 3

Table 5.4 shows the grain size of the deformed samples measured by the MIP4 software for all deformation conditions. The grain size increases as the temperature increases and when the strain rate decreases. The critical strain was measured for the experimental tests, as shown in Table 5.5.

Table 5.4 DRX grain size at different temperatures
and different strain rates at the end of upsetting

Temperature (°C)	Strain rate (s^{-1})	Grain size (µm)
1050	0.001	23.65
	0.01	23.06
	0.1	21.78
	1	20.14
1100	0.001	68.59
	0.01	56.6
	0.1	48.25
	1	25.27
1150	0.001	77.75
	0.01	64.66
	0.1	52.28
	1	40.76
1200	0.001	92.5
	0.01	72.58
	0.1	66.4
	1	39.83

Table 5.5 Critical strain for DRX initiation at
forging temperature

Temperature (°C)	Strain rate (s^{-1})	ε_c
1200	0.001	0.02
	0.01	0.113
	0.1	0.127

By comparing the microstructure evolution of the simulation results and the experimental one at similar conditions, it is seen that the implemented equations for the DRX fraction, DRX grain size, and critical strain for DRX initiation could accurately predict the microstructure evolution of a large size ingot.

Figures 5.13a and 5.13b depict the distribution of damage value over the external surface of a deformed sample and in its central section, respectively. Similar to the simulation results

shown in Figure 5.11, the damage value is maximum at the surface of the sample. Figure 5.13c represents the microstructure of the deformed sample at the location with the maximum damage value. As it can be seen, the microstructure is composed of a mix of large size and small size grains characteristic of a partially recrystallized microstructure. These non-uniformities of microstructure and high damage value of the surface could make this location sensitive area for crack formation.
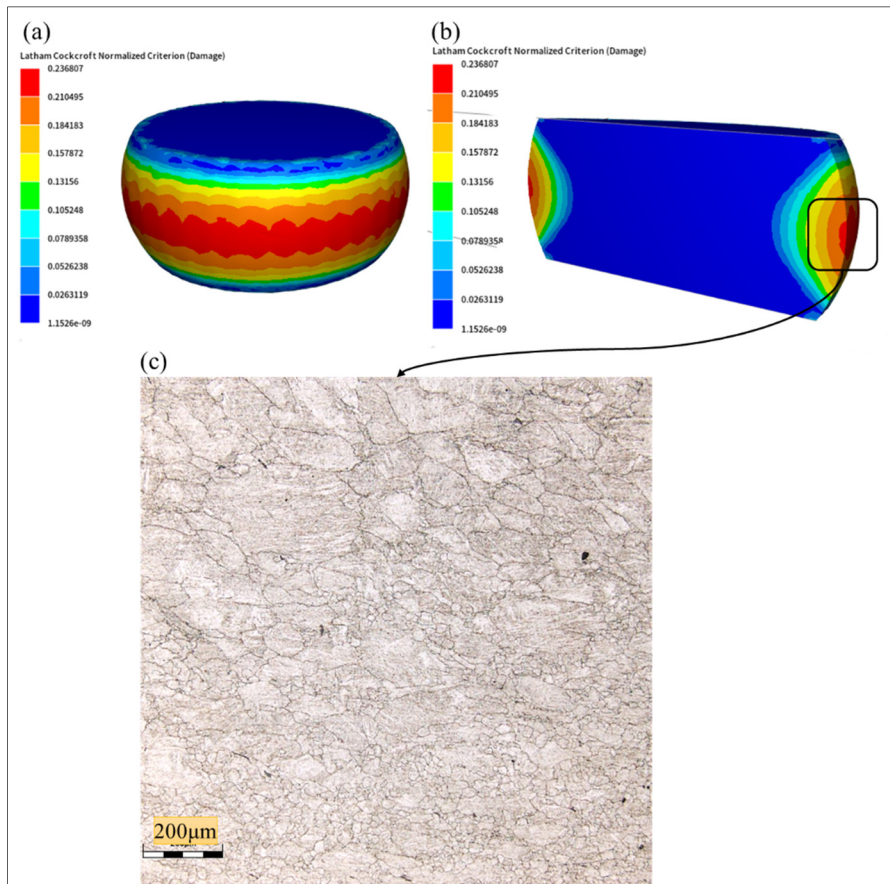
Figure 5.13 Distribution of Cockcroft and Latham damage criteria of X12Cr13 stainless steel (a) whole sample (b) inside deformed sample (c) micrographs of the deformed sample with a maximum damage value

5.4   Conclusions

In this chapter, numerical simulation and experimental studies were carried out on the upsetting process at a high temperature of X12Cr13 stainless steel. The evolution of the working parameters involved was analyzed, leading to the following conclusions:

1. The constitutive equation and microstructure evolution models were implemented into the finite element code through a user subroutine and a coupling of models showed very good agreement with the experimental findings for the investigated steel.

2. The evolution of the microstructure, particularly, the extent of softening due to dynamic recrystallization, was determined for the industrial size ingot. Such quantification allows for the design of optimum forging schedules to obtain improved mechanical properties and higher-quality finished products.

3. The damage analysis results showed that cracking susceptibility is higher in the regions with mixed microstructures (recrystallized and non-recrystallized). Such regions are often close to the surface of the forging.

In Chapter 6, the results and analysis from Chapter 5 were used to simulate the forging process and modify the forging parameters to investigate the influence of forging parameters on microstructure evolution during forging and also to explore the risky conditions of the process. A part of the last objective has attained in the following chapter. The results of CHAPTER 6 will be submitted to The *Journal of Material Processing Technology in December 2022.*

CHAPTER 6

INFLUENCE OF HOT WORKING PARAMETERS ON THE MICROSTRUCTURE EVOLUTION OF MARTENSITIC STAINLESS STEEL DURING OPEN DIE FORGING

Summary

The final mechanical and metallurgical properties of forged products are primarily determined by the microstructure evolution during the forging process. The most important working parameters that affect the microstructure evolution are deformation temperature, strain rate, and strain at a given material composition. In this chapter, the influence of changes in working parameters on the dynamic recrystallization fraction, final grain size, critical strain for initiation of DRX, and damage criteria have been investigated through the 3D simulation. It is concluded that the changes in strain have the most influence on the microstructure evolution rather than other working parameters. The distribution of damage criteria shows that the ingot's surface is more susceptible to cracking during the plastic deformation process.

6.1   Literature Review

Metals and alloys are subjected to complex working parameter histories during the forming process (Di Schino, 2021). A particular metallurgical phenomenon (microstructural evolution) is produced by a particular combination of thermo-mechanical parameters (strain rate, temperature, and strain). Microstructural changes during the hot-forming process have an impact on the mechanical properties and final product quality, such as the flow stress, toughness, and impact properties (Zhbankov, Aliieva, & Malii, 2020). Therefore, finding the effects of working parameters on the microstructure evolution is of great importance for forming industries (hot rolling, forging, and extrusion). Researchers conducted several studies on these concerns. Jin et al. (Jin et al., 2015) studied the microstructure evolution of a commercial as-extruded Q235 during the thermoplastic deformation by conducting the experimental hot compression tests and then modeled the process through the finite element method. It is found that there is a deformation heterogeneity and the maximum softening mechanism fraction occurs easily in the central zone of the sample where there is maximum deformation degree. Wang et al. (S. Wang et al., 2016) investigated the microstructure evolution of the nuclear power plant pipe, AP1000, during the open die forging process and reported the non-uniform strain and grain size evolution at the end of the forging process. Chen et al. (F. Chen et al., 2014) investigated the microstructure evolution of austenitic stainless steels both experimentally and numerically through double-pass hot compression experiments using a Gleeble-1500 thermo-mechanical simulator. The kinetic equations and grain evolution equations were also developed. Lin et al. (Y. C. Lin et al., 2008) studied the effect of working parameters on microstructure evolution of 42CrMo. They reported that DRX fraction increases with increasing deformation temperature and decreasing strain rate. They also reported that the distribution of DRX volume fraction, temperature, strain, and strain is not uniform in the deformed block. Akhmed'yanov et al. (Akhmed'yanov, Rushchits, & Smirnov, 2016) studied the hot deformation of supermartensitic stainless steel through compression tests using the Gleeble machine and reported that with a decrease in deformation temperature and an increase in the strain rate, the flow stress and peak strain both increases. Zhou et al. (Y. Zhou et al., 2021) worked on the microstructure evolution of 05Cr17Ni4Cu4Nb through flow stress

modelling and processing maps during hot plastic deformation. Several studies on hot deformation and constitutive model establishment have been conducted but few studies have worked on the microstructural evolution of MSS at high temperatures during forging. The studies worked on the microstructure evolution during forging were explained in section 5.1. Most of the studies investigated the high-temperature behavior of MSS during forging on the laboratory scale and there is no investigation of microstructure evolution numerically on a large scale for MSS. In addition, lack of published data exists for the effect of working parameters on the microstructure evolution of large size ingot of MSS.

In this chapter, the forging process of MSS was numerically simulated with the industrial forging process conditions. Based on the results from the thermomechanical experiments and metallographic analysis, Chapter 5, all constants of all microstructure models were calculated and established for MSS for the first time. The microstructure evolution parameters including critical strain for initiation of DRX (ε_c), DRX fraction (X_{DRX}), DRX grain size (D_{DRX}), and damage criteria were taken into consideration in this model. Integration of thermomechanical coupled finite element methods has been used to investigate the effects of thermomechanical parameters and deformation history on microstructural evolution and grain size. The forging process of the 13.5-ton ingot was simulated using the developed system. The distribution and evolution of microscopic field variables during the forging process were analyzed.

6.2 Mathematical Modelling for Microstructural Evolution

X12Cr13 MSS with the given chemical composition, Table 5.1, was used in this investigation. All experimental measurements and constant calculations of microstructure evolution models were explained step by step in Chapter 5. The dynamic recrystallization phenomenon during deformation starts when the deformation degree, strain, exceeds the critical value with the driving force of dislocation annihilation. As shown in Table 5.2, the DRX is a function of the strain, strain rate, deformation temperature, and initial grain size. The onset of recrystallization occurs at the critical strain which is a function of initial grain size, strain rate, and deformation temperature. $\varepsilon_{0.5}$ is a strain that the material is recrystallized 50% which is in the DRX fraction

equation. DRX grain size is calculated as a function of DRX fraction, strain, and deformation temperature. All microstructure evolution models were implemented into the Forge NxT 3.1® software through user subroutines. The current implemented material model, Hansel-spittle, existing in the software was not able to predict the material behavior of the studied steel, Figure 4.9. Therefore, another phenomenological constitutive model was utilized to provide the prediction of MSS flow stress. The predictability of Arrhenius model was shown in Figure 4.12, and the comparison between the experimental and predicted flow stress signifies that the second model could predict the flow behavior of the studied alloy with good agreement. The constitutive equation and microstructure models were integrated with FEM software for numerical simulation, Forge NxT 3.1®, for the first time. In this chapter, the effect of working parameters on the microstructure evolution was investigated by changing the working parameters temperature, strain rate, and strain as a modified design (MD). The simulation parameters for both original and modified designs were shown in Table 6.1. It should be mentioned that for each simulation just one parameter (T, ε, $\dot{\varepsilon}$) was changed and the values of other parameters were similar to original design.

Table 6. 1 Simulation parameters

Original design (OD)		Modified design (MD)		
Simulation Parameters	Value			
Unit	SI			
Young's modulus at 1200°C (GPa)	96			
Elastic Modulus (GPa)	200	1st : Effect of forging temperature		
Poisson's ratio	0.35	Forging temperature = 1100 °C		
Forging temperature °C	1200			
Friction factor	0.35			
Solution step definition (s/step)	With time 0.04	2nd : Effect of strain rate		
Die temperature (°C)	400	Die velocity = 15 mm/s		
Environment temperature (°C)	35			
Die velocity (mm/s)	23.35			
Initial billet height (mm)	1960			
Final billet height (mm)	1143			
Element number of billet	848,140	3rd : Effect strain		
Node number of billet	168,700	Final billet height = 900 mm		
Upsetting step	816			

6.3   Numerical Simulation of the 3-D Upsetting Process

Three-dimensional hot-upsetting numerical simulation has been conducted. By integrating the thermo-mechanical coupled finite element method with the derived microstructure models, it is examined how processing parameters such as deformation temperature, strain rate, and strain affect microstructure evolution and damage sensitivity of deformed X12Cr13 steel. The distribution of temperature, critical strain, strain rate, strain, dynamic recrystallization, and DRX grain size during the hot upsetting of X12Cr13 steel were predicted. The heavy ingot is deformed by a hydraulic press with the 5000-ton capacity as a first sequence of forging. Figure 6.1(a-e) shows the as-cast ingot, CAD model of the whole ingot, meshed models, one-quarter of the model, and the upsetting process. The upper and lower dies are considered as being rigid and the workpiece as being plastic. The 3D linear tetrahedral mesh with volumetric elements was selected and the mesh size is fine enough to assure high convergence in the calculation.

158

Figure 6.1 As-cast ingot (b) CAD model of ingot (c) Meshed model of 360° 3D
(d) 90° of the model (one quarter) (e) Upsetting process

6.4   Results and Discussion

6.4.1   Effect of Forging Temperature on Microstructural Evolution

Forging temperature plays a crucial role in microstructural evolution. As explained in chapter 3, it was concluded that a forging temperature of 1260 °C is higher than the melting point of the eutectic phase which leads to local melting at zones where this phase exists. Therefore, it is suggested to industry reduce the forging temperature to 1200 °C which is lower than the eutectic phase melting point. However, increasing the forging temperature is in favor of recrystallization and the higher is forging temperature the lower the critical strain for DRX initiation.

Figure 6.2 shows the DRX fraction diagram of 4 different temperatures and strain rate of 0.01 s^{-1} derived from experiment test measurements, Chapter 4. It is seen that decreasing forging temperature reduces the volume fraction of DRX. These restoration processes are controlled by a thermally activated mechanism. When the temperature increases, DRX takes place more rapidly since it causes an acceleration in migration of HABs, more annihilation of dislocation substructures, increasing the number of operating different slip systems, dissolving precipitates and all lead to more homogenous deformation. On the other hand, decreasing deformation temperature leads to decreasing the final grain size of the deformed samples which is in favor of mechanical properties, Table 5.4. Therefore, the upsetting process is simulated by a temperature reduction.
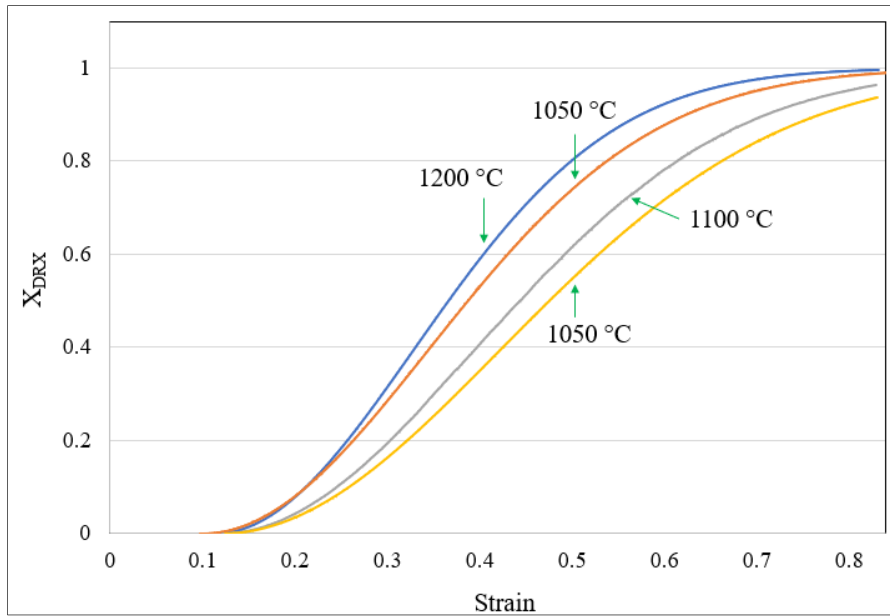
Figure 6.2 Predicted volume fraction of dynamic recrystallization
achieved under different temperatures at constant
strain rate of 0.01 s^{-1}

A new simulation was conducted with the temperature reduction with 100 °C to see the microstructural changes. All simulation parameters are the same as in Table 6.2 except forging temperature. There is a limitation in reducing forging temperature due to the specified range of fully austenitic zone as shown in Figure 3.6. The forging temperature should be in the range of austenite zone and lower than the eutectic phase melting point.

Figure 6.3a and 6.3b show the map of DRX fraction for the original forging temperature, 1200 °C, and the modified one at 1100 °C. As it is shown, the DRX fraction decreases by reducing the forging temperature at the end of the upsetting. Moreover, Figure 6.3c and 6.3d show the volume of the material with up to 100% of DRX fraction. It is seen that this volume decreases significantly even by reducing 100 °C of the forging temperature and little amount of material experiences complete recrystallization.
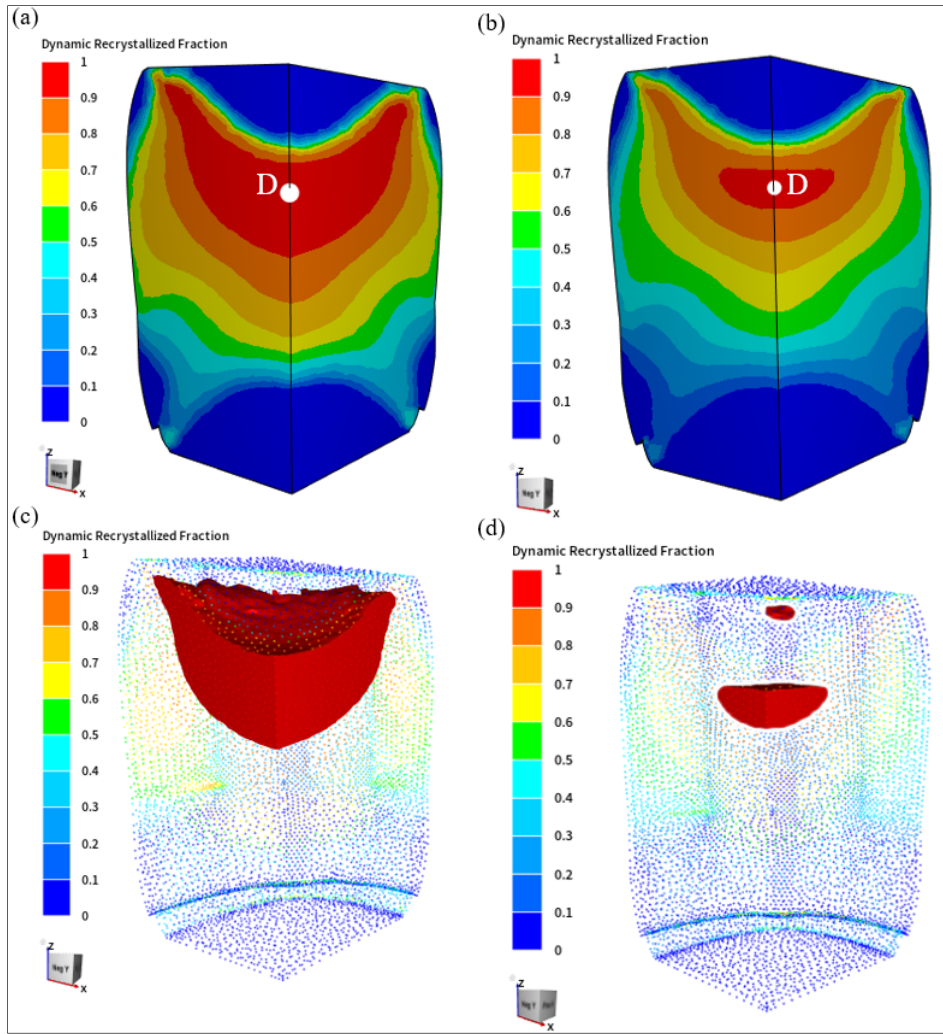
Figure 6.3 (a) DRX fraction at the temperature of 1200 °C
(b) DRX fraction at the temperature of 1100 °C (c) Volume fraction
of 100% of DRX at temperature of 1200 °C (d) Volume
fraction of 100% of DRX at temperature of 1100 °C

According to Table 6.1, the critical strain for DRX initiation increases by decreasing the forging temperature at the given strain rate. Figure 6.4a and 6.4b show the ε_c and X$_{DRX}$ evolution for the one selected point, D, which shows the maximum DRX fraction. Figure 6.4a shows that more amount of deformation is needed to start DRX by reducing the temperature. In addition, at the given strain, the DRX fraction decreases with decreasing temperature, Figure 6.4b.
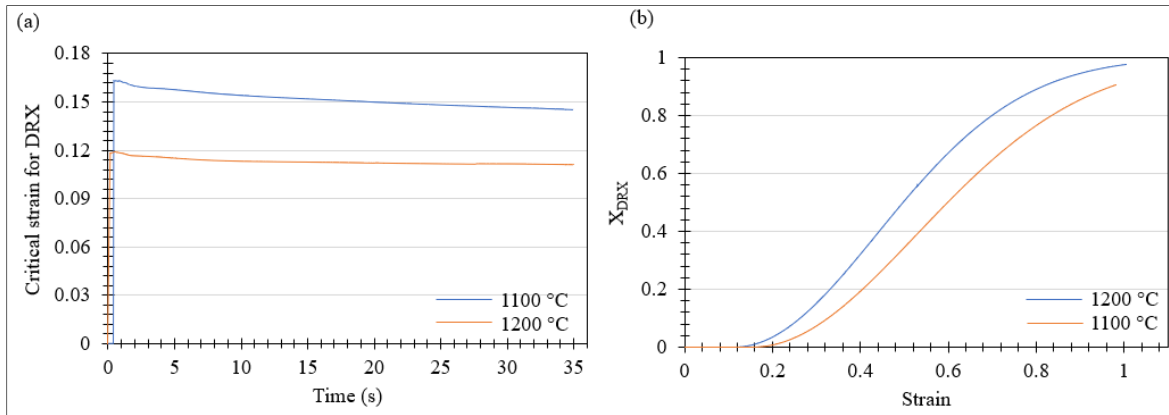
Figure 6.4 Comparison of (a) critical strain evolution of two temperatures (b) DRX fraction evolution of two temperatures

It can be observed that even 100 °C temperature reduction in forging, the microstructure evolution changes considerably. By reducing the volume of DRX fraction, the non-uniformity of microstructure increases. This leads to producing the heterogeneities in mechanical and physical properties of final forging products which is undesired for industry. However, the DRX grain size has a direct relationship with the forging temperature. Figure 6.5 shows two microstructures of experimental tests at the maximum and minimum hot compression tests and strain rate of 0.01 s^{-1}. The average grain size at the center of the specimen is 70 μm and 21 μm for the compression at 1200 °C and 1050 °C respectively.
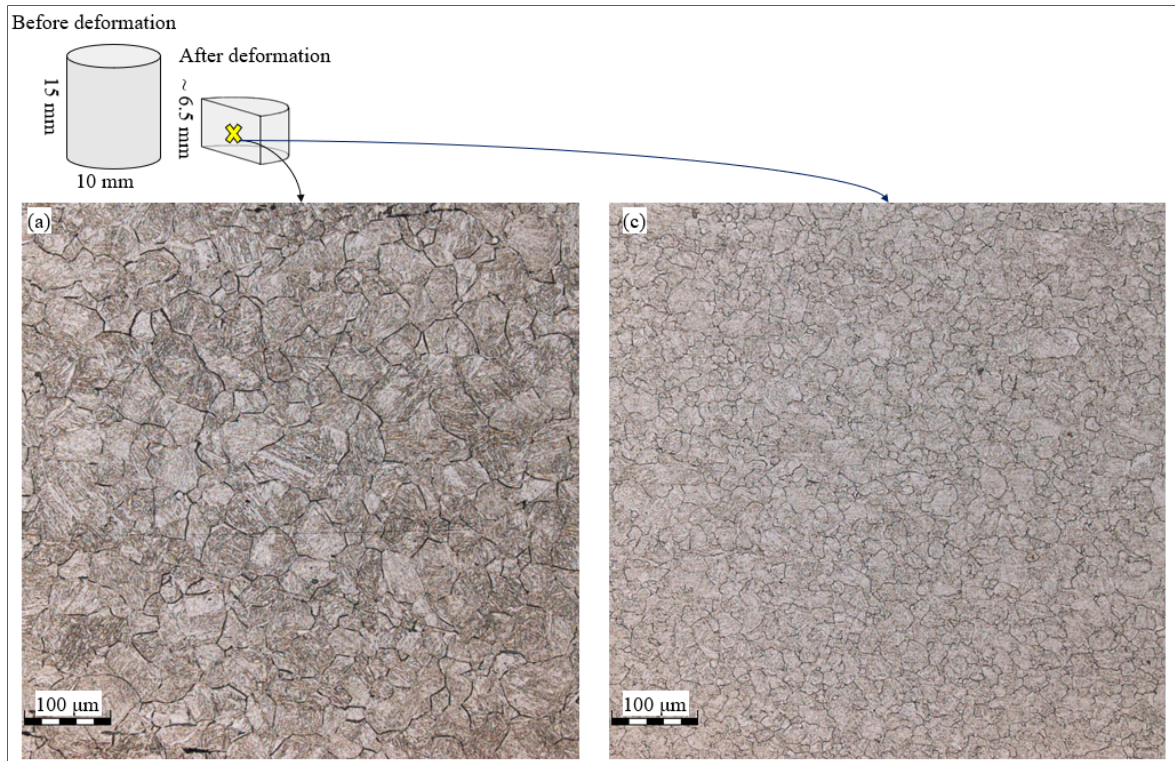
Figure 6.5 Microstructure of deformed samples at the strain of 0.01 s^{-1}
and temperature of (a) 1200 °C (b) 1050 °C

The simulation results of the DRX grain size at the forging temperatures of 1200°C and 1100°C is illustrated in Figure 6.6a and 6.6b respectively and the DRX evolution at point D is provided in Figure 6.6c. In conclusion, reducing the forging temperature decreases the level of DRX fractions, increases the critical strain for DRX initiation, and increases the non-uniformity distribution of the microstructure. However, reducing forging temperature leads to a reduction in DRX grain size.
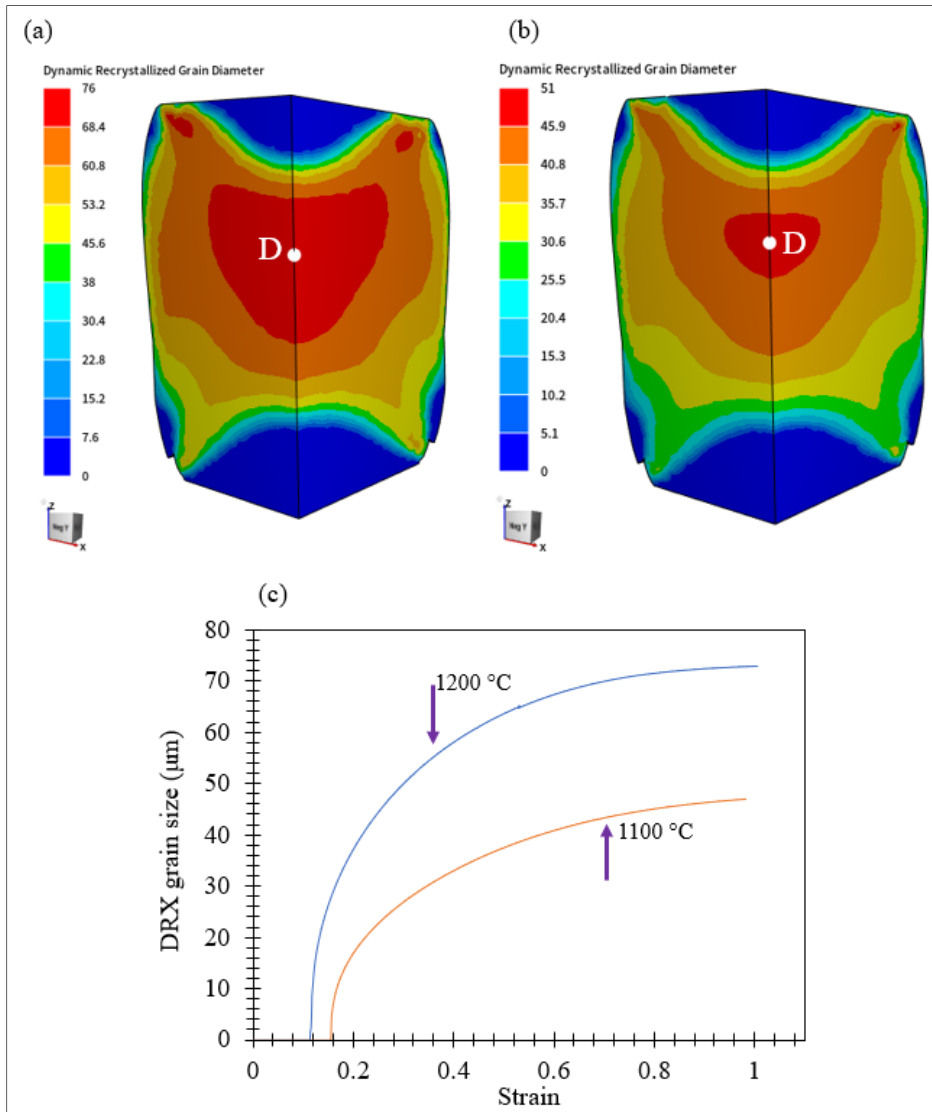
Figure 6.6 DRX grain diameter at temperature of (a) 1200 °C (b) 1100 °C
(c) diagram of DRX grain size vs. strains of two temperatures

6.4.2 Effect of Strain Rate on Microstructure Evolution of MSS Steel

The DRX fractions were calculated for all deformation conditions of the experimental tests using the equation in Table 6.1. Based on the method proposed by Poliak and Jonas (Jonas & Poliak, 2003), the critical strain can be calculated by plotting the strain hardening rate ($\theta = \frac{d\sigma}{d\varepsilon}$) as a function of stress and the inflection point of ($\theta - \sigma$) curves indicates the critical stress

(σ_c) for the initiation of DRX, and critical strain can be found from the related stress, Figure 6.7a. It is found clearly that at the constant temperature, the critical stress and critical strain decrease with decreasing the strain rate. This means that by lowering the strain rate, higher DRX fraction evolves at the given amount of deformation. Figure 6.7b indicates the curves of $\theta - \varepsilon$ which the minimum points in each curve demonstrate the strains at which the dynamic softening rate is maximized, ε^*. The lower the strain rates, the lower the strain needed for maximum softening rates which means that at lower levels of deformation, the forging with a lower strain rate, reaches complete recrystallization at the given strain. Figure 6.7c shows the DRX fraction as a function of the strain at different strain rates with a constant temperature of 1200 °C. This diagram clearly shows the effect of the strain rate on the DRX fraction. At the given level of deformation, the volume fraction of DRX is higher for the deformation with a lower strain rate.
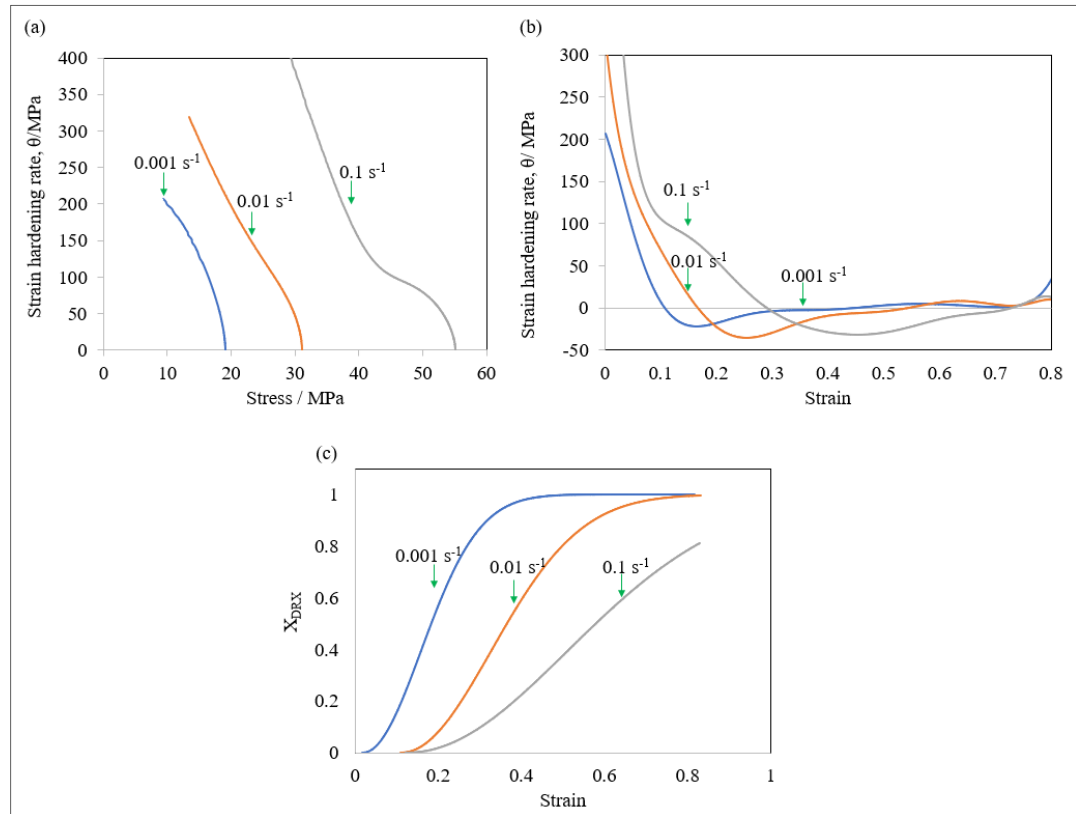
Figure 6.7 The curves of (a) $\theta - \varepsilon$ (b) strain hardening rates-strain
(c) Predicted volume fraction of DRX for MSS deformed at
1200 °C and different strain rates

It is concluded that decreasing the strain rate is in favor of microstructure evolution. Therefore, a simulation of the upsetting process on the industrial scale was conducted by decreasing the strain rate which is smaller than the original die velocity. It should be noted that the strain rate cannot be reduced significantly due to the loss of ingot temperature, especially at the surface which causes low workability. Table 6.2 shows the original and new strain rates for this design. Figure 6.8 shows the comparison between old and new strain rate evolution during the upsetting process. The new strain rate is about 1.5 times lower than the original one with an average of 0.02 s^{-1}. The processing time increases by 20 s because of lower die velocity.
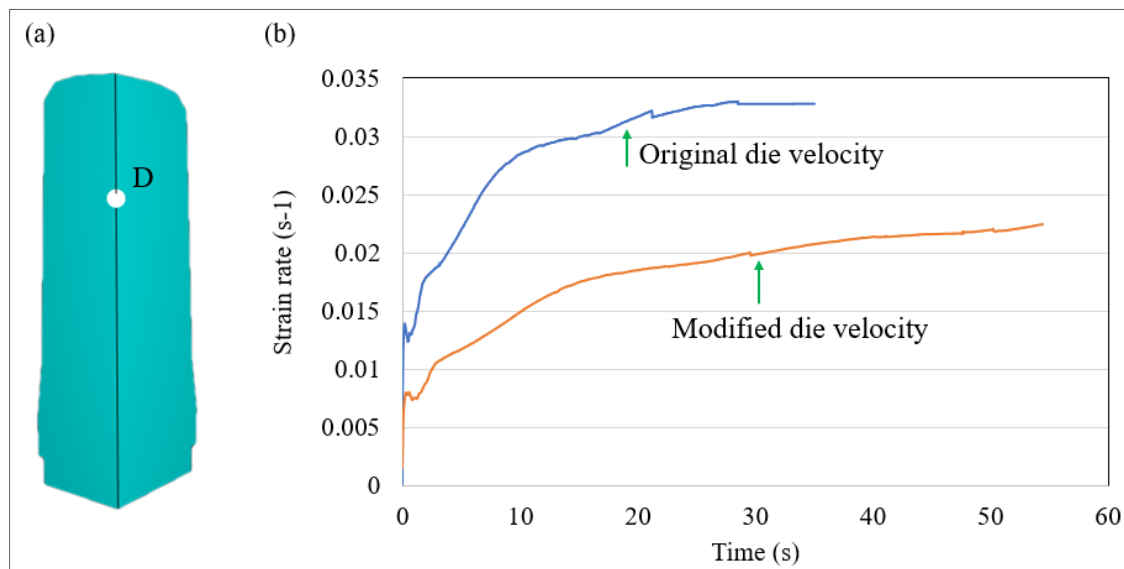
Figure 6.8 (a) CAD model of the ingot and selected points to track the changes (b) diagram of strain rate evolution vs. process time of two different strain rates

As discussed above, the DRX volume fraction increases by decreasing the strain rate at a given strain. Figure 6.9a and 6.9b show selected point for reading the data during upsetting and the comparison between the original and new DRX fraction by changing the strain rate, respectively. It is seen that reducing the strain rate is not that much to increase the DRX fraction significantly. However, the strain rate reduction has changed the DRX fraction distribution. Figure 6.9c and 6.9d show the DRX distribution with the original die velocity and the modified one respectively. The numbers on the images show the distance from the top and bottom of the ingot with no or very little amount of recrystallization. It is seen that by reducing the strain

rate, the volume of the ingot which is not undergone the recrystallization has decreased both from the top and bottom. This means that reducing the strain rate helps to increase the recrystallized volume of the ingot, Figure 6.10. In this figure, the volume of non-recrystallized material is shown with the Iso volume option in the Forge NxT software.
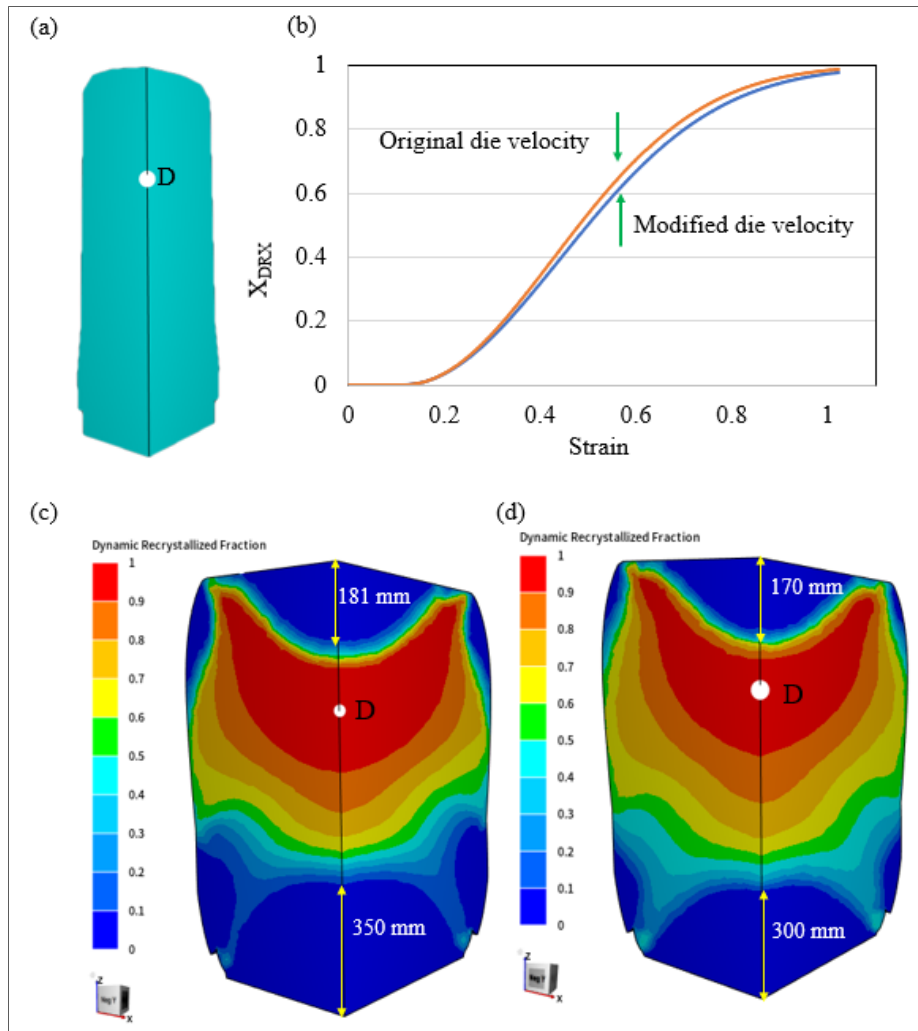
Figure 6.9 (a) Selected point on the CAD model (b) Comparison of DRX fraction between two different strain rates (c) Map of DRX fraction of old die velocity (d) Map of DRX fraction of new die velocity
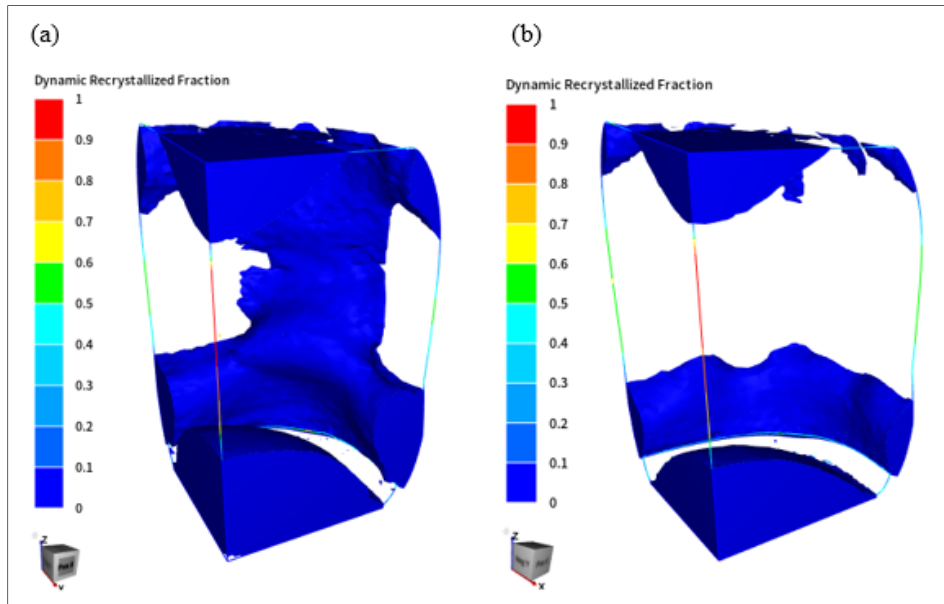
Figure 6.10 Volume fraction of non-recrystallized material of
(a) Original die velocity (b) Modified die velocity

The strain rate reduction affects the final grain size. According to Table 6.1, DRX grain size has a direct relationship with the strain rate in which by reducing the strain rate, DRX grain size decreases. The simulation results approve this relationship. Figure 6.11a and 6.11b show the locations where the grain size was measured and DRX grain size evolution during the upsetting respectively. Figure 6.11c and 6.11d illustrate the map of DRX grain size at the end of upsetting.
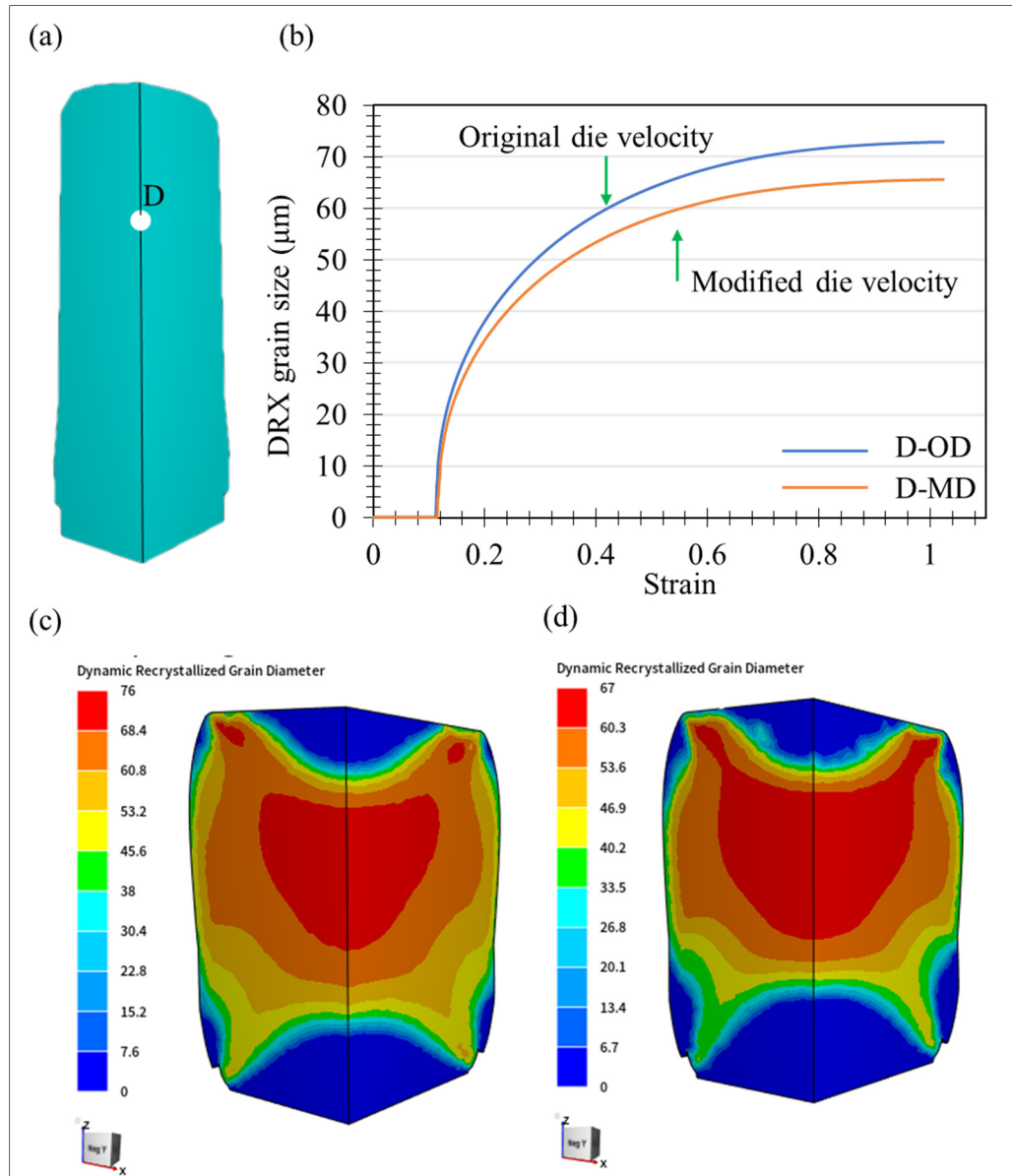
Figure 6.11 (a) Selected point on the CAD model (b) DRX grain
size vs. strain (c) Map of DRX grain diameter of old die velocity
(d) Map of DRX grain diameter of new die velocity

The grain size reduction occurs by reducing the strain rate of the upsetting process. The grain size of fully recrystallized material is around 70 μm with the original forging schedule in the industry while by reducing the die velocity this value dropped to around 65 μm. In addition, the map of grain size shows that the grain size is finer at all points of the ingot. As the strain

rate decreases, the processing time will increase which leads to losing more temperature, particularly at the surface and the ingot becomes more susceptible to surface cracking. Therefore, in order to obtain more amount of DRX fraction, the value of the strain rate could not be selected lower. Figure 6.12 shows the map of temperature distribution at the end of upsetting with modified die velocity, 55 s process time. 5 points were selected to measure the temperature evolution. All points except B1 experience temperature increases due to the heat generated during the hot-forming process (adiabatic heating). The final surface temperature of the ingot is in the range of the austenitic region which means that this time of the process is acceptable.
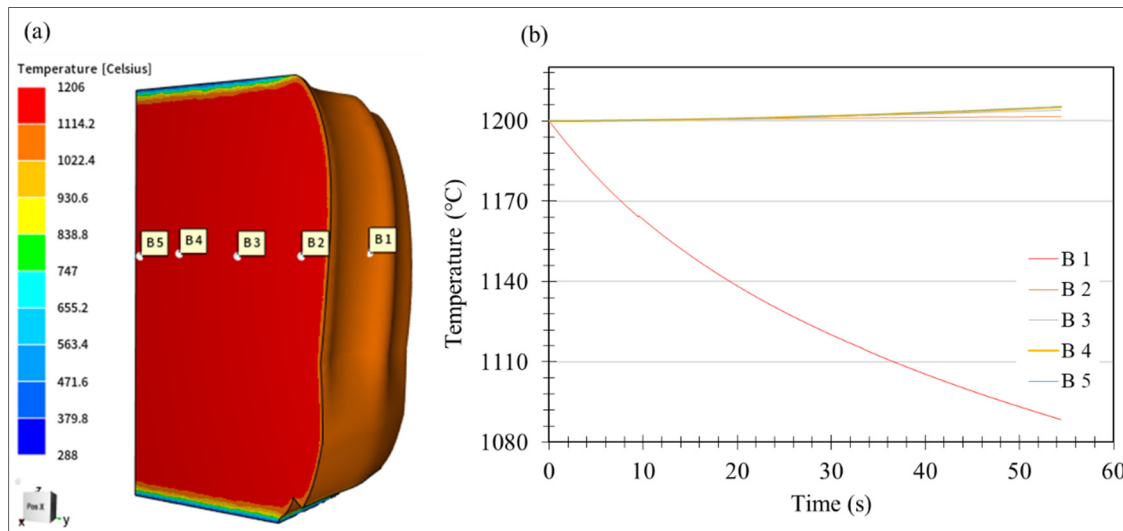
Figure 6.12 (a) Map of temperature distribution at the end of the upsetting
(b) Temperature evolution during the upsetting of 5 points

6.4.3　Effect of Strain on the Microstructure Evolution of MSS Steel

As explained above, the DRX fraction has a direct relation with the strain, Figure 6.7c. Therefore, a new simulation was conducted with a higher amount of deformation, and a smaller final billet height, to see its effect on microstructure evolution. The final billet height is the only parameter that has been changed for this setup, Table 6.2. Figure 6.13 (a-c) shows the ingot geometry, as-cast, after upsetting with the original design, after upsetting with the modified design respectively.
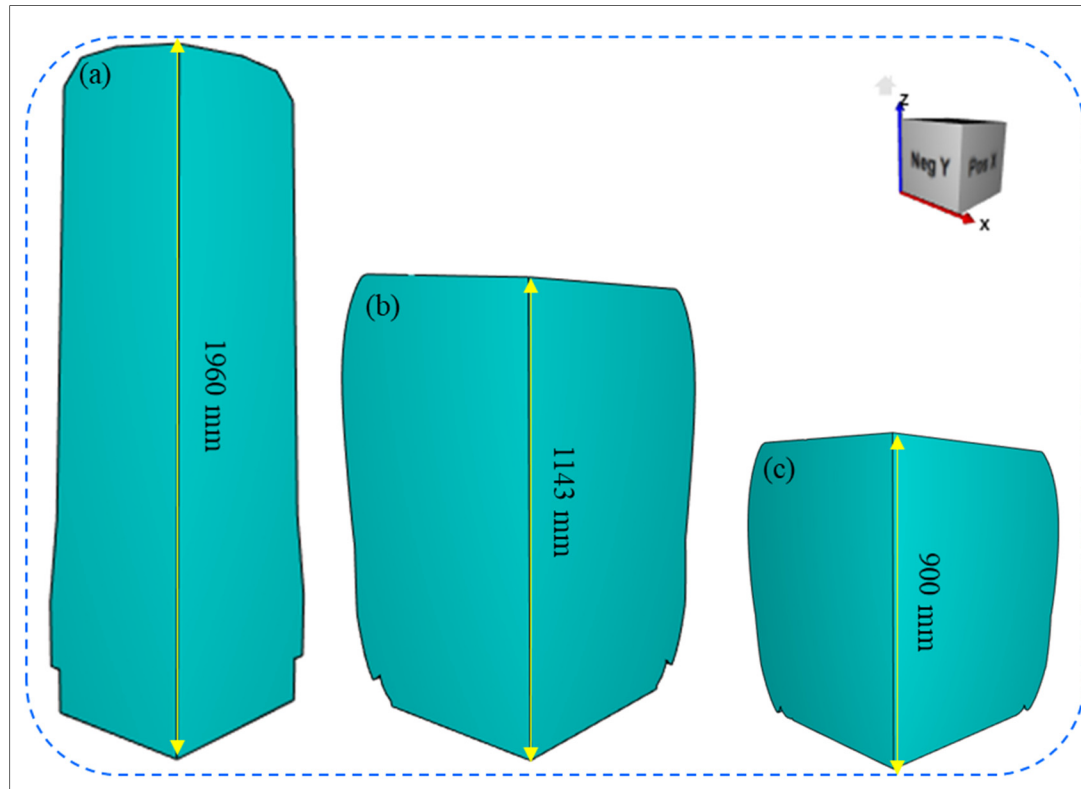
Figure 6.13 Ingot geometry of (a) As-cast (b) Original design (c) Modified design

The strain distribution of the two simulations is provided in Figure 6.14a and 6.14b. The strain value increases throughout the ingot by increasing the height reduction. Figure 6.14c shows the maximum strain evolution point (D) during the upsetting of two simulations.
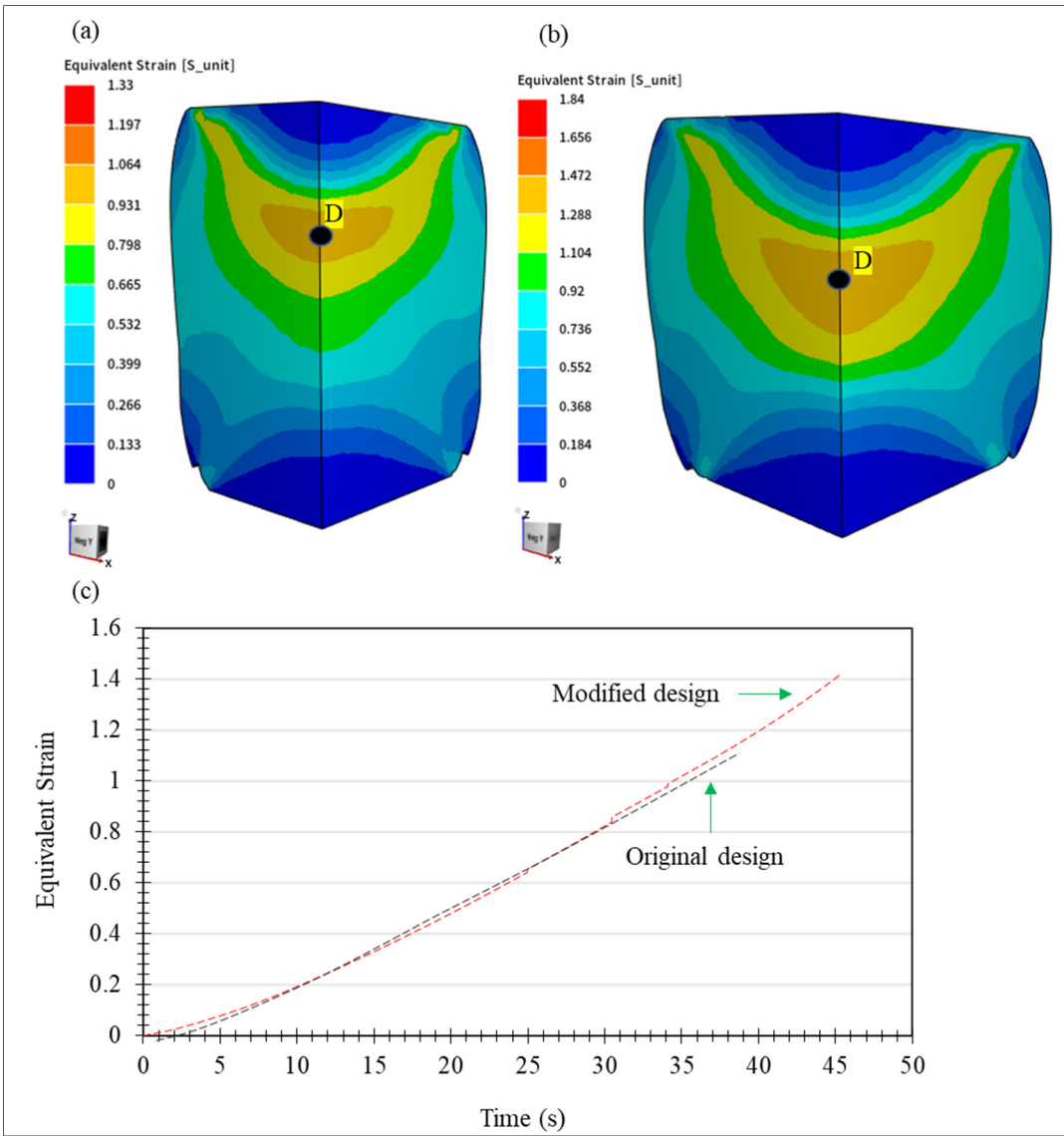
Figure 6.14 Map of (a) Effective strain distribution of old deformation degree (b) Effective strain distribution of new deformation degree (c) Evolution of strain during the upsetting process

As explained above in previous sections, the DRX volume fraction increases with increasing the deformation degree (strain). Figure 6.15a and 6.15b show the map of DRX fraction with higher height reduction. After passing the required amount of deformation for complete DRX, one cycle of recrystallization completes, and again continuous rise of strain leads to the next cycle of DRX phenomena as shown in Figure 6.15c.
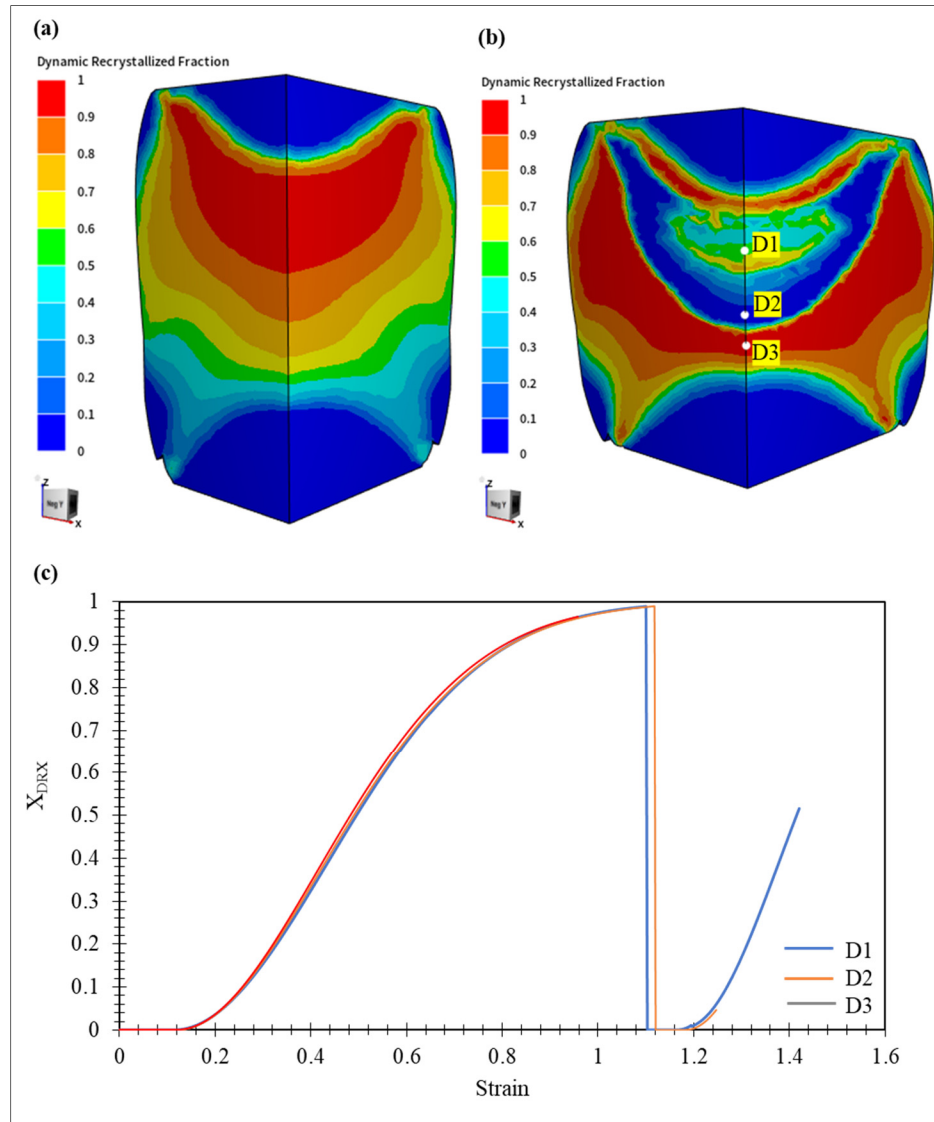
Figure 6.15 (a) Map of DRX fraction with original design (b)
Map of DRX fraction with modified design (c) Comparison of DRX
evolution between three points of modified design

DRX grain size is shown in Figure 6.16. In this figure, D1 and D2 passed the first cycle of recrystallization so the grain size evolution again starts after reaching the critical strain for recrystallization. D1 passes the first cycle of DRX then the second cycle starts with 50% of DRX. D2 which is similar to D1 passes the first cycle but because of the lower strain at that point, the DRX fraction is lower in the second cycle. At the point of D3, the material reaches

100% of DRX but the deformation degree is not enough to go for the second cycle. By increasing the deformation degree, more volume of the ingot undergoes the DRX phenomena, and microstructure evolution increases.
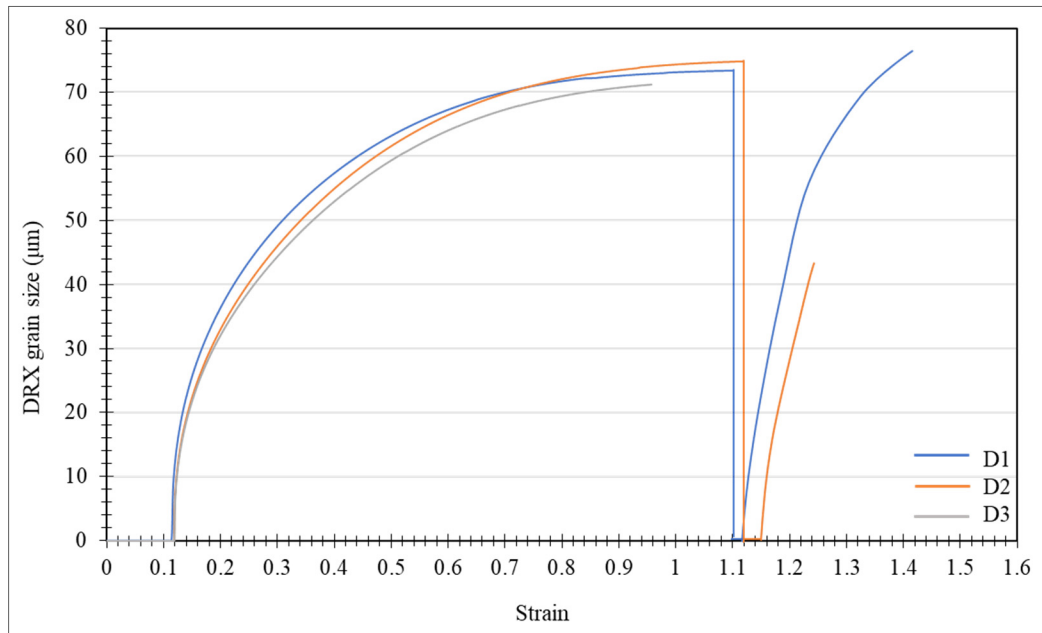
Figure 6.16 DRX grain size evolution of three points with increasing
the deformation degree

Figure 6.17 presents the DRX volume fraction with the comparison between the two simulations. The whole of the ingot is shown instead of ¼ to distinguish the difference between fully recrystallized materials. It is seen that the amount of 100% of recrystallized material increased with increasing strain.
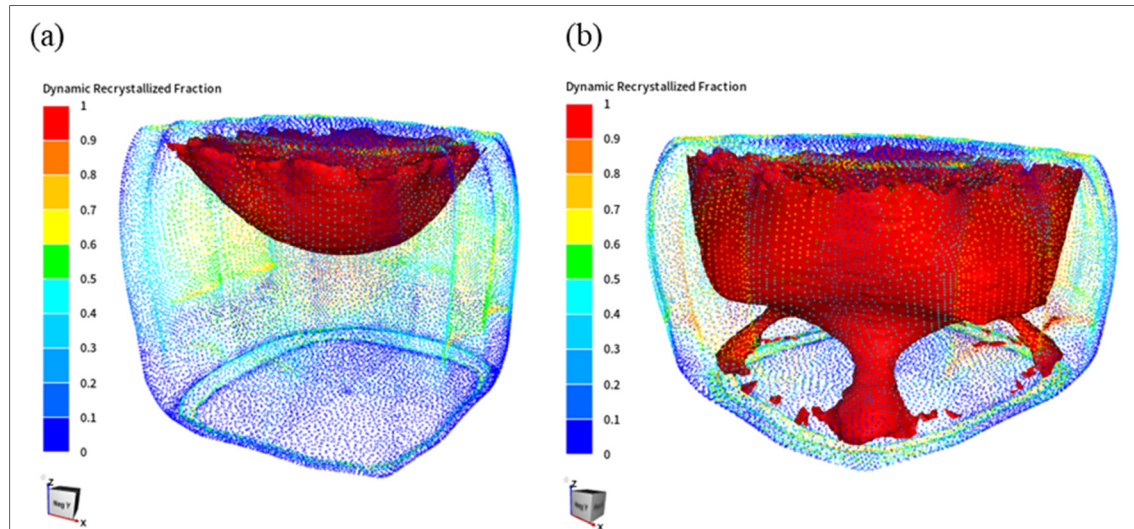
Figure 6.17 Volume fraction of 100% of recrystallization of (a)
Old deformation degree (b) New deformation degree

6.4.4   Effect of Working Parameters on Damage Criteria

As explained in Chapter 5, damage criteria are determined to find and predict the location with a higher risk of cracking susceptibility. The fracture model proposed by Latham and Cockroft (Cockcroft & Latham, 1968) involves standardizing stress by dividing maximum stress by equivalent stress. The simulation results show that the surface of the ingot has the highest value of the damage criteria, and the minimum value belongs to the center of the ingot. The evolution of this criterion is investigated in 4 different forging schedules. Figure 6.18a shows the distribution of these criteria at the end of the upsetting and the red zone possesses the higher value of the criteria. The higher the damage criteria value means a higher risk of damage and cracking. Figure 6.18b shows the evolution of the damage criteria between two points for all forging schedules.
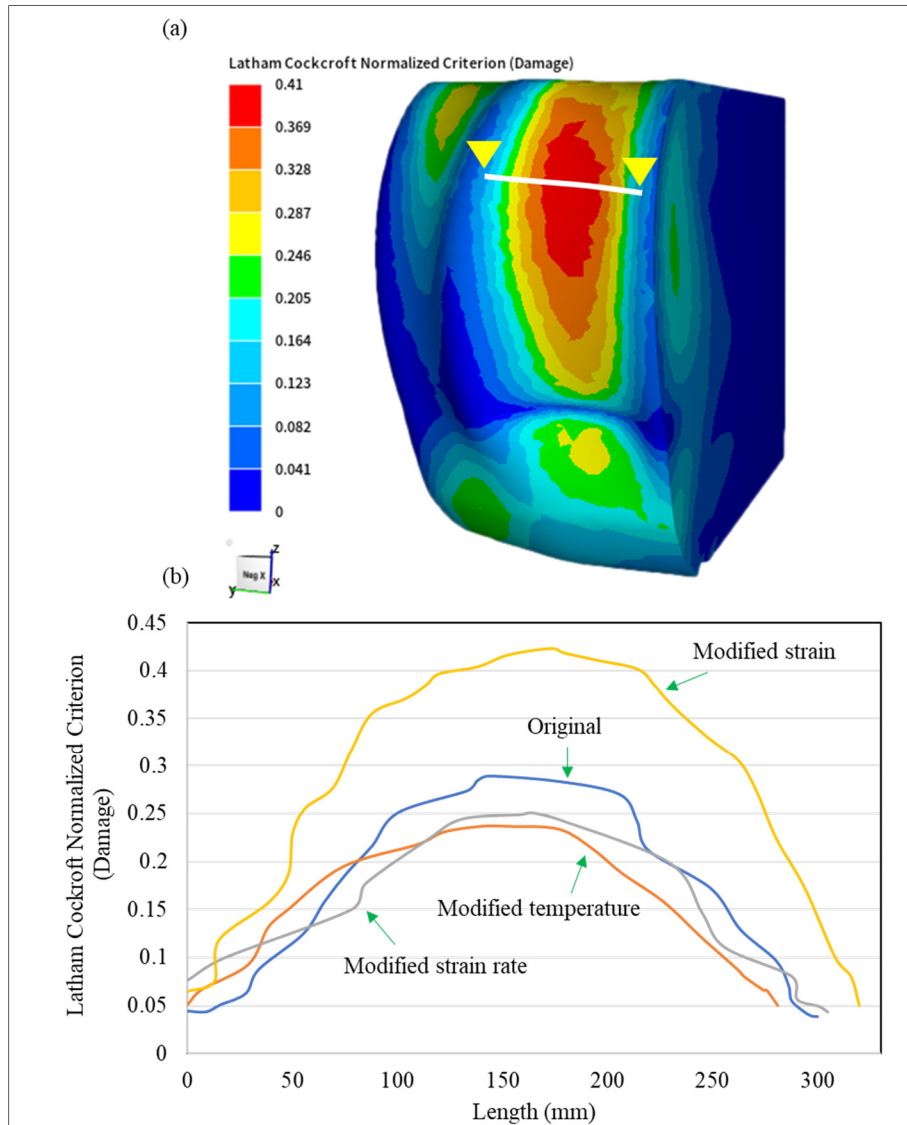
Figure 6.18 (a) Map of Latham Cockroft criterion (b) evolution of
damage criteria between two points of 4 deformation state

Figure 6.18 shows that strain increment has the highest impact on damage criteria evolution
and doubled the value. However, strain rate and temperature reduction lead to decreasing the
damage value. Figure 6.19 shows the histogram chart for all simulation designs. The damage
criterion, DRX fraction, final grain size, and critical strain were compared together. Among
three forging schedules, increasing strain (decreasing the final height) has the most impact on
the microstructure evolution and all microstructure parameters.
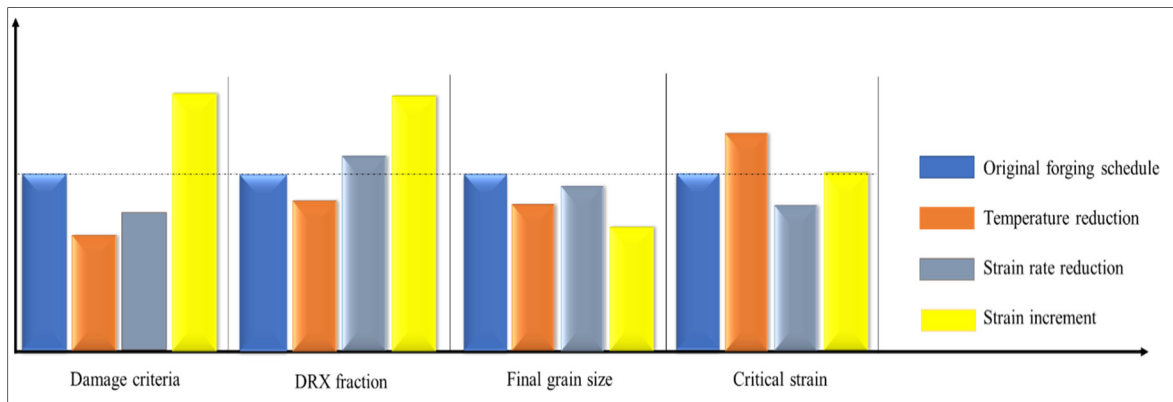
Figure 6.19 Comparison between all designs of upsetting process and their effect on microstructure evolution

6.5   Conclusion

Based on the data obtained from thermomechanical tests and metallographic research, the mathematical models for microstructure evolution of X12Cr13 steel were developed in this chapter. The thermo-mechanical coupled finite element method with derived microstructure evolution models was developed to investigate how processing parameters, such as temperature, strain rate, and strain affect microstructure evolution during the hot upsetting. The results show that the distribution of DRX fraction is not uniform after upsetting. The results of microstructure observations confirmed this non-uniformity. The simulation and experimental results depict that the region with a higher deformation degree experiences the higher DRX fraction. The simulation findings demonstrate that the DRX fraction reduces with decreasing temperature and increases with increasing strain and strain rate. With a reduction in strain rate and an increase in deformation temperature, the critical strain for the start of DRX increases. The predicted average DRX grain size decreases with decreasing temperature and increases with strain and decreases with decreasing strain rate. The parameter that mostly affects the damage criteria is deformation degree. Increasing strain increases the damage criteria significantly and makes the ingot susceptible to cracking during the upsetting. The comparison between the predicted and experimental findings reveals a good degree of agreement,

demonstrating the applicability of the thermo-mechanical coupled finite element method for predicting the microstructure evolution of the hot upsetting process for X12Cr13 steel.

All findings driven from previous chapters were employed to meet the last and main objective of this project which was the optimization of the large size forging process of MSS including three steps (Upsetting, FM, and Cogging), and it is written as a 7th CHAPTER. The results of CHAPTER 7 will be submitted to The *ISIJ International in January 2023*.

CHAPTER 7

OPTIMIZATION OF OPEN DIE FORGING OF 13.5-TON MARTENSITIC STAINLESS STEEL FORGING INGOTS THROUGH STRAIN CONTROLLING

Summary

Producing sound forgings of large size ingots necessitates the compression of defects generated during the solidification process of the steel ingot. An open die forging process for producing large size ingots has been optimized through the three-dimensional finite element method (FEM). This scale of production is very expensive and it is very difficult to find the best process parameters by trial and error within an industrial environment. In this chapter, the FEM was used to optimize the 13.5-ton forging process which includes 3 steps, Upsetting, FM, and Cogging. From an analysis of the results, changing the strain has the greatest influence on the microstructure evolution during forging. The map of DRX fraction and DRX grain size at the last step of the process in the optimized design show an increase in the uniformity of microstructure evolution in comparison with the original design. Moreover, more and more amount of material is recrystallized at the end of each step in the optimized design. The damage analysis in the optimized design shows there is no significant increase in damage criteria by increasing the strain.

7.1   Literature Review

A workpiece is deformed using flat or shaped dies with a series of repetitive blows during the metal forming process known as "open die forging". The operation is started by significant height reduction and followed by the workpiece rotation between blows. The large components such as turbine shafts, spindles, and rolling mill rolls, made in heavy forging industries, are in great demand. The forging process has always been an industrial challenge due to achieving the desired geometry as well as a high-quality product. The first step in the production of such a large component is the use of open die forging which usually starts with "Upsetting" by reducing the ingot height. After that, the ingot is deformed by repetitive pressing and alternate rotation until it reaches the final target shape. Several parameters define the quality of the final product such as ingot shape, working parameters, die geometry, pass schedule, etc. (Dudra & Im, 1990).

It is difficult to determine optimal process parameters in an industrial environment by trial and error for producing large components. Therefore, the open die forging process has been modeled with the aid of FE calculations (Choi et al., 2006). The forging process was optimized by changing the die geometry, number of passes, and die velocity. Kotous et al. (Kotous, Kubec, Duchek, & Studecký, 2020) optimized the open-die forging by using the V-shape die geometry and analyzed the fracture condition by changing the shape of the die. Wolfgarten et al. (Wolfgarten & Hirt, 2016)worked on the optimization of open-die forging with superimposed manipulator displacements. They added extra angle (bending) to the ingot during forging by a manipulator to improve the properties. Choi et al. (Choi et al., 2006) investigated the effect of round shape die on the non-uniformity of deformation. Among the various studies worked on the forging process optimization, few researchers optimized the process by modification of the process parameters particularly for MSS.

In this chapter, the three-dimensional finite element method (FEM) was performed in order to optimize the microstructure evolution of the ingot by analyzing the effect of the working

processes such as temperature, strain rate, and strain. Through FEM simulation in combination with the experimental sectioning investigation, all thermomechanical and microstructure models have been successfully proposed. Based on this proposal, the optimized working parameters were defined from the previous chapter and the forging process was redesigned with the aim of improving the quality by increasing the deformation uniformity and improving the properties.

7.2   Simulation of Three Stages Open Die Forging (Upsetting, FM, Cogging)

All meshing information, boundary conditions, and material properties of MSS were explained in the previous chapter. The convergence tolerance was used in the calculations. Figure 7.1 shows the process of the as-cast manufacturing and CAD model of the ingot. Figure 7.2 shows the overall forging sequence from upsetting to a square cross-section bar. Forging of ingot after casting starts with upsetting which is the most important step of the process because having the greatest amount of deformation at one hit leads to the breakdown of the chemical (macrosegregation) and microstructural structure (as-cast dendritic) inhomogeneity. The next step of forging is called FM (Free from Mannesmann effect) when the ingot is rotated 90° and another height reduction was performed. The previous two stages have the most amount of deformation degree which makes them very important. The final step of forming is called cogging which the ingot is placed between two dies and pressed repetitively with several passes. During the cogging process, the ingot becomes longer after each pass. The ideal forging process includes breaking up the as-cast and coarse grain structure and replacing it with finer grains, healing the gas porosity, voids, micro-shrinkage, and all segregation inherent in the cast metal. The size of the ingot defines the cogging process time and the metal needs reheating to continue the next steps of forging to remain malleable.
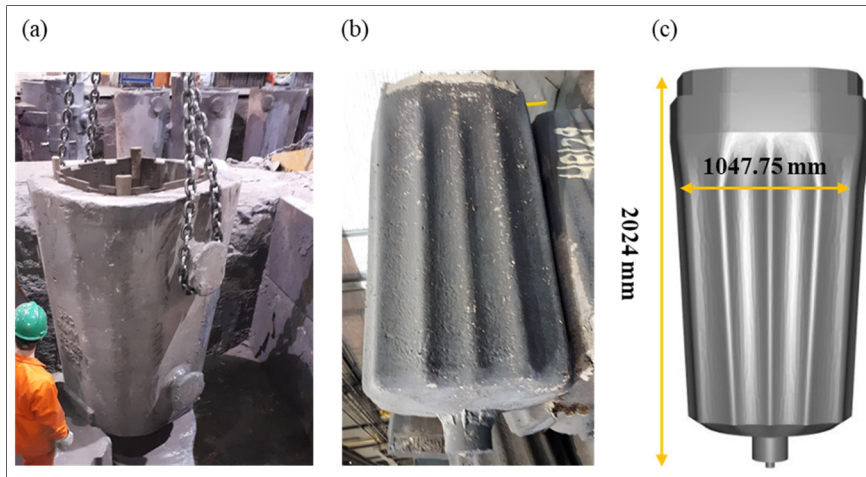
Figure 7.1 (a) Ingot mold (b) As-cast 42" ingot
(c) CAD model of 42" ingot
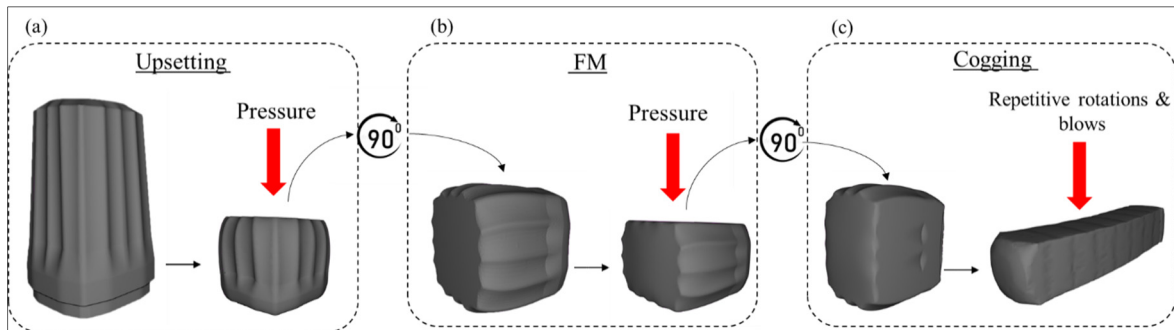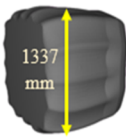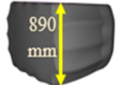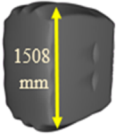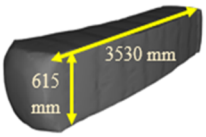
Figure 7.2 Forging process (a) Upsetting (b) FM (c) Cogging

The implementation of the constitutive equation and microstructure equation and their validation with experimental data were explained in the previous chapter. The simulation parameters of the whole process, upsetting to cogging, were measured from industrial data shown in Table 7.1.

Table 7.1 Simulation parameters of three forging steps (Upsetting, FM, Cogging)

Upsetting

Simulation Parameters	Value
Unit	SI
Young's modulus at 1200°C (GPa)	96
Elastic Modulus (GPa)	200
Poisson's ratio	0.35
Forging temperature °C	1200
Friction factor	0.35
Solution step definition (s/step)	With time 0.04
Die temperature (°C)	400
Environment temperature (°C)	35
Element number of billet	848,140
Node number of billet	168,700
Die velocity (mm/s)	23.35
Initial billet height (mm)	1960
Final billet height (mm)	1143
Process time (s)	35

FM

Die velocity (mm/s)	7.2
Initial billet height (mm)	1337
Final billet height (mm)	890
Process time (s)	52

Cogging

Die velocity (mm/s)	7.2
Initial billet height (mm)	1337
Final billet dimension (mm)	615*615*3530
Process time (min)	14

7.3 Results and Discussion

7.3.1 Preliminary Forging Schedule

FM Simulation Results:

In Chapter 5, the microstructure evolution during upsetting and the effect of working parameters were comprehensively explained. In this chapter, FM and cogging process are analyzed. Figure 7.3 shows the map of the strain, DRX fraction, and grain size at the end of the FM process. It is seen that even after another height reduction, the microstructure in a portion of the top and bottom of the ingot remained unchanged due to the low amount of deformation in these zones (dead zone). Figure 7.4 illustrate the strain and DRX evolution at two points located in the non-recrystallized region. It is seen that the deformation degree is not enough for DRX initiation even after the FM process.
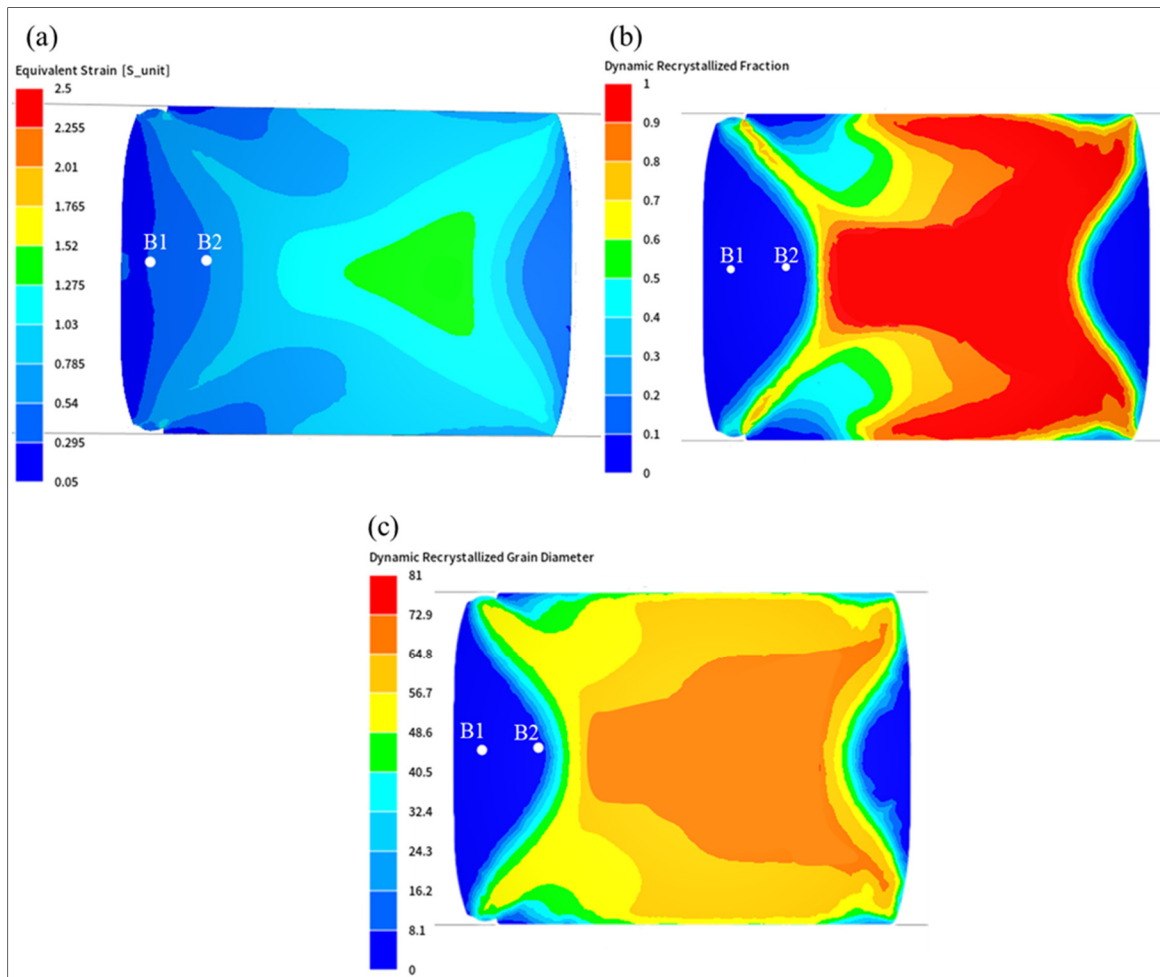
Figure 7.3 Simulation results at the end of FM (a) Strain distribution (b) DRX fraction (c) DRX grain size
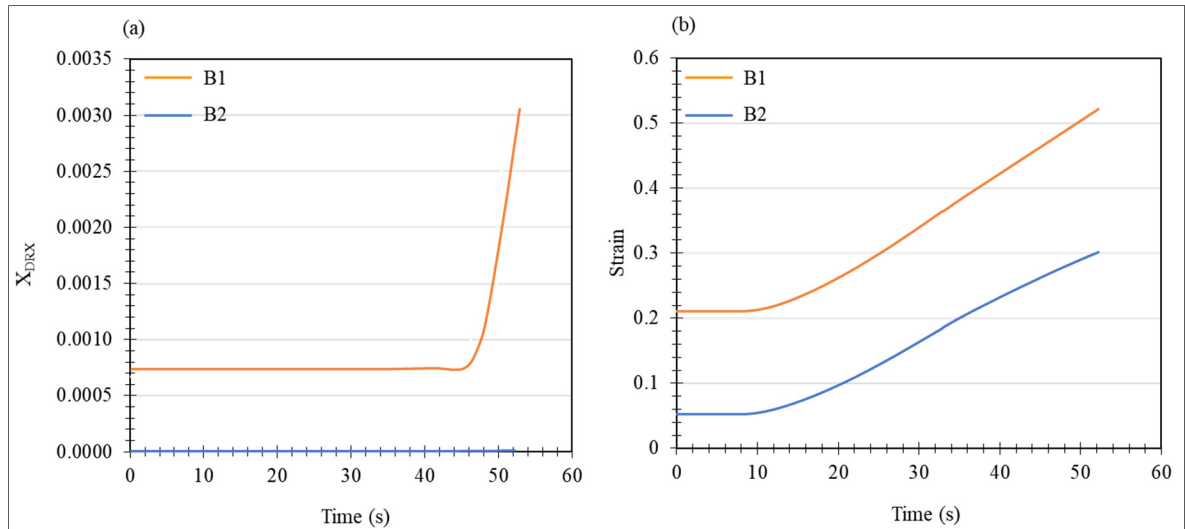
Figure 7.4 Comparison of two sensors during FM (a) DRX fraction (b) Strain

Figure 7.3a shows the strain distribution at the end of FM. DRX fraction distribution and grain size are uneven due to uneven deformation degree throughout the ingot. As compared with the end of upsetting, recrystallized material has increased at the end of the FM while the amount of non-recrystallized material has not changed notably, Figure 7.5.
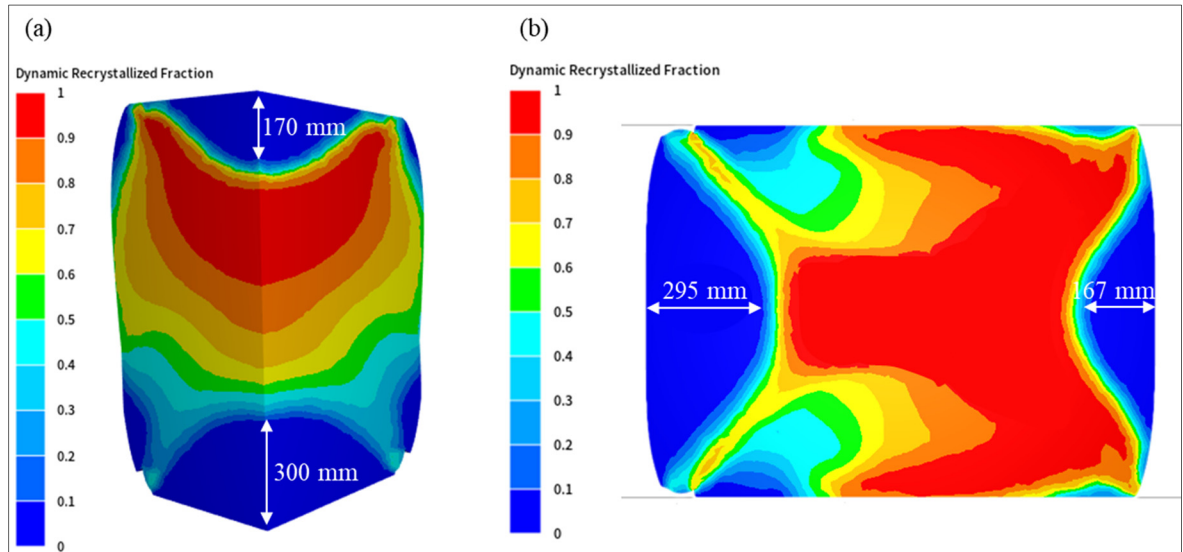
Figure 7.5 Comparison of non-recrystallized material between (a) Upsetting and (b) FM

Cogging Simulation Results:

The next stage of the simulation is cogging with several passes and hits. The number of passes, the amount of height reduction in each hit, and the die velocity were calculated from the press data recorded by industry's equipment. During cogging, the ingot is grabbed by a forging manipulator and rotated after each pas until a square cross-section, Figure 7.6a, the tooling for the press is a set of two flat dies, the upper die which is connected to the hydraulic press, and it moves up and down to form the ingot, Figure 7.6b. Another die, lower die, is fixed on the ground. The cogging process sequences in the industry are shown in Figure 7.7 and the initial and final ingot size for the cogging process is shown in Table 7.1.

Figure 7.6 (a) Forging manipulator (b) Forging Die
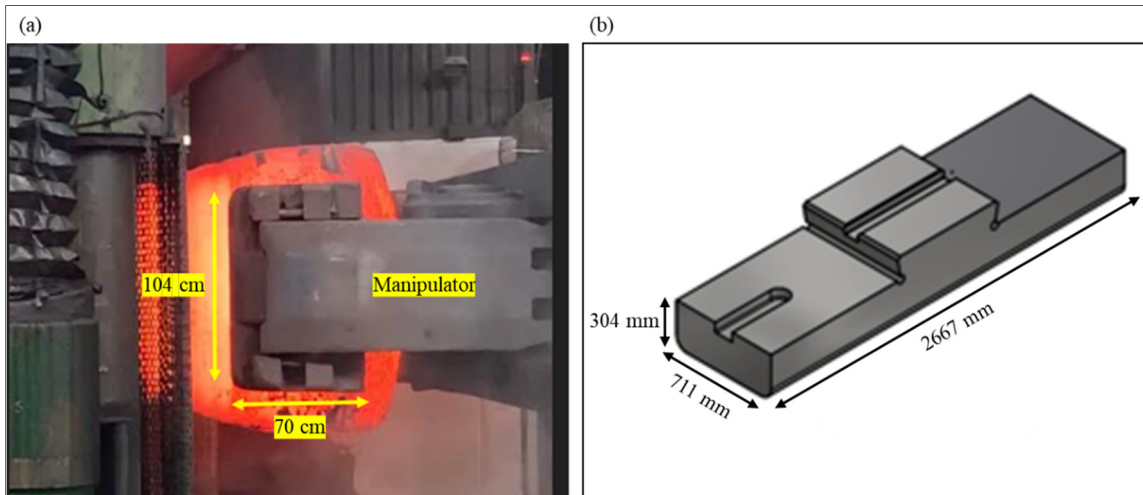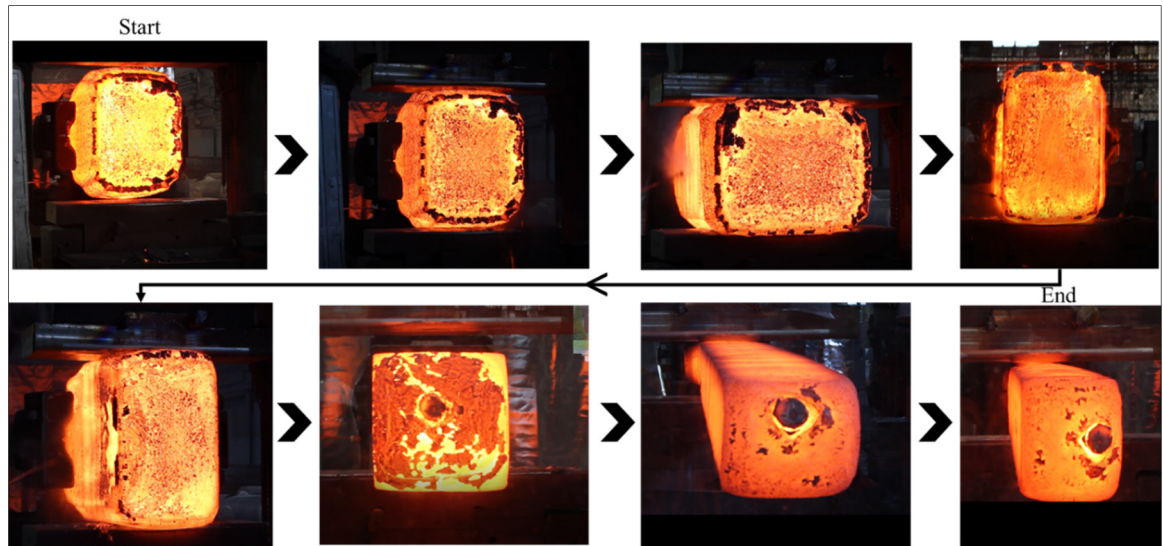
Figure 7.7 Industrial Cogging process at Sorel

The strain distribution, DRX fraction, and DRX grain size are shown in Figure 7.8. It is seen that even after several passes and reduced cross-section, the microstructure is non-uniform and the deformation degree is low in some regions which causes not full recrystallization. The lower amount of DRX is related to the top and bottom of the ingot which experiences the lowest deformation degree.
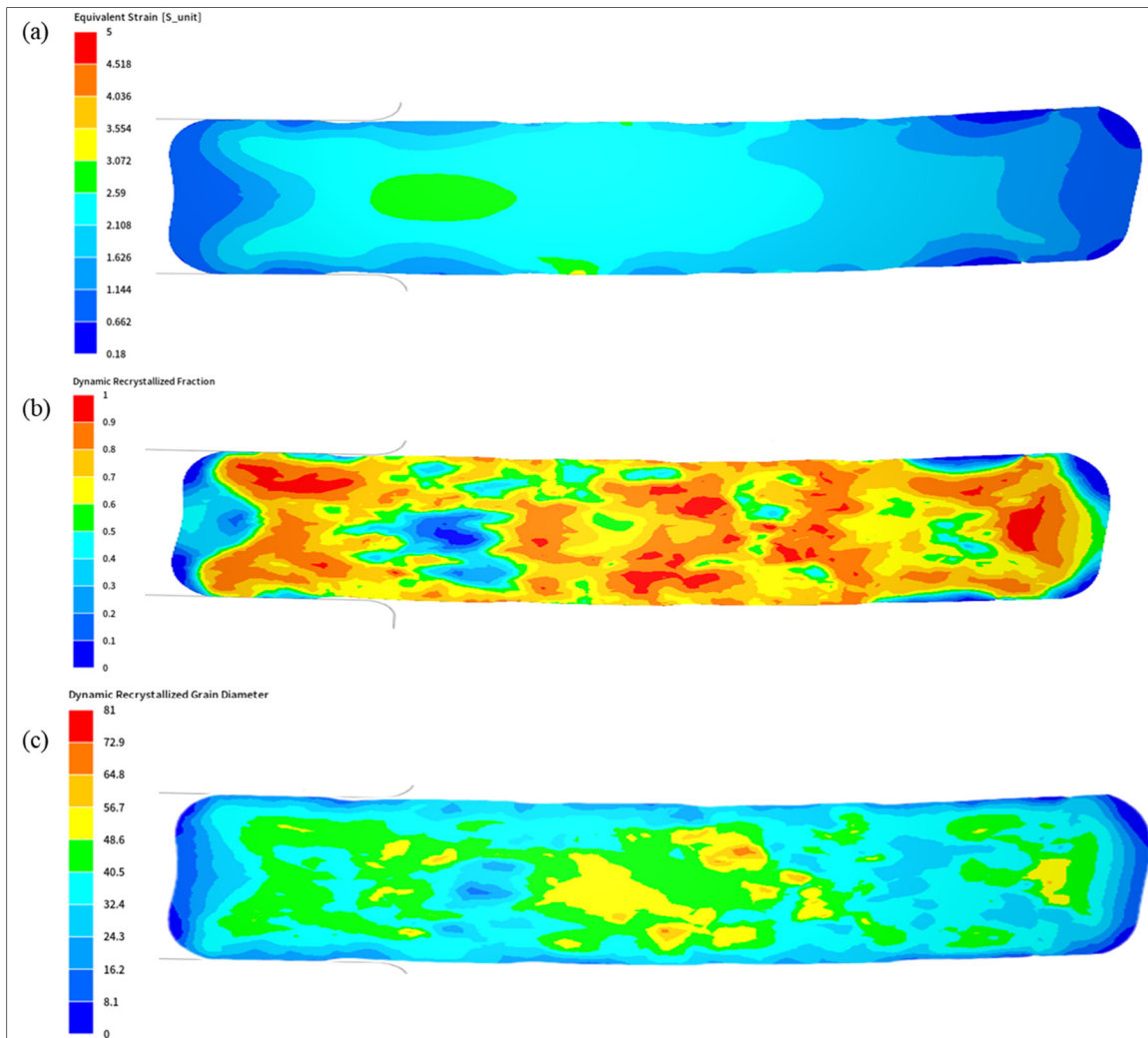
Figure 7.8 Cogging simulation results of the distribution of (a) Strain (b) DRX fraction (c) DRX grain size

As explained in Chapter 5, one of the most challenging forging defects is surface cracking occurs due to different factors. With the aim of the fracture model, the region which is more susceptible to cracking and damage was predicted. As forging is a multiaxial process, it is difficult to analyze fractures during forging. Consequently, the fracture formula must consider multiple axes. The formula of Cockcroft and Latham has been used for this purpose which is implemented in Forge NxT software using a user subroutine, explained in Chapter 5. Figure 7.9 shows the distribution of damage criteria at the end of cogging. It is seen that surface of

the ingot has the highest value of damage criteria and is more susceptible to cracking rather than other parts of the ingot.
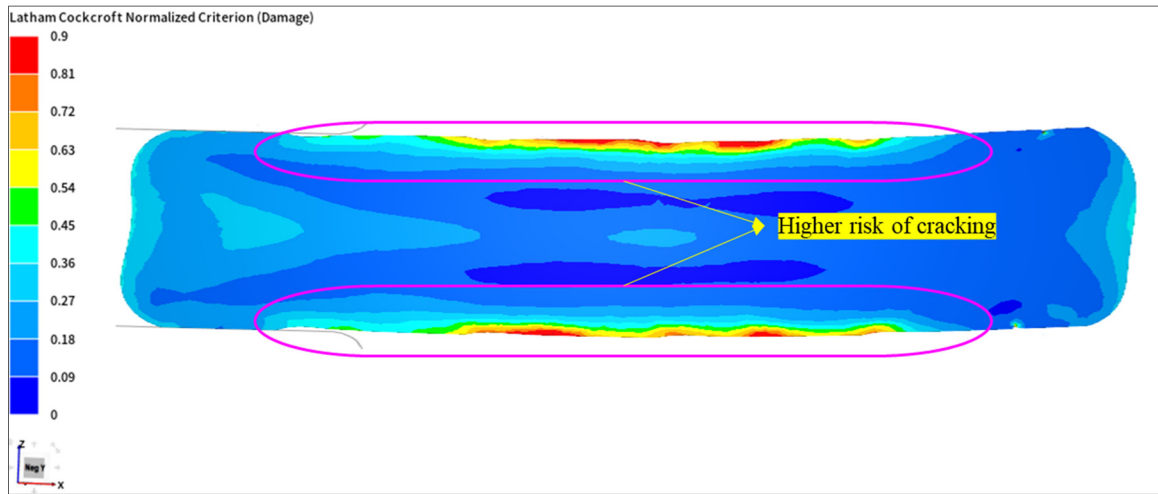
Figure 7.9 Distribution of Craft-Latham damage inside deformed ingot after cogging

Within the context, both the experimental and simulation results revealed that there is a non-uniformity in strain distribution and microstructure evolution even after cogging steps. According to microstructure observation, the cracking occurs at the surface of the ingot and propagates inside the ingot. The simulation results demonstrate this phenomenon in which the damage value is higher at the surface rather than other parts of the ingot. Therefore, according to the effect of working parameters on the microstructure evolution and damage criteria, a new forging schedule was designed to optimize the properties of the forged ingot.

7.3.2 Optimized Forging Schedule

In order to increase the uniformity of the microstructure evolution and based on the effect of working parameters investigated in Chapter 6, a new forge plan was designed. In Chapter 6, it is found that changing the final height or increasing the strain has the most impact on the microstructure evolution and increases the amount of recrystallized material. In this new design, the only parameter that has changed is the final height (1000 mm) which is bigger than the selected one in chapter 6 due to the industrial limitation in height reduction. All simulation

parameters except the final height are the same as Table 7.1. Figure 7.10 shows the strain distribution, DRX fraction, and the DRX grain evolution at the end of upsetting and compared with the original design. It reveals that more volume of material undergoes deformation and the dead zone volume is reduced, Figure 7.10a and 7.10b. Regarding DRX fraction, more volume of the material is recrystallized with the new design and even in some parts of the ingot the material finishes the first cycle of DRX and starts the new one, yellow dotted lines in Figure 7.10d.
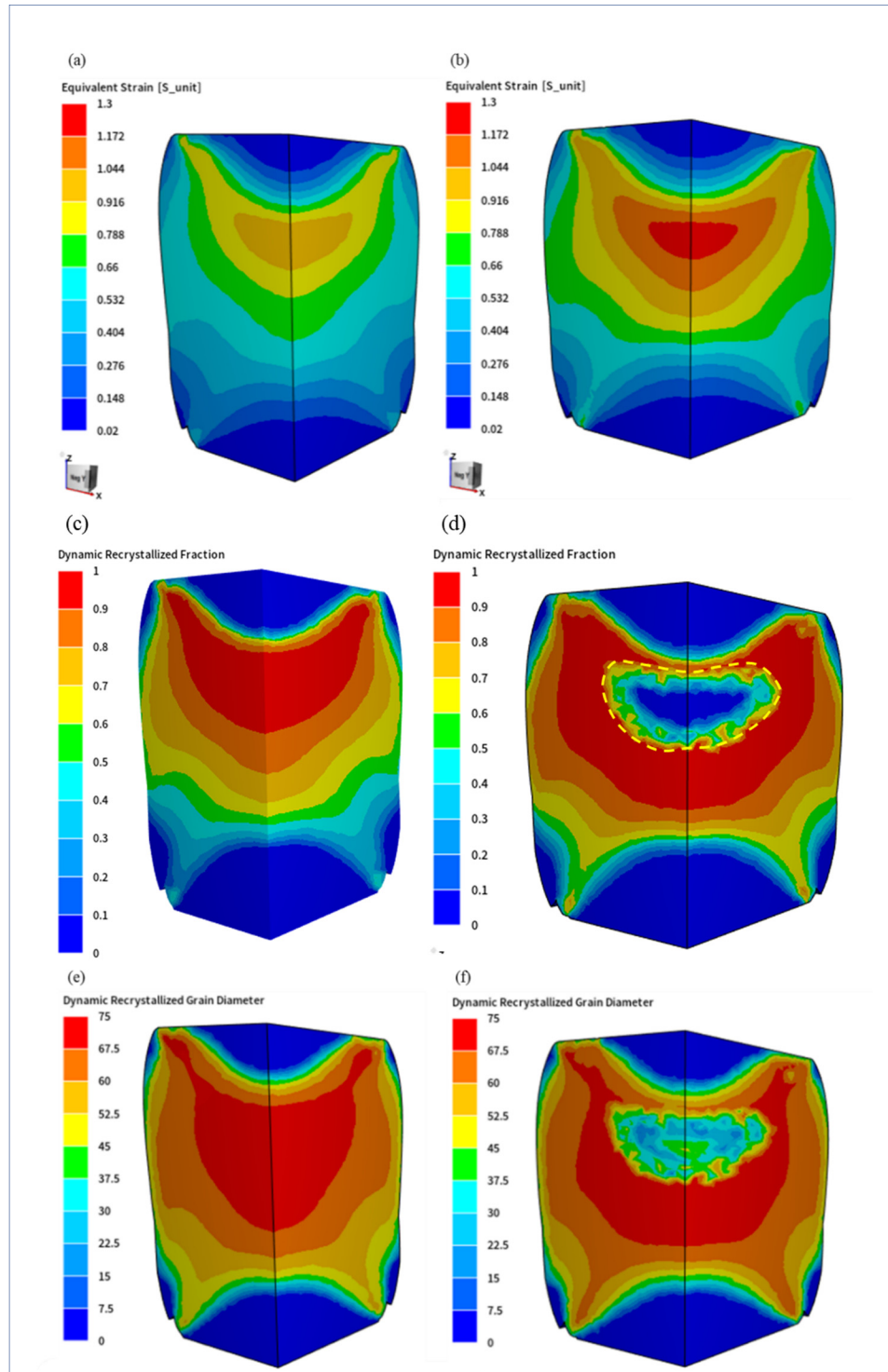
Figure 7.10 Strain distribution (a, b) DRX fraction (c, d) DRX grain size (e, f) at the end of upsetting for (a, c, e) Original design and (b, d, f) Optimized design

By rotating the ingot 90°, the FM simulation was conducted. Figure 7.11 shows the comparison between the working parameters of the original and old design. Similar to the upsetting, deformation degree and DRX fraction increased notably in the new design.
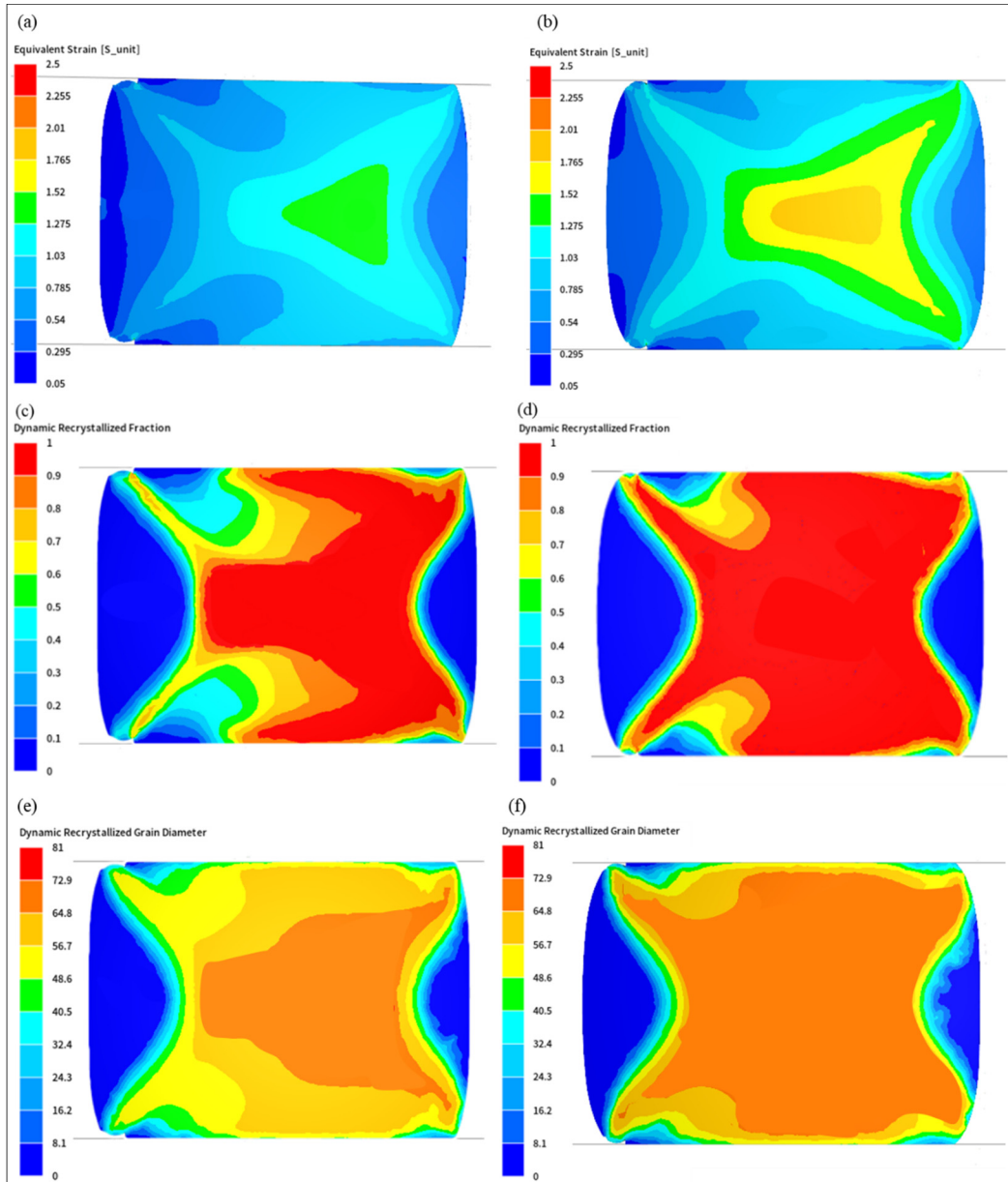
Figure 7.11 Strain distribution (a, b) DRX fraction (c, d) DRX grain size
(e, f) at the end of the FM for (a, c, e) Original design and
(b, d, f) Optimized design

The cogging simulation and sequences were shown in Figure 7.7. The deformed ingot after FM process with all histories of the results was used for cogging simulation. Figure 7.12 shows the distribution of the working parameters.
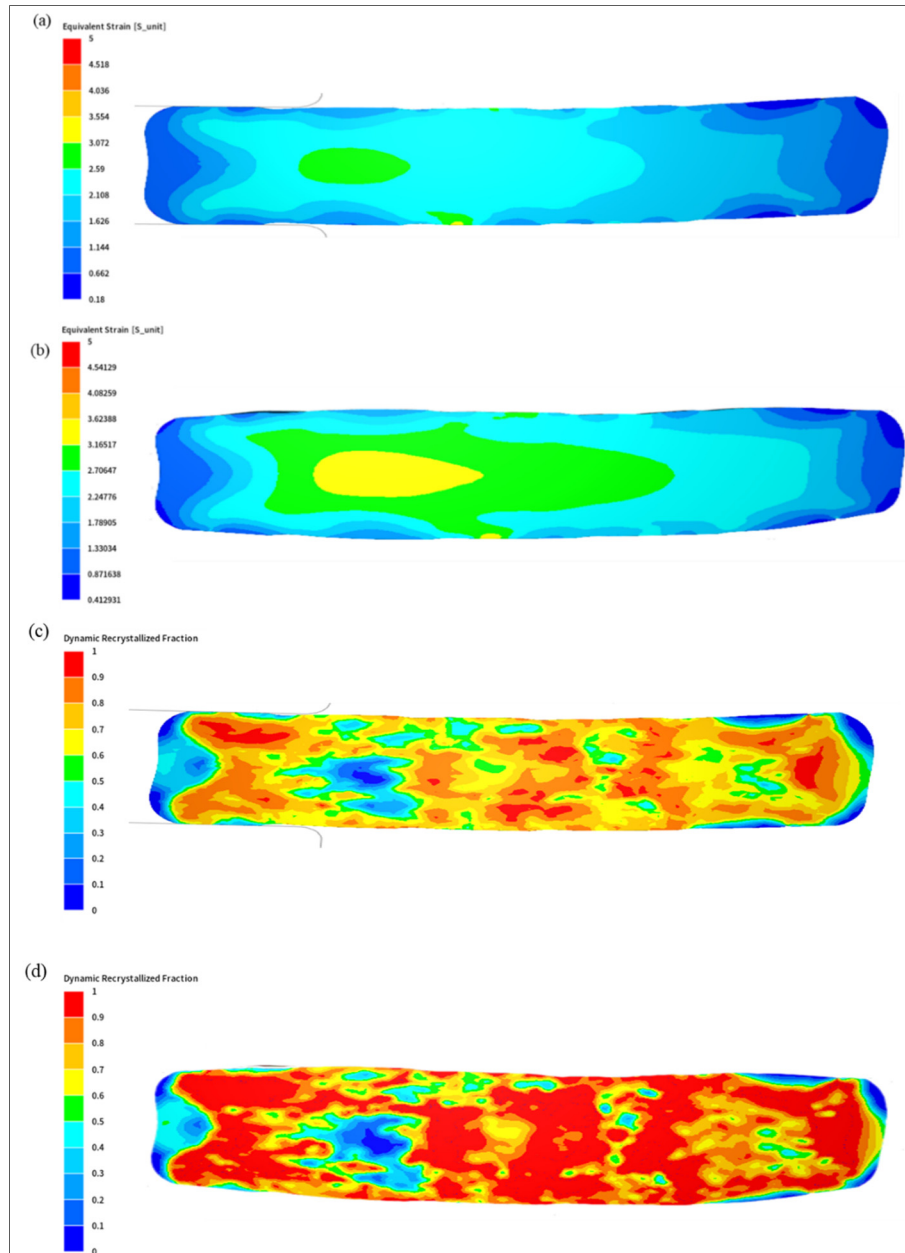
Figure 7.12 Strain distribution (a, b), DRX fraction (c, d),
DRX grain size (e, f) at the end of the cogging for (a, c, e)
Original design and (b, d, f) Optimized design (continue)
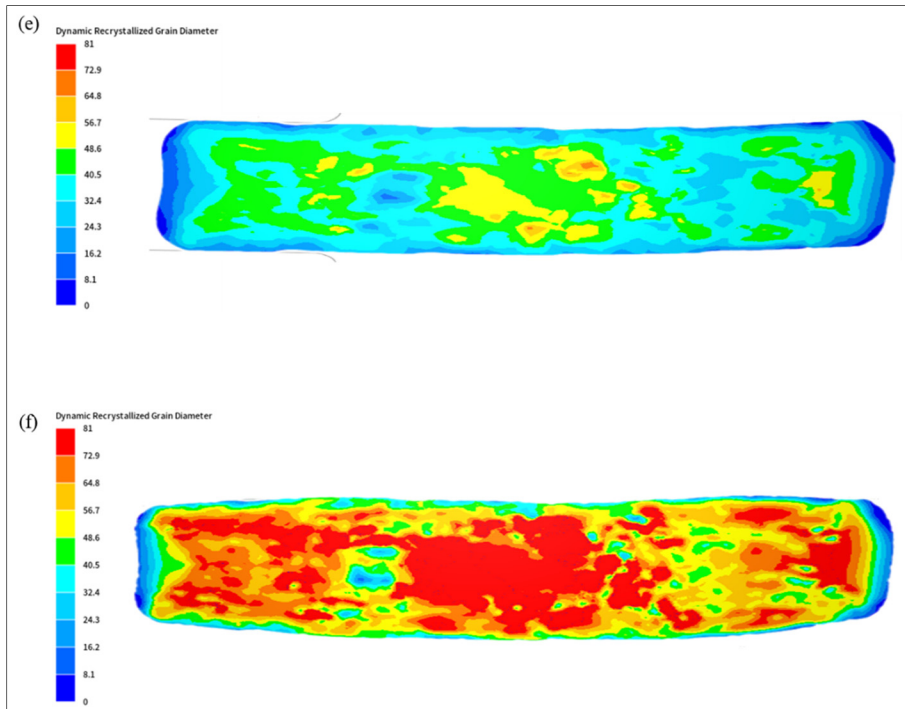
Figure 7.13 Strain distribution (a, b), DRX fraction (c, d),
DRX grain size (e, f) at the end of the cogging for (a, c, e)
Original design and (b, d, f) Optimized design

According to Figure 7.12, the distribution of all parameters including strain, DRX fraction, and DRX grain size has become more even in comparison with the original design after cogging. This means that by reducing the final height of the billet in the upsetting step, the microstructure evolution has increased significantly and there is a shrinkage in the dead zone area. Figure 7.13 displays the damage criteria evolution of old and new forging design, Figures 7.13a and 7.13b respectively. As it is shown, reducing the initial height has not changed the distribution of damage criteria which means that the new design has not increased the risk of surface cracking. Therefore, the new design is applicable in the industry.
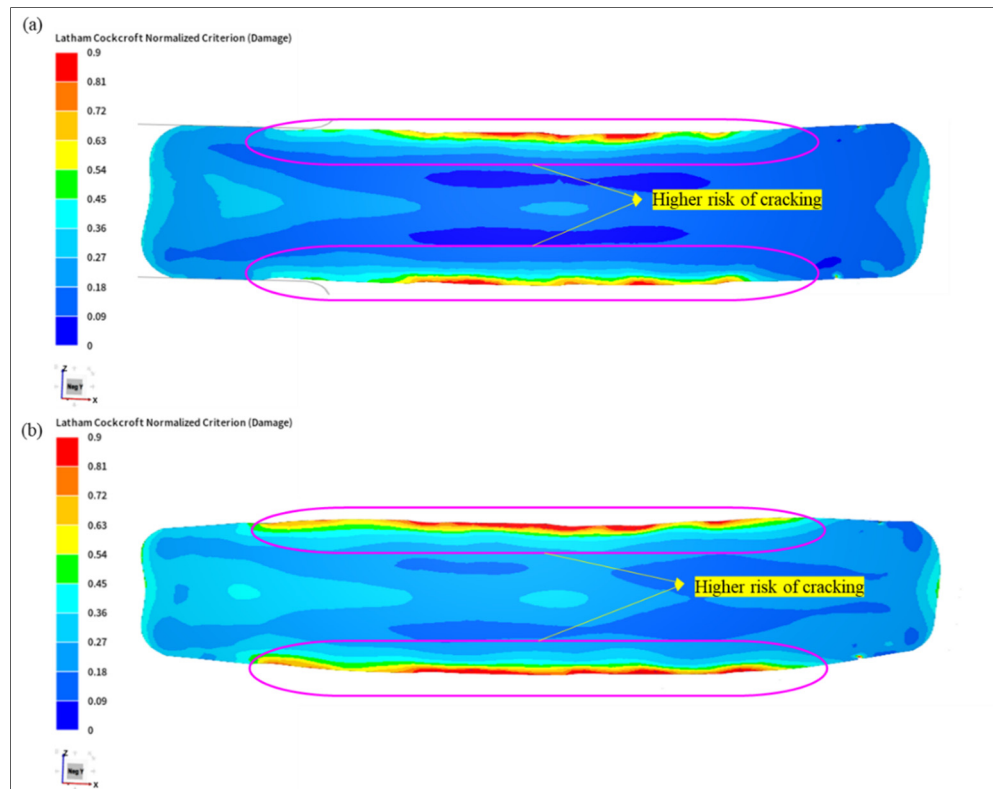
Figure 7.14 Distribution of Craft-Latham damage inside deformed
ingot after cogging (a) old design (b) new design

7.4   Conclusion

The simulation of the hot forging process, upsetting, FM, and cogging, on X12Cr13 MSS ingot has been done using Forge NxT 3.1. After designing the new forge plan, the following observations are explained:

1. With the increase of strain, the final height in the upsetting step, the bigger volumes of the ingot underwent deformation and the dead zones shrunk significantly. The volume of the fully recrystallized material has increased at the end of cogging and the DRX distribution has become more even.

2. By increasing forging strain, the grain size was distributed more evenly and the homogeneity of grain size increased.

3. Changing the forging strain has not affected the damage criteria distribution notably which means that with the new forging design the cracking susceptibility has not increased.

CONCLUSION

In forging and manufacturing industries, producing a product with acceptable precision of shape dimensions of the final product, quality, and the desired properties is a determining factor in keeping the competitivity in a very challenging market. Particularly, in order to obtain the optimum mechanical properties in a repeatable manner it is critical to understand the relationship between microstructure development and hot forging (i.e., thermomechanical) variables. Forging process optimization in heavy manufacturing industries such as oil, gas, aerospace, automotive is difficult due to the expensive and time-consuming process of trial and error. Microstructure based simulation could therefore be an excellent alternative advanced manufacturing tool to achieve the above objective in a rapid and reliable way. However, the most difficult challenge is to identify the most important fundamental mechanisms controlling microstructure evolution and quantify their impact at large scale. In this study, the constitutive equations describing microstructure evolution of a of a martensitic Stainless steel were determined and changes in the microstructure during the entire hot forging process of a 13.5-ton ingot, including upsetting, FM, and cogging were modeled and experimentally validated. Numerical modeling of the forging process was carried out using Forge NxT 3.1® material forming simulation software which allows for the thermomechanical simulation of the plastic processing process. The following are the listed conclusions of all objectives of this research:

1.   First objective achievements:

As mentioned in Chapter 1, the large ingots in the as-cast state include several defects and segregations that deteriorate the mechanical properties, and an optimum design of the forging process could reduce/eliminate these heterogeneities. Therefore, as a first step, the microstructure evolution and phase precipitation during solidification of large size MSS ingot were characterized. The parameters that change the morphology of the phase precipitated were determined. The results show how forging temperature affects the quality of final forged products due to the presence of the eutectic phase. Finally, the suggested forging temperature was proposed to improve the mechanical properties.

2.   Second objective achievements:

The hot compression tests of X12Cr13 MSS alloy at different temperatures of 1050-1200 °C and strain rate of 0.001-1 s^{-1} were carried out to establish a precise model that could predict the high-temperature flow stress. Two types of constitutive models (Hansel-Spittle model and SC-Arrhenius model) were established and compared with each other to predict the hot deformation behavior of the studied alloy. The validity of the Arrhenius model was confirmed showing a more accurate prediction than the Hansel-Spittle model. Therefore, it was integrated into the finite element code to simulate the hot compression process for verification of the model. This microstructure-based model could predict the effect of working parameters on microstructure evolution under different working conditions. The microstructure observations of all deformed samples showed that the DRX fraction increases with decreasing strain rate and increasing temperature. Moreover, with increasing strain rate and decreasing temperature, grain size decreases.

3.   Third objective achievements:

After developing the microstructure-base constitutive model, the next objective was to predict the microstructure evolution of a large size ingot during the open die forging process. The constitutive equation and microstructure evolution models were implemented into the finite element code by writing a user subroutine and the coupling of the models was done for the first time for a martensitic stainless steel. The FEM simulation results that were integrated with the theoretical models to predict the deformation behavior and microstructure evolution of the X12Cr13 alloy are in good agreement with the experimental findings. Based on the simulation work, it was possible to mapping the entire ingot grain size distribution map; thereby, allowing for optimum selection of upsetting process parameters. The simulation findings demonstrate that the DRX fraction reduces with decreasing temperature and increases with increasing strain and strain rate. The critical strain for initiation of DRX decreases with the decrease of the strain rate and increases with the decrease of deformation temperature. The size of the predicted

average DRX grain becomes finer with the decrease of temperature and becomes coarser with the increase of the strain and decrease of the strain rate. The parameter that mostly affects the damage criteria is deformation degree. According to the effect of working parameters on microstructure evolution, increasing strain, increases the damage criteria significantly and makes the ingot susceptible to cracking during the upsetting.

4.   The last objective achievements:

Optimizing the entire forging schedule was the last and a very important goal of this project, particularly, for the industrial partner. To investigate the effect of working parameters on the microstructure evolution during forging, three simulations were conducted by changing the temperature, strain rate, and strain. A new forge plan was designed and the results show that a much larger volume of the ingot could reach the critical strain for DRX with a significant increase of the volume of fully recrystallized material at the end of the cogging process. Moreover, the grain size was distributed more evenly, and the homogeneity of grain size distribution increased. The damage analysis of the new forging schedule showed that the cracking susceptibility has not increased compared to the existing process; thereby, further confirming the benefits of the proposed modified forging schedule.

LIST OF REFERENCES

Akhmed'yanov, A. M., Rushchits, S. V., & Smirnov, M. A. (2016). Hot deformation of martensitic and supermartensitic stainless steels. *Materials Science Forum*, *870*. https://doi.org/10.4028/www.scientific.net/MSF.870.259

Alaneme, K. K., & Okotete, E. A. (2019). Recrystallization mechanisms and microstructure development in emerging metallic materials: A review. *Journal of Science: Advanced Materials and Devices*, Vol. 4. https://doi.org/10.1016/j.jsamd.2018.12.007

Anoop, C. R., Prakash, A., Giri, S. K., Narayana Murty, S. V. S., & Samajdar, I. (2018). Optimization of hot workability and microstructure control in a 12Cr-10Ni precipitation hardenable stainless steel: An approach using processing maps. *Materials Characterization*, *141*. https://doi.org/10.1016/j.matchar.2018.04.025

Apel, M., Böttger, B., Rudnizki, J., Schaffnit, P., & Steinbach, I. (2009). Grain growth simulations including particle pinning using the multiphase-field concept. *ISIJ International*, *49*(7). https://doi.org/10.2355/isijinternational.49.1024

Ashtiani, H. R. R., & Shahsavari, P. (2016). Strain-dependent constitutive equations to predict high temperature flow behavior of AA2030 aluminum alloy. *Mechanics of Materials*, *100*. https://doi.org/10.1016/j.mechmat.2016.06.018

Babu, K. A., Mandal, S., Athreya, C. N., Shakthipriya, B., & Sarma, V. S. (2017). Hot deformation characteristics and processing map of a phosphorous modified super austenitic stainless steel. *Materials and Design*, *115*. https://doi.org/10.1016/j.matdes.2016.11.054

Balmforth, M. C., & Lippold, J. C. (2000). New ferritic-martensitic stainless steel constitution diagram. *Welding Journal (Miami, Fla)*, *79*(12).

Banaszek, G., Bajor, T., Kawałek, A., & Garstka, T. (2021). Investigation of the influence of open-die forging parameters on the flow kinetics of AZ91 magnesium alloy. *Materials*, *14*(14), 1–17. https://doi.org/10.3390/ma14144010

Becker, W. T., & Shipley, R. J. (2018). Failures Related to Metalworking. *Failure Analysis and Prevention*, *11*, 81–102. https://doi.org/10.31399/asm.hb.v11.a0003507

Bitterlin, M., Loucif, A., Charbonnier, N., Jahazi, M., Lapierre-Boire, L. P., & Morin, J. B. (2016). Cracking mechanisms in large size ingots of high nickel content low alloyed steel. *Engineering Failure Analysis*, *68*. https://doi.org/10.1016/j.engfailanal.2016.05.027

Boccalini, M., & Goldenstein, H. (2001). Solidification of high speed steels. *International Materials Reviews*, Vol. 46. https://doi.org/10.1179/095066001101528411

Bontcheva, N., & Petzov, G. (2003). Microstructure evolution during metal forming processes. *Computational Materials Science*, *28*(3-4 SPEC. ISS.), 563–573. https://doi.org/10.1016/j.commatsci.2003.08.014

Brozzo, P., Deluca, B., & Rendina, R. (1972, October). A new method for the prediction of formability limits in metal sheets. In Proc. 7th biennial Conf. IDDR . (n.d.).

Burton, J. A., Kolb, E. D., Slichter, W. P., & Struthers, J. D. (1953). Distribution of solute in crystals grown from the melt. Part II. Experimental. *The Journal of Chemical Physics*, *21*(11). https://doi.org/10.1063/1.1698729

Cardoso, P. H. S., Kwietniewski, C., Porto, J. P., Reguly, A., & Strohaecker, T. R. (2003). The influence of delta ferrite in the AISI 416 stainless steel hot workability. *Materials Science and Engineering A*, *351*(1–2), 1–8. https://doi.org/10.1016/S0921-5093(01)01740-3

Castellanos, J., Rieiro, I., Cars, M., Muoz, J., & Ruano, O. A. (2007). Analysis of adiabatic heating in high strain rate torsion tests by an iterative method: Application to an ultrahigh carbon steel. *WIT Transactions on Engineering Sciences*, *57*. https://doi.org/10.2495/MC070221

Chadha, K., Shahriari, D., & Jahazi, M. (2016). Constitutive modelling of ingot breakdown process of low alloy steels. *Metallurgia Italiana*, *108*(4).

Chadha, K., Shahriari, D., Tremblay, R., Bhattacharjee, P. P., & Jahazi, M. (2017). Deformation and Recrystallization Behavior of the Cast Structure in Large Size, High Strength Steel Ingots: Experimentation and Modeling. *Metallurgical and Materials Transactions A: Physical Metallurgy and Materials Science*, *48*(9). https://doi.org/10.1007/s11661-017-4177-8

Chae, D., & Koss, D. A. (2004). Damage accumulation and failure of HSLA-100 steel. *Materials Science and Engineering A*, *366*(2). https://doi.org/10.1016/j.msea.2003.08.040

Chamanfar, A., Jahazi, M., Gholipour, J., Wanjara, P., & Yue, S. (2014). Evolution of flow stress and microstructure during isothermal compression of Waspaloy. *Materials Science and Engineering A*, *615*, 497–510. https://doi.org/10.1016/j.msea.2014.07.093

Chegini, M., Aboutalebi, M. R., Seyedein, S. H., Ebrahimi, G. R., & Jahazi, M. (2020). Study on hot deformation behavior of AISI 414 martensitic stainless steel using 3D processing map. *Journal of Manufacturing Processes*, *56*. https://doi.org/10.1016/j.jmapro.2020.05.008

Chen, F., Cui, Z., & Chen, J. (2014). Prediction of microstructural evolution during hot forging. *Manufacturing Review*, *1*. https://doi.org/10.1051/mfreview/2014006

Chen, F., Ren, F., Chen, J., Cui, Z., & Ou, H. (2016a). Microstructural modeling and numerical simulation of multi-physical fields for martensitic stainless steel during hot forging process of turbine blade. *International Journal of Advanced Manufacturing Technology*, *82*(1–4). https://doi.org/10.1007/s00170-015-7368-8

Chen, F., Ren, F., Chen, J., Cui, Z., & Ou, H. (2016b). Microstructural modeling and numerical simulation of multi-physical fields for martensitic stainless steel during hot forging process of turbine blade. *International Journal of Advanced Manufacturing Technology*, *82*(1–4), 85–98. https://doi.org/10.1007/s00170-015-7368-8

Chen, Y., Luo, C., Zhang, F., Wei, J., & Zhao, Y. (2015). Effect of temperature on segregation and deformation mechanism of α+Ti2Cu alloy during semi-solid forging. *Xiyou Jinshu Cailiao Yu Gongcheng/Rare Metal Materials and Engineering*, *44*(6). https://doi.org/10.1016/s1875-5372(15)30091-6

Cho, J. R., Jeong, H. S., Cha, D. J., Bae, W. B., & Lee, J. W. (2005). Prediction of microstructural evolution and recrystallization behaviors of a hot working die steel by FEM. *Journal of Materials Processing Technology*, *160*(1). https://doi.org/10.1016/j.jmatprotec.2004.01.001

Choi, S. K., Chun, M. S., Van Tyne, C. J., & Moon, Y. H. (2006). Optimization of open die forging of round shapes using FEM analysis. *Journal of Materials Processing Technology*, *172*(1), 88–95. https://doi.org/10.1016/j.jmatprotec.2005.09.010

Clift, S. E., Hartley, P., Sturgess, C. E. N., & Rowe, G. W. (1990). Fracture prediction in plastic deformation processes. *International Journal of Mechanical Sciences*, *32*(1). https://doi.org/10.1016/0020-7403(90)90148-C

Cockcroft, M. G., & Latham, D. J. (1968). Ductility and the workability of metals. *J Inst MetalsJournal of the Institute of Metals*, Vol. 96.

Cojocaru, E. M., Nocivin, A., Răducanu, D., Angelescu, M. L., Cinca, I., Balkan, I. V., … Cojocaru, V. D. (2021). Microstructure evolution during hot deformation of uns s32750 super-duplex stainless steel alloy. *Materials*, *14*(14), 1–12. https://doi.org/10.3390/ma14143916

Cowie, J. G., & Tuler, F. R. (1991). The influence of second-phase dispersions on shear instability and fracture toughness of ultrahigh strength AISI 4340 steel. *Materials Science and Engineering A*, *141*(1). https://doi.org/10.1016/0921-5093(91)90704-Q

Davis, J. R. (1994). Asm Specialty Handbook: Stainless Steels. In *ASM International: Materials Park, OH* (Vol. 37).

De Oliveira, T. S., Silva, E. S., Rodrigues, S. F., Nascimento, C. C. F., Leala, V. S., & Reis, G. S. (2017). Softening mechanisms of the AISI 410 martensitic stainless steel under hot torsion simulation. *Materials Research*, *20*(2), 395–406. https://doi.org/10.1590/1980-5373-MR-2016-0795

Di Schino, A. (2021). Open die forging process simulation: a simplified industrial approach based on artificial neural network. *AIMS Materials Science*, *8*(5), 685–697. https://doi.org/10.3934/matersci.2021041

Dieter, G. E., Kuhn, H. a., & Semiatin, S. L. (2003). Handbook of Workability and Process Design. In *Handbook of Workability and Process Design*.

Dimiduk, D. M., Martin, P. L., & Kim, Y. W. (1998). Microstructure development in gamma alloy mill products by thermomechanical processing. *Materials Science and Engineering A*, *243*(1–2). https://doi.org/10.1016/s0921-5093(97)00780-6

Dindorf, R., & Wos, P. (2020). Energy-saving hot open die forging process of heavy steel forgings on an industrial hydraulic forging press. *Energies*, *13*(7). https://doi.org/10.3390/en13071620

Ding, H., Hirai, K., Homma, T., & Kamado, S. (2010). Numerical simulation for microstructure evolution in AM50 Mg alloy during hot rolling. *Computational Materials Science*, *47*(4), 919–925. https://doi.org/10.1016/j.commatsci.2009.11.024

Duan, X., & Sheppard, T. (2003). Simulation and control of microstructure evolution during hot extrusion of hard aluminium alloys. *Materials Science and Engineering A*, *351*(1–2), 282–292. https://doi.org/10.1016/S0921-5093(02)00840-7

Dudra, S. P., & Im, Y. T. (1990). Analysis of void closure in open-die forging. *International Journal of Machine Tools and Manufacture*, *30*(1). https://doi.org/10.1016/0890-6955(90)90042-H

Ebrahimi, G. R., Keshmiri, H., Maldad, A. R., & Momeni, A. (2012a). Dynamic Recrystallization Behavior of 13%Cr Martensitic Stainless Steel under Hot Working Condition. *Journal of Materials Science and Technology*, *28*(5), 467–473. https://doi.org/10.1016/S1005-0302(12)60084-X

Ebrahimi, G. R., Keshmiri, H., Maldad, A. R., & Momeni, A. (2012b). Dynamic Recrystallization Behavior of 13%Cr Martensitic Stainless Steel under Hot Working Condition. *Journal of Materials Science and Technology*, *28*(5). https://doi.org/10.1016/S1005-0302(12)60084-X

Ebrahimi, G. R., Keshmiri, H., Mazinani, M., Maldar, A., & Haghshenas, M. (2013). Multi-stage thermomechanical behavior of AISI 410 martensitic steel. *Materials Science and Engineering A*, *559*, 520–527. https://doi.org/10.1016/j.msea.2012.08.136

Ebrahimi, G. R., Keshmiri, H., & Momeni, A. (2011). Effect of heat treatment variables on microstructure and mechanical properties of 15Cr-4Ni-0.08C martensitic stainless steel. *Ironmaking and Steelmaking*, *38*(2), 123–128. https://doi.org/10.1179/030192310X12816231892468

Ebrahimi, G. R., Keshmiri, H., Momeni, A., & Mazinani, M. (2011). Dynamic recrystallization behavior of a superaustenitic stainless steel containing 16%Cr and 25%Ni. *Materials Science and Engineering A*, *528*(25–26). https://doi.org/10.1016/j.msea.2011.05.081

Ebrahimi, G. R., Momeni, A., & Ezatpour, H. R. (2018). Modeling the viscoplastic behavior and grain size in a hot worked Nb-bearing high-Mn steel. *Materials Science and Engineering A*, *714*(September 2017), 25–35. https://doi.org/10.1016/j.msea.2017.12.094

Ezatpour, H. R., Torabi-Parizi, M., Ebrahimi, G. R., & Momeni, A. (2018). Effect of Micro-Alloy Elements on Dynamic Recrystallization Behavior of a High-Manganese Steel. *Steel Research International*, *89*(7), 1–10. https://doi.org/10.1002/srin.201700559

F. A. Freudenthal, in The Inelastic Behaviour of Solids, John Wiley and Sons, New York, 1950, pp. 1–70.

Formenti, A., Eliasson, A., Mitchell, A., & Fredriksson, H. (2005). Solidification sequence and carbide precipitation in Ni-base superalloys IN718, IN625 and IN939. *High Temperature Materials and Processes*, *24*(4). https://doi.org/10.1515/HTMP.2005.24.4.239

Gao, P., Fu, M., Zhan, M., Lei, Z., & Li, Y. (2020). Deformation behavior and microstructure evolution of titanium alloys with lamellar microstructure in hot working process: A review. *Journal of Materials Science and Technology*, *39*. https://doi.org/10.1016/j.jmst.2019.07.052

Gao, P., Zhan, M., Fan, X., Lei, Z., & Cai, Y. (2017). Hot deformation behavior and microstructure evolution of TA15 titanium alloy with nonuniform microstructure. *Materials Science and Engineering A*, *689*. https://doi.org/10.1016/j.msea.2017.02.054

Garrison, W. M., & Amuda, M. O. H. (2017). Stainless Steels: Martensitic. *Reference Module in Materials Science and Materials Engineering*, (November 2015), 1–9. https://doi.org/10.1016/b978-0-12-803581-8.02527-3

Ghadar, S., Momeni, A., Tolaminejad, B., & Soltanalinezhad, M. (2019). A comparative study on the hot deformation behavior of 410 stainless and K100 tool steels. *Materials Science and Engineering A*, *760*. https://doi.org/10.1016/j.msea.2019.06.016

Ghazani, M. S., & Eghbali, B. (2018). A Ductile Damage Criterion for AISI 321 Austenitic Stainless Steel at Different Temperatures and Strain Rates. *Arabian Journal for Science and Engineering*, *43*(9), 4855–4861. https://doi.org/10.1007/s13369-018-3191-5

Goetz, R. L., & Semiatin, S. L. (2001). The adiabatic correction factor for deformation heating during the uniaxial compression test. *Journal of Materials Engineering and Performance*, *10*(6). https://doi.org/10.1361/105994901770344593

Guo, J., Liu, L. G., Li, Q., Sun, Y. L., Gao, Y. K., Ren, X. J., & Yang, Q. X. (2013). Characterization on carbide of a novel steel for cold work roll during solidification process. *Materials Characterization*, *79*. https://doi.org/10.1016/j.matchar.2013.02.011

Hallberg, H. (2011). Approaches to modeling of recrystallization. *Metals*, Vol. 1. https://doi.org/10.3390/met1010016

Hansel A, Spittel T. 1978. « Kraft- und Arbeitsbedarf bildsamer Formgeburgsverfahren.Leipzig ». VEB DeutscherVerlag fur Grundstoffindustrie.

Han, Y., Qiao, G., Sun, J., & Zou, D. (2013). A comparative study on constitutive relationship of as-cast 904L austenitic stainless steel during hot deformation based on Arrhenius-type and artificial neural network models. *Computational Materials Science*, *67*. https://doi.org/10.1016/j.commatsci.2012.07.028

Hauri, J., Graf, M., Awiszus, B., & Kawalla, R. (2018). Closing of shrinkage cavities by means of open-die forging. *Materials Science Forum*, *918 MSF*, 77–84. https://doi.org/10.4028/www.scientific.net/MSF.918.77

Higashi, K., Nieh, T. G., Mabuchi, M., & Wadsworth, J. (1995). Effect of liquid phases on the tensile elongation of superplastic aluminum alloys and composites. *Scripta Metallurgica et Materiala*, *32*(7). https://doi.org/10.1016/0956-716X(94)00003-Z

Hodgson, P. D., & Gibbs, R. K. (1992). A Mathematical Model to Predict the Mechanical Properties of Hot Rolled C-Mn and Microalloyed Steels. *ISIJ International*, *32*(12). https://doi.org/10.2355/isijinternational.32.1329

https://www.flukeprocessinstruments.com.

http://en.metsofts.ir/index.html.

https://alloysintl.com/closed-die-forging/

https://www.canforge.com/open-die-forging/

https://www.forgedproduct.com/open-die-forging.html

http://www.sorelforge.com/

https://www.steelforging.org/common-defects-of-steel-forgings/

https://www.totalmateria.com/

https://www.transvalor.com/

Hull, F. C. (1973). Delta Ferrite and Martensite Formation in Stainless Steels. *Welding Journal (Miami, Fla)*, *52*(5).

208

Humphreys, F. J., & Hatherly, M. (2004). Hot Deformation and Dynamic Restoration. *Recrystallization and Related Annealing Phenomena*, (1981), 415–V. https://doi.org/10.1016/b978-008044164-1/50017-7

Humphreys, F. J., & Matherly, M. (2004). 6.1.1 The occurrence of recovery. *Recrystallization and Related Annelaling Phenomena*, 437–444.

Ivaniski, T. M., Epp, J., Zoch, H. W., & Da Silva Rocha, A. (2019). Austenitic grain size prediction in hot forging of a 20mncr5 steel by numerical simulation using the JMAK model for industrial applications. *Materials Research*, *22*(5). https://doi.org/10.1590/1980-5373-MR-2019-0230

Jabbari Taleghani, M. A., Ruiz Navas, E. M., Salehi, M., & Torralba, J. M. (2012). Hot deformation behaviour and flow stress prediction of 7075 aluminium alloy powder compacts during compression at elevated temperatures. *Materials Science and Engineering A*, *534*. https://doi.org/10.1016/j.msea.2011.12.019

Jandová, D., Meyer, L. W., Mašek, B., Nový, Z., Kešner, D., & Motyčka, P. (2003). The influence of thermo-mechanical processing on the microstructure of steel 20MoCrS4. *Materials Science and Engineering A*, *349*(1–2). https://doi.org/10.1016/S0921-5093(02)00373-8

Jang, Y. S., Ko, D. C., & Kim, B. M. (2000). Application of the finite element method to predict microstructure evolution in the hot forging of steel. *Journal of Materials Processing Technology*, *101*(1), 85–94. https://doi.org/10.1016/S0924-0136(99)00460-4

Janovec, J., Svoboda, M., & Blach, J. (1998). Evolution of secondary phases 12% Cr steel during quenching and tempering. *Materials Science and Engineering A*, *249*(1–2). https://doi.org/10.1016/s0921-5093(98)00526-7

Jeong, H. S., Cho, J. R., & Park, H. C. (2005). Microstructure prediction of Nimonic 80A for large exhaust valve during hot closed die forging. *Journal of Materials Processing Technology*, *162–163*(SPEC. ISS.). https://doi.org/10.1016/j.jmatprotec.2005.02.101

Jiang, W. G., Wang, G. C., Lu, S. Q., & Li, J. W. (2007). Prediction of microstructure evolution of Al-1% Mg alloy during hot forming and sequential heat treatment. *Journal of Materials Processing Technology*, *182*(1–3). https://doi.org/10.1016/j.jmatprotec.2006.08.005

Jin, Z., Li, K., Wu, X., & Dong, H. (2015). Modelling of Microstructure Evolution during Thermoplastic Deformation of Steel by a Finite Element Method. *Materials Today: Proceedings*, *2*, S460–S465. https://doi.org/10.1016/j.matpr.2015.05.062

Johnson, G. R., & Cook, W. H. (1983). A constitutive model and data for metals subjected to large strains, high strain rates and high temperatures. The 7th International Symposium on Ballistics. *Proceedings of the 7th International Symposium on Ballistics*, *547*.

Jonas, J. J., & Poliak, E. I. (2003). The critical strain for dynamic recrystallization in rolling mills. *Materials Science Forum*, *426–432*(1), 57–66. https://doi.org/10.4028/www.scientific.net/msf.426-432.57

Jonas, J. J., Quelennec, X., Jiang, L., & Martin, É. (2009). The Avrami kinetics of dynamic recrystallization. *Acta Materialia*, *57*(9), 2748–2756. https://doi.org/10.1016/j.actamat.2009.02.033

Kakimoto, H., & Arikawa, T. (2014). Prediction of surface crack in hot forging by numerical simulation. *Procedia Engineering*, *81*(October), 474–479. https://doi.org/10.1016/j.proeng.2014.10.025

Kane, S. N., Mishra, A., & Dutta, A. K. (2016). Preface: International Conference on Recent Trends in Physics (ICRTP 2016). *Journal of Physics: Conference Series*, *755*(1). https://doi.org/10.1088/1742-6596/755/1/011001

Katajarinne, T., Somani, M., Karjalainen, P., & Porter, D. (2004). Evolution of non-uniform grain structure during hot deformation of a Nb-Ti microalloyed steel. *Revista de Metalurgia (Madrid)*, *40*(5), 329–334. https://doi.org/10.3989/revmetalm.2004.v40.i5.283

Kawulok, P., Opěla, P., Schindler, I., Kawulok, R., Rusz, S., Sauer, M., & Konečná, K. (2022). Hot Deformation Behavior of Non-Alloyed Carbon Steels. *Materials*, *15*(2). https://doi.org/10.3390/ma15020595

Kim, S. Il, & Yoo, Y. C. (2001). Dynamic recrystallization behavior of AISI 304 stainless steel. *Materials Science and Engineering A*, *311*(1–2). https://doi.org/10.1016/S0921-5093(01)00917-0

Kim, W. J., & Jeong, H. T. (2020). Easy construction of processing maps for metallic alloys using a flow instability criterion based on power-law breakdown. *Journal of Materials Research and Technology*, *9*(3). https://doi.org/10.1016/j.jmrt.2020.03.030

Kim, Y., Cho, J., & Bae, W. (2011). Efficient forging process to improve the closing effect of the inner void on an ultra-large ingot. *Journal of Materials Processing Technology*, *211*(6), 1005–1013. https://doi.org/10.1016/j.jmatprotec.2011.01.001

Kipelova, A., Belyakov, A., & Kaibyshev, R. (2013). The crystallography of M23C6 carbides in a martensitic 9% Cr steel after tempering, aging and creep. *Philosophical Magazine*, *93*(18). https://doi.org/10.1080/14786435.2013.765995

Kotous, J., Kubec, V., Duchek, M., & Studecký, T. (2020). Optimization of workability technological testing for open-die forging. *IOP Conference Series: Materials Science and Engineering*, *723*(1). https://doi.org/10.1088/1757-899X/723/1/012015

Krauss, G. (1999). Martensite in steel: Strength and structure. *Materials Science and Engineering A*, *273–275*, 40–57. https://doi.org/10.1016/s0921-5093(99)00288-9

Krishna, R. H., & Jena, D. P. (2019). Analytical and numerical modelling of open-die forging process for elliptical cross-section of billet. *Measurement: Journal of the International Measurement Confederation*, *134*, 855–865. https://doi.org/10.1016/j.measurement.2018.12.023

Kukuryk, M. (2021). Analysis of deformation, the stressed state and fracture predictions for cogging shafts with convex anvils. *Materials*, *14*(11). https://doi.org/10.3390/ma14113113

Kwon, D., & Asaro, R. J. (1990). A study of void nucleation, growth, and coalescence in spheroidized 1518 steel. *Metallurgical Transactions A*, *21*(1). https://doi.org/10.1007/BF02656430

Laasraoui, A., & Jonas, J. J. (1991). Prediction of steel flow stresses at high temperatures and strain rates. *Metallurgical Transactions A*, *22*(7). https://doi.org/10.1007/BF02667368

Li, S., Li, L., He, H., & Wang, G. (2019). Influence of the deformation heating on the flow behavior of 6063 alloy during compression at medium strain rates. *Journal of Materials Research*, *34*(2). https://doi.org/10.1557/jmr.2018.367

Li, W., Liang, C., & Zhang, X. (2022). Numerical simulation of microstructure evolution of high-purity tantalum during rolling and annealing. *Modelling and Simulation in Materials Science and Engineering*, *30*(3). https://doi.org/10.1088/1361-651X/ac4d78

Li, Y., Liu, J., Zhang, Q., & Huang, W. (2021). Casting defects and microstructure distribution characteristics of aluminum alloy cylinder head with complex structure. *Materials Today Communications*, *27*. https://doi.org/10.1016/j.mtcomm.2021.102416

Li, Y. P., Onodera, E., Matsumoto, H., & Chiba, A. (2009). Correcting the stress-strain curve in hot compression process to high strain level. *Metallurgical and Materials Transactions A: Physical Metallurgy and Materials Science*, *40*(4). https://doi.org/10.1007/s11661-009-9783-7

Liang, Q., Liu, X., Li, P., Ding, P., & Zhang, X. (2020). Development and application of high-temperature constitutive model of hni55-7-4-2 alloy. *Metals*, *10*(9). https://doi.org/10.3390/met10091250

Lin, Y. C., Chen, M. S., & Zhong, J. (2008). Numerical simulation for stress/strain distribution and microstructural evolution in 42CrMo steel during hot upsetting process. *Computational Materials Science*, *43*(4), 1117–1122. https://doi.org/10.1016/j.commatsci.2008.03.010

Lin, Yong Cheng, & Chen, M. S. (2009). Numerical simulation and experimental verification of microstructure evolution in a three-dimensional hot upsetting process. *Journal of Materials Processing Technology*, *209*(9), 4578–4583. https://doi.org/10.1016/j.jmatprotec.2008.10.036

Lin, Yong Cheng, Chen, M. S., & Zhang, J. (2009). Modeling of flow stress of 42CrMo steel under hot compression. *Materials Science and Engineering A*, *499*(1–2). https://doi.org/10.1016/j.msea.2007.11.119

Loucif, A., Ben Fredj, E., Harris, N., Shahriari, D., Jahazi, M., & Lapierre-Boire, L. P. (2018). Evolution of A-Type Macrosegregation in Large Size Steel Ingot After Multistep Forging and Heat Treatment. *Metallurgical and Materials Transactions B: Process Metallurgy and Materials Processing Science*, *49*(3), 1046–1055. https://doi.org/10.1007/s11663-018-1255-2

Loucif, A., Shahriari, D., Zhang, C. P., Jahazi, M., Lapierre-Boire, L. P., & Tremblay, R. (2017). Macrosegregation of alloying elements in hot top of large size high strength steel ingot. *Materials Science Forum*, *879*. https://doi.org/10.4028/www.scientific.net/MSF.879.1176

Loucif, A., Zhang, C., Jahazi, M., & Lapierre-Boire, L. P. (2020). Macrosegregation characteristics of ferrite and austenite stabilizer elements in large size high strength steel ingot. *Key Engineering Materials*, *846 KEM*. https://doi.org/10.4028/www.scientific.net/KEM.846.82

Lu, S. Y., Yao, K. F., Chen, Y. B., Wang, M. H., Liu, X., & Ge, X. (2015). The effect of tempering temperature on the microstructure and electrochemical properties of a 13 wt.% Cr-type martensitic stainless steel. *Electrochimica Acta*, *165*, 45–55. https://doi.org/10.1016/j.electacta.2015.02.038

Ma, D. shen, Chi, H. xiao, Zhou, J., & Yong, Q. long. (2012). Microstructure and Mechanical Properties of Martensitic Stainless Steel 6Cr15MoVn. *Journal of Iron and Steel Research International*, *19*(3), 56–61. https://doi.org/10.1016/S1006-706X(12)60074-0

Ma, Q., Lin, Z. Q., & Yu, Z. Q. (2009). Prediction of deformation behavior and microstructure evolution in heavy forging by FEM. *International Journal of Advanced Manufacturing Technology*, *40*(3–4), 253–260. https://doi.org/10.1007/s00170-007-1337-9

Mahmoudi, B., Torkamany, M. J., Sabour Aghdam, A. R., & Sabbaghzadeh, J. (2011). Effect of laser surface hardening on the hydrogen embrittlement of AISI 420: Martensitic stainless steel. *Materials and Design*, *32*(5). https://doi.org/10.1016/j.matdes.2011.01.028

Marchattiwar, A., Sarkar, A., Chakravartty, J. K., & Kashyap, B. P. (2013). Dynamic recrystallization during hot deformation of 304 austenitic stainless steel. *Journal of Materials Engineering and Performance*, *22*(8). https://doi.org/10.1007/s11665-013-0496-0

Matsubara, Y., Sasaguri, N., Shimizu, K., & Kon Yu, S. (2001). Solidification and abrasion wear of white cast irons alloyed with 20% carbide forming elements. *Wear*, *250–251*(1–12). https://doi.org/10.1016/S0043-1648(01)00599-3

McQueen, H. J., & Jonas, J. J. (1975). RECOVERY AND RECRYSTALLIZATION DURING HIGH TEMPERATURE DEFORMATION. *Plast Deform of Mater*. https://doi.org/10.1016/b978-0-12-341806-7.50014-3

McQueen, H. J., & Ryan, N. D. (2002). Constitutive analysis in hot working. *Materials Science and Engineering A*, *322*(1–2). https://doi.org/10.1016/S0921-5093(01)01117-0

Miettinen, J. (1997). Calculation of solidification-related thermophysical properties for steels. *Metallurgical and Materials Transactions B: Process Metallurgy and Materials Processing Science*, *28*(2). https://doi.org/10.1007/s11663-997-0095-2

Miotti Bettanini, A., Hannard, F., Mithieux, J. D., Badinier, G., Jacques, P. J., Pardoen, T., & Delannay, L. (2018). Residual ferrite in martensitic stainless steels: The effect of mechanical strength contrast on ductility. *Materials Science and Engineering A*, *731*(April), 495–505. https://doi.org/10.1016/j.msea.2018.06.012

Momeni, A., & Dehghani, K. (2010a). Characterization of hot deformation behavior of 410 martensitic stainless steel using constitutive equations and processing maps. *Materials Science and Engineering A*, *527*(21–22), 5467–5473. https://doi.org/10.1016/j.msea.2010.05.079

Momeni, A., & Dehghani, K. (2010b). Prediction of dynamic recrystallization kinetics and grain size for 410 martensitic stainless steel during hot deformation. *Metals and Materials International*, *16*(5), 843–849. https://doi.org/10.1007/s12540-010-1024-5

Momeni, A., Dehghani, K., Heidari, M., & Vaseghi, M. (2012). Modeling the flow curve of AISI 410 martensitic stainless steel. *Journal of Materials Engineering and Performance*, *21*(11). https://doi.org/10.1007/s11665-012-0172-9

Momeni, A., Ebrahimi, G. R., Jahazi, M., & Bocher, P. (2014). Microstructure evolution at the onset of discontinuous dynamic recrystallization: A physics-based model of subgrain critical size. *Journal of Alloys and Compounds*, *587*, 199–210. https://doi.org/10.1016/j.jallcom.2013.10.180

Monajati, H., Jahazi, M., Yue, S., & Taheri, A. K. (2005). Deformation characteristics of isothermally forged UDIMET 720 nickel-base superalloy. *Metallurgical and Materials Transactions A: Physical Metallurgy and Materials Science*, *36*(4), 895–905. https://doi.org/10.1007/s11661-005-0284-z

Moore, J. J., & Shah, N. A. (1983). Mechanisms of formation of a- and v-segregation in cast steel. *International Metals Reviews*, *28*(1). https://doi.org/10.1179/imtr.1983.28.1.336

Na, Y. S., Yeom, J. T., Park, N. K., & Lee, J. Y. (2003). Simulation of microstructures for Alloy 718 blade forging using 3D FEM simulator. *Journal of Materials Processing Technology*, *141*(3). https://doi.org/10.1016/S0924-0136(03)00285-1

Nanba, S., Kitamura, M., Shimada, M., Katsumata, M., Inoue, T., Imamura, H., … Hattori, S. (1992). Prediction of Microstructure Distribution in the Through-thickness Direction during and after Hot Rolling in Carbon Steels. *ISIJ International*, *32*(3). https://doi.org/10.2355/isijinternational.32.377

Nasraoui, M., Forquin, P., Siad, L., & Rusinek, A. (2012). Influence of strain rate, temperature and adiabatic heating on the mechanical behaviour of poly-methyl-methacrylate: Experimental and modelling analyses. *Materials and Design*, *37*. https://doi.org/10.1016/j.matdes.2011.11.032

Niessen, F., Tiedje, N. S., & Hald, J. (2017). Kinetics modeling of delta-ferrite formation and retainment during casting of supermartensitic stainless steel. *Materials and Design*, *118*, 138–145. https://doi.org/10.1016/j.matdes.2017.01.026

Oyane, M., Sato, T., Okimoto, K., & Shima, S. (1980). Criteria for ductile fracture and their applications. *Journal of Mechanical Working Technology*, *4*(1). https://doi.org/10.1016/0378-3804(80)90006-6

Park, N. K., Kim, I. S., Na, Y. S., & Yeom, J. T. (2001). Hot forging of a nickel-base superalloy. *Journal of Materials Processing Technology*, *111*(1–3). https://doi.org/10.1016/S0924-0136(01)00489-7

Pasoodeh, B., Alimirzaloo, V., & Tagimalek, H. (2021). The Numerical and experimental evaluation of upsetting process of hexagonal cylindrical billet of AISI-1045 steel The Numerical and experimental evaluation of upsetting process of hexagonal cylindrical billet of AISI-1045 steel. (August).

Pickering, E. J. (2013). Macrosegregation in steel ingots: The applicability of modelling and characterisation techniques. *ISIJ International*, Vol. 53. https://doi.org/10.2355/isijinternational.53.935

Pineda, D. A., & Martorano, M. A. (2013). Columnar to equiaxed transition in directional solidification of inoculated melts. *Acta Materialia*, *61*(5). https://doi.org/10.1016/j.actamat.2012.12.002

Poliak, E. I., & Jonas, J. J. (1996). A one-parameter approach to determining the critical conditions for the initiation of dynamic recrystallization. *Acta Materialia*, *44*(1). https://doi.org/10.1016/1359-6454(95)00146-7

Porter, D. A., Easterling, K. E., & Sherif, M. Y. (2021). Phase Transformations in Metals and Alloys, Fourth Edition. In *Phase Transformations in Metals and Alloys, Fourth Edition*. https://doi.org/10.1201/9781003011804

Prasad, Y. V. R. K. (2013). Processing maps: A status report. *Journal of Materials Engineering and Performance*, *22*(10), 2867–2874. https://doi.org/10.1007/s11665-013-0732-7

Prasad, Y. V. R. K., Rao, K. P., & Sasidhara, S. (2015). Hot Working Guide: A Compendium of Processing Maps. In *ASM International*.

Pu, E., Zheng, W., Xiang, J., Song, Z., & Li, J. (2014). Hot deformation characteristic and processing map of superaustenitic stainless steel S32654. *Materials Science and Engineering A*, *598*. https://doi.org/10.1016/j.msea.2014.01.027

Qi, R. S., Jin, M., Guo, B. F., Liu, X. G., & Chen, L. (2015). Hot-deformation behavior and hot-processing maps of AISI 410 martensitic stainless steel. *High Temperature Materials and Processes*, *2015*(9), 929–940. https://doi.org/10.1515/htmp-2015-0145

Qin, F., Zhu, H., Wang, Z., Zhao, X., He, W., & Chen, H. (2017). Dislocation and twinning mechanisms for dynamic recrystallization of as-cast Mn18Cr18N steel. *Materials Science and Engineering A*, *684*. https://doi.org/10.1016/j.msea.2016.12.095

Qin, X. yu, Su, Y., Chen, J., & Liu, L. jun. (2019). Finite element analysis for die casting parameters in high-pressure die casting process. *China Foundry*, *16*(4). https://doi.org/10.1007/s41230-019-8088-8

Quan, G. Z., Kang, B. S., Ku, T. W., & Song, W. J. (2011). Identification for the optimal working parameters of Al-Zn-Mg-Cu alloy with the processing maps based on DMM. *International Journal of Advanced Manufacturing Technology*, *56*(9–12), 1069–1078. https://doi.org/10.1007/s00170-011-3241-6

Quan, G. Z., Li, G. S., Chen, T., Wang, Y. X., Zhang, Y. W., & Zhou, J. (2011). Dynamic recrystallization kinetics of 42CrMo steel during compression at different temperatures and strain rates. *Materials Science and Engineering A*, *528*(13–14), 4643–4651. https://doi.org/10.1016/j.msea.2011.02.090

Rao, K. P., Prasad, Y. V. R. K., & Suresh, K. (2011). Hot working behavior and processing map of a γ-TiAl alloy synthesized by powder metallurgy. *Materials and Design*, *32*(10). https://doi.org/10.1016/j.matdes.2011.06.003

Ren, F. C., Chen, J., & Chen, F. (2014). Constitutive modeling of hot deformation behavior of X20Cr13 martensitic stainless steel with strain effect. *Transactions of Nonferrous Metals Society of China (English Edition)*, *24*(5), 1407–1413. https://doi.org/10.1016/S1003-6326(14)63206-4

Rudra, A., Das, S., & Dasgupta, R. (2019). Constitutive Modeling for Hot Deformation Behavior of Al-5083 + SiC Composite. *Journal of Materials Engineering and Performance*, *28*(1). https://doi.org/10.1007/s11665-018-3813-9

216

Ruijie, Z., Chunlei, Z., Bo, L., Peijun, Z., Guhui, G., Yongqiang, Y., & Fucheng, Z. (2022). Effect of non-uniform microstructure on rolling contact fatigue performance of bainitic rail steel. *International Journal of Fatigue*, *159*(October 2021). https://doi.org/10.1016/j.ijfatigue.2022.106795

Saksala, T. (2019). Numerical modeling of adiabatic heat generation during rock fracture under dynamic loading. *International Journal for Numerical and Analytical Methods in Geomechanics*, *43*(9). https://doi.org/10.1002/nag.2935

Samantaray, D., Mandal, S., & Bhaduri, A. K. (2009). A comparative study on Johnson Cook, modified Zerilli-Armstrong and Arrhenius-type constitutive models to predict elevated temperature flow behaviour in modified 9Cr-1Mo steel. *Computational Materials Science*, *47*(2). https://doi.org/10.1016/j.commatsci.2009.09.025

Sanrutsadakorn, A., Uthaisangsuk, V., Suranuntchai, S., & Thossatheppitak, B. (2012). Finite element modeling for hot forging process of AISI 4340 steel. *Advanced Materials Research*, *410*. https://doi.org/10.4028/www.scientific.net/AMR.410.263

Sellars, C. M., & McTegart, W. J. (1966). On the mechanism of hot deformation. *Acta Metallurgica*, Vol. 14. https://doi.org/10.1016/0001-6160(66)90207-0

Sellars, C. M., & Whiteman, J. A. (1979). Recrystallization and grain growth'in hot rolling. *Metal Science*, *13*(3–4). https://doi.org/10.1179/msc.1979.13.3-4.187

Shokry, A., Gowid, S., Kharmanda, G., & Mahdi, E. (2019). Constitutive models for the prediction of the hot deformation behavior of the 10%Cr steel alloy. *Materials*, *12*(18). https://doi.org/10.3390/ma12182873

Sneddon, I. N., Hill, R., & Jahsman, W. E. (1965). Progress in Solid Mechanics, vol. 4. *Journal of Applied Mechanics*, *32*(2), 478–479. https://doi.org/10.1115/1.3625865

Srinivasan, N., Prasad, Y. V. R. K., & Rama Rao, P. (2008). Hot deformation behaviour of Mg-3Al alloy-A study using processing map. *Materials Science and Engineering A*, *476*(1–2). https://doi.org/10.1016/j.msea.2007.04.103

Stone, D. J., Alexandrov, B. T., & Penso, J. A. (2017). Control of retained delta ferrite in type 410 stainless steel. *American Society of Mechanical Engineers, Pressure Vessels and Piping Division (Publication) PVP*, *6A-2017*. https://doi.org/10.1115/PVP2017-65543

Suwas, S., & Ray, R. K. (2014). *Texture Evolution During Solidification and Solid-State Transformation*. https://doi.org/10.1007/978-1-4471-6314-5_4

Tang, B., Cheng, L., Kou, H., & Li, J. (2015). Hot forging design and microstructure evolution of a high Nb containing TiAl alloy. *Intermetallics*, *58*. https://doi.org/10.1016/j.intermet.2014.11.002

Uddagiri, M., Spee, J., Hubig, S., & Steinbach, I. (2020). Columnar-equiaxed transition in continuous casting based on a micro-macro solidification model with long-range solutal mixing. *IOP Conference Series: Materials Science and Engineering*, *861*(1). https://doi.org/10.1088/1757-899X/861/1/012014

Vaandrager, B. L., & Pharr, G. M. (1989). Compressive creep of copper containing a liquid bismuth intergranular phase. *Acta Metallurgica*, *37*(4). https://doi.org/10.1016/0001-6160(89)90102-8

Venugopal, S., Mannan, S. L., & Prasad, Y. V. R. K. (1992). Processing map for cold and hot working of stainless steel type AISI 304 L. *Materials Letters*, *15*(1–2). https://doi.org/10.1016/0167-577X(92)90016-D

Wang, S., Yang, B., Zhang, M., Wu, H., Peng, J., & Gao, Y. (2016). Numerical simulation and experimental verification of microstructure evolution in large forged pipe used for AP1000 nuclear power plants. *Annals of Nuclear Energy*, *87*(P2), 176–185. https://doi.org/10.1016/j.anucene.2015.07.042

Wang, Z., Xue, H., & Zhao, D. (2018). Microstructure evolution and surface cracking behavior of superheavy forgings during hot forging. *Advances in Materials Science and Engineering*, *2018*, 1–10. https://doi.org/10.1155/2018/4780638

Wei, H. lian, Liu, G. quan, Xiao, X., Zhao, H. tao, Ding, H., & Kang, R. mu. (2013). Characterization of hot deformation behavior of a new microalloyed C-Mn-Al high-strength steel. *Materials Science and Engineering A*, *564*, 140–146. https://doi.org/10.1016/j.msea.2012.11.099

Wen, D. X., Wang, J. K., Wang, K., Xiong, Y. B., Huang, L., Zheng, Z. Z., & Li, J. J. (2019). Hot tensile deformation and fracture behaviors of a typical ultrahigh strength steel. *Vacuum*, *169*. https://doi.org/10.1016/j.vacuum.2019.108863

Wolfgarten, M., & Hirt, G. (2016). New method for the manufacturing of curved workpieces by open-die forging. *CIRP Annals - Manufacturing Technology*, *65*(1), 285–288. https://doi.org/10.1016/j.cirp.2016.04.125

Wolfgarten, M., Rudolph, F., & Hirt, G. (2020). Analysis of process forces and geometrical correlations for open-die forging with superimposed manipulator displacements. *Journal of Materials Processing Technology*, *276*(September 2019), 116408. https://doi.org/10.1016/j.jmatprotec.2019.116408

Wu, X. Q., Jing, H. M., Zheng, Y. G., Yao, Z. M., Ke, W., & Hu, Z. Q. (2000). The eutectic carbides and creep rupture strength of 25Cr20Ni heat-resistant steel tubes centrifugally cast with different solidification conditions. *Materials Science and Engineering A*, *293*(1–2). https://doi.org/10.1016/S0921-5093(00)00984-9

Xiao, W., Wang, B., Wu, Y., & Yang, X. (2018). Constitutive modeling of flow behavior and microstructure evolution of AA7075 in hot tensile deformation. *Materials Science and Engineering A*, *712*. https://doi.org/10.1016/j.msea.2017.12.028

YE, X. jue, GONG, X. juan, YANG, B. biao, LI, Y. ping, & NIE, Y. (2019). Deformation inhomogeneity due to sample–anvil friction in cylindrical compression test. *Transactions of Nonferrous Metals Society of China (English Edition)*, *29*(2). https://doi.org/10.1016/S1003-6326(19)64937-X

Yeom, J. T., Kim, J. H., Park, N. K., Choi, S. S., & Lee, C. S. (2007). Ring-rolling design for a large-scale ring product of Ti-6Al-4V alloy. *Journal of Materials Processing Technology*, *187–188*. https://doi.org/10.1016/j.jmatprotec.2006.11.042

Zhang, C., Loucif, A., Jahazi, M., & Morin, J. B. (2022). FE modelling and prediction of macrosegregation patterns in large size steel ingots: Influence of filling rate. *Metals*, *12*(1). https://doi.org/10.3390/met12010029

Zhang, C., Loucif, A., Jahazi, M., Tremblay, R., & Lapierre, L. P. (2018). On the effect of filling rate on positive macrosegregation patterns in large size cast steel ingots. *Applied Sciences (Switzerland)*, *8*(10). https://doi.org/10.3390/app8101878

Zhang, Y., Guo, B., Li, Q., Li, X., Jian, J., Jin, Y., & Ao, J. (2021). Damage and Cracking Prediction of AISI 410 Martensitic Stainless Steel at Elevated Temperatures. *Steel Research International*, *92*(9). https://doi.org/10.1002/srin.202100030

Zhbankov, I., Aliieva, L., & Malii, K. (2020). Simulation of microstructure changes of steel during the open die forging process. *Journal of Chemical Technology and Metallurgy*, *55*(3), 523–529.

Zhou, B., Shen, Y., Chen, J., & Cui, Z. shan. (2011). Breakdown Behavior of Eutectic Carbide in High Speed Steel During Hot Compression. *Journal of Iron and Steel Research International*, *18*(1), 41–48. https://doi.org/10.1016/S1006-706X(11)60009-5

Zhou, Xiaoqin, Ma, W., Feng, C., & Zhang, L. (2020). Flow stress modeling, processing maps and microstructure evolution of 05Cr17Ni4Cu4Nb Martensitic stainless steel during hot plastic deformation. *Materials Research Express*, *7*(4). https://doi.org/10.1088/2053-1591/ab89d8

Zhou, Xuefeng, Fang, F., Gang, L. I., & Jiang, J. (2010). Morphology and properties of M2C eutectic carbides in AISI M2 steel. *ISIJ International*, *50*(8). https://doi.org/10.2355/isijinternational.50.1151

Zhou, Y., Lin, X., Kang, N., Wang, Z., Tan, H., & Huang, W. (2021). Hot deformation induced microstructural evolution in local-heterogeneous wire + arc additive manufactured 2219 Al alloy. *Journal of Alloys and Compounds*, *865*, 158949. https://doi.org/10.1016/j.jallcom.2021.158949

Zhou, Z., Fan, Q., Xia, Z., Hao, A., Yang, W., Ji, W., & Cao, H. (2017). Constitutive Relationship and Hot Processing Maps of Mg-Gd-Y-Nb-Zr Alloy. *Journal of Materials Science and Technology*, *33*(7). https://doi.org/10.1016/j.jmst.2015.10.019